BUREAU OF RECLAMATION

Technical Memorandum 86-68330-2020-07

Analysis of the March 4th, 2019 M_W 4.5 Earthquake and Its Aftershocks

Paradox Valley Unit, Colorado

Colorado River Basin Salinity Control Project
Upper Colorado Region

U.S. Department of the Interior **July 2020**

Mission Statements

The Department of the Interior (DOI) conserves and manages the Nation's natural resources and cultural heritage for the benefit and enjoyment of the American people, provides scientific and other information about natural resources and natural hazards to address societal challenges and create opportunities for the American people, and honors the Nation's trust responsibilities or special commitments to American Indians, Alaska Natives, and affiliated island communities to help them prosper.

The mission of the Bureau of Reclamation is to manage, develop, and protect water and related resources in an environmentally and economically sound manner in the interest of the American public.

Technical Memorandum 86-68330-2020-07

Analysis of the March 4th, 2019 M_W 4.5 Earthquake and Its Aftershocks

Paradox Valley Unit, Colorado

Colorado River Basin Salinity Control Project
Upper Colorado Region

Prepared by:

Bureau of Reclamation
Technical Service Center
Denver, Colorado

U.S. Department of the Interior **July 2020**

Acronyms and Abbreviations

3-D	three-dimensional
ft	feet
gpm	gallons per minute
km	kilometers
l/min	liters per minute
M_D	duration magnitude
mi	miles
M_L	local magnitude
MPa	Megapascal
M_W	Moment magnitude
NE	northeast
NW	northwest
psi	pounds per square inch
PVSN	Paradox Valley Seismic Network
PVU	Paradox Valley Unit
SE	southeast
SLU	Saint Louis University
SW	southwest
USBR	Bureau of Reclamation
U. S.	United States
USGS	United States Geological Survey
UTC	Coordinated Universal Time
UUSS	University of Utah Seismograph Stations

`

Technical Memorandum 86-68330-2020-07

Technical Approval

The results provided in this report are technically sound and consistent with current Reclamation practice.

LISA BLOCK
Digitally signed by LISA BLOCK
Date: 2020.07.26 13:36:32 -06'00'

Lisa Block, Geophysicist — Date

GLENDA BESANA-OSTMAN
Digitally signed by GLENDA BESANA-OSTMAN
Date: 2020.07.26 13:54:42 -06'00'

Glenda Besana-Ostman, Geophysicist — Date

Christopher M Wood
CHRISTOPHER WOOD
2020.07.27 08:59:13 -06'00'

Christopher Wood, Geophysicist — Date

Peer Review Certification

This document has been reviewed and is believed to be in accordance with the standards of the profession.

07 / 31 / 2020
Date

Jacob Walter, Geophysicist

Acknowledgements

The work described in this report and the continuous operation of the Paradox Valley Seismic Network (PVSN) are made possible through the considerable assistance and support of Andy Nicholas, site Project Manager at the Paradox Valley Unit, Bedrock, Colorado. We thank Scott Nakamura and Eric Mccaffery for valuable technical support of the PVSN data acquisition computer systems. We are grateful to Brad McKinney, Nucla Airport Manager, for supporting our operations there. We thank Justin Schwarzer and Justin Rittgers for help processing aftershocks of the March 2019 earthquake and Justin Ball and Justin Schwarzer for support of PVSN field sites.

`

Contents

Figures

`

`

`

`

Tables

Executive Summary

A widely felt earthquake occurred near the Paradox Valley Unit (PVU) injection well on March 4th, 2019, at 10:22:52 am local time (17:22:52 UTC time). Reports submitted by the public to a U. S. Geological Survey website indicate that ground shaking was felt as far as ~240 km (~150 miles) from the earthquake's epicenter. The strongest shaking reported was intensity V on the Modified Mercalli Intensity Scale, corresponding to moderate shaking. This level of shaking can produce very light damage, such as breaking of dishes and windows and overturning of unstable objects.

The earthquake was recorded by the Paradox Valley Seismic Network (PVSN), a local dense seismic array operated by the Bureau of Reclamation as a component of PVU. Analyses of the seismic data recorded by PVSN indicate that the March 2019 earthquake was induced by PVU brine injection. It is the largest PVU-induced earthquake to date, with a moment magnitude of M_W 4.5 (as reported by the University of Utah and U.S. Geological Survey). The earthquake's epicenter is 1.6 km southwest of the PVU injection well, at a location that has experienced induced seismicity since 1998. The focal depth of the earthquake is 3.9 km, consistent with the depths of previously induced events in this area and with the depths of injection target formations.

Precursors to the earthquake were not observed. No increase in the rates or maximum magnitudes of earthquakes in the vicinity of the M_W 4.5 earthquake, or anywhere within 10 km of the injection well, was observed in the year preceding the main shock. Rather, seismicity rates had decreased in 2018 compared to 2017 and remained low during the first two months of 2019, until the time of the M_W 4.5 earthquake on March 4th.

More than 2000 aftershocks were recorded through the end of August 2019. Six of these aftershocks have duration magnitude $\geq M_D$ 2.5, large enough to be potentially felt within Paradox Valley. The largest aftershock was an M_D 3.0 (M_W 2.5) earthquake that occurred on April 18th. Aftershocks have occurred as far as 1.7 km from the fault plane that ruptured during the March 4th main shock, indicating that the fault plane rupture altered stress conditions over a wide area. Aftershocks are expected to continue for years, at gradually decreasing rates.

Although the large number of aftershocks increased seismicity rates within 5 km of the PVU injection well to their highest levels in 20 years, analyses indicate that the occurrence of these events can be attributed solely to stress re-distribution from the fault plane rupture that occurred during the M_W 4.5 earthquake. These high near-well seismicity rates do not appear to indicate any other change in reservoir conditions, such as a breach of the confining layer. The temporal decay rate of the aftershocks fits the modified Omori aftershock relation with a reasonable range of parameters. Also, the spatial aftershock distribution is compared to initial Coulomb stress change modeling results presented in this study. Results indicate that the Coulomb stress change from the main shock fault rupture is generally consistent with the observed spatial pattern of aftershock distribution.

The earthquake rupture occurred on a fault striking ~N58°E and dipping 60° to 65° southeast. A fault zone consistent with the main shock focal mechanism is delineated by the aftershock distribution and is approximately 1.3 to 1.6 km in length with a vertical height of ~1 km and an along-dip height of ~1.15 km. This interpreted rupture plane extends from near the top of the primary target injection formation, the Leadville Limestone formation, into the Precambrian basement. The aftershocks also delineate a shallower, more steeply dipping (~78-80°) fault zone that extends upward from the Leadville formation to just above the Paradox salt, which is the confining layer for PVU injection. This aftershock zone may represent either an extension of the main shock rupture to shallower depths or slip on one or more steeply dipping faults due to stress redistribution following the main shock fault rupture. The main shock fault rupture appears to be bounded to the west by a major NW-trending fault that has been previously interpreted as forming a barrier to fluid flow and pore pressure diffusion from PVU injection.

Although the analyses completed to date do not definitively indicate whether the fault plane of the M_W 4.5 earthquake ruptured through the Paradox salt confining layer, they do provide evidence that the Paradox salt is acting as an effective confining layer for PVU injection. Aftershocks in the Leadville and deeper formations show distinctly different magnitude distributions, maximum magnitudes, and decay rates than the aftershocks occurring just above the Paradox salt confining layer. The different aftershock characteristics above and below the Paradox salt indicate that these regions have substantially different stress and pressure regimes, as would be expected if the Paradox salt is acting as an effective injection confining layer.

Based on an analytical flow model, the pore pressure at the time and hypocenter location of the March 4th earthquake was ~3750 psi above the pre-injection hydrostatic level, which corresponds to ~162% of the pre-injection pressure. Operational changes implemented in early 2017, which included a ~one-month shut-in and subsequent 5% decrease in flow rate, had caused pore pressure in this area to temporarily decrease. These operational changes were made in response to gradually increasing rates and magnitudes of induced earthquakes in late 2015 to early 2017. The pressure had just recovered from these operational changes and was at its maximum value at the time of the M_W 4.5 earthquake. By the end of October 2019, pore pressure at this location had declined by approximately 385 psi, to ~156% of its pre-injection value.

Prior to 2013, the pore pressure at the location of the March 4th earthquake decreased twice a year in response to biennial 20-day injection well shut-ins. Since 2013, when these extended biennial shut-ins were replaced with much shorter weekly shut-ins, the pore pressure at this location has been increasing very slowly but almost continuously (except for a relatively brief period following the 2017 injection well shut-in). In addition, spatial pressure gradients have decreased over time as average PVU injection flow rates have been reduced. Hence, at the time of the M_W 4.5 earthquake, pore pressure had been increasing mostly uninterrupted for nearly six years, and relatively large areas were likely experiencing similar pressure increases because spatial pressure gradients were low. The same pressure trends have been cited by others as contributing to the occurrence of large-magnitude induced earthquakes following injection well shut-ins and could potentially have contributed to the occurrence of the March 4th earthquake.

Previous analyses of PVU-induced seismicity indicate that near-well seismicity rates decrease following operational changes, such as extended shut-ins of the injection well or decreases in

injection rates. Pore pressure diffusion models suggest that the near-well seismicity rates increase again after pore pressures recover from these operational changes and begin to exceed their previous maximum values. This pattern, known as the Kaiser Effect, appears to be an important aspect of the seismicity induced by PVU fluid injection, at least within a few km of the injection well. Hence, keeping near-well pore pressures below their previous maximum values should reduce the probability of future large-magnitude induced earthquakes within ~4-5 km of the injection well. Because spatial pressure gradients have decreased over time, keeping the pressures reduced may be more critical now than in the past if the probability of large induced earthquakes is to be decreased. However, no potential injection scenario could achieve this objective in all areas, because areas more than a few km from the PVU injection well will experience increasing pressures for several years, even if no additional fluid is injected. In addition, even if pressures were maintained below their previous maximum values in a given area, the probability of a large induced earthquake in that region would be reduced but not eliminated.

Some examples of injection scenarios that maintain pore pressures below their previous maximum values at the location of the March 4th M_W 4.5 earthquake (1.6 km from the injection well) are presented in this report. These scenarios use injection rates of 60-69% of the rate that was being used prior to March 2019. They yield predicted maximum pressures ~600-950 psi less than the previous maximum value at the location of the M_W 4.5 earthquake. Only pressures at the location of the M_W 4.5 earthquake were evaluated. Additional modeling would be required to evaluate pressure trends at other locations or to evaluate different injection scenarios.

1 Introduction

A widely felt earthquake occurred in the Paradox Valley area on March 4th, 2019, at 17:22:52 Coordinated Universal Time (UTC) (10:22:52 am local time). Shaking from the event was felt as far as ~240 km (~150 miles) from the earthquake's epicenter, according to reports submitted by the public to a U. S. Geological Survey website (Figure 1-1). The strongest shaking reported was intensity V on the Modified Mercalli Intensity Scale, corresponding to moderate shaking. This level of shaking can produce very light damage, such as breaking of dishes and windows and overturning of unstable objects (https://earthquake.usgs.gov/learn/topics/mercalli.php). Very minor local damage was reported following the March 4th earthquake (overturned objects).

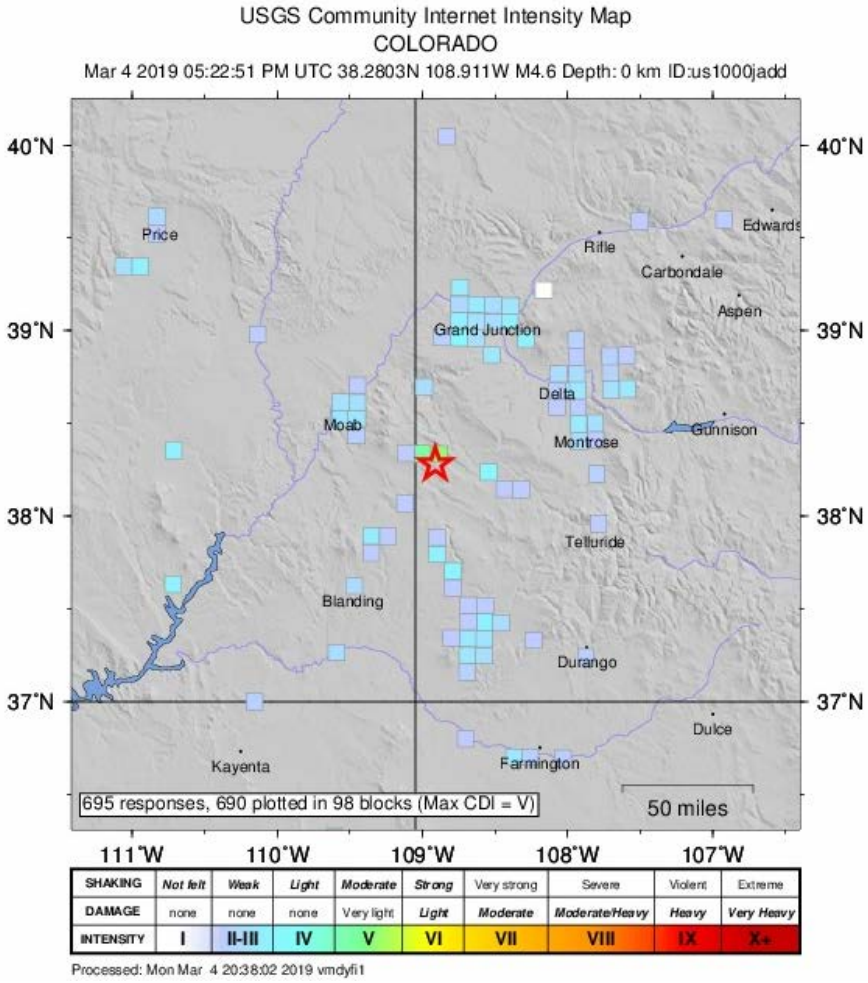

Figure 1-1: Shaking intensities reported by the public for the March 4th 2019 M_W 4.5 Paradox Valley earthquake (downloaded on March 4th, 2019 from https://earthquake.usgs.gov/earthquakes/eventpage/uu60315157). The red star represents the epicenter of the M_W 4.5 earthquake.

The March 4th earthquake occurred 1.6 km southwest of the Paradox Valley Unit (PVU) injection well, and available data indicate that it was induced by PVU brine disposal (Figure 1-2). The earthquake epicenter is within the previously identified near-well cluster of induced seismicity, a persistent zone of induced earthquakes surrounding the injection well to a distance of ~3 km. Induced earthquakes have been occurring within 500 m of the epicenter of the March 4th earthquake since 1998. The depth of the earthquake is 3.9 km (relative to the PVU wellhead),

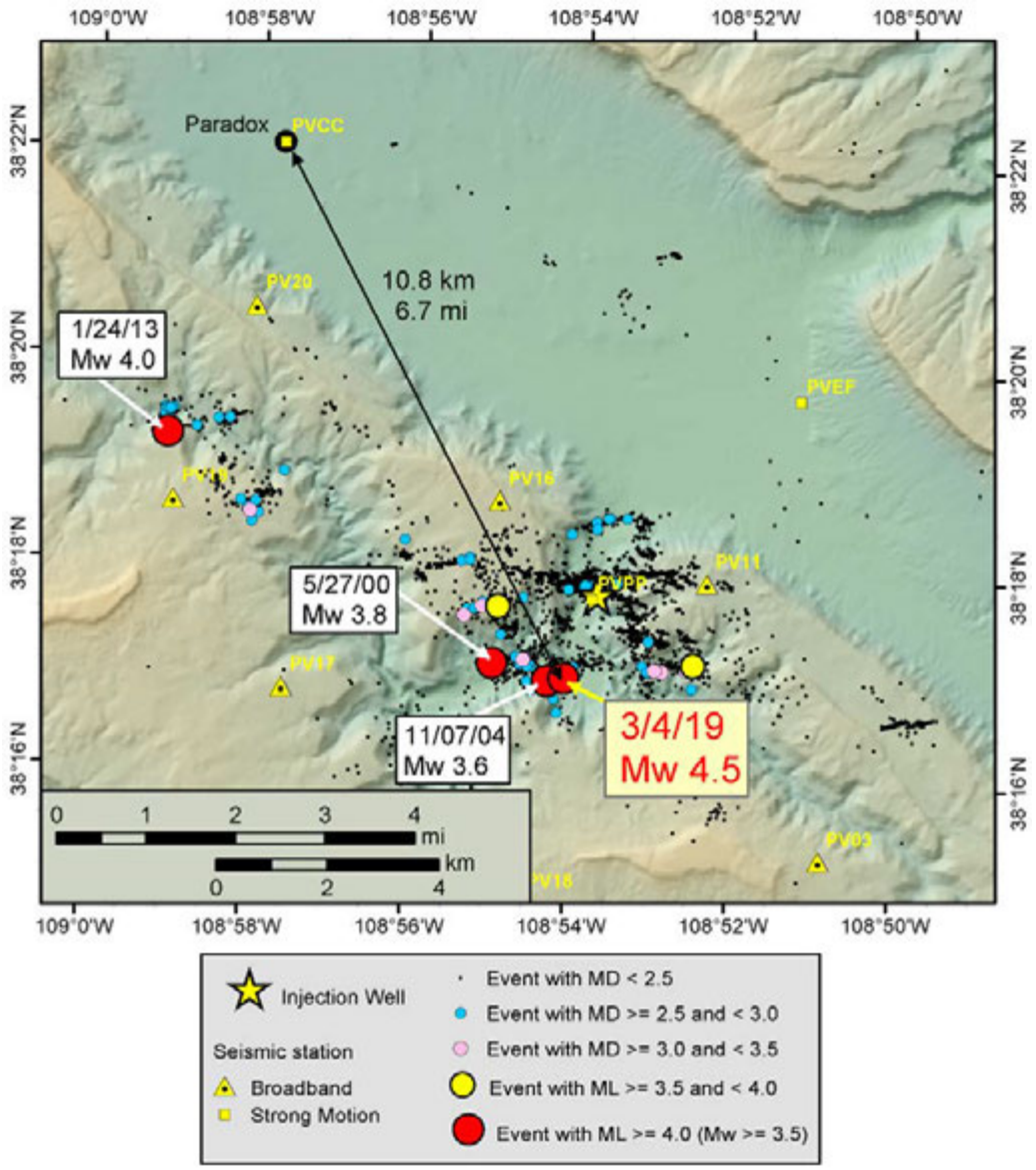

Figure 1-2: Location of the March 4th, 2019 M_W 4.5 earthquake and other induced earthquakes relative to the PVU injection well (yellow star), PVU extraction well field (PVEF), and the town of Paradox, Colorado (labeled arrow indicates distance from M_W 4.5 epicenter). The four largest induced earthquakes are labeled. See section 2.2.1 for a discussion of the different magnitude scales used.

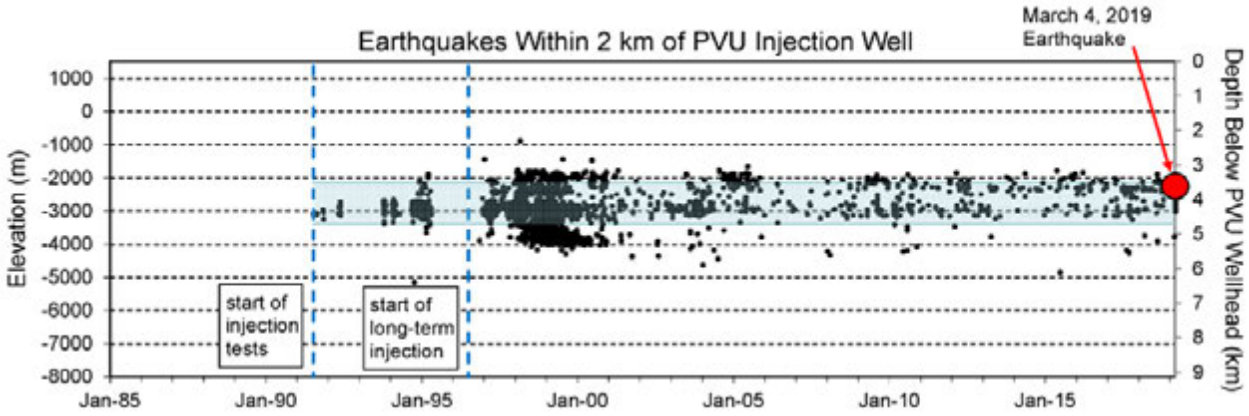

Figure 1-3: Vertical distribution of induced earthquakes within 2 km of the PVU injection well as a function of date. The March 4th, 2019 earthquake is represented by the filled red circle. The shaded blue zone represents the depth range of target injection formations within 2 km of the well (top of the Leadville formation to 50 m below the top of the Precambrian basement).

consistent with the depths of previously induced events in this area and with the depths of injection target formations (Figure 1-3). Natural earthquakes in the region tend to occur substantially deeper (> ~10 km; Block et al., 2014).

1.1 Project Background

Since 1996, Reclamation has been disposing of brine in a deep injection well southwest of Paradox Valley, Colorado, as part of the PVU salinity control project. This period of continuous injection was preceded by a series of injection tests conducted between 1991 and 1995. The PVU injection well disposes of brine that would otherwise enter the Dolores River, a tributary of the Colorado River. This project is authorized by the Colorado River Basin Salinity Control Act, passed by the U.S. Congress in 1974, and is an important component of the Colorado River Basin Salinity Control Program (CRBSCP), an effort to improve water quality in the Colorado River system. Further information on the Paradox Valley Unit can be found in Block et al. (2012) or at the Reclamation project website (see https://www.usbr.gov/uc/progact/paradox).

Microseismic monitoring of the Paradox Valley area began in 1983, with installation of the first stations of the Paradox Valley Seismic Network (PVSN). Network installation was timed to provide a pre-injection baseline of naturally occurring background seismicity, and stations were located to optimize monitoring of any earthquakes that might be induced in the vicinity of the PVU injection well. The seismic network has been continuously operated since 1985 and has been expanded and updated over the years to respond to changing seismicity patterns. The current network configuration consists of a surface array of 20 broadband high-gain three-component sensors (Figure 1-4). In addition, Reclamation operates three strong motion instruments for recording of ground motions from large earthquakes that may saturate the high-gain array. These strong motion instruments are located at the Community Center in the town of Paradox (PVCC), the PVU injection wellhead and pumping plant (PVPP), and the PVU extraction field and surface treatment facility (PVEF) (Figure 1-4).

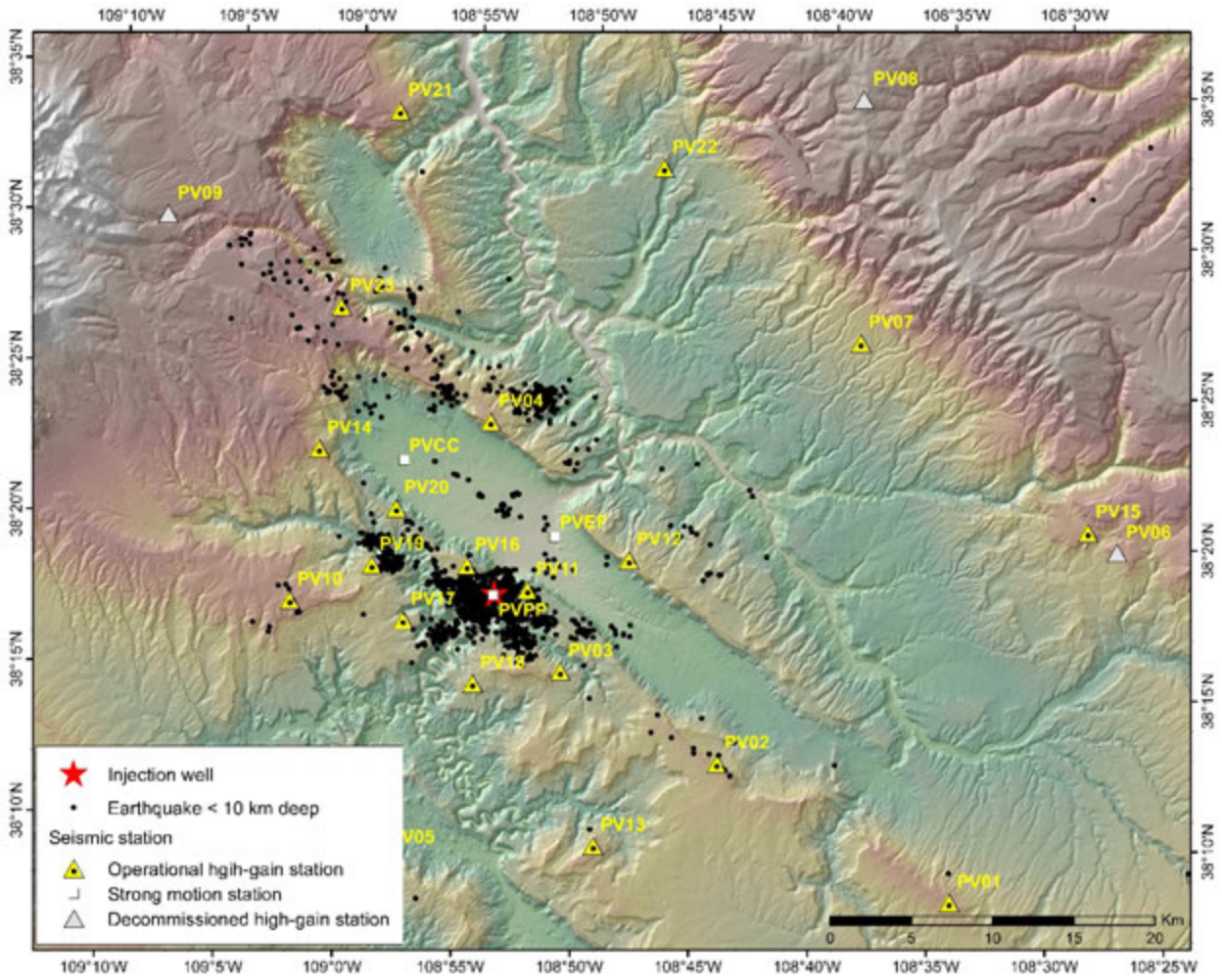

Figure 1-4: Locations of the Paradox Valley Seismic Network stations. The epicenters shown (black dots) are of shallow induced earthquakes (depth < 10 km) recorded from the time of initial injection tests in 1991 through the time of the March 4th 2019 *Mw* 4.5 earthquake.

No earthquakes were recorded within 18 km of the injection well during six years of pre-injection monitoring (Block et al., 2014). The data recorded during this period include just one local earthquake that occurred almost 19 km from the PVU injection well, at an estimated depth of ~14 km (relative to the PVU wellhead). Within days of the start of the initial injection test in 1991, seismic events were detected in the immediate vicinity of the injection well. During subsequent injection tests and continuous injection operations, induced earthquakes occurred at increasing distances from the injection well. Most of the earthquakes that have been recorded in the Paradox Valley area since the start of PVU injection have depths between 2 and 7 km (relative to the PVU wellhead), consistent with the depths of target injection formations. Focal depths of the few naturally-occurring tectonic events recorded in the area have exceeded 10 km (Block et al., 2014). The close correlation between injection operations and induced seismicity at PVU has been well established, as illustrated by Figure 1-5:.

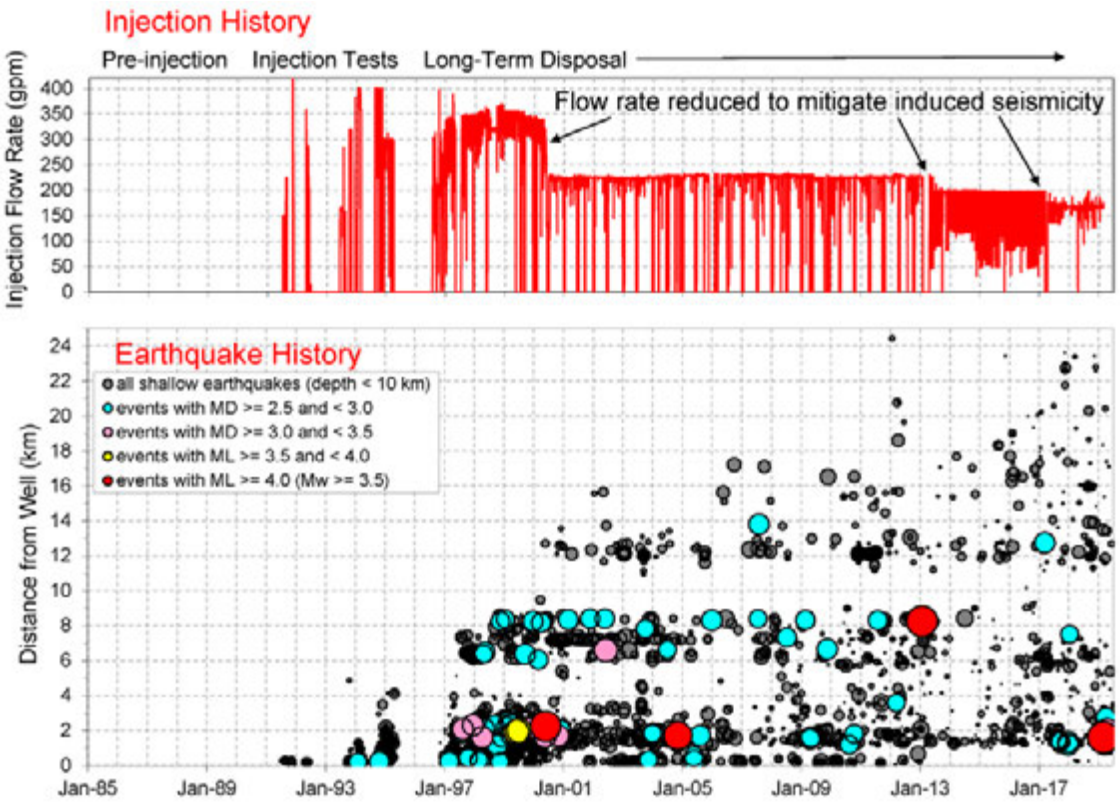

Figure 1-5: Correlation between injection flow rates (upper plot) and shallow seismicity (< 10 km depth) recorded by the Paradox Valley Seismic Network (lower plot). The network has been operated continuously since 1985, six years prior to injection, and no shallow earthquakes were observed before injection began. The large filled red circle on the right edge of the lower plot represents the March 4th, 2019 earthquake. See section 2.2.1 for a discussion of the different magnitude scales used.

At the time of the March 4th 2019 earthquake, the PVU injection well had been shut down for a few hours to accommodate previously-scheduled maintenance activities. PVU operational protocol requires the injection well to be temporarily shut down if an induced earthquake is felt at the injection facility. Following the *Mw* 4.5 earthquake, the injection well remained shut down for more than a year, while analyses of the seismic and injection data were conducted and aftershock activity was monitored. The well came back online temporarily for injection testing in late April 2020. Most of the analyses presented in this report were performed in the first few months following the March 2019 earthquake and generally utilize data acquired through July 2019.

2 Description of the Main Shock

2.1 Earthquake Location

The epicenter of the March 2019 earthquake is 1.6 km (1.0 mi) southwest of the PVU injection well and 10.8 km (6.7 mi) from the town of Paradox, Colorado (Figure 1-2). The epicentral coordinates, as computed using P- and S-wave arrival times and a local three-dimensional (3-D) velocity model developed previously, are latitude 38.2832° N, longitude 108.9018° W. The focal depth is 3.9 km below local ground surface, which is also the depth relative to the PVU injection wellhead. The epicenter of the March 2019 earthquake lies within 1.4 km of the epicenters of two of the three previous PVU-induced earthquakes with $M_W \geq 3.5$ (Figure 2-1).

PVSN earthquake locations are determined in three phases: (1) real-time automatic picking and location; (2) interactive picking of the three-component digital waveform data from each PVSN station and location by an analyst; and (3) waveform cross-correlation and relative event location. The real-time picks and locations are only used for preliminary analysis. All local earthquakes are subsequently repicked by an analyst using interactive graphical tools and relocated with a local 3-D velocity model. The interactive locations are substantially more accurate than the real-time locations, but they do not take advantage of the greater precision available from cross-correlating waveforms between earthquakes. The relative event locations typically are generated once a year, when seismic waveforms from the previous years' events are cross-correlated with each other and with waveforms from all previous events. Following the M_W 4.5 earthquake, however, the relative locations were updated every one to two months. The maps and cross sections in this report show hypocenters determined from the relative locations. Because many of the waveforms from the main shock were clipped, it was tied into the relative location using time differences from interactive picks. The epicentral coordinates of the M_W 4.5 earthquake from the event relative location are latitude 38.2828° N, longitude 108.9012° W, and the relative focal depth is 3.8 km below local ground surface. A mathematical description of the relative location procedure is provided in Appendix A, and additional details of our processing methods are provided in Block et al. (2015).

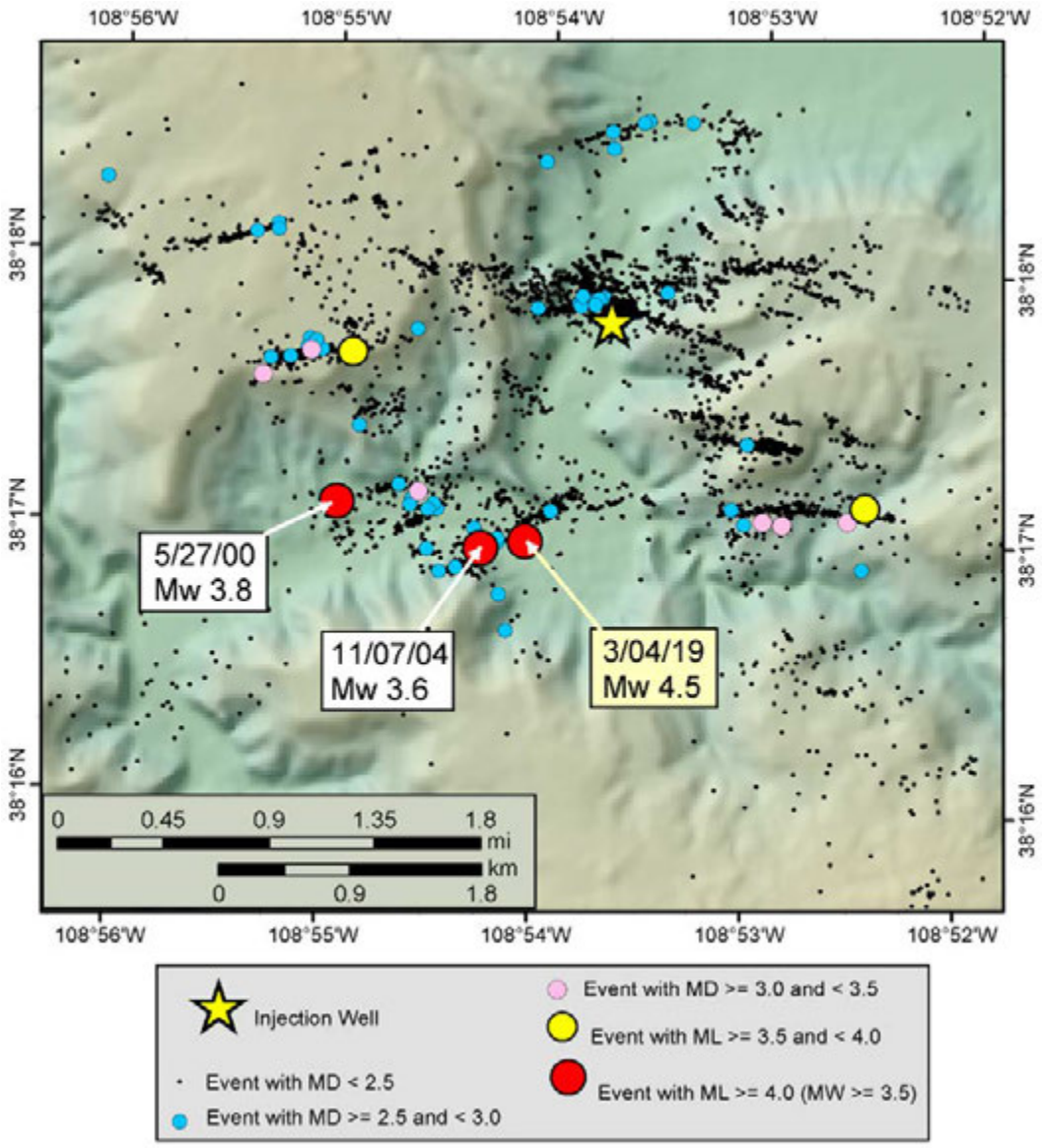

Figure 2-1: Location of PVU-induced seismicity in the near-well region. Events that occurred from the start of injection in 1991 to the time of the March 4th 2019 M_W 4.5 earthquake are shown. The size and color of the earthquake symbols are scaled by event magnitude, as indicated by the legend. See section 2.2.1 for a discussion of the different magnitude scales used. The epicenter of the second-largest induced earthquake, the 2013 M_W 4.0 event, plots outside the limits of this map but is shown in Figure 1-2.

2.2 Earthquake Magnitude

Earthquake magnitude typically is computed using measurements from seismic waveforms recorded at stations both near and far from the earthquake. The most common magnitude scale used today is the moment magnitude scale (M_W) (Hanks and Kanamori, 1979), which measures the strength, or moment, of a seismic source (for faults, seismic moment depends on the rigidity

of the crust, the fault area, and the average slip between the two sides of the fault). Seismic moment can be measured using several methods, including determining the long-period spectral levels of broadband seismic waveforms, geodetic measurements of the coseismic displacements at the earth's surface, or waveform modeling of broadband seismograms. Each of these methods has advantages and drawbacks, and all are subject to measurement and modeling errors (e.g., the distribution of seismic stations around the epicenter, assumptions about hypocentral depth, assumptions about crustal properties, etc.). For this reason, a range of moment magnitude estimates may be generated for a given earthquake, depending on the data and model parameters used.

Another common magnitude is the duration magnitude scale (M_D), which is often used for small- to moderate-sized earthquakes recorded by local seismic networks such as PVSN. Earthquakes previously induced by PVU fluid injection with magnitude of 3.5 or greater have been reported using the local magnitude scale, M_L. However, during the last several years, use of the moment magnitude scale has become increasingly prevalent and estimates of local magnitudes are no longer routinely available. For this reason, we use the moment magnitude scale when discussing the largest PVU-induced earthquakes in this report. A further discussion of different magnitude scales is included at the end of this section. Below, we review the moment magnitude estimates for the March 2019 earthquake and compare them to the magnitudes of other large PVU-induced earthquakes.

We computed a moment magnitude of M_W 4.3 for the March 4th earthquake, using only PVSN broadband waveform data and the hypocenter computed by Reclamation. However, many of the PVSN seismic waveforms were clipped and therefore not usable to estimate seismic moment. Unclipped P-wave and S-wave data were obtained from only four of the 20 PVSN stations, all on the eastern margin of the network. Unclipped P-wave data were obtained from five additional stations having a wider range of azimuths. Seismic moment, and hence moment magnitude, was estimated from the long-period displacement spectra at PVSN stations having unclipped, good-quality data. An ω^2 spectral model was assumed (Brune, 1970), including correction for high-frequency attenuation (Anderson and Hough, 1984), and model parameters were estimated from the spectra using standard methods (Anderson and Humphrey, 1991; Andrews, 1986; Boore, 1986; De Natale et al., 1987; Hough and Anderson, 1988; Kilb et al., 2012; Shearer et al., 2006; Snoke, 1987). The procedure included corrections for the spectral value kappa, determined previously for each PVSN station (Anderson and Humphrey, 1991; Kilb et al., 2012). Assuming a simple circular rupture model (Brune, 1970, 1971), we also determined estimates of the static stress drop of 8 - 53 bars and estimates of the rupture radius of 0.6 - 1.2 km.

Moment magnitudes also were computed by the University of Utah Seismograph Stations (UUSS) and the U. S. Geological Survey (USGS), from data recorded at regional stations throughout the western United States. The UUSS/USGS magnitudes range from M_w 4.4 to M_w 4.6 (personal communication, Jill McCarthy, U. S. Geologic Survey, 3/4/2019; also U.S. Earthquake Hazards Program website https://earthquake.usgs.gov/earthquakes/eventpage/uu60315157/technical, accessed 9/24/2019). The UUSS/USGS moment magnitude estimates rely on hypocenters determined using a regional velocity model. The UUSS/USGS hypocenters likely are less accurate than the Reclamation-determined hypocenter, which uses data from the dense array of local PVSN stations and a local

3-D velocity model. However, because the amount of useable waveform data from the PVSN stations is limited, and because the event was well-recorded at regional distances, we prefer the UUSS magnitude of M_w 4.5 for this earthquake.

The previous largest PVU-induced earthquake was the M_W 4.0 (M_L 4.4) earthquake of January 24th, 2013. The March 4th 2019 earthquake, with M_W 4.5, is 0.5 magnitude units larger than the January 2013 event, making it the largest PVU-induced earthquake to date and substantially larger than any earthquake previously induced by PVU brine injection. A comparison of the local and moment magnitudes of the four largest PVU-induced earthquakes recorded to date is provided in Table 2-1.

Table 2-1: Comparison of local and moment magnitudes for the three largest PVU-induced earthquakes. The source for each magnitude estimate is given in parentheses: UUSS = University of Utah Seismograph Stations; SLU = Saint Louis University; USGS = U. S. Geological Survey; USBR = Bureau of Reclamation. The magnitudes listed are the values available in September 2019.

Earthquake Date (UTC)	Local Magnitude (M_L)	Moment Magnitude (M_W)
5/27/2000	4.3 (USGS) 4.4 (UUSS)	3.8 (SLU)
11/7/2004	4.1 (UUSS)	3.6 (SLU)
1/24/2013	4.4 (USGS)	4.0 (USBR) 3.9 (UUSS, USGS)
3/4/2019	4.5 - 4.7 (SLU) 5.3 (UUSS)	4.5 (UUSS) 4.4 (USGS M_{WR}) 4.6 (USGS M_{WW}) 4.3 (USBR)

2.2.1 Magnitude Scales

Multiple magnitude scales are used to quantify the size of earthquakes. Each measures different characteristics of the seismic waveforms, which can result in different numerical values between the scales and inconsistencies between different regions (Chung and Bernreuter, 1981). The *duration* magnitude scale (M_D), which uses the logarithm of the duration of the seismic signals, is commonly used for computing magnitudes of local earthquakes recorded by microearthquake networks because it is easy to apply and provides consistent results (e.g., Lee and Stewart, 1981). Duration magnitudes work well for most of the induced earthquakes recorded by PVSN because they are small to moderate in size. Although the duration magnitude scale generally provides consistent results between earthquakes within a given network, it has certain drawbacks: (1) it may not be calibrated well between networks, especially for smaller-magnitude events; and (2) the duration magnitude scale may saturate for larger earthquakes (M > 3) recorded by PVSN due to truncation of long-duration records. Hence, other scales must be used to compare the largest PVU-induced events. The *local* magnitude scale (Richter, 1935), based on computing the logarithm of the peak amplitude of the seismic signal (corrected for a standard distance and

instrumentation type), has been reported for some larger PVU events by the USGS and UUSS. Other magnitude scales occasionally reported by the USGS include the *surface-wave* (M_S) and *body-wave* (m_b) magnitudes. As seismic instrumentation has improved in recent years, use of the *moment* magnitude scale (M or M_W) (Hanks and Kanamori, 1979) has become more standard.

2.3 Focal Mechanism

First-motion data from PVSN stations indicate that the earthquake was produced by predominately strike-slip faulting on either of two conjugate fault planes: (1) a fault striking N58°E and dipping 65° southeast (SE), or (2) a fault striking N29°W and dipping 83° southwest (SW) (Figure 2-2). The directions of compression (P-axis) and extension (T-axis) are N78°W and N17°E, respectively. The strike-slip mechanism is consistent with the previous findings of Ake et al. (2005), who found that strike-slip mechanisms accounted for 89% of 1345 well-determined mechanisms, and Block et al. (2015), who found that 83% of 600 re-analyzed focal mechanisms were strike-slip. Both earlier studies indicate a P-axis oriented to the northwest.

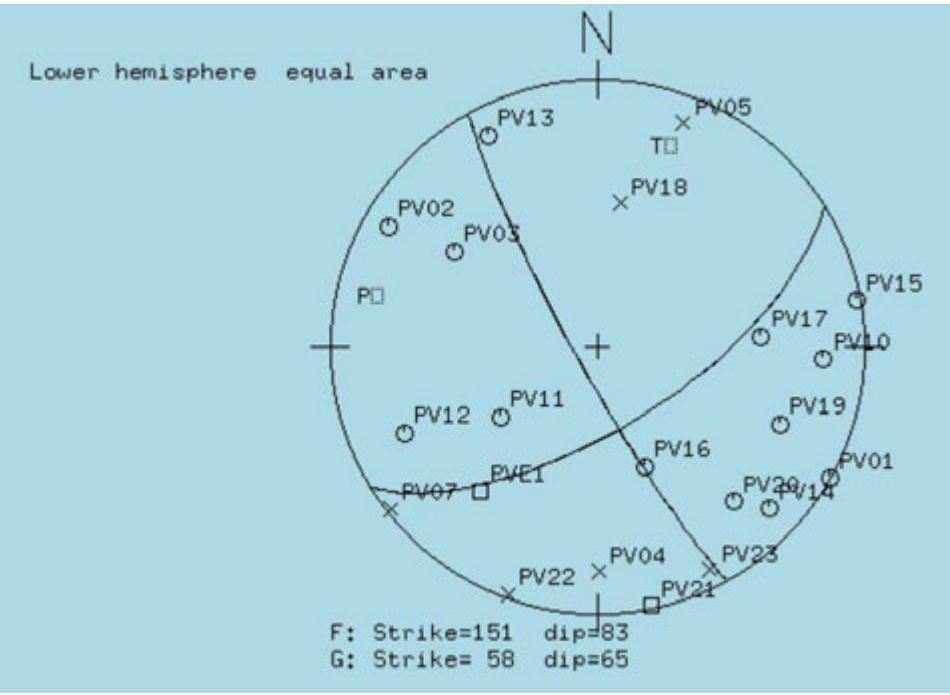

Figure 2-2: First breaks and focal mechanism of the March 4th 2019 M_W 4.5 earthquake plotted on a lower hemisphere equal-area projection. X and open circle symbols represent compressional and dilatational first breaks, respectively. Square symbols represent locations of the P and T axes, or stations having no clear first break. Two conjugate fault planes are possible from the first-motion data, a plane striking N58°E and dipping 65° to the southeast, and a plane striking N29°W and dipping 83° to the southwest. However, the plane striking N58°E and dipping to the southeast is consistent with the distribution of aftershocks shown in Figure 2-3, and is therefore interpreted to represent the rupture plane of the Match 4th earthquake.

First-motion data alone do not determine which conjugate plane is the true fault plane. However, precise relative locations of ~1850 aftershocks of the March 4th earthquake show a 1.5-km-long plane oriented approximately N60°E and dipping to the southeast, consistent with the northeast (NE)-striking focal plane (Figure 2-3). Hence, the aftershock distribution indicates that the first conjugate fault plane (strike N58°E, dip 65° SE) is the rupture plane of the March 4th earthquake.

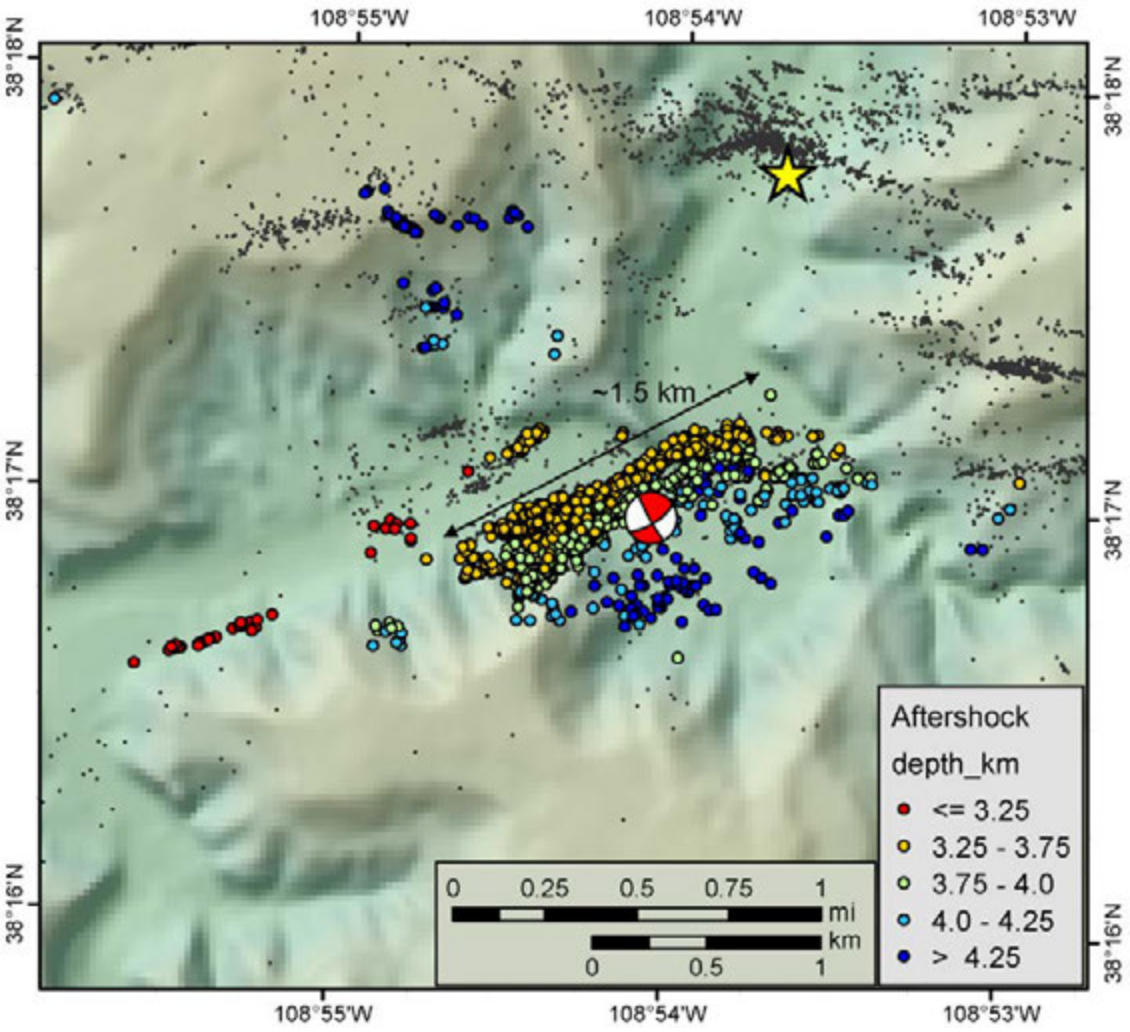

Figure 2-3: Distribution of ~1850 aftershocks with well-constrained hypocenters, recorded between the time of the March 4th M_W 4.5 earthquake and the end of July 2019. Hypocenters were computed with a relative location procedure using P-wave and S-wave time differences between events from waveform cross-correlation; the main shock was tied into the relative location using time differences from manual picks because many of its waveforms were clipped. The focal mechanism of the March 4th earthquake is plotted at the location of the event's epicenter.

The March 4th 2019 earthquake did not occur on any of the deep faults that were mapped during either the early (pre-injection) or more recent PVU geophysical investigations. Most of the faults mapped during these studies trend northwest, approximately parallel to Paradox Valley (Block et al., 2012; King et al., 2014; King et al., 2018). Because this orientation is close to the estimated direction of maximum horizontal stress of N55°W - N80°W (Ake et al., 2005; Block et al., 2015; King et al., 2018), these major fault structures are not optimally oriented for shear slip. The majority of the induced earthquakes observed at PVU occur on unmapped, previously aseismic faults. Because these faults may not have much net vertical offset, they may be difficult to resolve on deep seismic reflection data.

3 Fault Plane

3.1 Size and Location

The spatial distribution of hypocenters within the main aftershock cloud, in conjunction with focal mechanisms of larger aftershocks, can be used to estimate the size and location of the fault plane that ruptured on March 4th 2019. The main aftershock cloud delineates a plane about 1.5 km long, striking ~N60°E and dipping toward the southeast, as shown in Figure 2-3 and Figure 3-1.

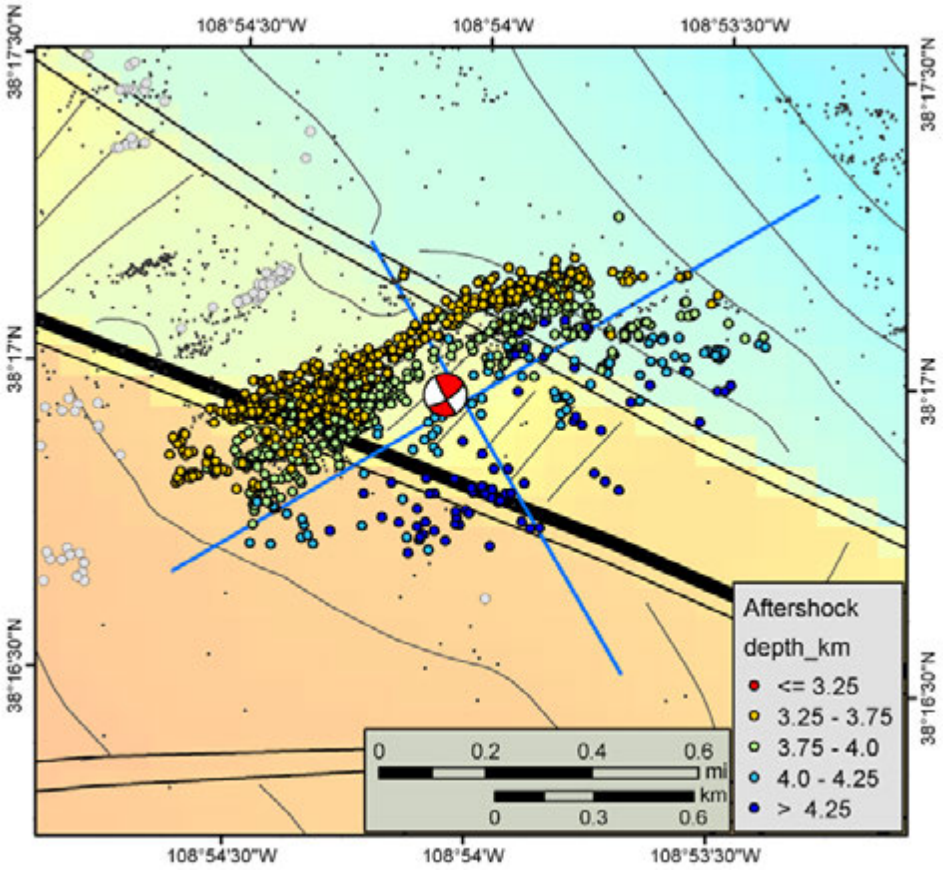

Figure 3-1: Locations of the cross sections presented in Figure 3-2, Figure 3-4, Figure 3-16, Figure 3-17, Figure 3-20, Figure 3-21, and Figure 3-22 (blue lines). Aftershocks of the M_W 4.5 earthquake that are projected onto the cross sections are color-coded by depth. Aftershocks that are not included in the cross sections are shown in gray. The focal mechanism of the M_W 4.5 earthquake is plotted at the location of its epicenter. The small black dots are the epicenters of previous PVU-induced earthquakes.

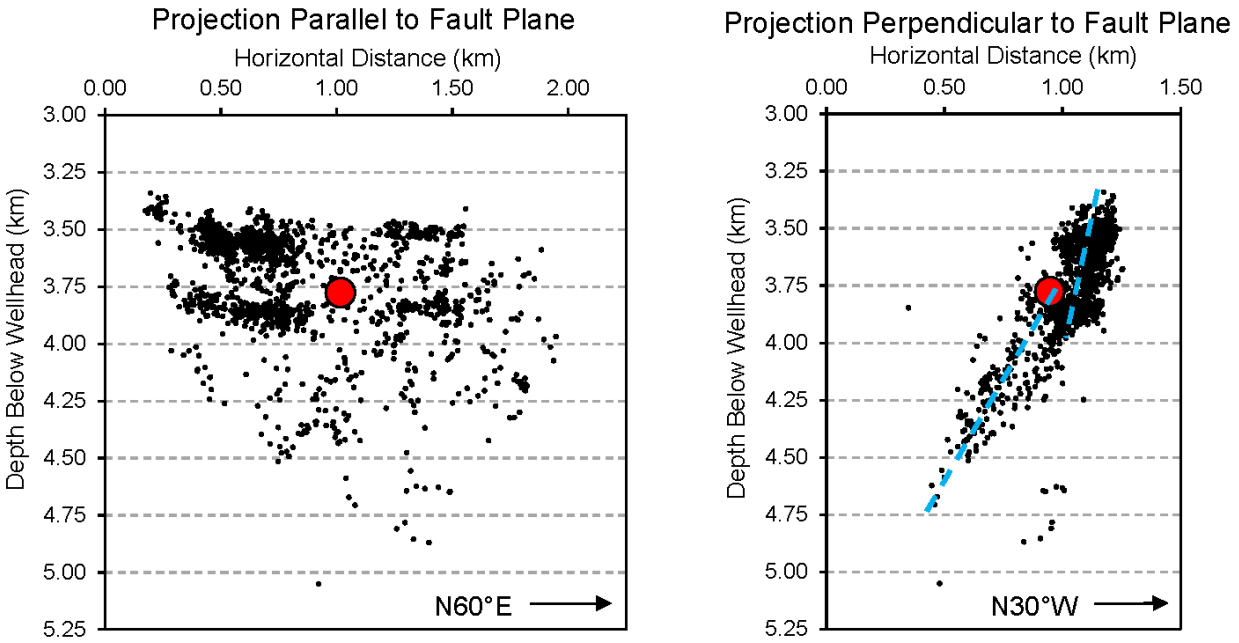

Figure 3-2: Vertical cross sections of the March 4th 2019 earthquake (filled red circle) and its main cloud of aftershocks recorded through July 2019 (black dots). The locations of the cross sections are shown in Figure 3-1. The section on the left is approximately parallel to the fault plane (N60°E). Earthquakes within 0.5 km of the section line are included. The section on the right is approximately perpendicular to the fault plane (striking N30°W), with earthquakes within 0.95 km of the section line projected. Each section includes 1672 events. Hypocenters were computed with a relative location procedure using P-wave and S-wave time differences between events from waveform cross-correlation. The main shock was tied into the relative location using time differences from manual picks because many of its waveforms were clipped, and therefore its position relative to the aftershocks may be less precise than the positions of the aftershocks relative to each other.

Cross-sectional views of the hypocenter distribution indicate a more complex pattern than can be discerned from the map view alone (Figure 3-2). The upper 0.5 km of the aftershock cloud contains most of the events, and these events are concentrated within two sub-horizontal layers. The lower ~0.75 km of the aftershock cloud is much less dense than the upper section, with the numbers of earthquakes tapering off gradually with depth. In addition, the lower section of the aftershock cloud exhibits a dip of ~60°, consistent with the focal mechanism solution of the main shock of 65°. In contrast, the upper section of the aftershock cloud exhibits a steeper dip of ~78°-80° (Figure 3-2, perpendicular section). The hypocenter of the March 4th earthquake lies near the junction of these two apparent planes (Figure 3-2, red circle). The hypocenters shown in these figures were computed with a relative location procedure, using precise P-wave and S-wave time differences derived from waveform cross-correlations. The main shock was tied into the relative location using time differences from manual picks because many of its waveforms were clipped and therefore robust cross-correlations could not be obtained.

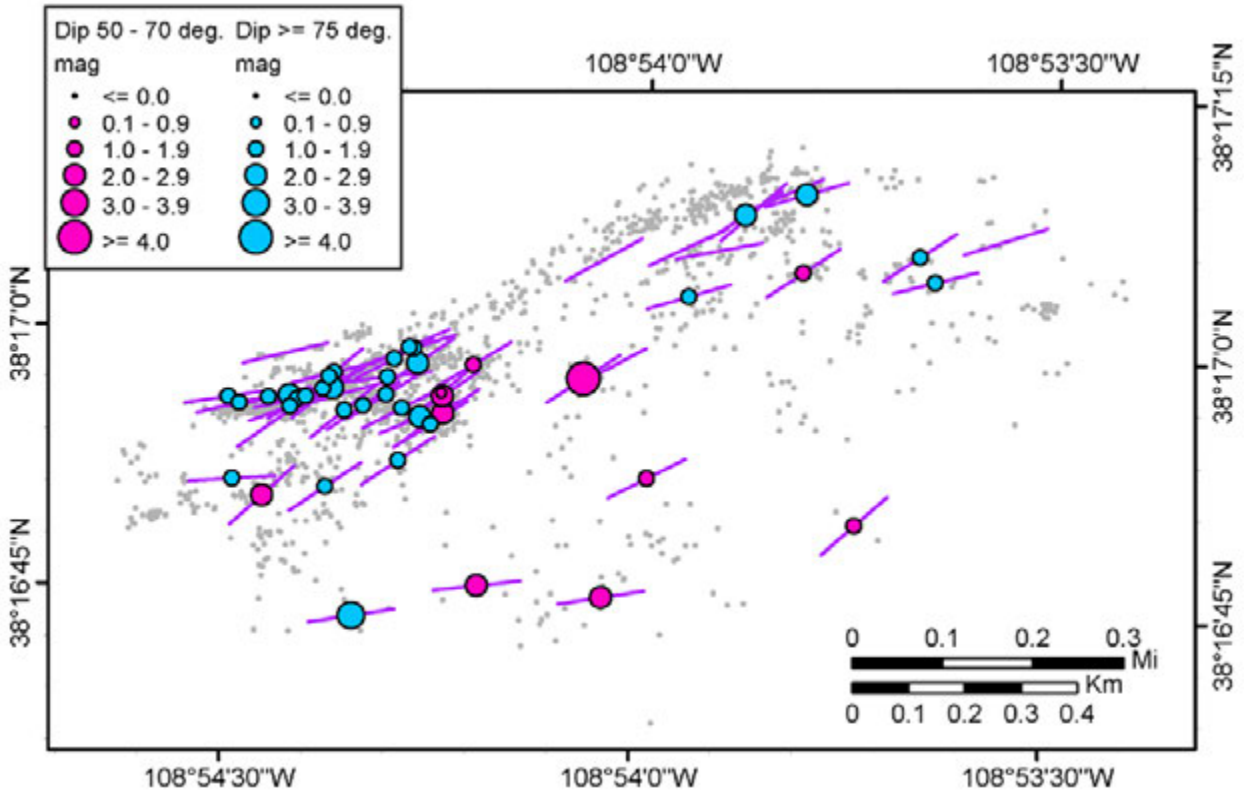

Figure 3-3: Focal mechanisms of the March 4th 2019 main shock and 53 larger aftershocks within the main aftershock cloud. The purple lines indicate the strikes of the northeast-striking nodal planes. The pink symbols represent earthquakes whose NE-striking nodal planes dip to the southeast with dip angles between 50° and 70° (consistent with the focal mechanism of the March 4th earthquake). The blue symbols represent earthquakes whose NE-striking nodal planes have dip angles ≥ 75°, dipping either to the southeast or northwest.

We use results of focal mechanism analyses to further evaluate the fault planes present within the main aftershock cloud. The purple lines in Figure 3-3 represent the northeast-striking nodal plane of the main shock and 53 of the larger aftershocks for which focal mechanisms were determined. (These preliminary mechanisms were determined using first-break motions only and an interactive graphical interface to manually determine the best-fit focal planes.) To see how well these mechanisms correlate with the spatial aftershock distribution, we identify two groups of aftershocks that meet these criteria: (1) northeast-striking fault plane with dip angle between 50° and 70° and dipping to the southeast, or (2) northeast-striking fault plane with dip angle ≥ 75°; dip direction may be southeast or northwest. (All mechanisms indicate predominatly right-lateral strike-slip motion.) The first set of focal mechanisms is consistent with that of the main shock and the hypocenter geometry of the lower part of the aftershock cloud. The second set of focal mechanisms is consistent with the steep fault plane inferred by the hypocenter distribution within the upper part of the aftershock cloud. Either a southeast or northwest dip direction is allowed for this set because for very steeply-dipping fault planes, the dip direction may not be well-constrained by the first break data. These criteria are satisfied by 78% of the 54 focal mechanisms available: the main shock and 10 aftershocks have focal planes falling into the first

set, and 31 aftershocks have focal planes falling into the second set. These two groups of focal mechanisms are indicated by the pink and blue symbols in Figure 3-3.

The spatial distribution of these two sets of focal mechanism nodal planes is consistent with a shallower-dipping fault plane at depth and more steeply dipping fault(s) above. The hypocenters of earthquakes with the shallower-dipping nodal planes preferentially occur within the lower (more southeastern) part of the main aftershock cloud, especially toward the center (Figure 3-3). In contrast, hypocenters of earthquakes with steeper-dipping nodal planes preferentially occur within the upper (more northwestern) part of the aftershock cloud. They are also present somewhat deeper on the NE and SW edges of the cloud (Figure 3-3). These patterns are shown in the cross sections in Figure 3-4. These cross sections show the earthquake hypocenters corresponding to focal mechanisms with the shallower- and steeper-dipping nodal planes in pink and blue, respectively. The shallower-dipping (pink) nodal planes are only present below a depth of 3.75 km. Most of the steeper-dipping (blue) nodal planes occur above 4.0 km depth.

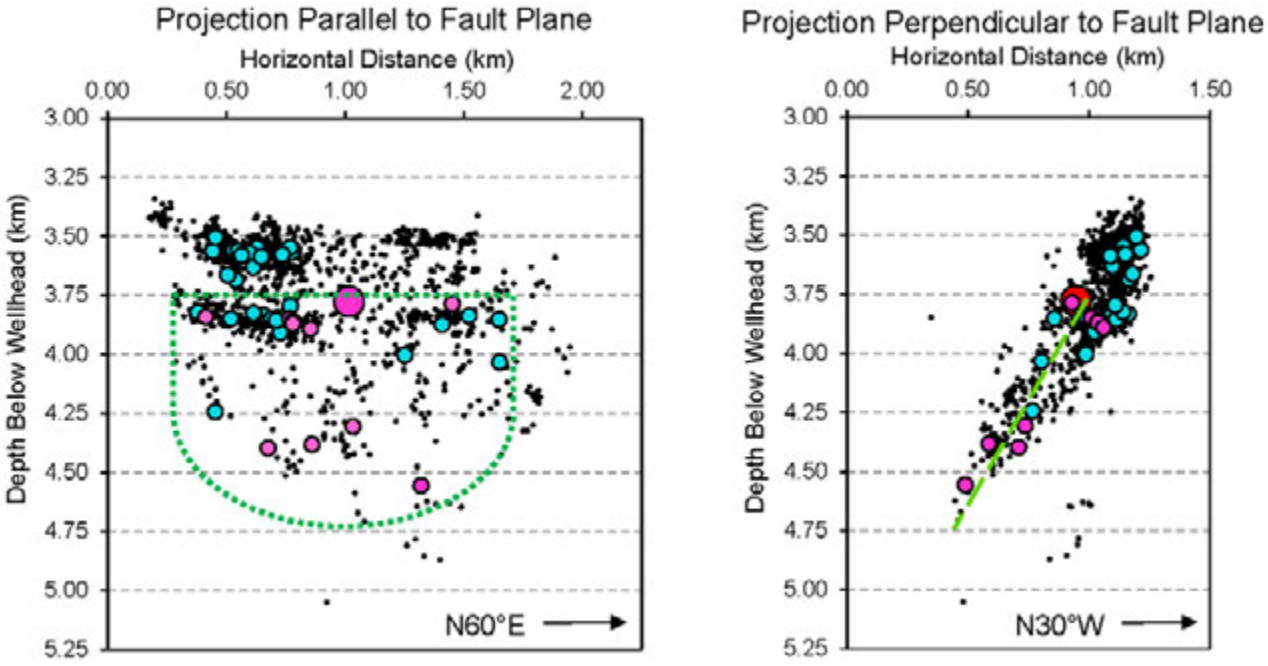

Figure 3-4: Same cross sections as in Figure 3-2, but with two sets of hypocenters colored by the dip range of their NE-striking focal mechanism nodal planes: 50°-70° (pink symbols) and ≥ 75° (blue symbols). For the focal mechanisms with the shallower dips, the dip direction is to the SE. For the focal mechanisms with the steeper dips, the dip direction is either SE or NW. The dashed green lines indicate the interpreted extent of the shallower-dipping fault plane.

Based on the spatial distribution of hypocenters and focal mechanisms, we have interpreted the approximate extent of the shallower-dipping fault plane, which has a geometry consistent with the focal mechanism of the *MW* 4.5 earthquake. This extent is indicated by the dashed green lines in Figure 3-4. This fault segment is interpreted to extend from the deeper sub-horizontal aftershock layer at ~3.75 km depth to ~4.75 km depth (relative to the injection wellhead), corresponding to a vertical height of 1.0 km and an along-dip height of 1.15 km. The length of the fault plane is less well-constrained, but is between 1.3 and 1.6 km. We interpret that this shallower-dipping fault plane ruptured during the *MW* 4.5 earthquake on March 4th, 2019.

The steeper-dipping (~78°-80°) upper section of the aftershock cloud and corresponding focal mechanisms may represent a steeper-dipping fault segment that also ruptured during the *MW* 4.5 earthquake. Alternatively, they may represent one or more steeply dipping faults that ruptured following the *MW* 4.5 earthquake in response to stress changes in overlying formations. Waveform modeling could potentially be used to further evaluate differing rupture plane interpretations, but that analysis is beyond the scope of this report.

3.2 Relation to Lithology and Geologic Structure

A northwest (NW)-trending normal fault with enough vertical throw to completely offset the primary PVU target injection formation, the Leadville, lies roughly 2 km southwest of the PVU injection well. This major structural feature was first interpreted as a barrier to lateral fluid flow through the Leadville formation and pore pressure diffusion from PVU injection in the 1980s, during technical studies used for siting the current injection well (Bremkamp and Harr, 1988) (Figure 3-6). More extensive geologic studies performed between 2015 and 2017, to evaluate locations for a potential second injection well, confirmed the presence of this major fault (Arestad, 2016, 2017). Hypocenters of earthquakes recorded since the start of PVU fluid injection support the hypothesis that this fault is a barrier to pore pressure diffusion from PVU injection. Very few earthquakes occur at the depth of the Leadville formation southwest of this fault (Figure 3-7). The earthquakes that have occurred southwest of the injection well generally have depths well above the Leadville formation and have been previously interpreted as likely triggered by stress changes caused by injection-related deformation of the reservoir and surrounding formations (Block et al., 2015; King et al., 2018). Both geologic models are based on the interpretation of two-dimensional (2-D) seismic reflection lines acquired in the 1960s to 1980s and data from relatively few, widely spaced deep wells.

Although both studies identified a barrier fault southwest of the PVU injection well, there are differences in the interpreted locations of the barrier fault, as well as the locations of other deep northwest-trending faults. The original geologic model places the barrier fault about 700 m southwest of the edge of the main cloud of aftershocks from the March 4th 2019 earthquake (Figure 3-8), whereas the more recent model shows the barrier fault intersecting the aftershock cloud near its southwestern end (Figure 3-9). The spatial pattern of hypocenters from all induced earthquakes suggests that the fault position in the recent model is approximately correct (Figure 3-7); the aftershock distribution suggests that the fault should be moved ~300 m relative to the aftershock hypocenters. Given the uncertainty in the absolute position of both the fault location and the earthquake hypocenters, it is reasonable to interpret the fault plane from the March 4th 2019 earthquake as being bounded by the barrier fault to the southwest.

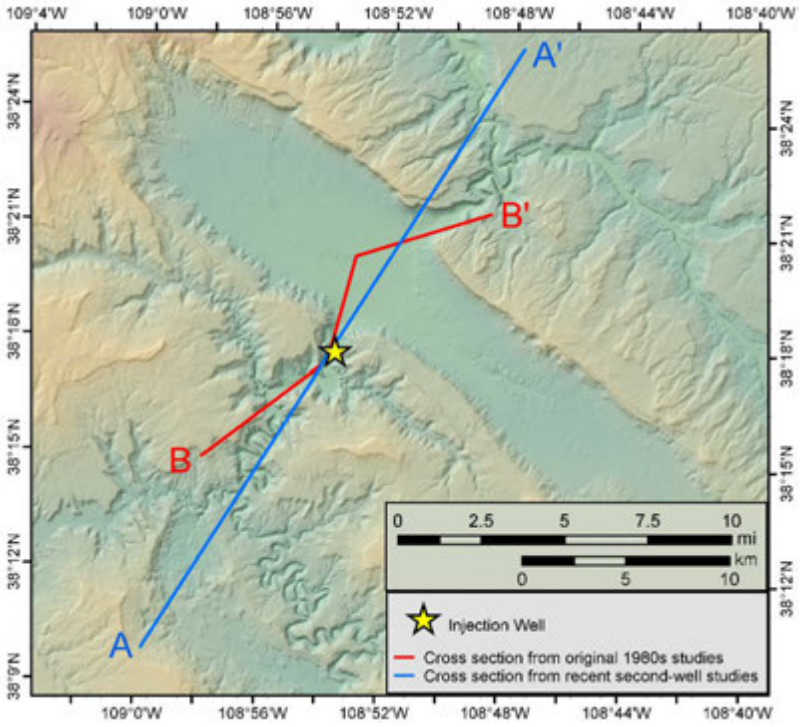

Figure 3-5: Map showing the locations of the geologic cross sections from the original (1980s) studies for the current PVU injection well (section B-B', red line) and the recent (2015-2017) studies for a potential second injection well (section A-A', blue line). The geologic cross sections are shown in Figure 3-6 and Figure 3-7.

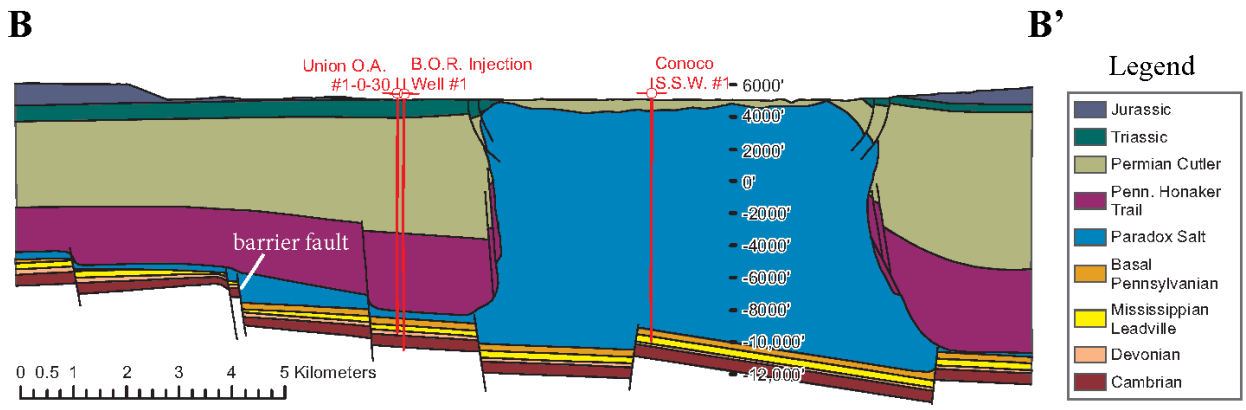

Figure 3-6: Geologic cross section developed in the 1980s, during technical studies performed to determine the location of the current PVU injection well. The fault ~2 km southwest of the PVU injection well that is interpreted to be a barrier to fluid flow from PVU injection is labeled. Figure taken from Block et al. (2015); originally adapted from Bremkamp and Harr (1988). The location of the cross section is shown in Figure 3-5.

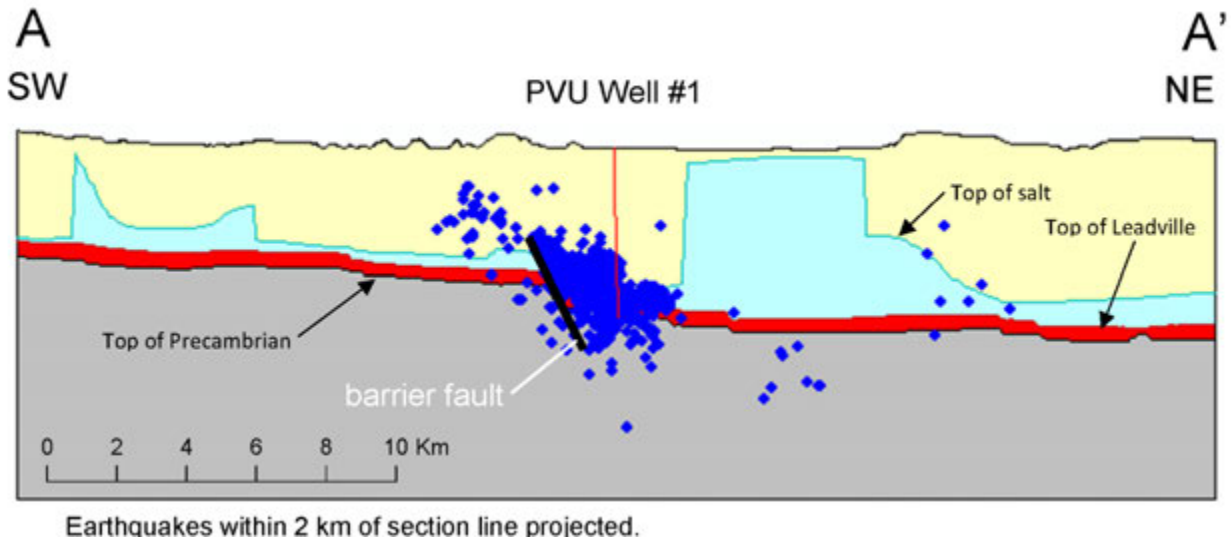

Figure 3-7: Geologic cross section developed during technical studies performed between 2015 and 2017, to evaluate locations for a potential second PVU injection well. The fault ~2 km southwest of the PVU injection well that is interpreted to be a barrier to fluid flow from PVU injection is labeled. Induced earthquakes that occurred between the start of injection in 1991 and the end of 2016 within 2 km of the section line are projected onto the section. Figure taken from King et al. (2018); based on the geologic model of Arestad (2016, 2017). The location of the cross section is shown in Figure 3-5.

Both geologic models also indicate a second NW-trending fault, northeast of the interpreted barrier fault. The original model places this fault immediately northeast of the aftershock cloud (Figure 3-8), whereas the more recent model shows the fault intersecting the aftershock cloud (Figure 3-9). The top of the Leadville formation defined by these two geologic models is shown in cross-sectional view in Figure 3-10. Aftershocks within 600 m of section line C-C', which is approximately perpendicular to the NW-trending faults (location shown in Figure 3-8 and Figure 3-9), are projected onto these cross sections. The projected aftershocks are identified by the colored circles on the maps in Figure 3-8 and Figure 3-9. The two sub-horizontal layers with high density of aftershocks seen in the cross sections suggest flat-lying, relative brittle geologic formations separated by a more plastic layer resistive to shear slip. This aftershock geometry suggests that the fault plane of the March 4th 2019 earthquake lies within a single structural fault block (with relatively flat-lying geologic layers), as indicated by the original geologic model.

Both models indicate that the hypocenter of the March 4th 2019 earthquake and the deeper dense layer of aftershocks lie near the top of the Leadville formation (Figure 3-10). Hence, one possible lithologic interpretation of the aftershock layers is that the deeper layer of aftershocks corresponds to the Leadville formation. This would then infer that the overlying zone with relatively few aftershocks, which suggests a layer resistive to shear slip, corresponds to the Paradox salt layer, the confining layer for PVU fluid injection. During previous studies, this geologic formation was interpreted as having isotropic stress conditions, which would make it highly resistive to shear slip (Wang et al., 2015 ; Yeck, 2015). The shallower dense layer of aftershocks would then be interpreted to occur within formations above the salt.

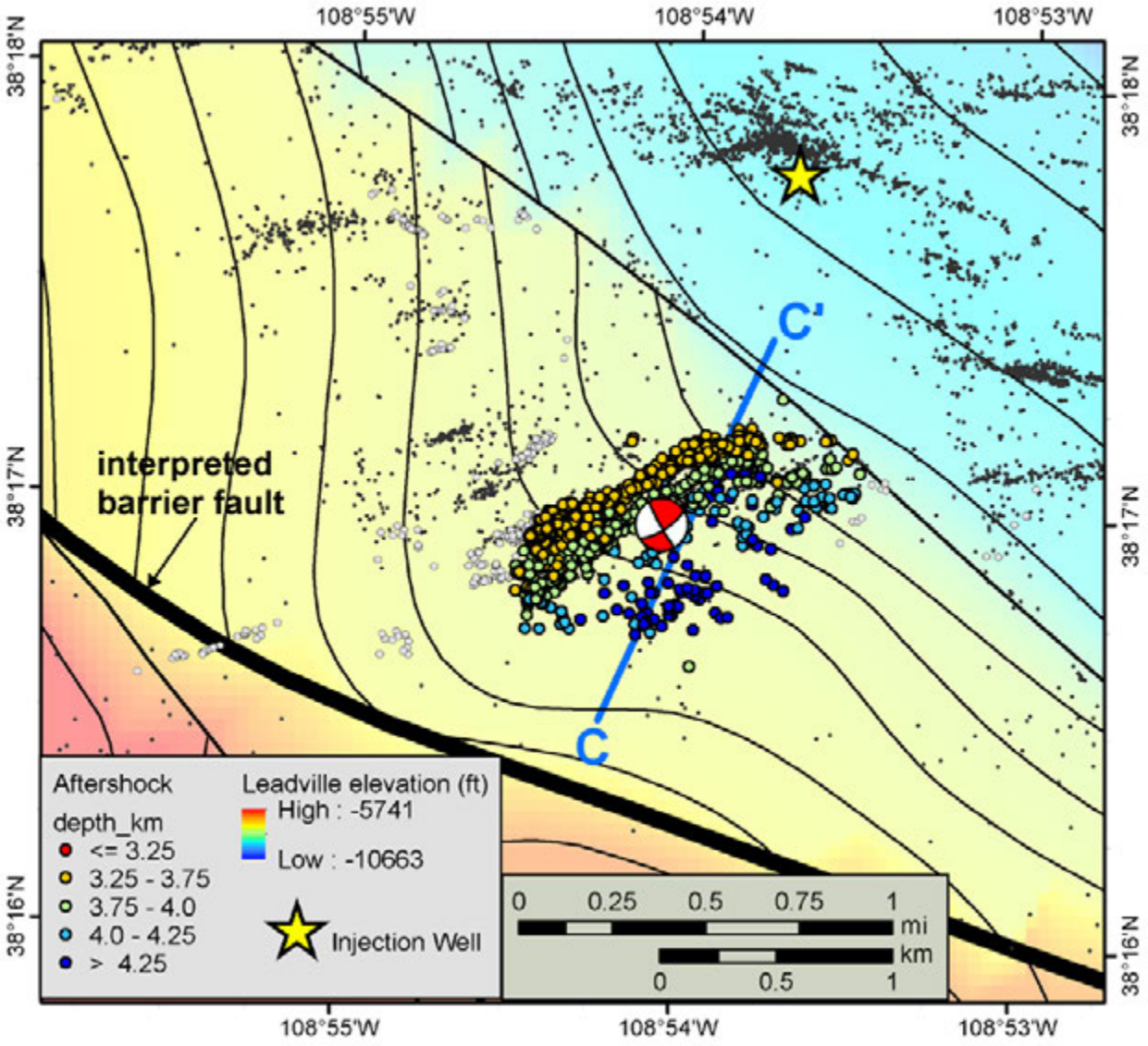

Figure 3-8: Structural map of the top of the Leadville formation from the original geologic model (Bremkamp and Harr, 1988), with the epicenters of the aftershocks of the March 4th 2019 earthquake (colored and gray circles) and previous seismicity (black dots) overlaid. The shaded surface and contours represent the top-of-Leadville elevation in feet; the contour interval is 100 ft. The thin black NW-trending lines are interpreted faults, and the thick black line represents the fault that is interpreted to act as a barrier to fluid flow and pore pressure increase from PVU injection. Aftershocks within 600 m of line C-C' are projected onto the cross section shown in Figure 3-10a and are color-coded by depth. Aftershocks that are not included in the cross section are shown in gray. The focal mechanism of the M_W 4.5 earthquake is plotted at the location of its epicenter.

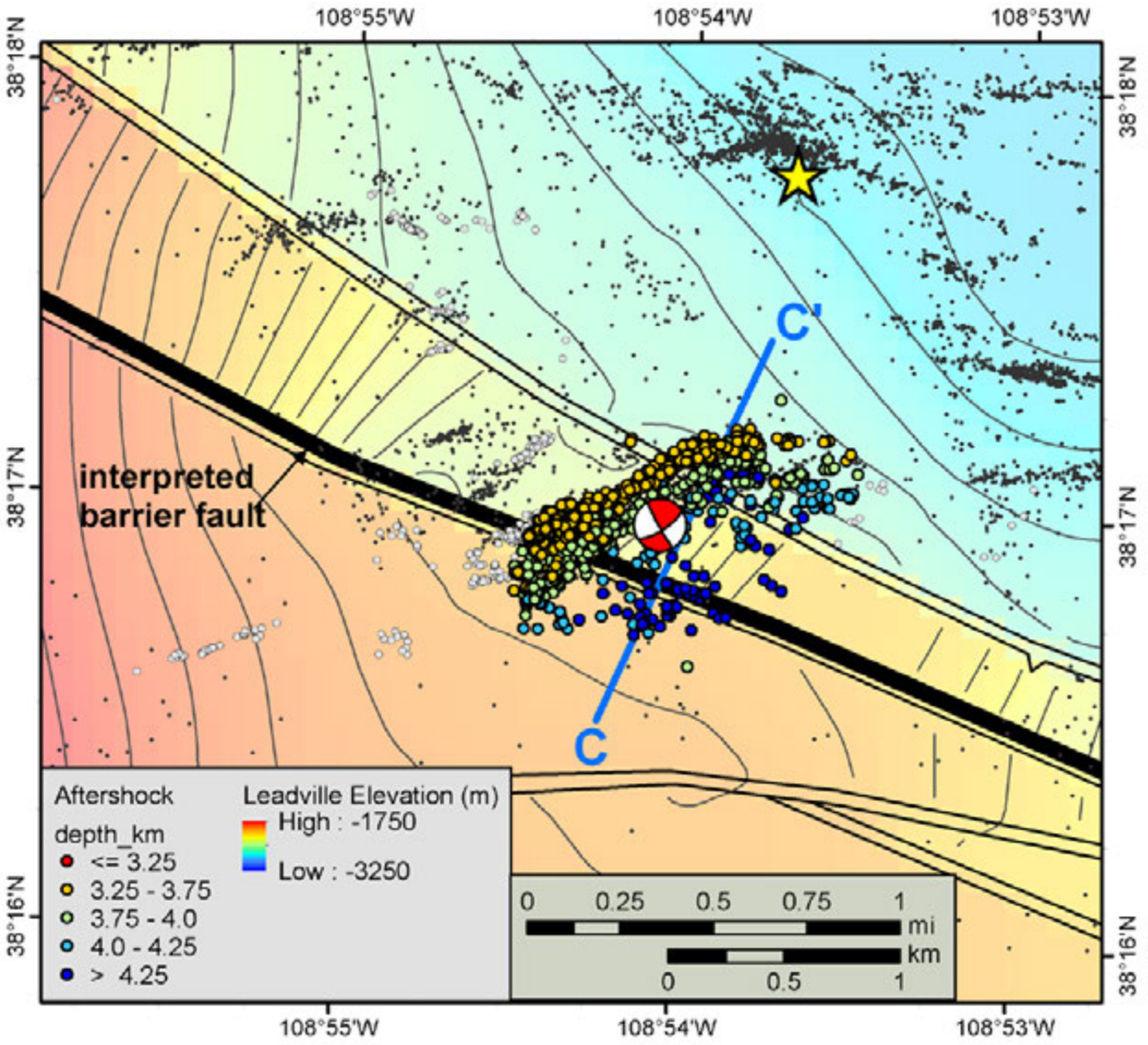

Figure 3-9: Structural map of the top of the Leadville formation from the most recent geologic model (Arestad, 2017), with the epicenters of the aftershocks of the March 4th earthquake (colored and gray circles) and previous seismicity (black dots) overlaid. The shaded surface and contours represent the top-of-Leadville elevation in meters; the contour interval is 50 m. The thin black NW-trending double lines are interpreted faults, and the thick black line represents the fault that is interpreted to act as a barrier to fluid flow and pore pressure increase from PVU injection. Aftershocks within 600 m of line C-C' are projected onto the cross section shown in Figure 3-10b and are color-coded by depth. Aftershocks that are not included in the cross section are shown in gray. The focal mechanism of the M_W 4.5 earthquake is plotted at the location of its epicenter.

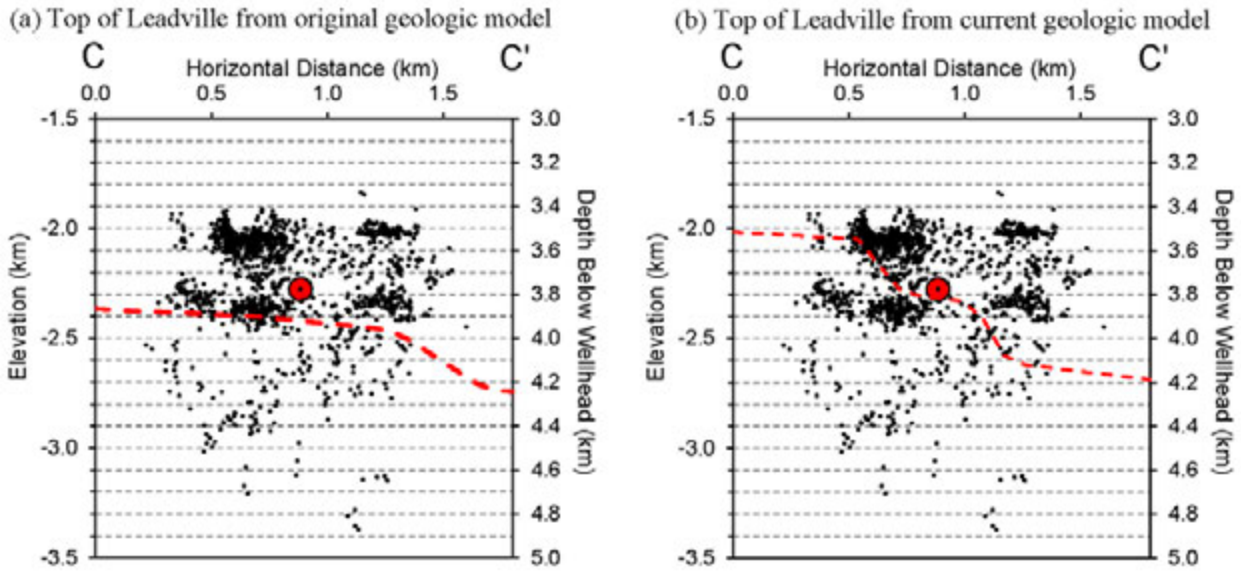

Figure 3-10: Vertical cross section C-C' showing the March 4th 2019 earthquake (red circle) and its aftershocks within 600 m of the section line (black dots). The interpreted top of the Leadville formation is indicated by the dashed red line: (a) original geologic model (Bremkamp and Harr, 1988) (b) most recent geologic model (Arestad, 2016, 2017). The location of the section line is shown in Figure 3-8 and Figure 3-9.

Because of the uncertainty in the absolute depths of the geologic formations as indicated by the geologic models and the uncertainty in the absolute depths of the earthquakes, additional information is needed to evaluate the lithologic interpretation described above. To obtain additional information, we performed an inversion of earthquake data in the vicinity of the March 2019 earthquake to determine a local P-wave velocity model. The P-wave velocity well log from the PVU injection well indicates a strong velocity contrast between the relatively high-velocity Leadville formation and the overlying formations (Figure 3-11). The Paradox salt has relatively low P-wave velocity compared to most other formations. We correlate the results from the local velocity inversion of the earthquake data to the P-wave velocity well log from the PVU injection well to determine formation depths at the location of the March 2019 earthquake.

The velocity inversion was performed using data from earthquakes in the area of the main aftershock cloud of the *Mw* 4.5 earthquake (Figure 3-12). The data set includes 1202 earthquakes occurring between June 1998 (the time of the first event in this area having a well-constrained hypocenter) and the end of April 2019. P-wave time differences between pairs of earthquakes computed by cross-correlation of vertical-component waveforms (with cross-correlation coefficient ≥ 0.75) were used. No absolute arrival times were included, and no S-wave time differences were used. Only earthquakes with hypocenters relatively well-constrained by P-wave time differences were included, as defined by the following criteria: P-wave time differences available from at least 6 stations; maximum azimuthal gap in time difference data $\leq 160°$; and distance to the closest station having time difference data divided by the event focal depth ≤ 2. To limit the possibility that unmodeled velocity variations outside the local grid would produce artifacts in the local velocity model, only data from earthquake pairs with hypocenters within

400 m of each other were included, and data from earthquake pairs with hypocenters more than 250 m apart were down-weighted. The final data set consisted of 533,761 time differences from 177,647 event pairs.

During the inversion, local P-wave velocities in the area indicated by the rectangle in Figure 3-12 and in the elevation interval from -1.9 to -3.0 km (~3.4 to 4.5 km depth below the PVU wellhead) varied, as well as the hypocenters of all earthquakes. Spacing of the velocity nodes within the local grid was 100 m in the horizontal directions and ranged from 50 m to 250 m in the vertical direction. Since no absolute time data were included and no event hypocenters were fixed, a center-of-mass hypocenter constraint was applied to stabilize the inversion. To further constrain and stabilize the inversion, velocity regularization was applied to control the smoothness of the final model, with the regularization weighted 12 times more in the horizontal direction than the vertical. Hence, the model is more layered than 3-D, because there is not enough redundancy in the data for a full 3-D inversion. The P-wave velocities within the local grid and the relative earthquake hypocenters were determined simultaneously using an iteratively re-weighted least squares inversion to approximate an L1 norm optimization, solved with a conjugate gradient algorithm. Appendix A contains a mathematical description of the relative hypocenter-velocity inversion.

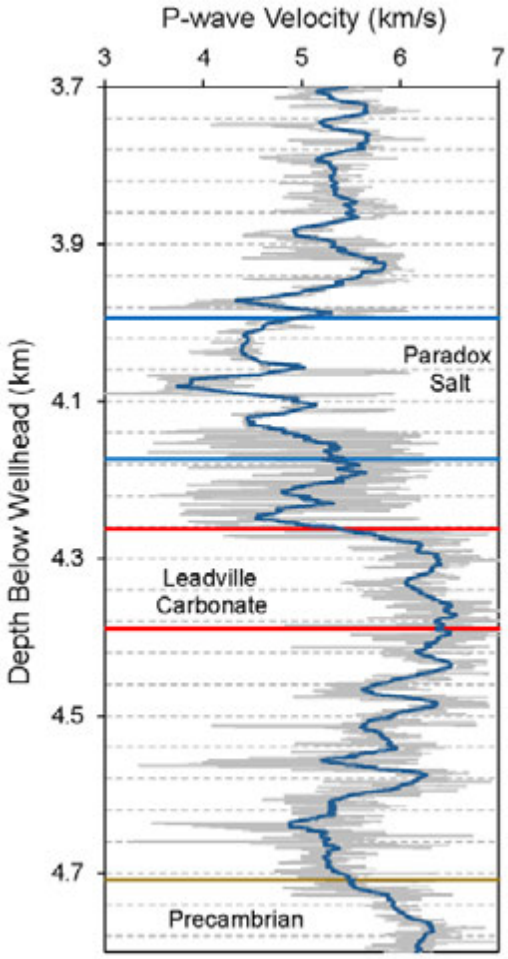

Figure 3-11: Sonic P-wave velocity log from the PVU injection well and the depth ranges of the Paradox salt confining layer (blue lines), the Leadville primary target injection formation (red lines), and the Precambrian basement (brown line) at the well. The raw well log is shown by the thin gray line, and a 20-m running average of the raw data is shown by the thicker blue line.

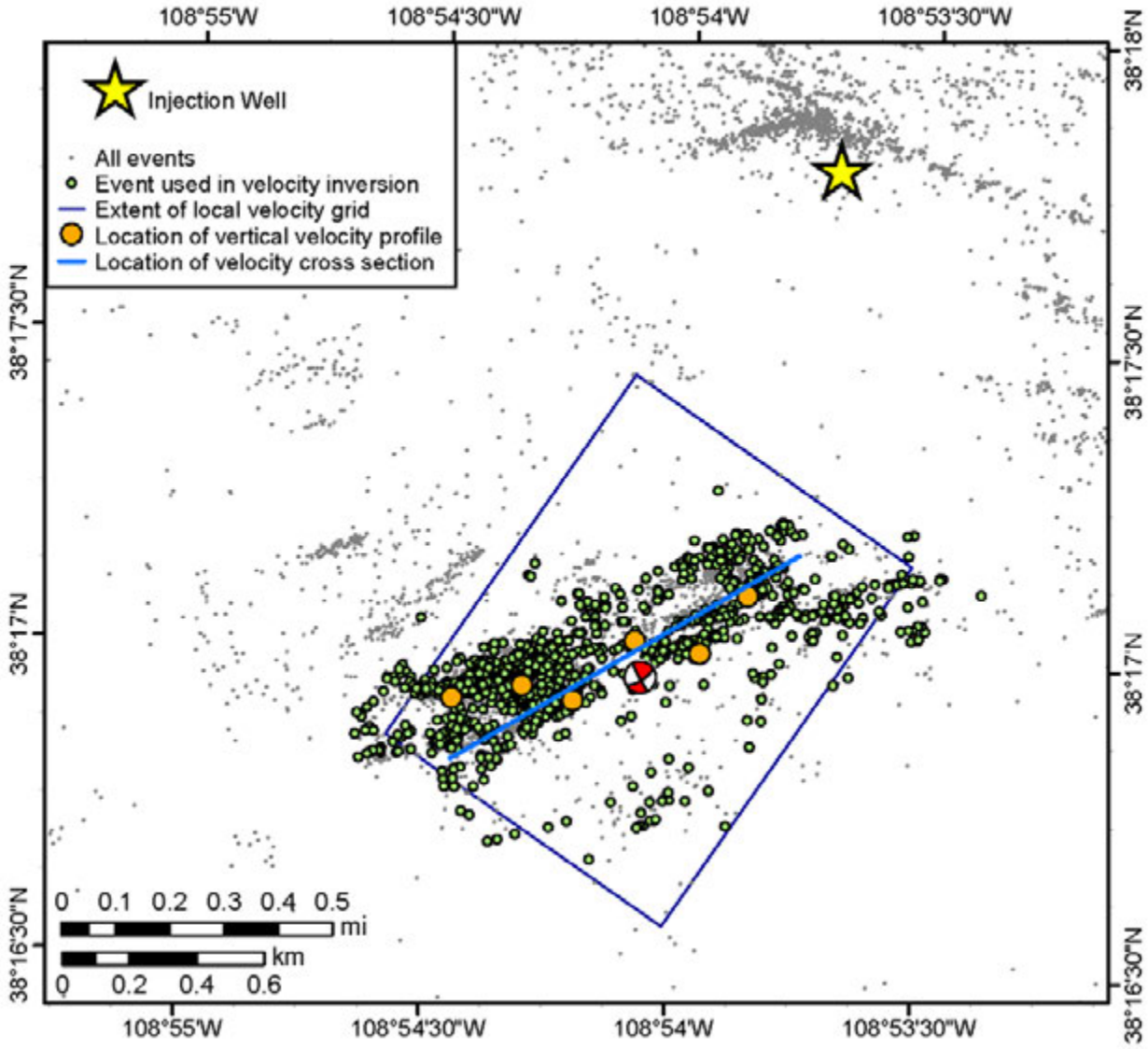

Figure 3-12: Extent of the velocity grid (rectangle) and locations of the earthquakes (green circles) used in the relative hypocenter-velocity inversion. This local velocity grid is aligned parallel to Paradox Valley, for consistency with the regional velocity model that is used outside the local grid boundaries. The focal mechanism symbol indicates the location of the March 4th 2019 M_W 4.5 earthquake. The blue line is the location of the cross section presented in Figure 3-14. The orange circles are the locations of the vertical P-wave velocity profiles plotted in Figure 3-15.

Initial, intermediate, and final P-wave time difference residuals for the relative hypocenter-velocity inversion show systematic improvement (Figure 3-13). The initial time difference residuals are those from the original (standard) event relative location, which utilizes both P-wave and S-wave data and a fixed regional velocity model. The mean absolute P-wave time

difference residual from this initial relative event location, for the subset of events included in the subsequent velocity inversion, is 4.4 x 10^{-3} s, or 4.4 ms (Figure 3-13, blue curve). The intermediate residuals shown in Figure 3-13 (red curve) are from a subsequent event relative location that utilizes only P-wave data, again with the regional velocity model fixed. Because S-wave data no longer must be satisfied, event locations can adjust to partially account for unmodeled P-wave velocity variations. Hence, even though the velocity model remains fixed, the P-wave time difference residuals improve substantially. The mean absolute time difference residual is 3.0 ms. The final P-wave time difference residuals are from the relative hypocenter-velocity inversion, in which only P-wave data are used and the P-wave velocities in the vicinity of the aftershocks vary (Figure 3-13, black curve). The final mean absolute time difference residual is 2.0 ms, a 33% reduction from the intermediate residuals and a 55% decrease compared to the original residuals.

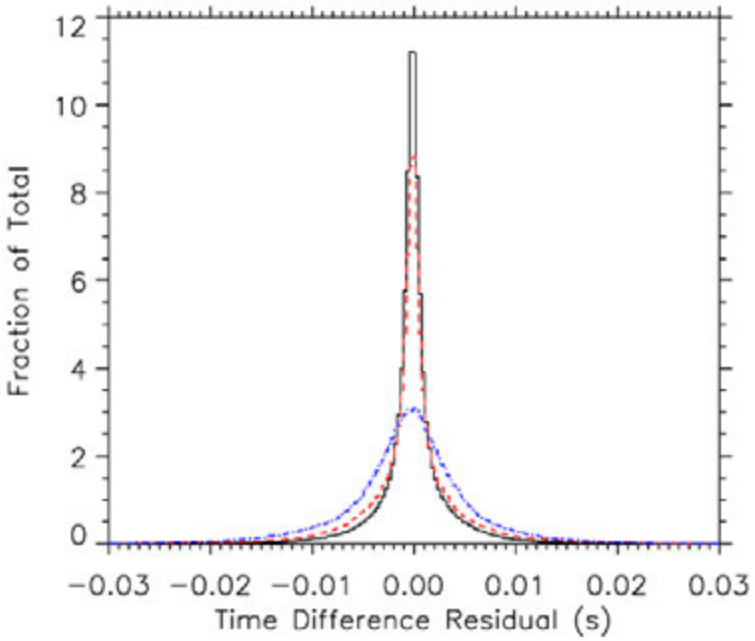

Figure 3-13: P-wave time difference residuals for the relative hypocenter-velocity inversion: initial residuals, from the original relative event location using P-wave and S-wave data with the regional velocity model fixed (blue; mean absolute residual = 4.4 ms); intermediate residuals from a relative event location using only P-wave data with the regional velocity model fixed (red; mean absolute residual = 3.0 ms); and final residuals using the derived local velocity model (black; mean absolute residual = 2.0 ms). Only residuals for the 1202 events included in the relative hypocenter-velocity inversion are included in the three histograms shown.

Results from the local velocity inversion show that the two sub-horizontal layers having high density of aftershocks of the March 2019 *Mw* 4.5 earthquake generally coincide with relatively high P-wave velocities, while the intervening layer with relatively few aftershocks generally corresponds to relatively low P-wave velocities. A vertical cross section through the center of the local velocity model and aligned parallel to the interpreted fault plane of the *Mw* 4.5 earthquake is presented in Figure 3-14. The upper plot shows the final hypocenters of the earthquakes used in the relative hypocenter-velocity inversion, and the lower plot shows all events within the main aftershock cloud of the *Mw* 4.5 earthquake (recorded through July 2019), with the relative locations that were previously determined using both P-wave and S-wave data. The highest P-wave velocities (~5.8 to ~6.1 km/s), indicated by orange and yellow colors of the cross section, coincide with the deeper aftershock layer (Figure 3-14, lower plot). Considerably lower P-wave velocities, as low as ~4.6 km/s, coincide with the overlying zone having relatively few

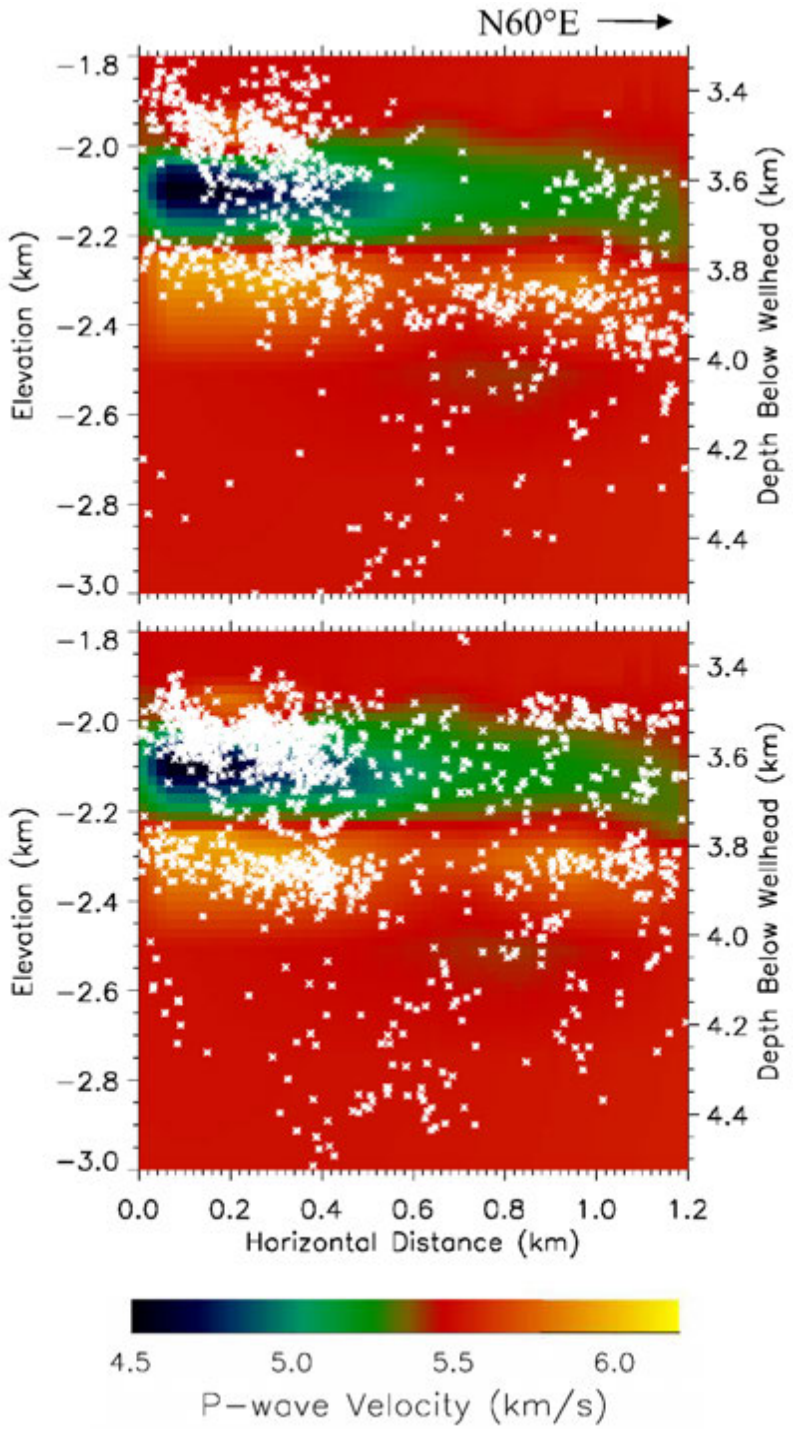

Figure 3-14: Vertical P-wave velocity cross section through and parallel to the main aftershock cloud of the March 2019 earthquake. In the upper plot, the final hypocenters of the earthquakes used in the local relative hypocenter-velocity inversion are overlaid. In the lower plot, the aftershocks of the March 2019 earthquake recorded through July 2019, whose relative locations were previously computed using both P-wave and S-wave data, are shown. In both plots, earthquakes within 500 m of the section are included. The location of the cross section is shown in Figure 3-12.

aftershocks. The upper aftershock layer lies just above the low velocity layer, where P-wave velocities begin transitioning to values of about 5.5 km/s.

To correlate the P-wave velocities from the local model in the area of the aftershock cloud to specific formations, we extracted vertical velocity profiles at several locations within the velocity grid (indicated by the orange circles in Figure 3-12) and compared them to the P-wave velocity profile from the sonic log in the PVU injection well. We achieve a reasonable correlation

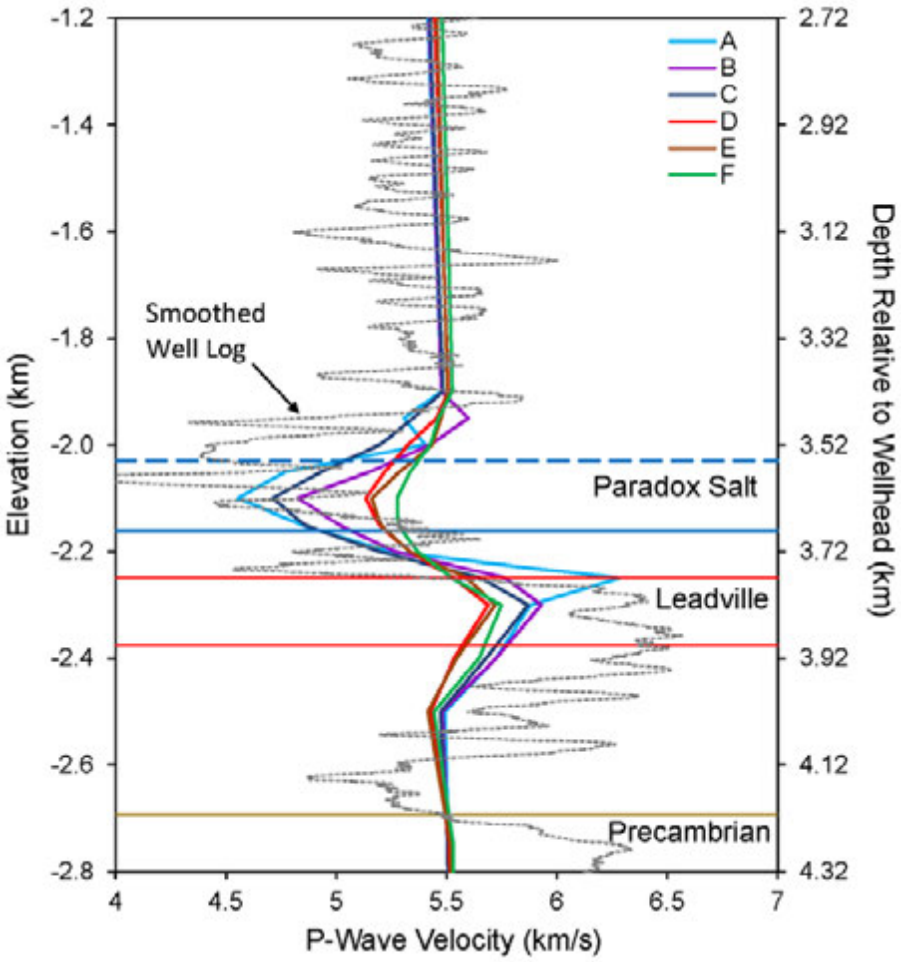

Figure 3-15: Vertical profiles from the velocity model in the area of the main aftershock cloud of the March 2019 M_W 4.5 earthquake (solid colored curves), compared to the P-wave velocity (sonic) well log from the PVU injection well (dotted gray curve). The locations of the velocity profiles from the model are indicated by the orange circles in Figure 3-12; the profiles are labeled alphabetically from west to east. Only velocities at and below -1.9 km elevation were determined during the local velocity inversion, and velocities below -2.5 km elevation were poorly constrained. The well log has been shifted vertically +490 meters. The formation interfaces shown by the horizontal solid lines (bottom Paradox salt, top and bottom Leadville, and top Precambrian) are taken from the geologic log in the PVU well and shifted vertically +490 m. The top of the Paradox salt (dashed blue line) is inferred from the top of the low P-wave velocity layer in the local velocity model and corresponds to a salt thickness 50 m less than at the PVU injection well.

between the profiles from the velocity model and the well log if we shift the well log vertically +490 m (Figure 3-15). This vertical shift is necessary to account for the shallowing of geologic layers southwest of the injection well, as previously interpreted from the seismic reflection studies (e.g., Figure 3-8 and Figure 3-9). To determine depths of formation interfaces, we also shift the formation tops and bottoms from the geologic log for the injection well +490 m (horizontal solid lines in Figure 3-15). This correlation assumes that the thicknesses of the formations at the location of the M_W 4.5 earthquake are the same as at the PVU injection well 1.6 km away. This is a reasonable assumption for all formations except the Paradox salt, which can vary dramatically in thickness over short distances. The bottom of the salt is constrained by the thickness of the underlying layers (since we correlate the velocity profiles and sonic log at the strong velocity contrast at the top of the Leadville formation). We adjusted the top of the salt to coincide with the top of the low-velocity layer in the local velocity model, as indicated by the horizontal dashed blue line in Figure 3-15. This adjustment infers a reduction in the thickness of the Paradox salt by 50 m, compared to its thickness at the PVU injection well.

The formation boundaries interpreted from the velocity correlation above are shown on cross sections parallel and perpendicular to the fault plane of the March 2019 earthquake in Figure 3-16. These cross sections include the main shock (red circle) and aftershocks in vicinity of the fault plane recorded through July 2019 (black dots). In addition to the formation boundaries, the cross sections also include the interpreted location of the barrier fault and the extent of the fault plane having a geometry consistent with the focal mechanism of the M_W 4.5 earthquake, interpreted previously (section 3.1). These cross sections show the top of the Paradox salt as being flat (dashed blue horizontal line), but the top of the salt may undulate. In particular, the salt thickness and configuration may become more complex in the vicinity of the barrier fault.

These lithologic interpretations indicate that the fault plane of the March 4th earthquake extends from at least the top of the Leadville formation into the upper Precambrian. Approximately half of the vertical extent of the fault plane shown in Figure 3-16 lies within the Leadville and underlying sedimentary units (~3.75 - 4.25 km depth), and the other half lies within the Precambrian crystalline basement (~4.25 – 4.75 km depth). The hypocenter of the March 4th 2019 earthquake coincides with the interpreted top of the Leadville formation. As discussed previously (section 3.1), the shallower aftershocks (< ~3.75 km depth) occur on one or more faults that have significantly steeper dips (~78-80°) than the dip of the fault segment on which the M_W 4.5 earthquake occurred (~60-65°). These aftershocks could have been triggered by stress changes related to rupture of the deeper fault plane. An alternate interpretation is that the main shock fault rupture continued to shallower depths, rupturing through the Paradox salt and into overlying formations at a steep angle.

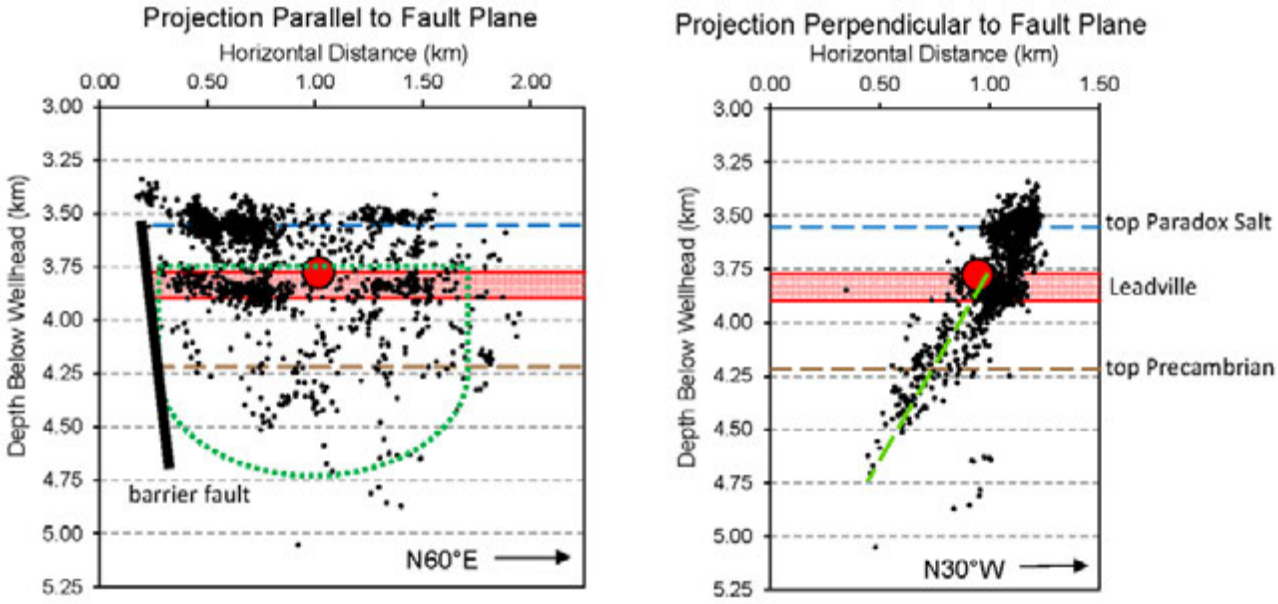

Figure 3-16: Vertical cross sections of the March 4th 2019 M_W 4.5 earthquake (filled red circle) and its main cloud of aftershocks recorded through July 2019 (black dots). The locations of the cross sections are shown in Figure 3-1. The section on the left is approximately parallel to the fault plane (N60°E). Earthquakes within 0.5 km of the section line are included. The section on the right is approximately perpendicular to the fault plane (striking N30°W), with earthquakes within 0.95 km of the section line projected. The interpreted locations of the barrier fault and major lithologic boundaries are labeled. The dashed green lines indicate the interpreted extent of the fault plane having a geometry consistent with the focal mechanism of the M_W 4.5 earthquake.

The largest aftershocks of the M_W 4.5 earthquake (recorded through July 2019) preferentially occur within the Leadville formation and upper Precambrian (Figure 3-17). The five aftershocks within the main aftershock cloud with $M_D \geq 2.5$ are indicated by the orange circles in Figure 3-17. The hypocenters of two of these events lie within the interpreted depth range of the Leadville formation, and the hypocenters of the other three aftershocks are within the upper Precambrian. Aftershocks with magnitude between M_D 1.5 and M_D 2.4 also preferentially occur within the Leadville and upper Precambrian (blue circles in Figure 3-17). In contrast, most of the events in the shallow aftershock layer, near the interpreted top of the Paradox salt, have magnitudes < M_D 1.5.

There are several possible reasons for the observed pattern in the spatial distribution of aftershock magnitudes. In early PVU geologic and geophysical studies, the Leadville formation was identified as the primary target formation for injection, while the upper Precambrian was identified as a secondary injection target formation, based on their porosities and permeabilities. It is possible that the greater porosities and permeabilities of these lithologies directly facilitate the occurrence of larger aftershocks, or perhaps these units are more affected by pore pressure increase from PVU injection than other formations and those elevated pore pressures facilitate larger aftershocks. Alternatively, the pattern may be strictly related to stress re-distribution after the fault plane rupture on March 4th 2019, with relatively large stress changes occurring in the

Leadville formation along the upper edge of the interpreted fault segment (either because rupture ended here or because the rupture plane changes dip at this depth) and within the upper Precambrian, near the bottom of the rupture plane. The relatively small magnitudes of the earthquakes within the shallow aftershock layer at the top of the Paradox salt may be related to pore pressures being low above the injection confining layer, making the faults less critically stressed (or critically stressed only over small fault segments). It could also indicate that stress changes caused by fault rupture during the *MW* 4.5 earthquake are relatively small above the salt, which would suggest that the main shock fault rupture did not extend through the salt.

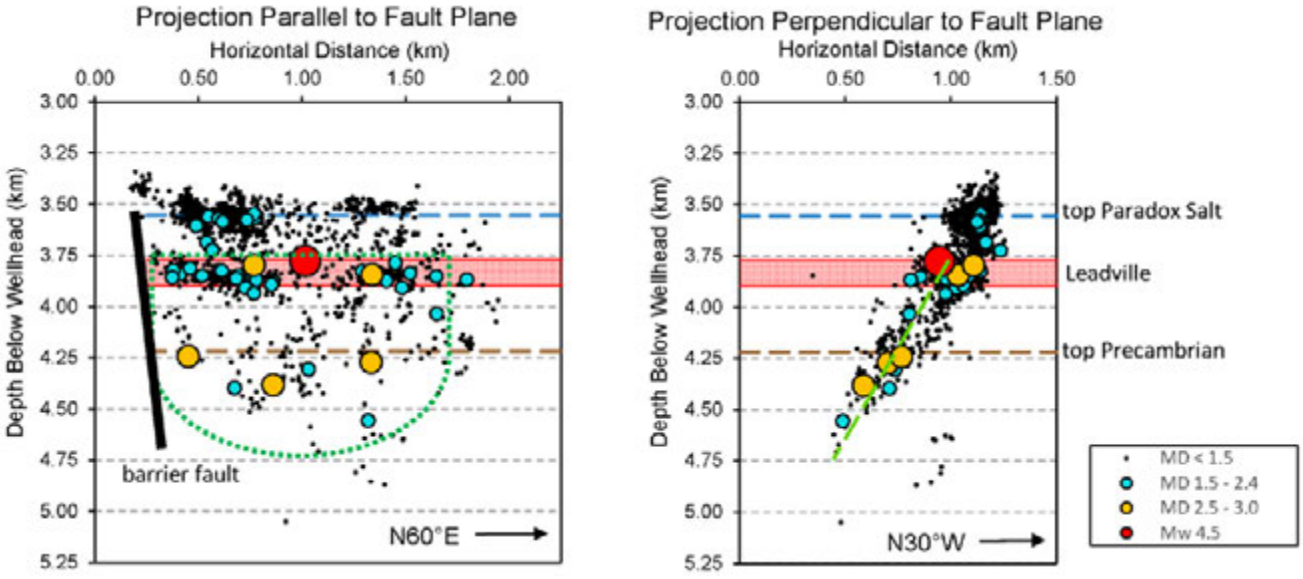

Figure 3-17: Same cross sections as in Figure 3-16, with the earthquake symbols sized and colored by magnitude range.

3.3 Previous Seismic Activity

When estimating the potential for future large-magnitude induced earthquakes, we have assumed that large-magnitude earthquakes will occur in areas that have previously produced smaller-magnitude induced earthquakes. For example, the second largest PVU-induced earthquake, the *MW* 4.0 earthquake of January 2013, occurred on a fault that had been seismically active for 14 years prior to its occurrence (Block et al., 2014). Nearly the entire length of the fault segment that ruptured during the *MW* 4.0 earthquake had been seismically active in the past. To see if this pattern is also valid for the March 4th, 2019 *MW* 4.5 earthquake, we examine the seismicity that occurred in the vicinity of its main aftershock cloud in the years prior to its occurrence.

A comparison of a map showing the epicenters of all events with reliable relative locations that occurred prior to the March 2019 *MW* 4.5 earthquake and a map showing the location of the *MW* 4.5 earthquake and its aftershocks indicates that much of the fault plane that ruptured on March 4th, 2019 was aseismic prior to the occurrence of the *MW* 4.5 event (Figure 3-18). On these maps,

(a) Events prior to the March 4th, 2019 M_W 4.5 earthquake

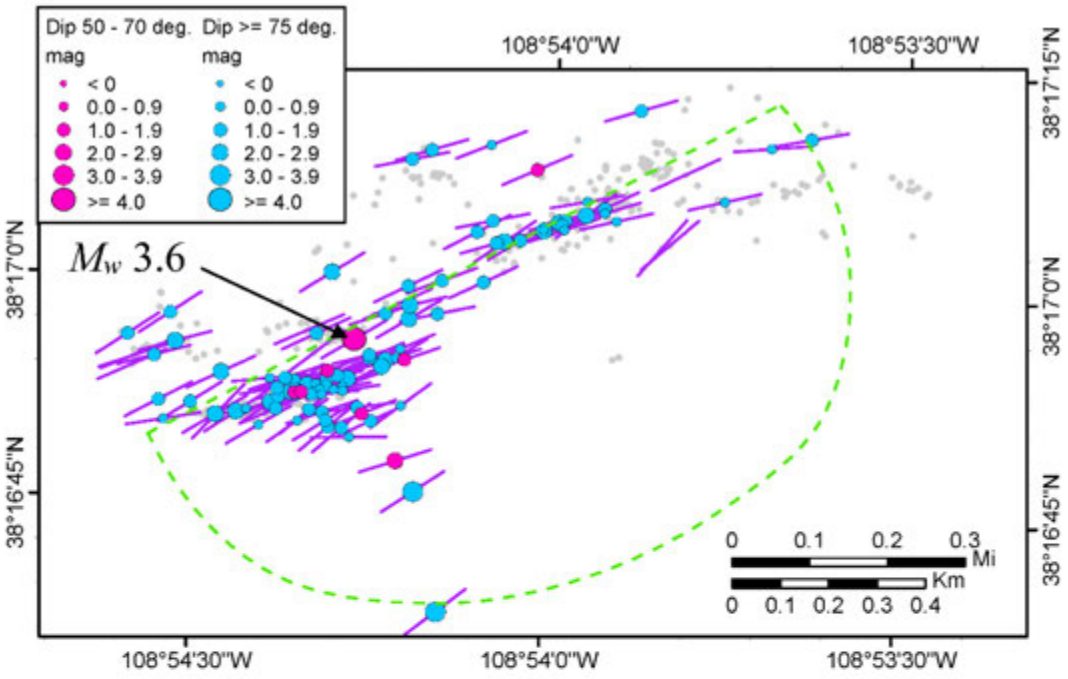

(b) March 4th, 2019 M_W 4.5 earthquake and its aftershocks through July 2019

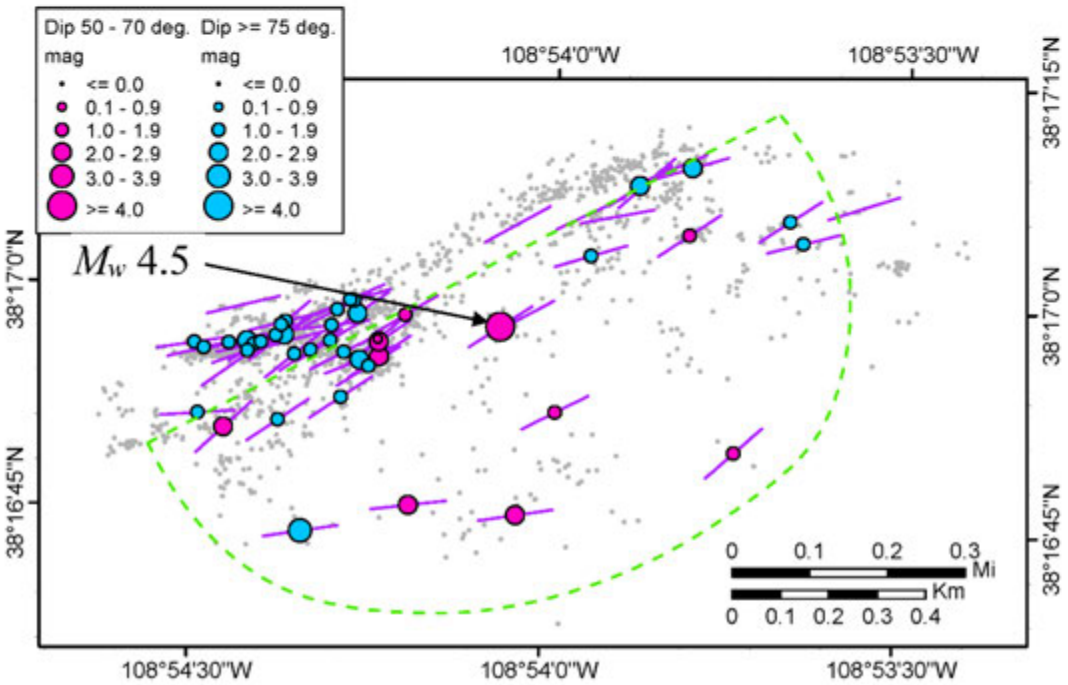

Figure 3-18: (a) Epicenter map of earthquakes with relatively relocated hypocenters that occurred prior to the March 4th, 2019 M_W 4.5 earthquake; data spans May 1997 – Jan. 2019 (b) Epicenter map of the March 4th, 2019 M_W 4.5 earthquake and its aftershocks with relatively relocated hypocenters recorded through July 2019. The dashed green lines indicate the interpreted extent of the fault plane having a geometry consistent with the focal mechanism of the M_W 4.5 earthquake.

the area within the dashed green outline is the estimated extent of the fault plane with ~60-65° dip that ruptured on March 4th, 2019. The map of historical seismicity, which includes events from May 1997 to January 2019, shows many epicenters along the northwestern (shallow) edge of the fault plane, but very few epicenters within much of the defined fault rupture area (Figure 3-18a). As we did previously (section 3.1), we also identify events that have focal mechanisms consistent with that of the March 4th earthquake (pink circles) and those with more steeply-dipping focal planes (blue circles). Most of the historical seismicity has focal mechanisms with NE-trending, steeply-dipping (≥ 75°) focal planes (Figure 3-18a, blue circles). A small cluster of earthquakes with NE-trending focal planes with shallower dips (50°-70°, dipping to the southeast), consistent with the focal mechanism of the March 4th earthquake, is seen near the southwestern end of the fault area (Figure 3-18a, pink circles). Among these events is the fourth-largest PVU-induced earthquake, the M_W 3.6 earthquake of November 2004 (Table 2-1). The focal mechanism of that event is very similar to the focal mechanism of the M_W 4.5 earthquake, as shown by the comparison in Figure 3-19. Five of the six nearby events with the same type of focal mechanism (Figure 3-18a) occurred within ~1.5 years of this M_W 3.6 earthquake and are likely aftershocks of it.

The historical seismicity from the map in Figure 3-18a is projected onto cross sections parallel and perpendicular to the fault plane of the M_W 4.5 earthquake in Figure 3-20. The location of the barrier fault, formation interfaces, and the extent of the fault plane having a geometry consistent with the focal mechanism of the M_W 4.5 earthquake (interpreted in previous sections) are shown for reference. The hypocenter of the March 2019 earthquake is also included (large open black circle). Most of the historical events occurred either within the Leadville formation in the northeastern half of the interpreted fault plane or in a relatively shallow cluster at and above the interpreted top of the Paradox salt further southwest, immediately northeast of the barrier fault (Figure 3-20, parallel section on left). The M_W 4.5 earthquake occurred at the southwestern end of the area containing most of the previous seismic activity within the Leadville. These cross sections re-affirm the observation that much of the relatively shallow-dipping (60-65°) fault plane that is interpreted to have ruptured in March 2019 was largely aseismic prior to the occurrence of the M_W 4.5 earthquake. Few hypocenters of historical events occur close to its interpreted fault plane below a depth of roughly 4 km (Figure 3-20, perpendicular section on right).

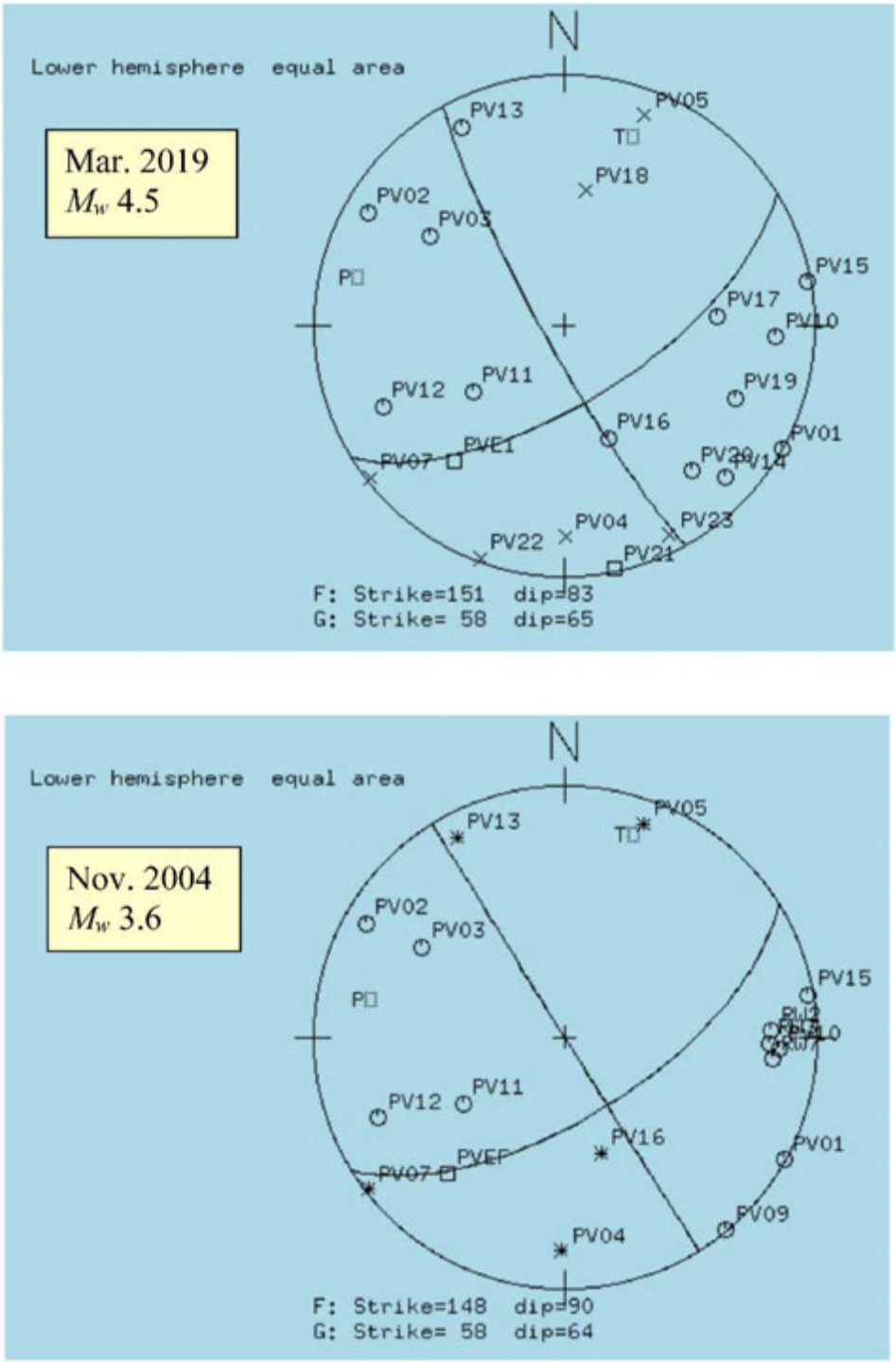

Figure 3-19: First breaks and focal mechanism of the March 2019 M_W 4.5 earthquake (upper plot) and November 2004 M_W 3.6 earthquake (lower plot), plotted on lower hemisphere equal-area projections. X and open circle symbols represent compressional and dilatational first breaks, respectively. Square symbols represent locations of the P and T axes, or stations having no clear first break. The preferred focal mechanism for each earthquake is the focal plane trending N58°E and dipping 64°-65° SE.

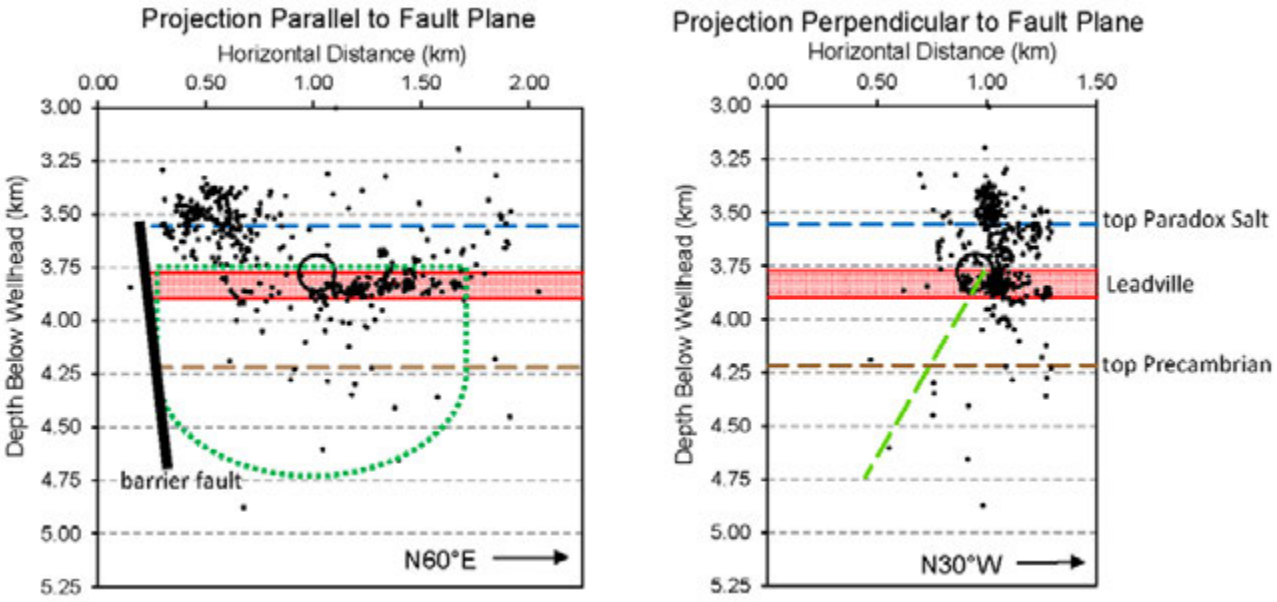

Figure 3-20: Earthquakes with relatively-relocated hypocenters that occurred prior to the March 2019 M_W 4.5 earthquake (from the map in Figure 3-18a; black dots), projected onto cross sections parallel (left) and perpendicular (right) to the fault plane of the March 2019 M_W 4.5 earthquake. The locations of the cross sections are shown in Figure 3-1. The interpreted locations of the barrier fault and formation interfaces are included as labeled (see section 3.2 for more details). The dashed green lines indicate the interpreted extent of the fault plane having a geometry consistent with the focal mechanism of the M_W 4.5 earthquake, based on aftershocks of that event. The hypocenter of the March 2019 M_W 4.5 earthquake is indicated by the large open black circle.

To further evaluate whether the November 2004 M_W 3.6 earthquake and its aftershocks with similar focal mechanisms occurred on the same fault as the March 2019 M_W 4.5 earthquake, we plot the hypocenters of the historical events color-coded by focal mechanism type on the cross sections (Figure 3-21). The hypocenters of both the M_W 3.6 earthquake and its aftershocks occur in the cluster of events at the upper boundary of the Paradox salt, just northeast of the barrier fault (Figure 3-21, parallel section on left). It appears that the November 2004 M_W 3.6 earthquake may have ruptured a shallower section of the ~65°-dipping fault plane that failed in March 2019 (Figure 3-21, perpendicular section on right). Based on data analyzed to date, neither earthquake appears to have ruptured both the upper and lower sections of the fault plane simultaneously. If such a rupture were to occur, it would correspond to a fault plane rupture radius of approximately 0.8 to 0.9 km and produce an earthquake somewhat larger than the M_W 4.5 event (Figure 3-22).

The interpretations presented here are based on a limited set of focal mechanism results, computed over the course of several years. A more thorough understanding of the relationship of the fault planes of the M_W 3.6 and M_W 4.5 earthquakes may be achieved if the focal mechanisms of all the larger events ($\geq$ ~M_D 1.0) in this area were re-computed and analyzed in a robust and systematic manner. A substantially improved understanding of the relationship between the fault planes and the geologic formations and barrier fault would likely only be possible if high-resolution 3-D seismic reflection data were to be acquired in this area.

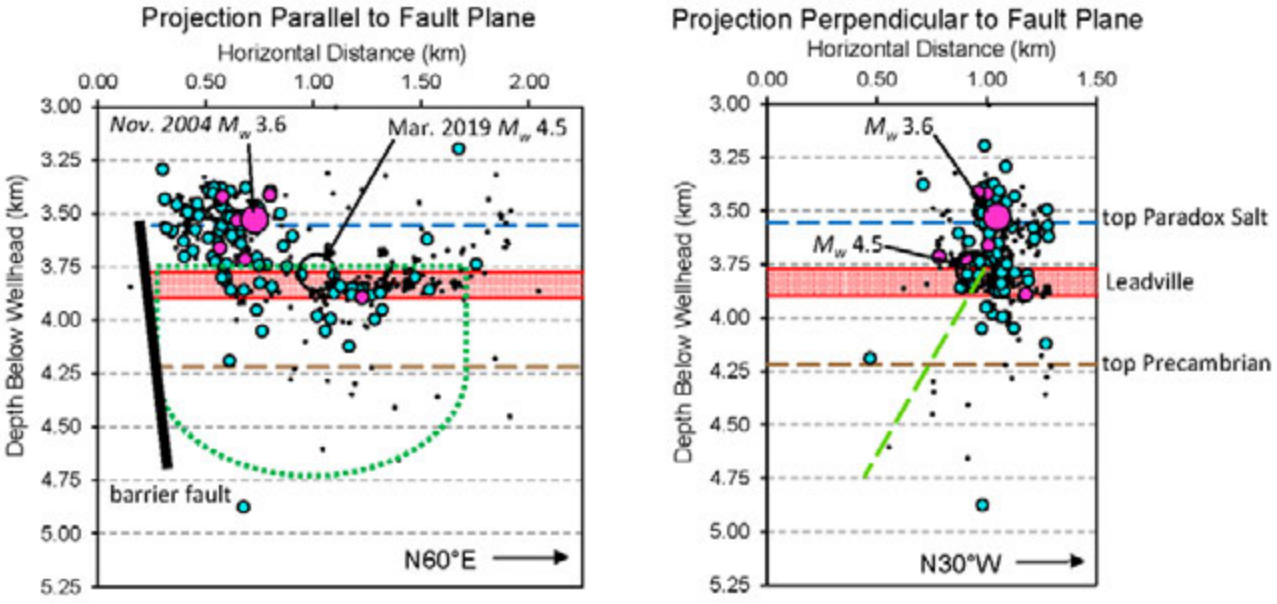

Figure 3-21: Earthquakes with relatively-relocated hypocenters that occurred prior to the March 2019 M_W 4.5 earthquake (from the map in Figure 3-18a; black dots), projected onto cross sections parallel (left) and perpendicular (right) to the fault plane of the March 2019 M_W 4.5 earthquake. The locations of the cross sections are shown in Figure 3-1. Two sets of hypocenters are colored by the dip range of their focal mechanisms: 50°-70° (pink symbols) and ≥ 75° (blue symbols). All focal mechanisms have fault planes striking northeast. For the focal mechanisms with the shallower dips, the dip direction is to the southeast. For the focal mechanisms with the steeper dips, the dip direction is either southeast or northwest. The interpreted locations of the barrier fault and formation interfaces are included as labeled (see section 3.2 for more details). The dashed green lines indicate the interpreted extent of the fault plane having a geometry consistent with the focal mechanism of the M_W 4.5 earthquake, based on aftershocks of that event. The hypocenter of the March 2019 M_W 4.5 earthquake is indicated by the large open black circle.

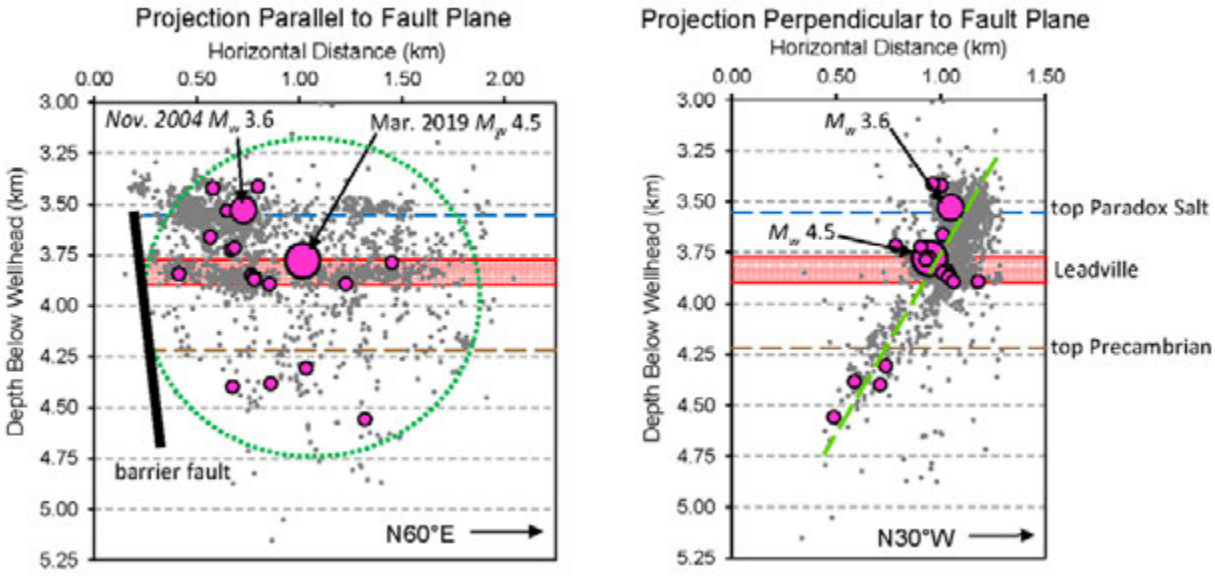

Figure 3-22: Cross sections parallel (left) and perpendicular (right) to the fault plane of the March 2019 M_W 4.5 earthquake, showing all seismicity recorded through July 2019 (black dots) and earthquakes with focal mechanisms similar to those of the November 2004 M_W 3.6 and March 2019 M_W 4.5 earthquakes (pink circles). The locations of the cross sections are shown in Figure 3-1. The green dashed lines represent a theoretical fault plane extent that encompasses the ruptures from both these earthquakes.

4 Coulomb Stress Change Modeling

4.1 Introduction

This section describes an initial attempt to model the Coulomb stress change ΔCS produced by the 2019 *Mw* 4.5 earthquake to determine if the aftershock distribution pattern can be associated with inferred stress changes. The earthquake occurred on March 4th of 2019 and was subsequently followed by thousands of aftershocks. The Coulomb Failure Function (CFF) model is a physical model for stress transfer and triggering for earthquakes and aftershock occurrence where the resulting model represents the response to ΔCS induced by the preceding event (Harris, 1998; King and Cocco, 2001; King et al., 1994; Stein, 1999).

Large earthquakes are associated with numerous aftershocks that decrease in frequency and magnitude according to known laws such as Bath's law for the difference in the magnitude of a mainshock and its largest aftershock (Bath, 1965), and the modified Omori's law for the temporal decay of aftershock rates (Utsu, 1961). Aftershocks can be viewed as the result of a relaxation process for stress concentration produced by the mainshock. The spatial correlation between shear stress increase from the mainshock and the resulting aftershock distribution was identified by Das and Scholz (1981).

The concept of ΔCS that involves a linear combination of shear and normal stress changes, where the positive ΔCS are responsible for earthquake triggering, was introduced and demonstrated by Stein et al. (1992) and King et al. (1994). One of the examples of Coulomb stress triggering studies related to large earthquakes is the 1992 M_w 7.3 Landers earthquake (Kilb et al., 2002; King et al., 1994). King et al. (1994) explored the changes in Coulomb conditions associated with earthquakes that trigger aftershocks on faults that are optimally oriented for failure relative to present regional stress and the stress change caused by the main event. In the case of the Landers earthquake, many aftershocks were found on areas where stress increased, while aftershocks were sparse on regions where Coulomb stress dropped (King et al., 1994). Aside from the aftershock clouds along regions of mean stress increase, location or occurrence of succeeding earthquakes along the Anatolia Fault seemed to have been triggered by transfer of stress by one earthquake to another, particularly relative to the earthquakes of 1939 up to 1992 (Durand et al., 2013; King et al., 2001; Stein et al., 1997). Nine out of ten events that occurred during this span of time are located where the mean stress increased due to the preceding event (Stein et al., 1997). In the case of the 1999 Chi-Chi earthquake, on the other hand, Ma et al. (2005) showed that sites of seismicity rate changes resemble the calculated Coulomb stress change but also highlights that the stress shadows clearly are areas where earthquakes rate dropped. Ma et al. (2005), therefore, concluded that the observations of stress shadows in the Chi-Chi earthquake is an important validation of the Coulomb hypothesis that strengthens the case for the role of stress shadows in suppressing seismicity.

Considering these published observations of correlation of earthquake triggering and aftershock location relative to positive and negative (shadow zones) ΔCS, this work presents several simple models of the ΔCS related to the 2019 March 4th earthquake, with basic inputs and assumptions, and compares the predicted ΔCS to the observed aftershock distribution.

4.2 Methods and Limitations

In this work, Coulomb stress calculations were made using the COULOMB 3.4.1 code (Lin and Stein, 2003; Toda et al., 2005). Assuming earthquakes are triggered on planes with maximum total Coulomb stress, the two idealized cases where stress are calculated within the COULOMB 3.4.1 code are: (1) fixed receiver fault mechanism, where strike, dip, and rake angles are fixed, or (2) optimally oriented planes. In this study, we only modeled the case of optimally oriented planes, where the main parameters are location and geometry of source faults.

In this modeling, the fault geometries like strike, dip and rake were defined from focal mechanisms, while the fault dimensions were based on the earthquake magnitude and aftershock plots (and some limited geologic information). The focal mechanism, fault location, and fault orientation adapted in the modeling are from section 2. The moment magnitude used is from the UUSS, as published by the USGS at https://earthquake.usgs.gov/earthquakes/eventpage/uu60315157/moment-tensor (downloaded on 12/18/2019), as discussed in section 2 of this report. The 1,999 hypocenters used were events recorded from March 4th 2019 to July 2019 (see Figure 5-5). Fault geometries were mapped and initial input files were built using a custom add-in for ArcGIS (Wood, 2018).

The isotropic poroelastic setting used for the CFF model is in accordance with previous studies (King et al., 2001; Stein et al., 1997), using an initial fixed value for the apparent friction coefficient μ of 0.6. Considering that the focus of this work is to determine if the aftershock distribution observed from the March 2019 earthquake can be defined by ΔCS distribution, the fault dimensions were limited to simple rectangular fault plane where the ΔCS were only calculated for optimally oriented planes. Throughout the modeling, the area, mean slip, and depth range of the rupture planes were adjusted considering the earthquake magnitude and focal mechanism as stated above. The assumed values for the rest of the parameters are as follows: Poisson's ratio of 0.25, Young's modulus of 8×10^5 bars (or 3.3×10^5 bars 3.3×10^{11} dyne-cm^{-2}), the maximum regional stress direction of N78°W from Block et al. (2015) and King et al. (2018), and regional in situ pore pressure gradient of ~0.47 psi/ft from King et al. (2018). Assuming multiple scenarios with the hypocenter at 3.9 km depth and a fault plane dip of 65°, as indicated in section 2, rupture planes were modeled with different combinations of fault lengths, ruptures widths, and top-of-rupture planes, with variable friction coefficient. A few of the results are shown in the next sub-section.

4.3 Modeling Results

In this work, ΔCS distributions were calculated for two assumed lengths of the fault rupture plane to investigate if the spatial aftershock pattern is consistent with the pattern of the elastic stresses transferred by the March 4th, 2019 M_W 4.5 earthquake. Considering that the defined length of the fault rupture was based on the main shock magnitude and aftershock analysis, rupture planes with lengths of 1.4 km and 600 m are presented, with varying widths along dip and top-of-rupture depths. Figure 4-1 shows the area of calculations and cross-sections at different directions across the main fault plane. In the resulting cross sections, the seismicity plotted are those events within 0.5 km of both sides of the section line.

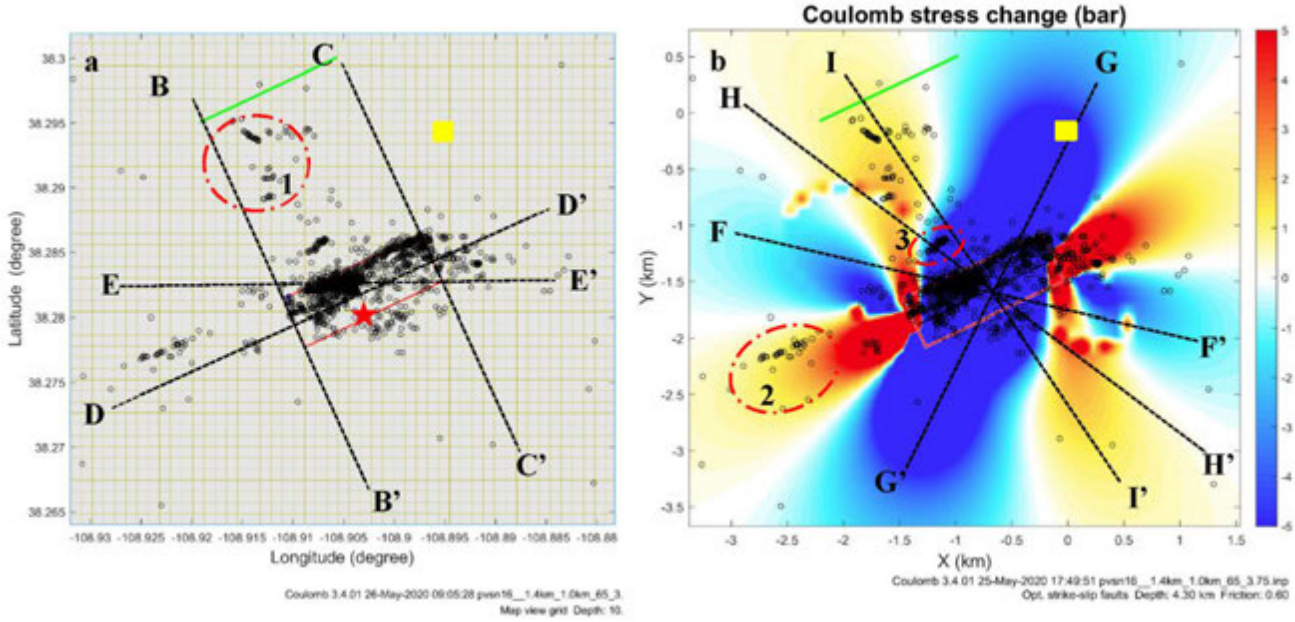

Figure 4-1: (a) Map of the area of Coulomb stress calculations with aftershocks (open black circles). The dashed black lines indicate cross sections: BB' and CC" are perpendicular to the southern and northern ends of the fault plane, DD' is parallel to the fault plane and along positive ΔCS, and EE' is an east-west line cutting through the fault plane. (b) Sample map of ΔCS with cross-section lines: FF' and GG" are through negative ΔCS regions, HH' is across the shallow aftershock cluster 3, and II' is along positive ΔCS. The thin black line shows the middle of the fault plane (red rectangle), and the green line shows its surface projection. Also shown on (a) map are locations of the main shock (red star) and the injection well (yellow square). See the main text for descriptions of aftershock clusters (red dashed ellipses): cluster 1 transected by BB' and II', cluster 2 by DD', and cluster 3 by HH'.

On the first and second sets of models shown in Figure 4-2 to Figure 4-5, the fault rupture planes have lengths of 1.4 km dipping 65°, with 1 km widths along dip and top of the fault at 3.75 km (Figure 4-2) and 3.45 km (Figure 4-3); and widths of 750 m with top of the fault at 3.75 km (Figure 4-4) and 3.45 km (Figure 4-5). The 65° dip is consistent with our focal mechanism and aftershock analyses (section 2.3 and section 3.1). On these results, it is noted that despite the variation in fault plane character with 1.4 km length, the resulting models indicate that most parts

of the fault and immediate areas south southwest and north northeast of the fault plane have negative ΔCS (plots d-i on Figure 4-2 to Figure 4-5). Most of the aftershocks along the fault plane are located on negative ΔCS regions. On the other hand, at both the northeast and southwest fault terminations, as well as the upper edges of the fault planes, positive ΔCS are noted where aftershocks are observed. At the fault terminations, the negative and positive ΔCS plotting side by side along the fault has dip that correlates with the aftershocks (plots b and c on Figure 4-2 to Figure 4-5). At the lower edges, however, there are no aftershocks observed or located on those regions despite the positive ΔCS (lower portion of plots b, c, f - i on Figure 4-2 to Figure 4-5). On the models with shallower fault planes (top of fault at 3.45 km), most of the aftershocks along the fault plane plot on negative ΔCS (Figure 4-3, Figure 4-5). Aside from the aftershock distribution along and adjacent to the fault plane, other sets of interesting aftershock distributions are the deep events in the northwest part of the study area, the shallow events southwest of the main shock, and a group of aftershocks immediately northwest of the southwest end of the fault, herein called clusters 1, 2, and 3, identified in dashed red ellipses on Figure 4-1. All clusters 1, 2, and 3 are generally located on areas with positive ΔCS, as can be seen on plots b, d, and i on Figure 4-2 to Figure 4-5, although cluster 3 plots on regions with negative ΔCS on the models with shallower fault planes on plots h and i on Figure 4-3, and Figure 4-5.

The third and fourth sets of models shown in Figure 4-6 to Figure 4-9 are results for fault planes with 600 m lengths, with dips of 65°. Fault planes with widths of 600 m, with the top of the fault at 3.75 km and 3.45 km, are shown in Figure 4-6 and Figure 4-7, respectively, while Figure 4-8 and Figure 4-9 show models with narrower widths along dip (400 m), with the top of the fault at 3.75 km and 3.45 km, respectively. Interestingly, for these sets of models where the fault planes are shorter in length and smaller in width, the aftershock distributions mostly plot on areas with positive ΔCS. On these model results, most parts of the fault, including immediate areas on both northeast and southwest fault terminations, both on the upper and lower edges of the fault planes, as well as along and perpendicular to the fault plane, correlate with positive ΔCS (Figure 4-6 to Figure 4-9). Most of the aftershocks are located on regions of positive ΔCS. The south-southwest and north-northeast regions have negative ΔCS (cross-sections on plots g and h on Figure 4-6 to Figure 4-9), similar to the previous models. In these third and fourth sets of models, furthermore, there are very few aftershocks that plot on areas with negative ΔCS. On the other hand, near the end of the fault termination, the negative and positive ΔCS plot side by side right along the fault plane, which correlate with the aftershocks (plots b, c and f on Figure 4-6 to Figure 4-9). On both the upper and lower edges of the fault plane, there are aftershocks on those regions where stress had increased (lower portion of plots b-i on Figure 4-6 to Figure 4-9). On these models with smaller fault planes, with either the deeper (3.75 km) or shallower (3.45 km) fault planes, most of the aftershocks are generally plotting on positive ΔCS. With regard to clusters 1, 2, and 3, all clusters of aftershocks are located on areas with positive ΔCS, as can be seen on plots b, d, f, g, and i on Figure 4-6 to Figure 4-9.

Models with lengths of 1 km and as short as 500 m with varying widths, dip angles, and value of friction coefficient were also processed to see if their ΔCS distribution would match the aftershock distribution better. Patterns and distribution of both positive and negative ΔCS are similar to the trends shown in Figure 4-2 to Figure 4-9, and changing the value of the friction coefficient has none to very little effect on the resulting ΔCS distribution.

Overall, the models with fault plane 1.4 km in length indicate that the fault rupture area of the March 4th, 2019 earthquake has undergone stress relaxation, or regions of shadow zones, with mean slip that ranges from 0.1 m to 0.2 m. Most of the aftershocks near the rupture plane are located on negative ΔCS regions or shadow zones on the first and second sets of models. The models with smaller fault planes of 600 m in length and mean slip that ranges from 0.55 m to 0.8 m, on the other hand, show stress increase along and at the terminations of the rupture area. Moreover, aftershock clusters 1 and 2, located northwest and southwest at different distances and depths relative to the main fault rupture, are located on places where ΔCS is positive on all models. Cluster 3 plots on either shadow zones or between positive and negative ΔCS on the models with longer fault lengths and plots on positive ΔCS on models with shorter fault lengths. The aftershocks near and along the southern fault rupture termination, however, plot on positive ΔCS on models with smaller fault planes. It is noted that on all models, the injection well is located on a shadow zone, as can be seen on plots a and g on Figure 4-2 to Figure 4-9.

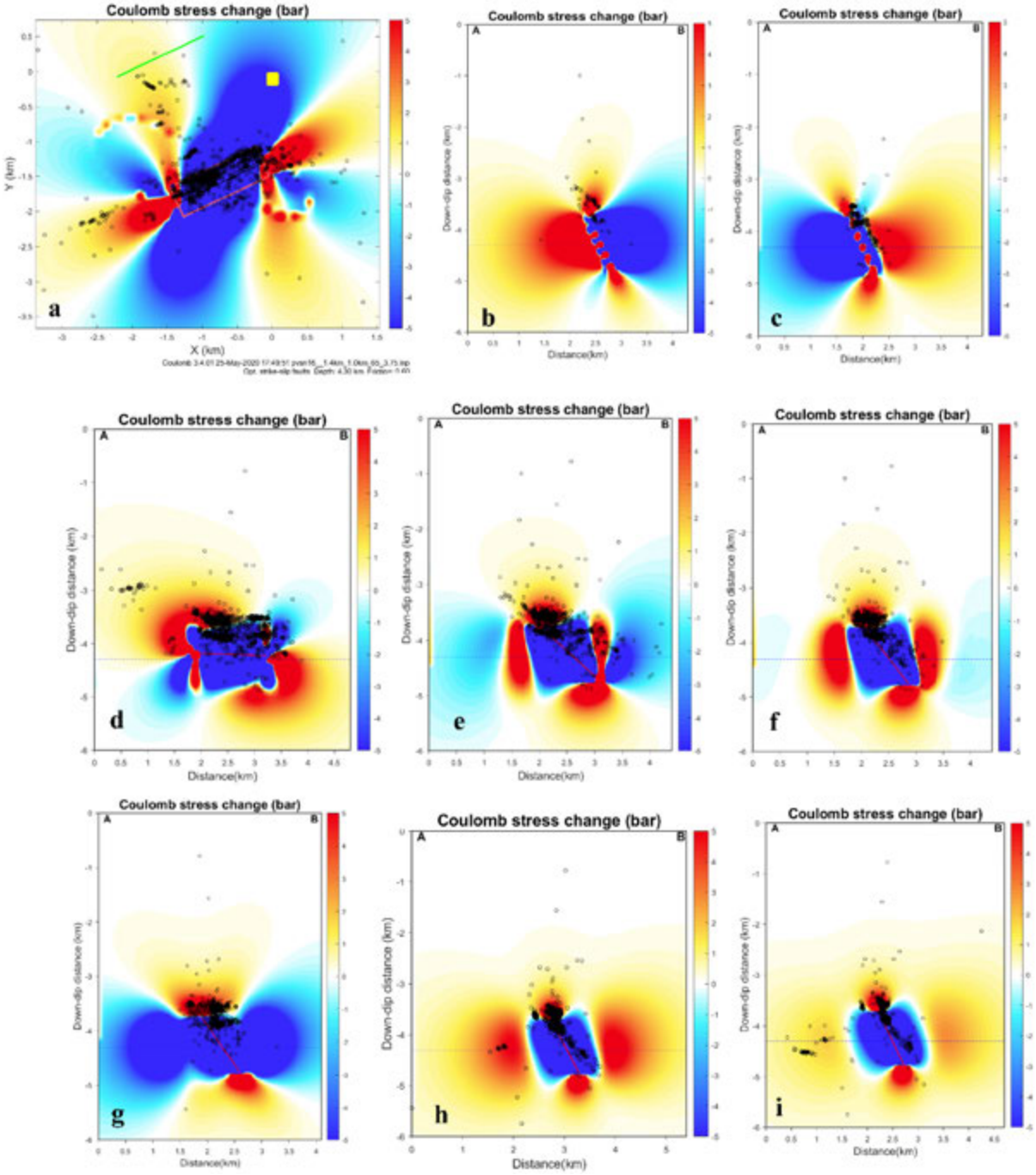

Figure 4-2: Sections through the Coulomb stress model for a 1.4 km x 1 km rupture plane, with the top of the rupture at 3.75 km, dipping 65° SE. Yellow and red colors indicate positive ΔCS while blue colors represent negative ΔCS. Aftershocks within 0.5 km of each section are shown (black circles). (a) Map showing the horizontal section at 4.3 km depth across the fault plane (red rectangle) with fault surface projection (green line), and location of injection well (yellow square). Vertical cross sections are as follows: (b) BB' and (c) CC' are perpendicular to the southern and northern end of the fault plane, respectively, (d) DD' is parallel to the fault plane and along positive ΔCS, (e) EE' is east-west line cutting through the fault plane, (f) FF' and (g) GG' are along the negative ΔCS distributions, (h) HH' is across the shallow aftershock cluster 3, and (i) II' is along positive ΔCS. Clusters 1 and 3 are shown on (i) II' and (h) HH', while cluster 2 is shown on (d) DD'.

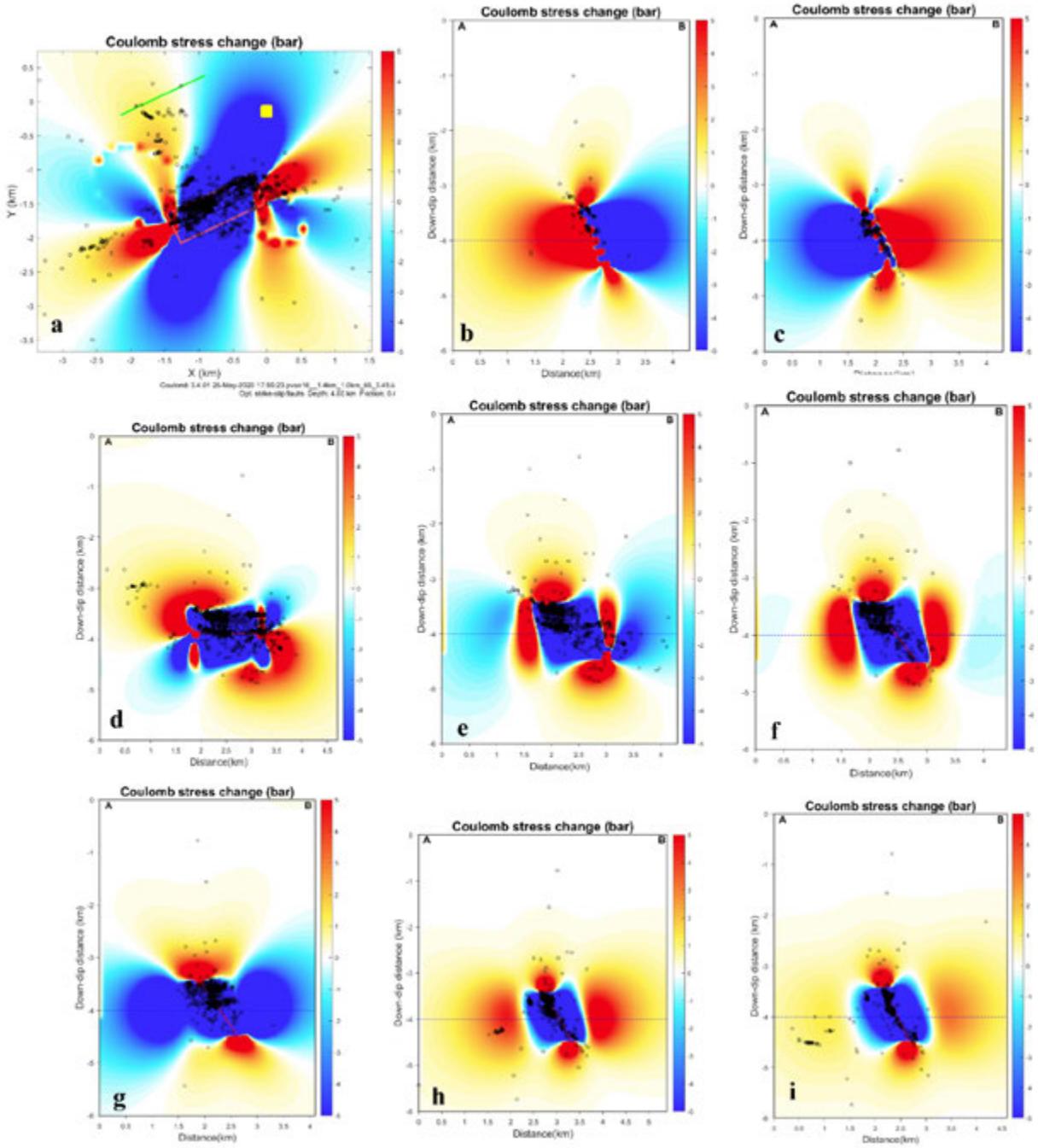

Figure 4-3: Sections through the Coulomb stress model for a 1.4 km x 1 km fault plane, with top of the fault rupture at 3.45 km, dipping 65º SE. Yellow and red colors indicate positive stress changes, while blue colors represent negative changes. Aftershocks within 0.5 km of each section are shown (black circles). (a) Horizontal section at 4.0 km depth as indicated by black line across the fault plane (red rectangle); fault surface projection (green line); and location of injection well (yellow square). Vertical cross sections are as in Figure 4-2. Black dashed line on all vertical sections is the location of horizontal section on (a).

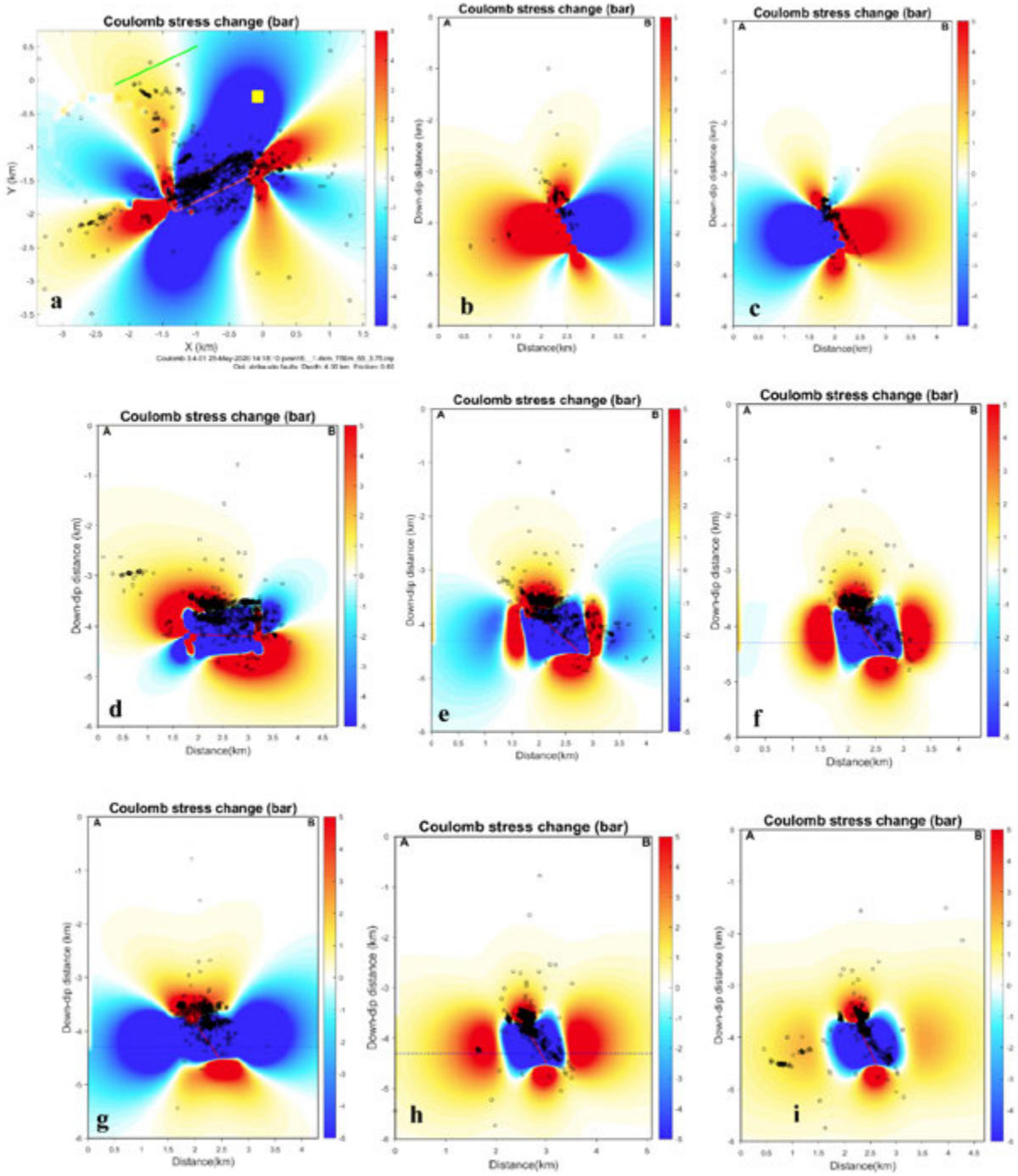

Figure 4-4: Sections through the Coulomb stress model for a 1.4 km x 750 m rupture plane, with the top of the rupture at 3.75 km, dipping 65° SE. Yellow and red colors indicate positive stress changes, while blue colors represent negative changes. Aftershocks within 0.5 km of each section are shown (black circles). (a) Horizontal section at 4.3 km depth as indicated by black line across the fault plane (red rectangle); fault surface projection (green line); and location of injection well (yellow square). Vertical cross sections are as in Figure 4-2. Black dashed line on all vertical sections is the location of horizontal section on (a).

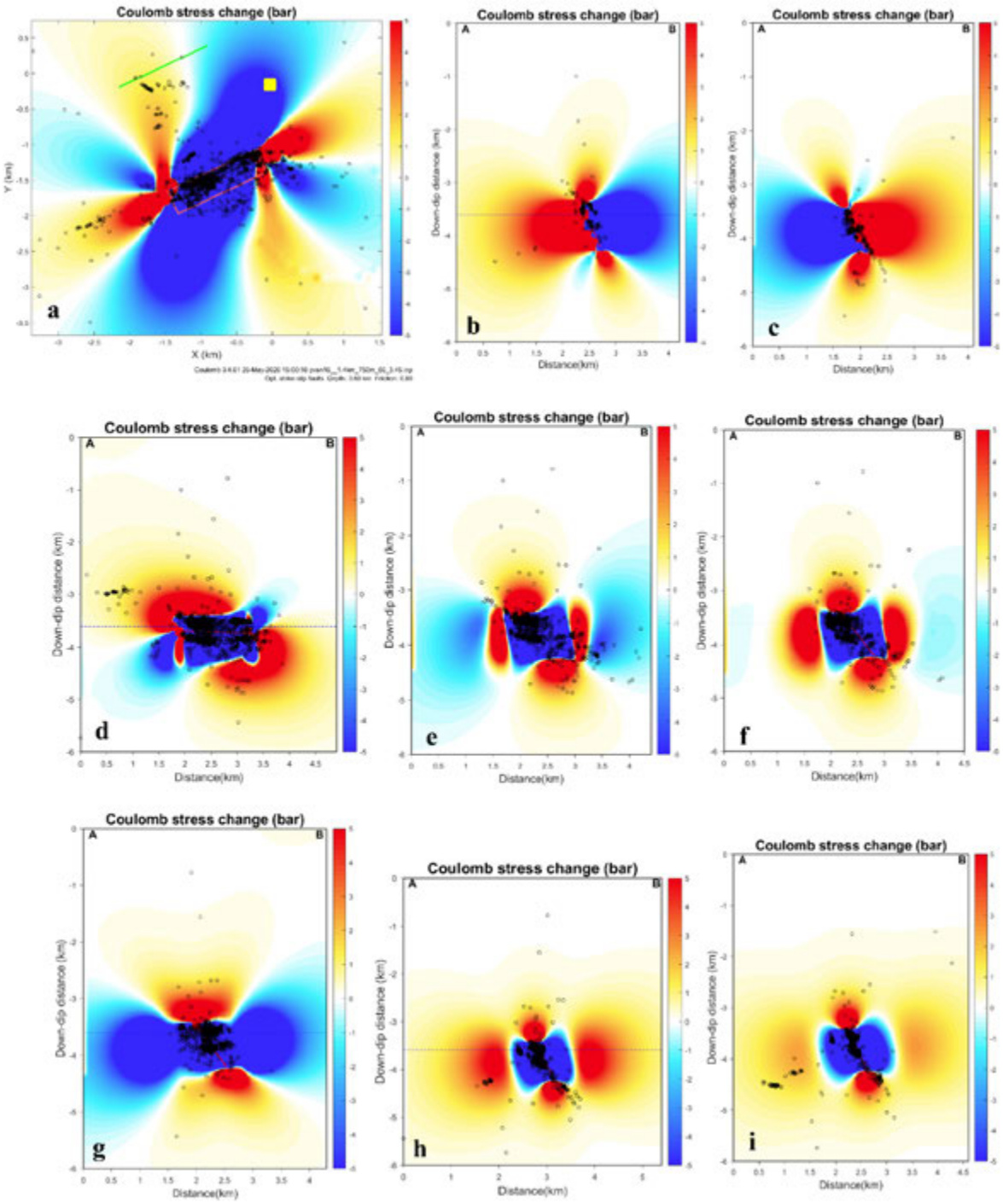

Figure 4-5: Sections through the Coulomb stress model for a 1.4 km x 750 m rupture plane, with the top of the rupture at 3.45 km, dipping 65° SE. Yellow and red colors indicate positive stress changes, while blue colors represent negative changes. Aftershocks within 0.5 km of each section are shown (black circles). (a) Horizontal section at 3.6 km depth as indicated by black line across the fault plane (red rectangle); fault surface projection (green line); and location of injection well (yellow square). Vertical cross sections are as in Figure 4-2. Black dashed line on all vertical sections is the location of horizontal section on (a).

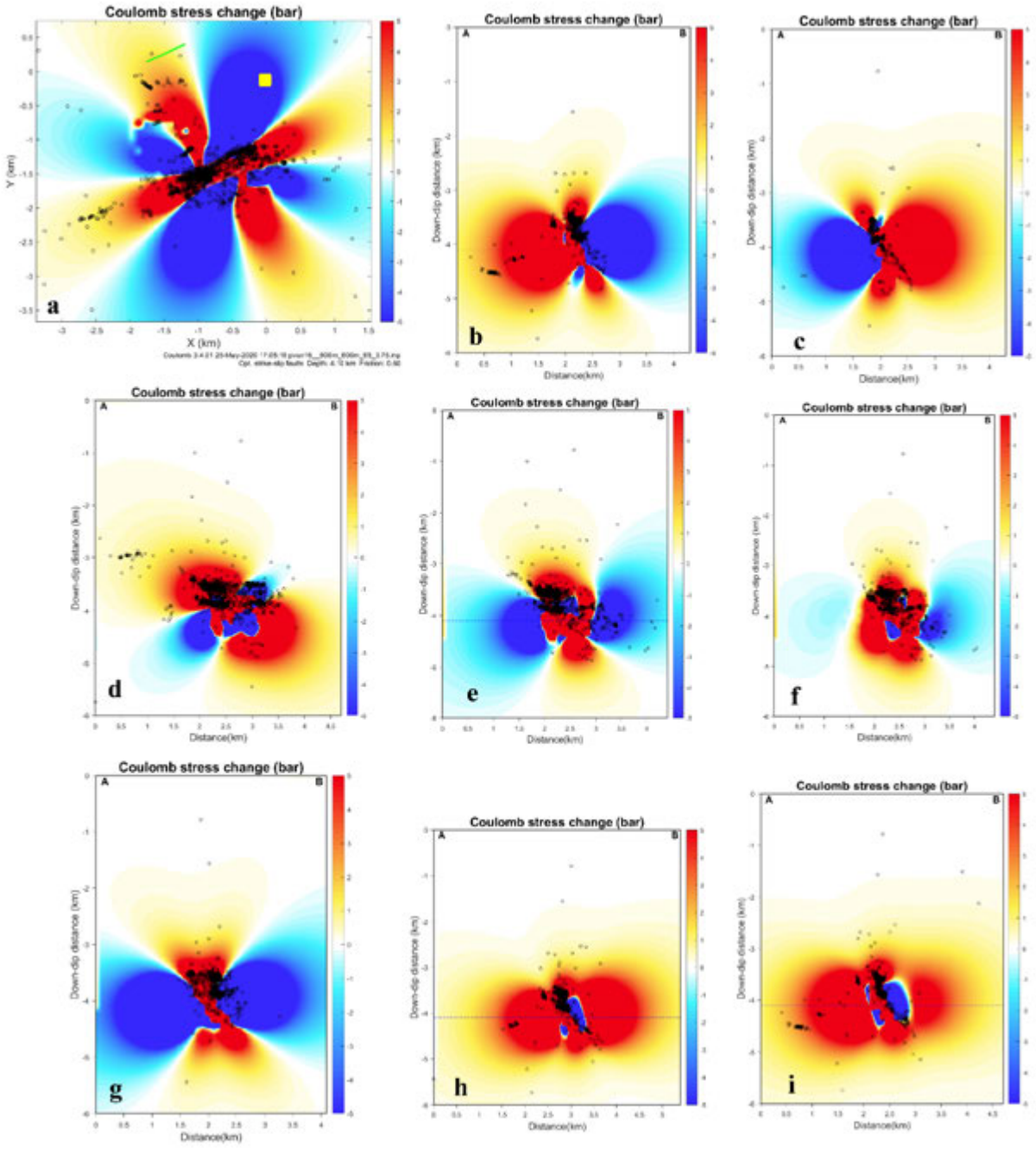

Figure 4-6: Sections through the Coulomb stress model for a 600 m x 600 m rupture plane, with the top of the rupture at 3.75 km, dipping 65° SE. Yellow and red colors indicate positive stress changes, while blue colors represent negative changes. Aftershocks within 0.5 km of each section are shown (black circles). (a) Horizontal section at 4.1 km depth as indicated by black line across the fault plane (red rectangle); fault surface projection (green line); and location of injection well (yellow square). Vertical cross sections are as in Figure 4-2. Black dashed line on all vertical sections is the location of horizontal section on (a).

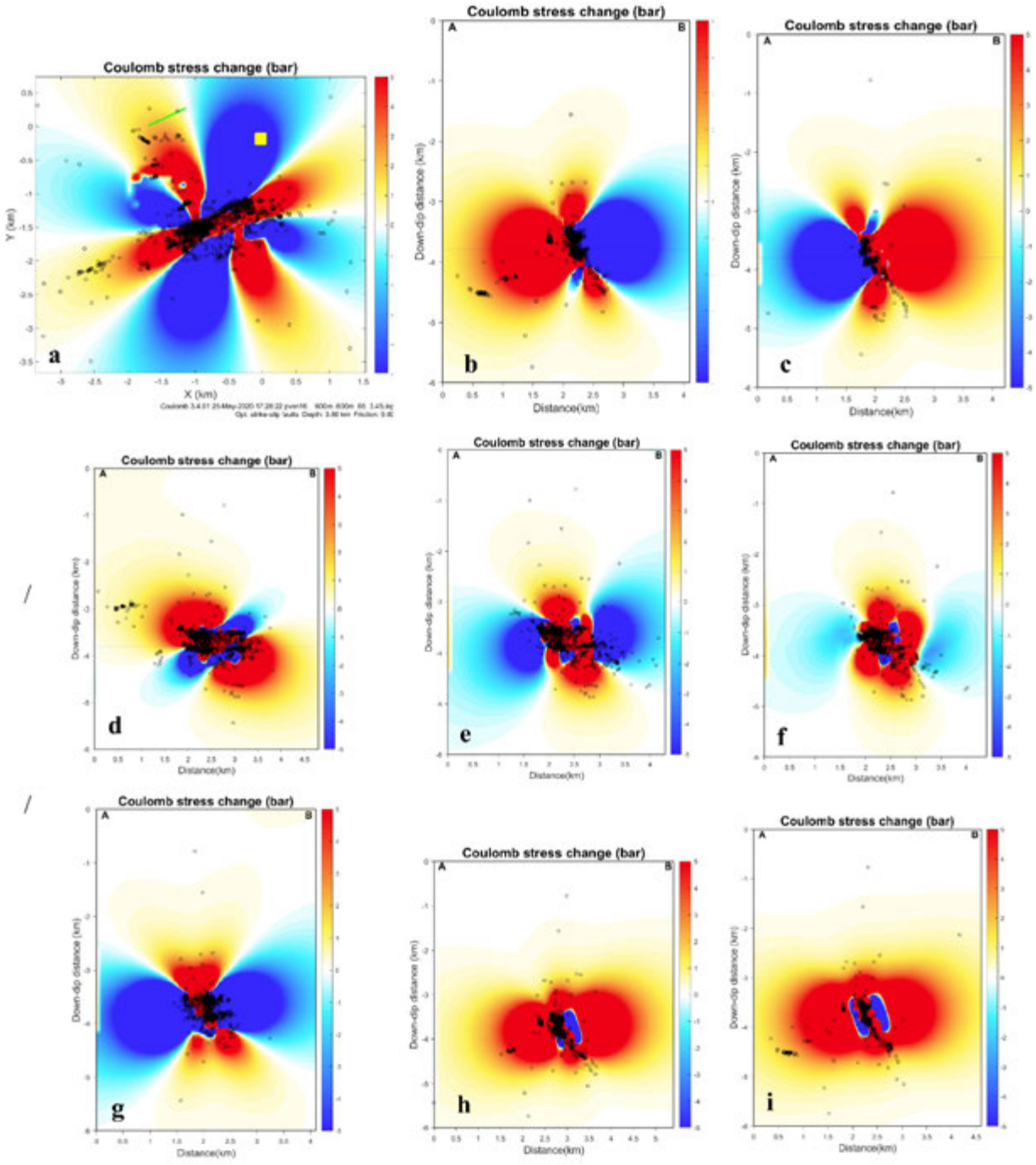

Figure 4-7: Sections through the Coulomb stress model for a 600 m x 600 m rupture plane, with the top of the rupture at 3.45 km, dipping 65° SE. Yellow and red colors indicate positive stress changes, while blue colors represent negative changes. Aftershocks within 0.5 km of each section are shown (black circles). (a) Horizontal section at 3.8 km depth as indicated by black line across the fault plane (red rectangle); fault surface projection (green line); and location of injection well (yellow square). Vertical cross sections are as in Figure 4-2. Black dashed line on all vertical sections is the location of horizontal section on (a).

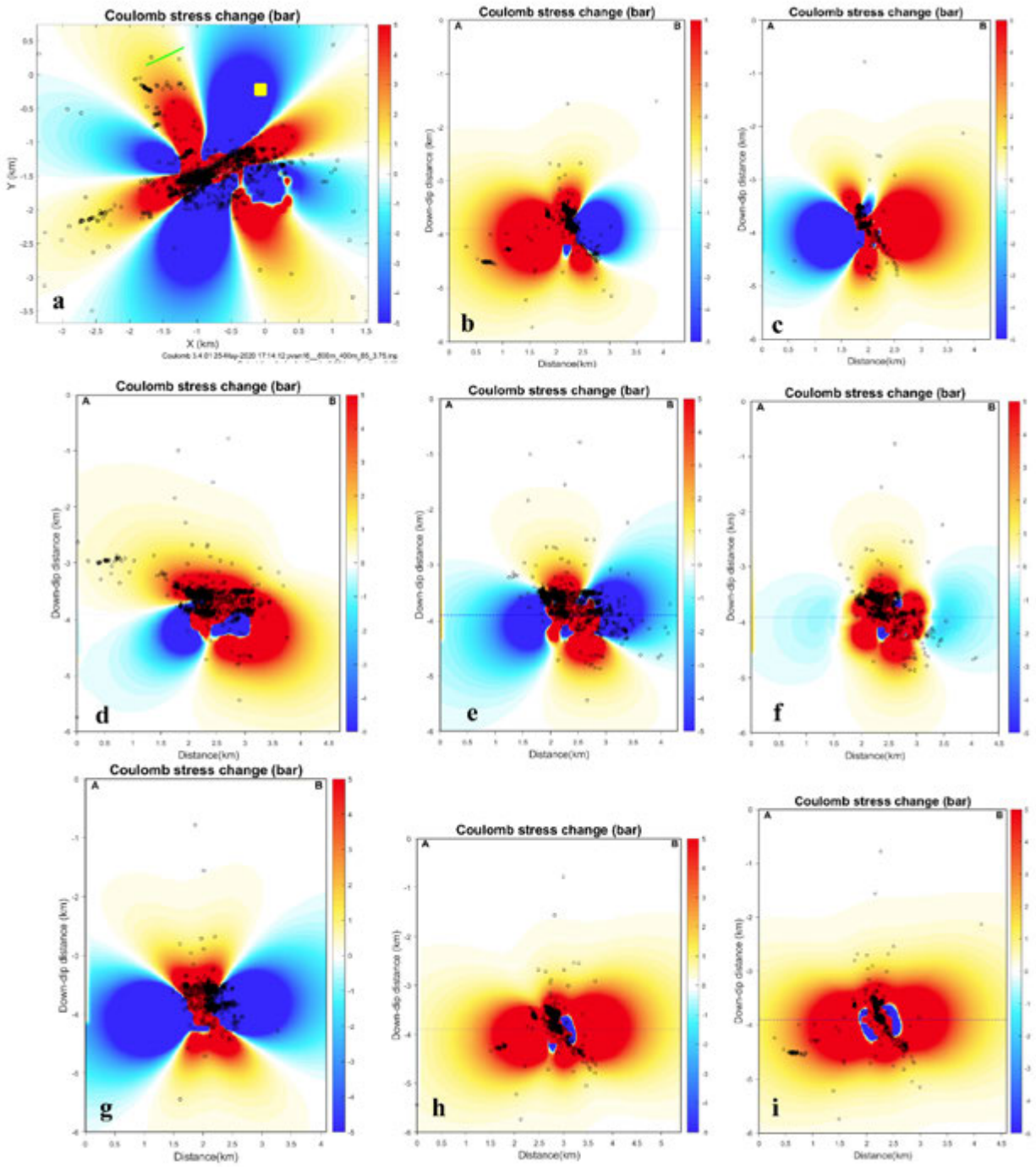

Figure 4-8: Sections through the Coulomb stress model for a 600 m x 400 m rupture plane, with the top of the rupture at 3.75 km, dipping 65° SE. Yellow and red colors indicate positive stress changes, while blue colors represent negative changes. Aftershocks within 0.5 km of each section are shown (black circles). (a) Horizontal section at 3.9 km depth as indicated by black line across the fault plane (red rectangle); fault surface projection (green line); and location of injection well (yellow square). Vertical cross sections are as in Figure 4-2. Black dashed line on all vertical sections is the location of horizontal section on (a).

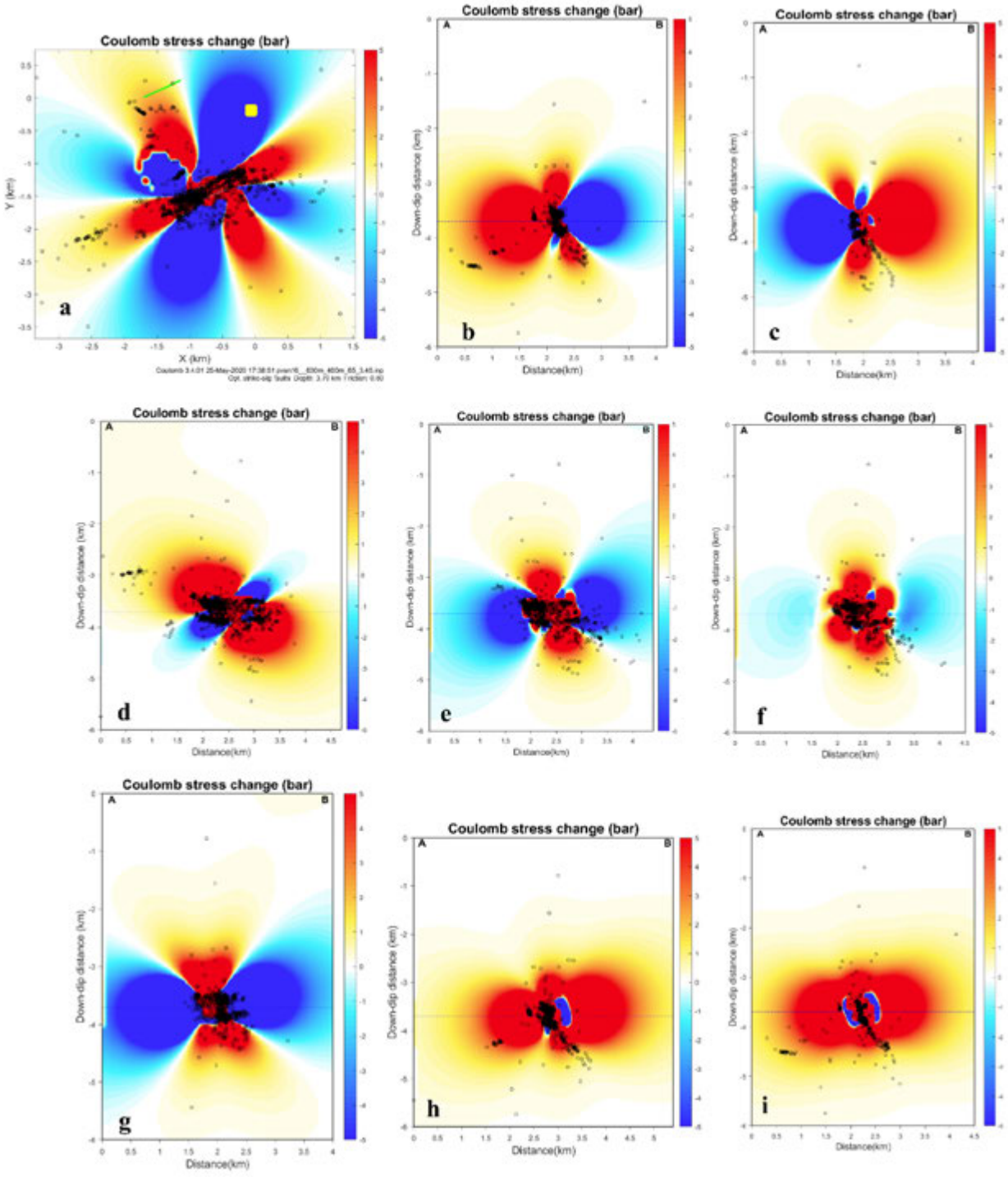

Figure 4-9: Sections through the Coulomb stress model for a 600 m x 400 m rupture plane, with the top of the rupture at 3.45 km, dipping 65° SE. Yellow and red colors indicate positive stress changes, while blue colors represent negative changes. Aftershocks within 0.5 km of each section are shown (black circles). (a) Horizontal section at 3.7 km depth as indicated by black line across the fault plane (red rectangle); fault surface projection (green line); and location of injection well (yellow square). Vertical cross sections are as in Figure 4-2. Black dashed line on all vertical sections is the location of horizontal section on (a).

4.4 Discussion

The concept that underlies the Coulomb model is that a mainshock rupture can produce significant changes in shear stress, and in normal effective stress; positive stress changes tend to favor the generation of future earthquakes, and negative stress (or shadow zones) tend to inhibit them (Harris, 1998). Toda et al. (2005) utilized the Coulomb model mainly to explain aftershock sequences after large or intermediate sized events and to show the generation process of fluid related phenomena such as magmatic dike progression and the accompanying earthquake swarm.

Modeling results for a 1 km or longer fault plane indicate that most of the area of the March 4th event and its main aftershock cloud plots within a zone that has decreased Coulomb stress. Therefore, most of the aftershocks are located within negative ΔCS regions or shadow zones. Assuming the fault rupture is defined by the aftershock distribution – and is truly more than 1 km in length, as shown in the previous section – then the aftershock events on the negative ΔCS regions, particularly along the fault rupture, could indicate other process(es) in those regions. The deep seismicity cluster 1 and shallow seismicity cluster 2 plot within regions with positive ΔCS while shallow cluster 3 plots within shadow zones. The aftershocks within the shadow zones may be due to heterogenous slip during the main earthquake rupture. It should be noted that the Coulomb stress change modeling does not take into account other important parameters that may be responsible for inducing stress changes, such as fluid flow (Cocco and Rice, 2002), viscoelastic relaxation (Freed and Lin, 2001), aseismic slip on the main shock fault plane, and delayed aftershock triggering (Dieterich, 1994). Aside from these unmodeled parameters, another potentially important factor not accounted for in the modeling is the complex geology of this area; complex geology may account for some aftershocks plotting within negative shadow zones.

The models with a smaller fault plane produced ΔCS distributions that mostly complement the aftershock distribution along and on the edges of the ruptures. If the March 4th event has a smaller fault rupture area, then the aftershock distribution plots mostly within regions with positive ΔCS. There are good correlations of these patterns particularly on NE and SW fault terminations, where the ΔCS region more or less dips along the fault dip direction. Along the fault rupture area, aftershocks plot within the positive ΔCS regions, while very few aftershocks plot within small shadow zones. The deep aftershock cluster 1 and shallow aftershock clusters 2 and 3 also plot within regions with increased or positive ΔCS.

Our models of the March 4th earthquake can be compared to Coulomb stress change studies undertaken for the Basel geothermal system by Catalli et al. (2013) and for the Oklahoma wastewater injection by Qin et al. (2018). At the Basel geothermal system, about 75% of induced earthquakes plotted consistently within regions of positive ΔCS. Catalli et al. (2013) also noted that the performance of the Coulomb model (i.e., its correlation with earthquake occurrence) increases with time and distance from injection compared to the role of pore pressure. In Woodward, Oklahoma, Qin et al. (2018) explored the role of Coulomb stress transfer from fault reactivation due to wastewater injection, where Coulomb stress transfer occurred along each fault segment. Fault reactivation appeared to initiate at fault bends, and was attributed to interevent stress interaction in regions where the amplitude of Coulomb stress transfer was at least comparable to pore pressure and poroelastic stress changes from fluid injection. If the

March 4th earthquake in Paradox resulted from rupture of a shorter fault, it is notable that the shallower aftershocks with steeper dipping focal planes, particularly those aftershocks southwest of the fault termination, plot on regions of positive ΔCS. These shallower aftershocks to the southwest, as well as the deeper aftershocks in the Precambrian layer, might be an interesting case of events triggered by positive ΔCS or Coulomb stress transfer on fault bends both along strike and at depth. This is an interesting hypothesis considering what was observed in Oklahoma.

Our model of the ΔCS distribution for the M_w 4.5 induced earthquake is relatively simple, consisting of simple rectangular fault planes oriented and dipping based on focal mechanism solutions in this study. Sensitivity tests were done to account for variations in fault location, as well as variations in fault length, dip and width. Steacy et al. (2005) showed the importance of using well-constrained fault geometries, independently of the details of slip on the rupture plane, in order to estimate mainshock-aftershock stress triggering. Thus, although smaller fault planes generally correlate well with the aftershock distribution, other models cannot be discounted completely. The stress change distribution may not be fully captured because parameters like slip distribution, slip heterogeneities, and heterogeneity of the rock precondition, which can significantly influence stress calculations (Hainzl and Marsan, 2008; Marsan, 2006), were not considered in our models.

In this work, Coulomb stress change modeling for the M_W 4.5 earthquake in Paradox Valley was undertaken to gain more understanding about the main shock rupture plane characteristics and aftershock pattern. We used the Coulomb 3.4 software by Toda et al. (2005), and input parameters based on data from this report and other applicable studies. We considered a range of dip angles (60°, 64°, 75°, and 80°), as well as different values of friction coefficient μ (0.2, 0.4 and 0.8), to examine the sensitivity of our results to these parameters. Results indicate that the fault planes with shallower dip angle fit the aftershock distribution better, while the change in friction coefficient value has very little effect on the ΔCS distribution. Models with a smaller fault plane produce ΔCS distributions that mostly complement the aftershock distribution.

5 Seismicity Rates

5.1 Trends

No increase in the rates or maximum magnitudes of earthquakes in the vicinity of the M_W 4.5 earthquake, or anywhere within 10 km of the injection well, was observed in the year preceding the main shock. Rather, seismicity rates had decreased in 2018 compared to 2017 and remained low during the first two months of 2019, until the time of the M_W 4.5 earthquake on March 4th. Seismicity rates decreased 69% within 5 km of the injection well, and 32% at distances of 5-10 from the well, from 2017 to 2018 (Figure 5-1; Table 5-1). These decreases in rates of induced earthquakes within 10 km of the injection well followed a nearly one-month shut-down of the injection well and subsequent ~5% decrease in flow rate implemented in March 2017. These operational changes were made in response to increasing rates of earthquakes within 10 km of the well observed in 2016 and early 2017 (Figure 5-1 a and b). Rates remained relatively high through 2017 and subsequently fell in early 2018. Rates of induced earthquakes occurring more than 10 km from the well have increased steadily since 2013 and are relatively insensitive to operational changes (Figure 5-1c).

Table 5-1: Annual rates of earthquakes ≤ 10 km deep (relative to the ground surface at the injection well) and having duration magnitude $M_D \geq 0.5$, the approximate historical PVSN magnitude completeness threshold.

Year	Within 5 km of the Well		5 to 10 km from the Well		More than 10 km from the Well	
	Number of Earthquakes with $M_D \geq 0.5$	Percent Change from Previous Year	Number of Earthquakes with $M_D \geq 0.5$	Percent Change from Previous Year	Number of Earthquakes with $M_D \geq 0.5$	Percent Change from Previous Year
2012	26		20		11	
2013	13	-50%	17	-15%	4	-64%
2014	7	-46%	3	-82%	7	75%
2015	10	43%	3	0%	10	43%
2016	26	160%	14	367%	14	40%
2017	45	73%	19	36%	18	29%
2018	14	-69%	13	-32%	29	61%

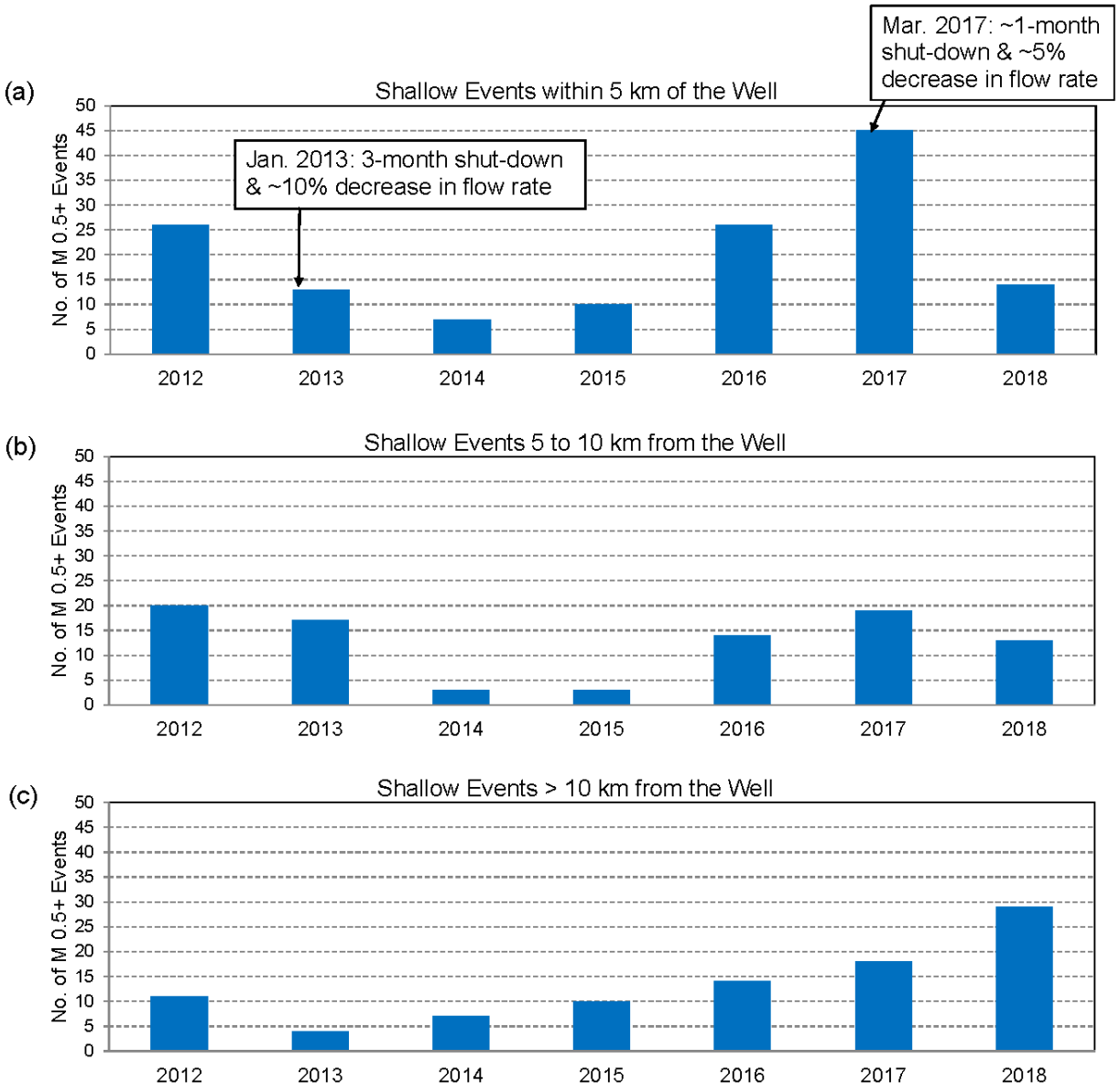

Figure 5-1: Annual seismicity rates from 2012 to 2018: (a) within 5 km of the injection well, (b) at distances between 5 and 10 km from the well, and (c) greater than 10 km from the well. During this time period, two changes in injection operations were implemented in response to induced seismicity trends: a ~three-month shut-down starting in January 2013, followed by injection at a 10% reduced flow rate; and a ~one-month shut-down starting in March 2017, followed by injection at a 5% reduced flow rate. These changes are indicated in the top plot.

The long-term trend of induced seismicity in the vicinity of the March 2019 M_W 4.5 earthquake shows sporadic behavior (Figure 5-2). Induced seismicity was first recorded near the fault plane of the M_W 4.5 earthquake in 1995, and the seismicity recorded since then is characterized by periods of increased rates and maximum magnitudes separated by periods with relatively low seismicity rates and magnitudes. In general, the seismicity rate in this area has been a little more consistent since 2009 than in earlier years. The last period of increased seismicity rate occurred in August-September 2017, when several events with magnitudes between M_D 2.0 and M_D 2.5 were recorded.

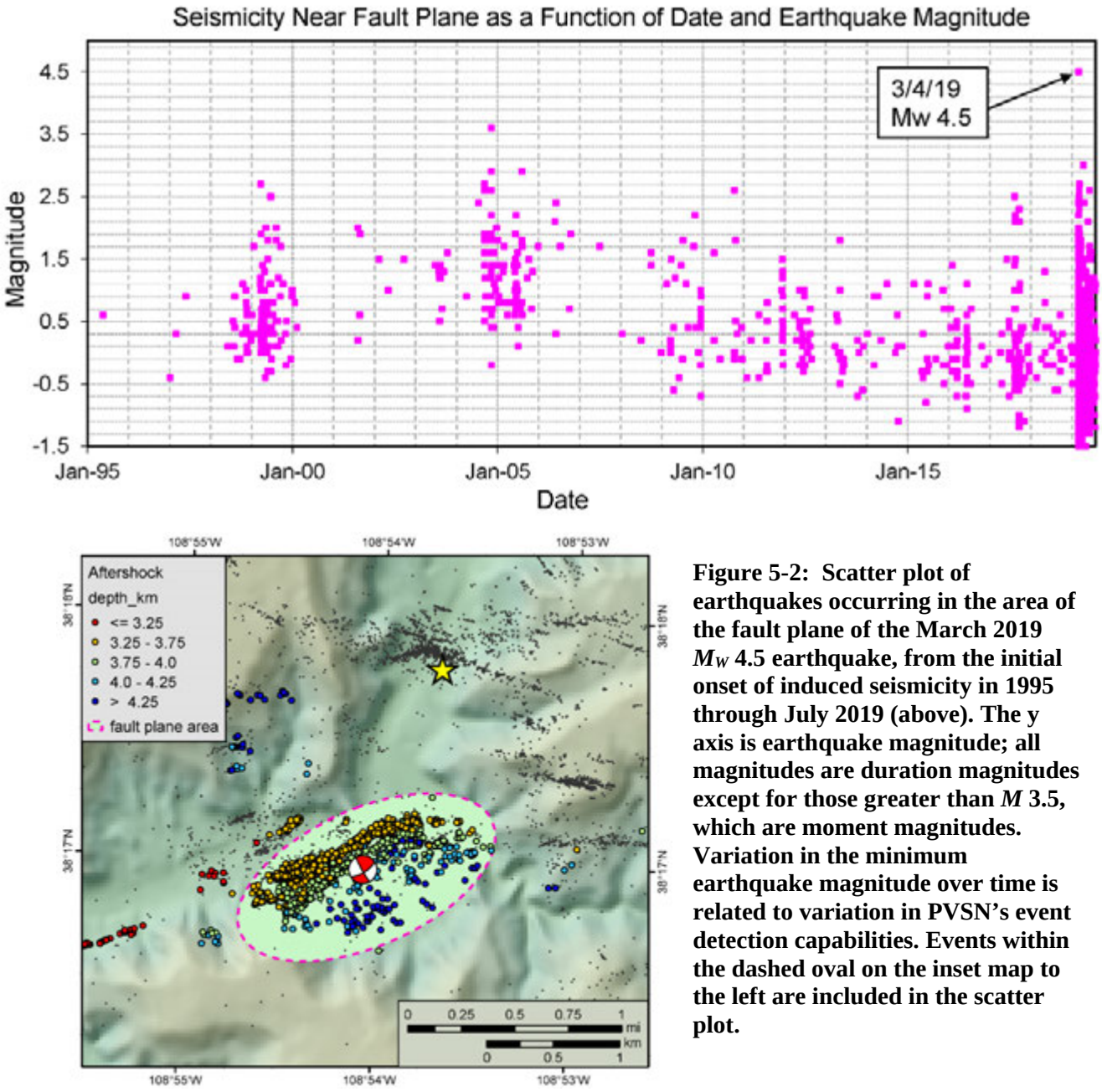

Figure 5-2: Scatter plot of earthquakes occurring in the area of the fault plane of the March 2019 M_W 4.5 earthquake, from the initial onset of induced seismicity in 1995 through July 2019 (above). The y axis is earthquake magnitude; all magnitudes are duration magnitudes except for those greater than *M* 3.5, which are moment magnitudes. Variation in the minimum earthquake magnitude over time is related to variation in PVSN's event detection capabilities. Events within the dashed oval on the inset map to the left are included in the scatter plot.

Although no foreshocks of the *MW* 4.5 earthquake were observed, numerous aftershocks have been recorded. Rates of earthquakes occurring within 5 km of the well increased abruptly following the *MW* 4.5 earthquake. Because of the proximity of these earthquakes to the main shock (Figure 2-3) and the abrupt increase in the seismicity rate starting at the time of that event (Figure 5-3), we interpret these earthquakes as aftershocks triggered by the redistribution of stress associated with the fault plane rupture that occurred during the *MW* 4.5 earthquake. Mathematical analysis of the temporal variation of the rate of these events, presented in section 5.2 below, provides additional confirmation that these earthquakes are aftershocks triggered by stress redistribution and therefore do not indicate any other change in reservoir conditions, such as a breach of the confining layer or an impermeable fault boundary. Aftershocks have occurred up to 1.7 km from the fault plane of the *MW* 4.5 earthquake, indicating that stress conditions have changed over a wide area.

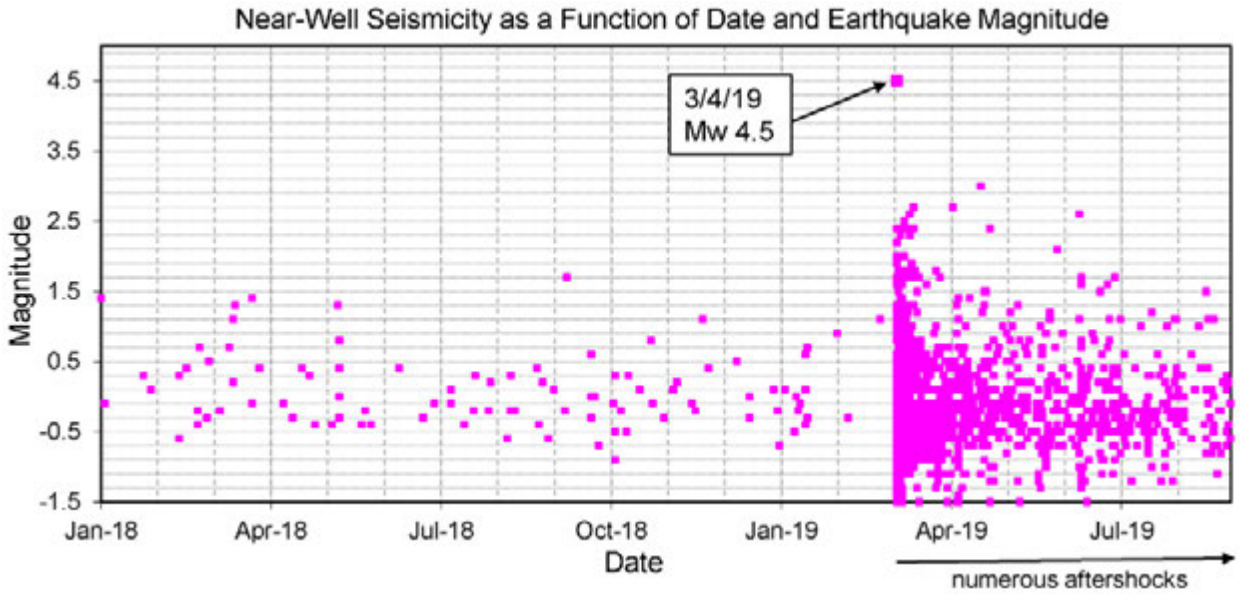

Figure 5-3: Scatter plot of earthquakes occurring within 5 km of the injection well from January 2018 through August 2019. The y axis is earthquake magnitude; all magnitudes are duration magnitudes except for that of the main shock on March 4th 2019, which is moment magnitude.

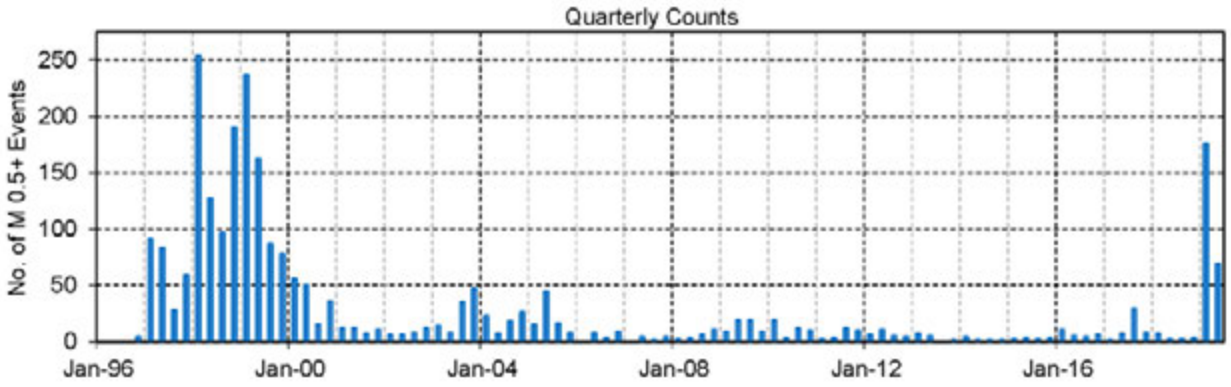

Figure 5-4: Quarterly rates of earthquakes (with $M_D \geq 0.5$) within 5 km of the injection well from 1996 through June 2019.

Between the time of the March 4th 2019 main shock and the end of August 2019, 2053 aftershocks were recorded. To put this number into perspective, it far exceeds the total number of earthquakes that occurred within the entire Paradox Valley area during the preceding eight years combined (2011-2018), which was 1550. The large number of aftershocks increased the rate of induced earthquakes in the near-well region to the highest rate in 20 years (Figure 5-4). Six of the aftershocks recorded through the end of August 2019 have magnitude ≥ M_D 2.5, large enough to be potentially felt within Paradox Valley. The largest aftershock through August 2019 was an M_D 3.0 (M_W 2.5) earthquake that occurred on April 18th. It was the second largest induced earthquake to occur within 5 km of the injection well in the last 15 years, second only to the March 2019 M_W 4.5 earthquake.

5.2 Aftershock Rates

In this section, we present a mathematical analysis of the aftershock rate from the March 2019 M_W 4.5 earthquake. This analysis has several benefits. First, it helps us evaluate whether the high seismicity rate observed in the near-well area can be attributed solely to stress redistribution from the fault plane rupture associated with the M_W 4.5 earthquake or whether it suggests that other reservoir changes may have occurred. Secondly, we can compare the aftershock decay rate from the March 2019 earthquake to that from the second largest PVU-induced earthquake to look for any anomalous behavior. Finally, we can use the mathematical model developed during this analysis to predict the expected rate of aftershocks for the next several years.

5.2.1 Modified Omori Aftershock Relation

We examined the activity rate of the aftershocks from the M_W 4.5 earthquake over time using the modified Omori rate law:

$$n(t) = K\,(t + c)^{-p},$$

where $n(t)$ is the rate of aftershocks at time t, and K, c, and p are constants. The original Omori law (in which a constant value of 1 was used in place of the exponent p) was developed in the 1890s, and the current modified form has been in use since the 1920s (Utsu et al., 1995). This empirical relation is widely used to model the aftershock sequences of earthquakes and has been successfully applied to earthquakes worldwide.

We fit the modified Omori relation to the aftershocks of the March 2019 M_W 4.5 earthquake recorded from the time of the main event to the end of July 2019. We then used the parameters determined from this fit to estimate the occurrence rate of future aftershocks for the next several years. In addition, we applied the same analysis to the aftershock data from the January 24th, 2013 M_W 4.0 induced earthquake, in order to compare the activity and decay rates of aftershocks from the two largest PVU-induced earthquakes.

5.2.2 Aftershocks of the March 4th, 2019 M_W 4.5 Earthquake

Events in the vicinity of the March 2019 M_W 4.5 earthquake were selected for inclusion in the aftershock analysis based on the following geographic bounds: latitude 38.257° to 38.317° and longitude -108.95° to -108.85°. Events that occurred between the time of the main shock on March 4th and the end of July 2019 were included. The map in Figure 5-5 shows the distribution of the 1,999 earthquakes that occurred within the defined region during this time period.

The magnitudes of the selected events range from M_D -2.0 to M_D 3.0. In order to fit the Omori aftershock relation to these data, a threshold magnitude must be specified. Only events with magnitude at or above the threshold magnitude are included in the analysis. This threshold magnitude should be equal to the magnitude completeness threshold, or greater, to prevent events in a magnitude range that is not completely represented by the data from biasing the results. To test the robustness of the fit of the Omori aftershock relation to the aftershocks of the M_W 4.5 earthquake, we independently performed the fit using five magnitude thresholds: M_D -0.5, M_D 0.0, M_D 0.5, M_D 1.0, and M_D 2.0. Preliminary maximum likelihood estimates of the three Omori constants (K, c, and p) were determined using a program that minimizes the negative log-likelihood function by the Davidson-Fletcher-Powell algorithm (Ogata, 1983, 2006). Final values were computed using a dense grid search around the initial estimates. The final values minimize the sum of the absolute differences between the observed and computed cumulative number of aftershocks (at the times of all observed aftershocks).

The Omori parameters computed for each of the five magnitude thresholds are listed in Table 5-2, and the observed and computed cumulative number of aftershocks for each of the five models are presented in Figure 5-6. These results demonstrate that the rate of aftershock decay with time is consistent with the Omori aftershock relation. Reasonable fits to the observed data are obtained for all values of threshold magnitude used. As expected, the Omori K value decreases with increasing threshold magnitude, since earthquake distributions contain fewer larger-magnitude events than smaller-magnitude events. The Omori c parameter, which can be used to account for a delay in seismic monitoring after the occurrence of the main shock, is very small for these models because seismic monitoring was already in place at the time of the M_W 4.5 earthquake. The estimates of the Omori p parameter, which represents the rate at which

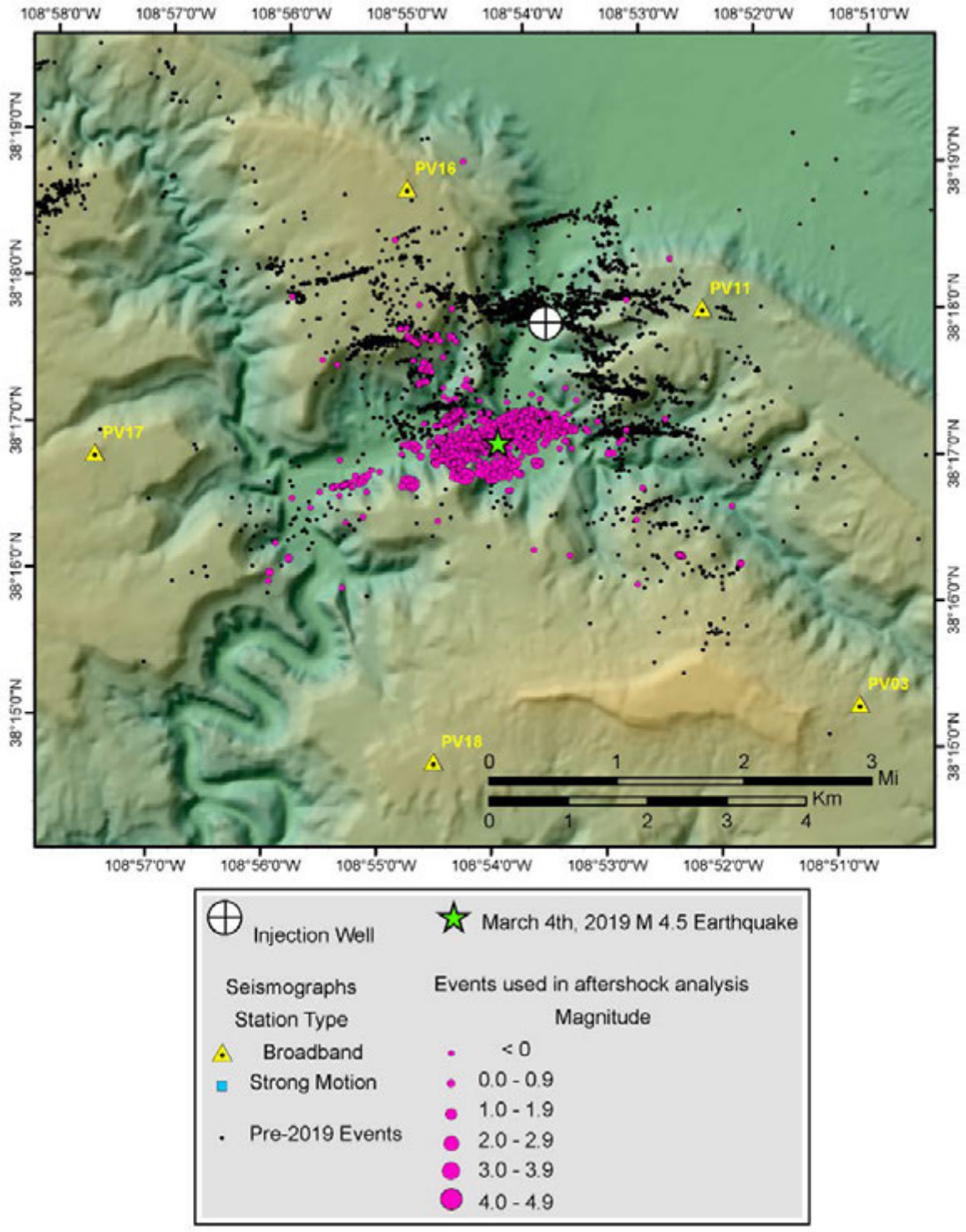

Figure 5-5: Map showing the locations of events selected for aftershock analysis of the March 4th, 2019 M_W 4.5 earthquake. The selected 1,999 events occurred between the time of the main shock and the end of July 2019.

Table 5-2: Omori parameters computed from the aftershock data of the March 4th, 2019 M_W 4.5 earthquake, for five magnitude thresholds. Aftershocks recorded between the time of the main shock and the end of July 2019 were included in the analyses.

Threshold Magnitude (M_D)	Number of Aftershocks Included	K	c	p
-0.5	1416	133.500	0.034	0.831
0.0	641	68.295	0.066	0.869
0.5	247	28.660	0.094	0.895
1.0	111	12.595	0.055	0.919
2.0	20	1.990	0.002	0.864

aftershock occurrence decreases, are similar for the five models. The computed p values range from 0.83 to 0.92, with a mean value of 0.88 and median value of 0.87. These values are near the low end of the expected range (p generally ranges from ~0.6 to ~2.5; Utsu et al. (1995)), which indicates that the occurrence of aftershocks from the March 2019 earthquake is decaying relatively slowly.

The observed and computed daily rates of aftershocks ≥ the threshold magnitude are presented in Figure 5-7. The actual aftershock rates have considerable variability, with few aftershocks occurring on some days and many aftershocks occurring on other days. In contrast, the Omori aftershock decay relations indicate a gradual reduction in the aftershock rate. Hence, these models represent the change in the average aftershock rate over time.

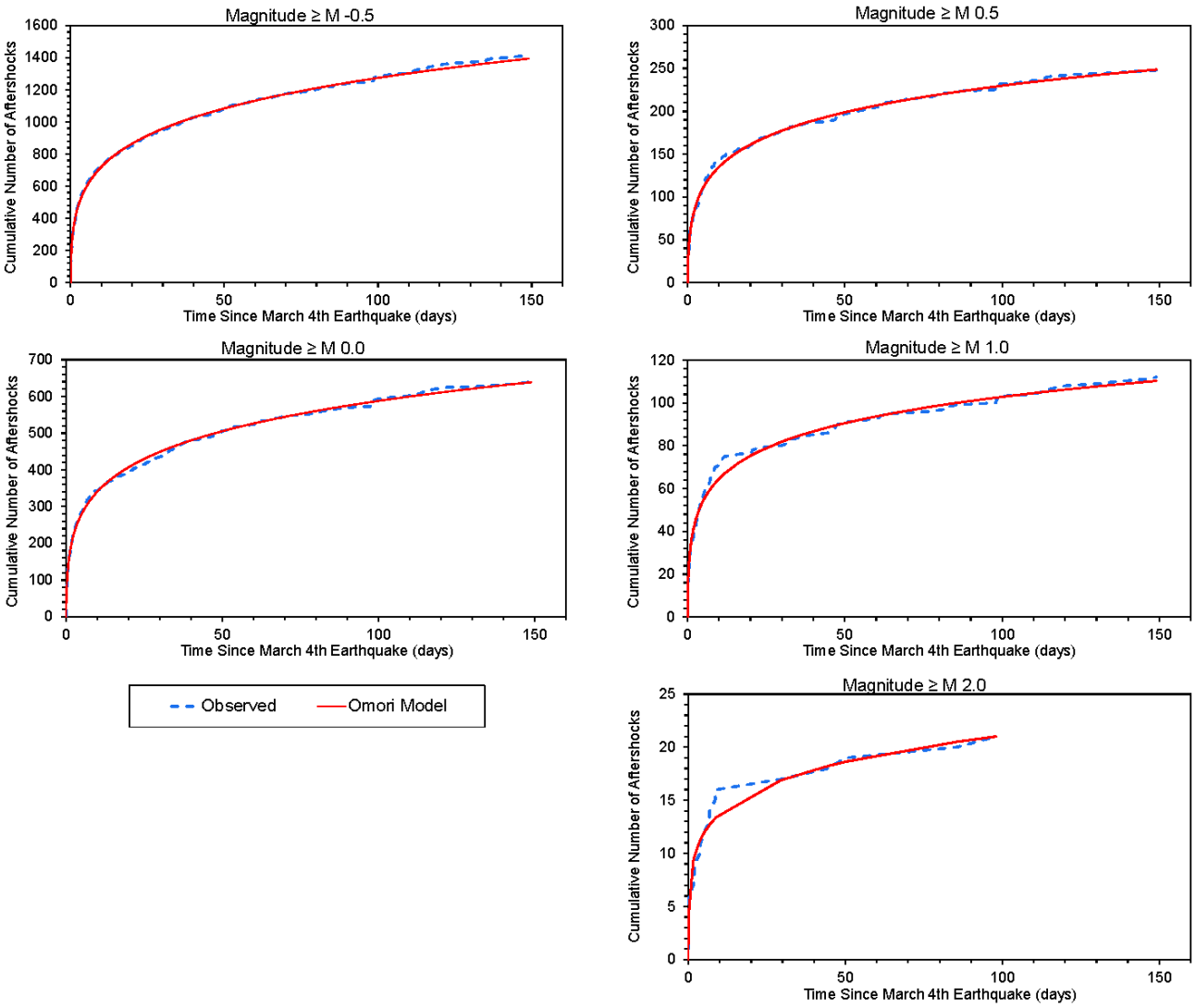

Figure 5-6: Fit of the Omori model to the cumulative number of aftershocks from the March 4th, 2019 M_W 4.5 earthquake. Results are shown for five magnitude thresholds; all magnitudes are duration magnitudes (M_D). Data recorded through the end of July 2019 (149 days after the main shock) were included in the modeling. The fit for aftershocks with magnitudes ≥ M_D 2.0 only extends to 98 days after the main shock because no aftershocks with $M_D \geq 2.0$ were recorded between mid-June and the end of July.

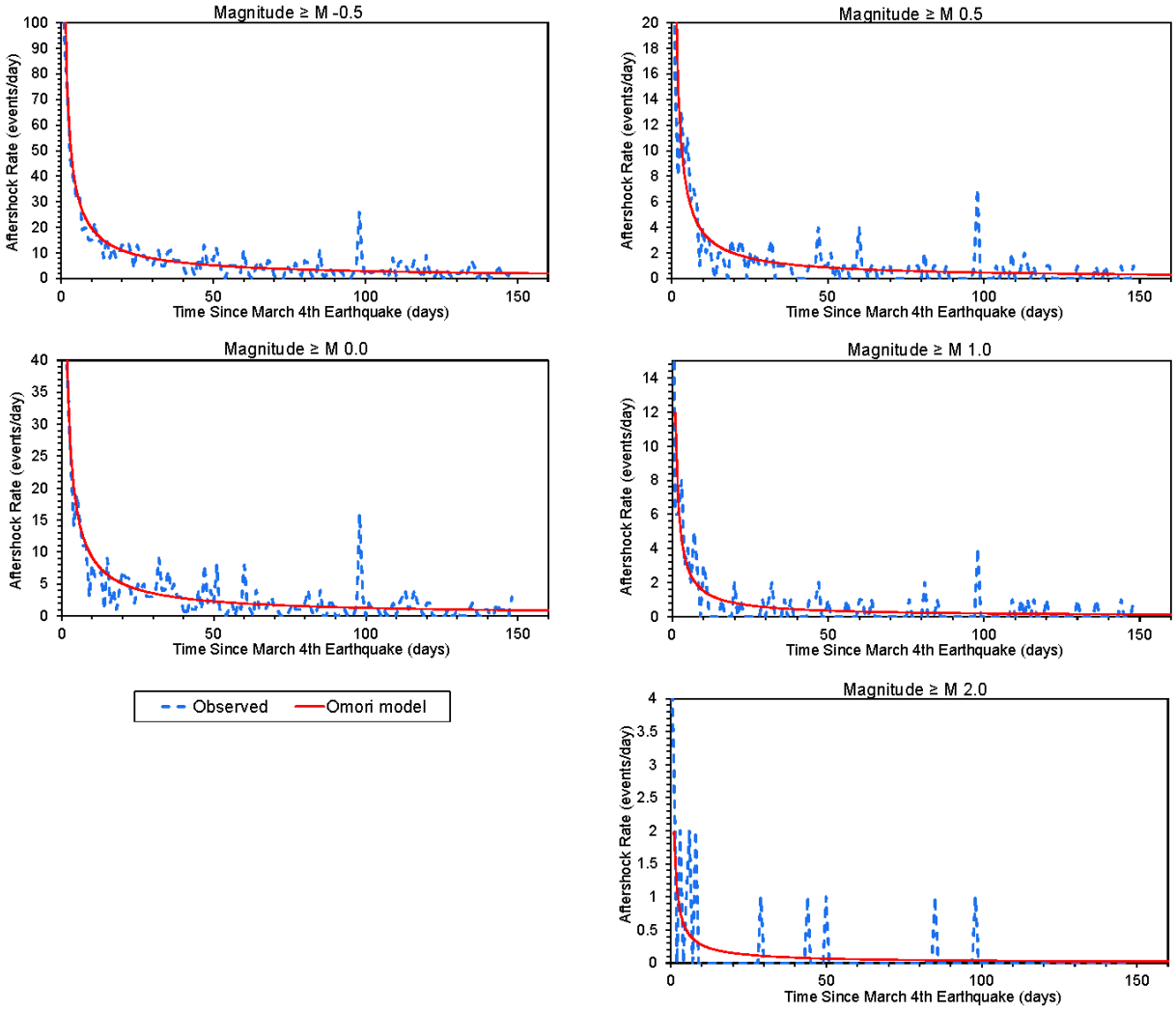

Figure 5-7: Fit of the Omori model to the daily rates of aftershocks from the March 4th, 2019 M_W 4.5 earthquake. Results are shown for five magnitude thresholds; all magnitudes are duration magnitudes (M_D). Data recorded through the end of July 2019 (149 days after the main shock) were included in the modeling.

We used these Omori aftershock relations to predict future rates of aftershocks related to the March 2019 M_W 4.5 earthquake. Using the Omori parameters derived for each of the five magnitude thresholds, we computed monthly (30-day) aftershock rates for up to five years following the main shock (Figure 5-8; Table 5-3). The results indicate that the average rates of aftershocks will decline very slowly over the next several years. For example, one year after the main shock (March 2020), a rate of ~31 aftershocks with $M_D \geq$ -0.5 per month is predicted, which decreases to ~17 aftershocks/month at two years, ~12 aftershocks/month at three years, ~10 aftershocks/month at four years, and ~8 aftershocks/month at five years (March 2024). The rates for larger-magnitude events are lower, with an average rate of 1.7 aftershocks with $M_D \geq$ 1.0 per month expected at one year (March 2020), declining to an average rate of 0.4 aftershocks/month (or ~5 aftershocks/year) at five years.

The rate of aftershocks is expected to remain higher than the background seismicity rate (i.e., the rate of events in the same area that are not aftershocks of the M_W 4.5 earthquake) for about two to four years. This is illustrated in Figure 5-9, which compares the monthly rate of aftershocks predicted from the Omori aftershock relation for a magnitude threshold of M_D 0.5 to estimates of the near-well background seismicity rate. Three estimates of the near-well background seismicity rate were determined from the numbers of induced earthquakes with $M_D \geq 0.5$ within 5 km of the injection well recorded during periods of one year, five years, and ten years prior to the March 2019 M_W 4.5 earthquake. We computed these background seismicity rates using data from three different time periods because the rate varies over time, and it is not possible to predict how the background seismicity rate will vary over the next several years. (No de-clustering of the earthquake catalog was performed prior to computing these background seismicity rates.) The predicted rate of aftershocks with $M_D \geq 0.5$ (solid red line in Figure 5-9) remains above these historical background seismicity levels for two to four years, before declining below them.

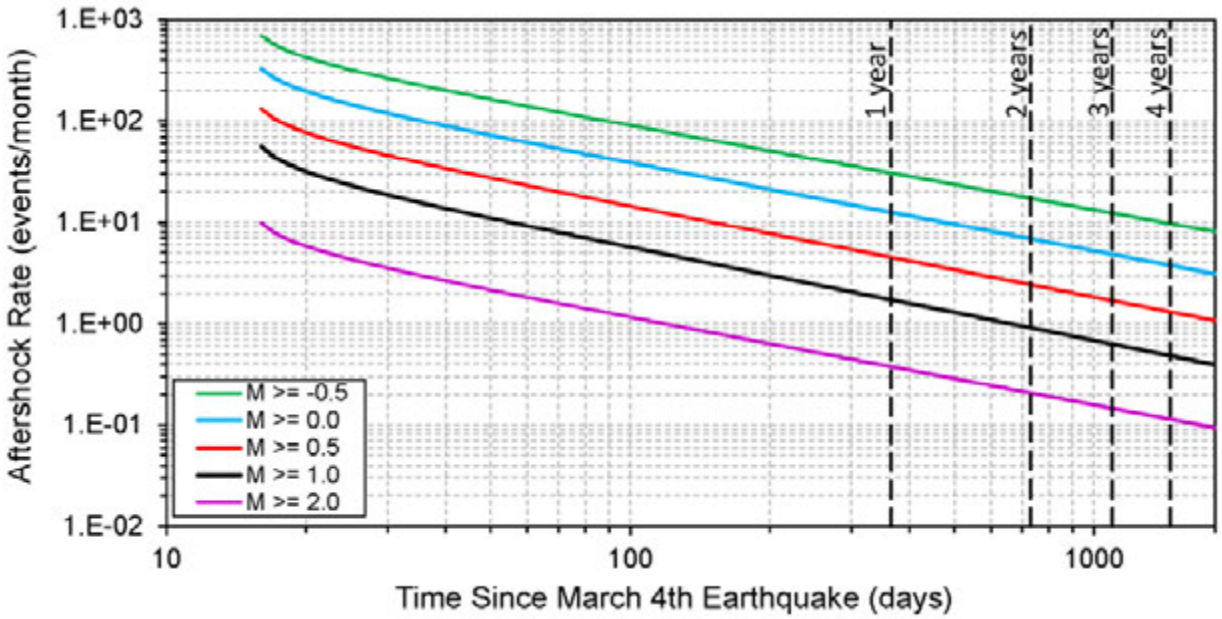

Figure 5-8: Log-log plot of monthly aftershock rates predicted by the Omori aftershock relations, for up to five years following the March 4th, 2019 M_W 4.5 earthquake. Results are shown for five magnitude thresholds; all magnitudes are duration magnitudes (M_D).

Table 5-3: Monthly aftershock rates predicted by the Omori aftershock relations, for up to five years following the March 4th, 2019 M_W 4.5 earthquake.

Threshold Magnitude (M_D)	Predicted Monthly Aftershock Rate					
	6 months	1 year	2 years	3 years	4 years	5 years
-0.5	54.6	30.7	17.3	12.3	9.7	8.1
0.0	22.9	12.6	6.9	4.8	3.8	3.1
0.5	8.4	4.5	2.4	1.7	1.3	1.1
1.0	3.3	1.7	0.9	0.6	0.5	0.4
2.0	0.7	0.4	0.2	0.1	0.1	0.1

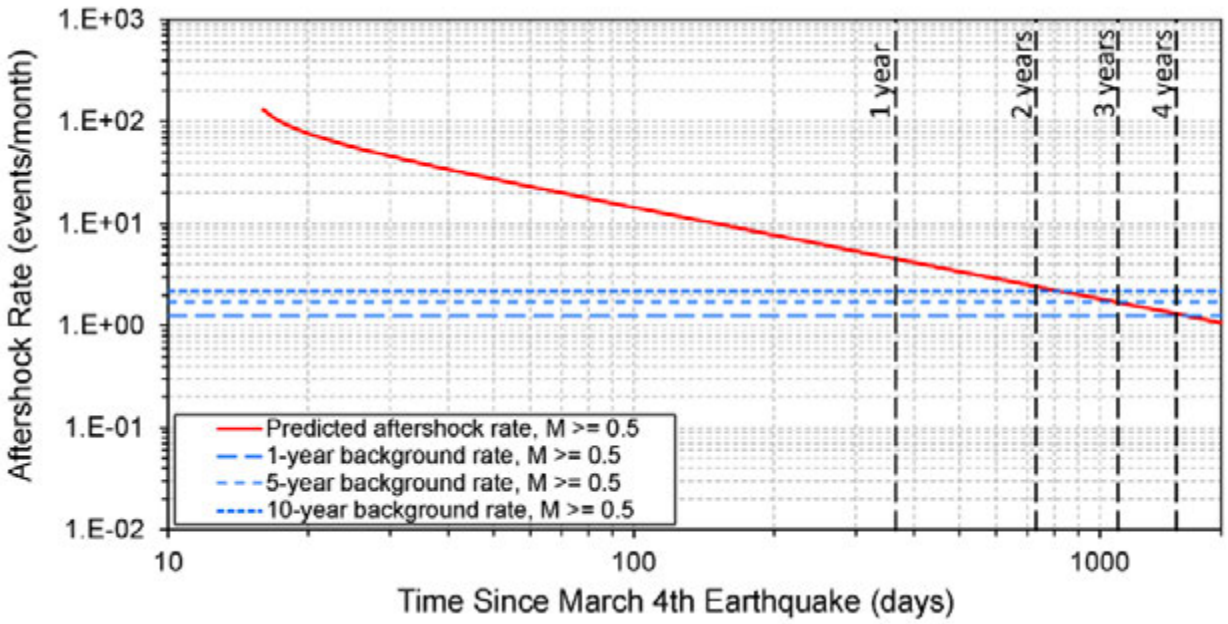

Figure 5-9: Log-log plot of the monthly aftershock rate predicted by the Omori aftershock relation for a magnitude threshold of M_D 0.5 (solid red line), compared to estimates of the near-well background seismicity rate (horizontal blue dashed and dotted lines). Three estimates of the near-well background seismicity rate were determined from the numbers of induced earthquakes with $M_D \geq$ 0.5 within 5 km of the injection well recorded during periods of one year, five years, and ten years prior to the March 2019 M_W 4.5 earthquake.

According to the geologic interpretations presented in section 3.2, aftershocks of the March 2019 M_W 4.5 earthquake are occurring both above and below the Paradox salt formation. The Paradox salt is the confining layer for PVU deep well brine disposal, and therefore pore pressures should be substantially elevated below that formation. Formations above the salt are expected to be affected by poroelastic stress changes related to injection (due to deformation of the reservoir and surrounding formations), with only minor associated changes in pore pressures. Because stress and pore pressure conditions are expected to be substantially different above and below the Paradox salt, the aftershock decay rates of the shallow (above salt) and deep (sub-salt) aftershocks may be different. To investigate this possibility, we performed Omori fits of the shallow and deep aftershocks separately.

For these analyses, we only used aftershocks within the main aftershock cloud (as seen in Figure 3-1), because the geologic interpretation discussed in section 3.2 is restricted to that area. As before, data recorded through the end of July 2019 were used. We separated the aftershocks into a shallow group with depths ≤ 3.65 km (relative to PVU wellhead) and a deep group with depths > 3.65 km. The analyses were performed with magnitude thresholds of M_D -0.5, M_D 0.0, M_D 0.5, and M_D 1.0. The number of aftershocks used for each analysis and the model parameters for the Omori fits are listed in Table 5-4. Plots of the observed and modeled daily aftershock rates and cumulative numbers of aftershocks are presented in Figure 5-10.

Table 5-4: Omori parameters computed from the shallow (depth ≤ 3.65 km) and deep (depth > 3.65 km) aftershocks of the March 4th, 2019 M_W 4.5 earthquake. Aftershocks within the main aftershock cloud recorded between the time of the main shock and the end of July 2019 were included in the analyses.

Aftershock Group	Threshold Magnitude (M_D)	Number of Aftershocks Included	K	c	p
shallow (above salt) (depth ≤ 3.65 km)	-0.5	675	46.6	0.014	0.690
	0.0	264	19.5	0.015	0.723
	0.5	83	6.9	0.026	0.774
	1.0	30	2.2	0.001	0.774
deep (below salt) (depth > 3.65 km)	-0.5	583	65.2	0.032	0.932
	0.0	306	38.2	0.072	0.947
	0.5	139	15.1	0.039	0.881
	1.0	69	8.5	0.049	0.962

The results indicate that the deep aftershocks, below the Paradox salt, are decaying at a slightly faster rate than the shallow aftershocks above the salt. The Omori *p* parameter, which indicates the rate of decay, ranges from 0.69 to 0.77 for the shallow aftershock models and ranges from 0.88 to 0.96 for the deep aftershock models (Table 5-4). Higher *p* values indicate a faster rate of decay.

The Omori fits also indicate that the magnitude distributions are different for the shallow and deep aftershocks. The shallow aftershocks contain a relatively larger fraction of smaller-magnitude events, whereas the deep aftershocks contain a relatively larger fraction of larger-magnitude events. For example, the plot of daily aftershock rates shows a higher rate of shallow aftershocks with $M_D \geq$ -0.5 than deep aftershocks (Figure 5-10, upper left plot). When the magnitude threshold is increased to M_D *1.0,* the daily rate of deep aftershocks is greater than the daily rate of shallow aftershocks (Figure 5-10, lower left plot). The difference in the magnitude distributions of the shallow and deep aftershocks is shown more explicitly in Figure 5-11, which shows the number of events above a given magnitude. The magnitude distribution of the deep aftershocks satisfies the Gutenberg-Richter (GR) relation (Gutenberg and Richter, 1954) with a b-value of 0.62, up to magnitude 2.2. The magnitude distribution of the shallow aftershocks satisfies the Gutenberg-Richter relation with a b-value of 0.92, up to magnitude 1.0. The difference in b-value for the shallow and deep aftershocks clearly indicates that the shallow aftershock distribution contains a greater fraction of smaller-magnitude events, whereas the deep aftershock distribution contains a greater fraction of larger-magnitude events.

The differences in both the aftershock decay rates and the magnitude distributions of the shallow and deep aftershocks provide additional evidence that these two sets of events are occurring within geologic units separated by the Paradox salt formation, which acts as a boundary between different stress and pressure regimes. The relatively bigger fraction of larger-magnitude events in the deep aftershock distribution (with lower b-value), compared to the distribution of the shallow

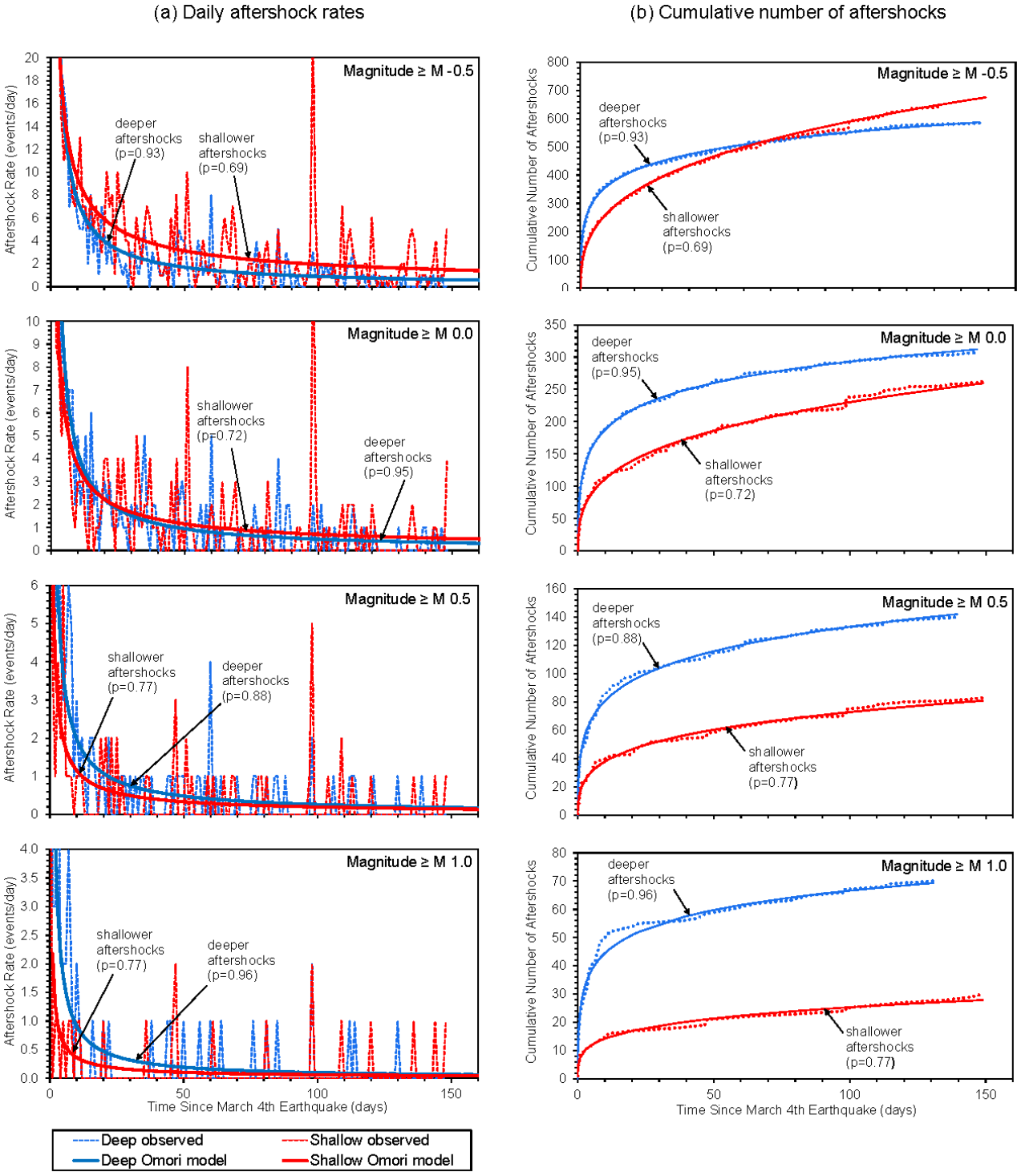

Figure 5-10: Fit of the Omori model to the shallower (depth ≤ 3.65 km) and deeper (depth > 3.65 km) aftershocks from the March 4th, 2019 M_W 4.5 earthquake: (a) daily aftershock rates (b) cumulative number of aftershocks. Results are shown for magnitude thresholds of M_D -0.5, M_D 0.0, M_D 0.5, and M_D 1.0. Data recorded through the end of July 2019 (149 days after the main shock) within the main aftershock cloud were included in the modeling.

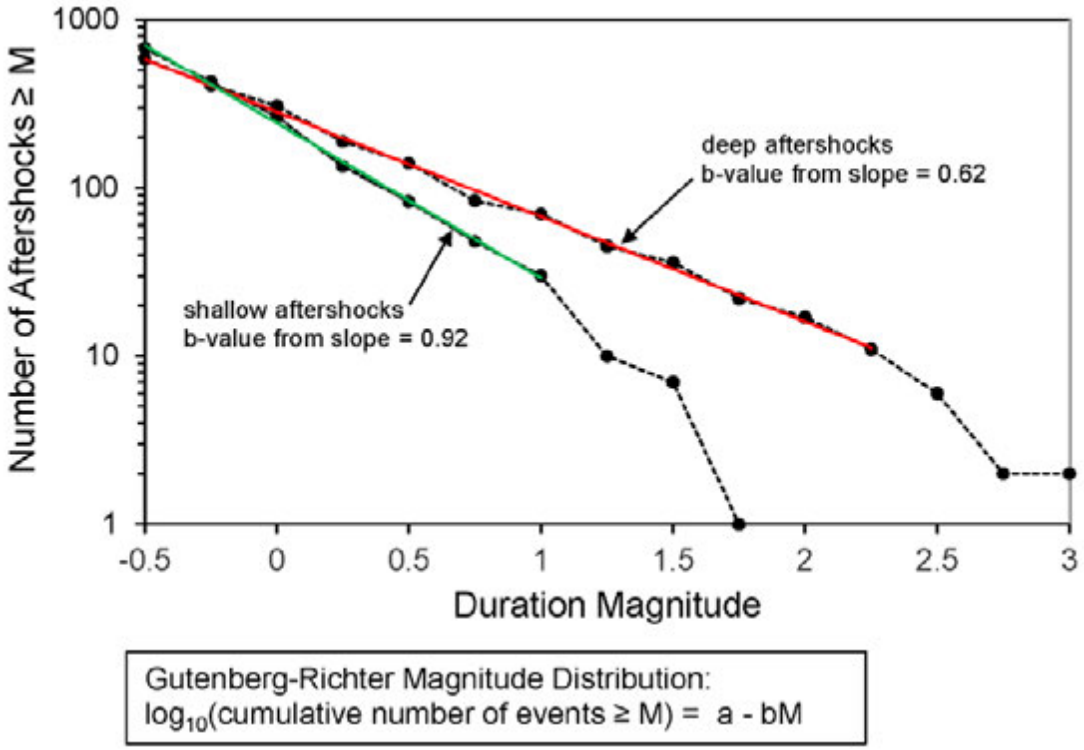

Figure 5-11: Magnitude distributions of shallow aftershocks (depth ≤ 3.65 km) and deep aftershocks (depth > 3.65 km) within the main aftershock cloud of the March 2019 M_W 4.5 earthquake. The analyses were performed using duration magnitudes.

aftershocks (with higher b-value), may be related to substantially elevated pore pressures in the target injection formations below the Paradox salt confining layer. Pore pressure diffusion modeling indicates that the pore pressures in the vicinity of the M_W 4.5 earthquake were approximately 162% of pre-injection hydrostatic pressures at the time of the main shock (section 6.1). Another possibility is that the differences in b-value are due to relatively large stress changes from the rupture of the M_W 4.5 fault plane beneath the salt, compared to substantially lower rupture-related stress changes above the salt.

Decreasing pore pressures within the geologic units in which the deeper aftershocks are occurring could be contributing to the relatively faster rate of decay of the deep aftershocks compared to the shallow aftershocks. Pressure diffusion modeling indicates that pore pressures in the vicinity of the M_W 4.5 earthquake began decreasing within approximately one month of the injection well shut-in on March 4th, 2019 (section 6.1).

Using the Omori fits of the shallow and deep aftershocks presented above, we predicted future aftershock rates for up to five years after the March 2019 M_W 4.5 earthquake. These rates are presented in Table 5-5 and Figure 5-12. Because of the differences in the magnitude distributions and rates of decay of the shallow and deep aftershocks, the relative trends of shallow and deep aftershocks are predicted to change over time. The overall rate ($M_D \geq -0.5$) of the shallow aftershocks is predicted to remain higher than the rate of the deep aftershocks, with the

difference in the rates increasing with time (diverging solid red and blue lines in Figure 5-12). The trend is similar for the rates of aftershocks with $M_D \geq 0.0$ (diverging long dashed red and blue lines in Figure 5-12). The rates of aftershocks with $M_D \geq 0.5$ (including those with $M_D \geq 1.0$), which are currently higher below the Paradox salt layer than above it, are predicted to become similar above and below the Paradox formation after about three years (converging short dashed and dotted lines in Figure 5-12).

Table 5-5: Monthly aftershock rates predicted by the Omori relations for the shallow and deep aftershock groups, for up to five years following the March 4th, 2019 M_W 4.5 earthquake. These predicted rates only include aftershocks within the main aftershock cloud.

Aftershock Group	Magnitude Threshold	Predicted Monthly Aftershock Rate					
		6 months	1 year	2 years	3 years	4 years	5 years
shallow (above salt)	-0.5	39.7	24.7	15.3	11.5	9.5	8.1
	0.0	14.0	8.5	5.1	3.8	3.1	2.7
	0.5	3.8	2.2	1.3	0.9	0.8	0.6
	1.0	1.2	0.7	0.4	0.3	0.2	0.2
deep (below salt)	-0.5	15.8	8.3	4.3	3.0	2.3	1.8
	0.0	8.5	4.4	2.3	1.6	1.2	1.0
	0.5	4.8	2.6	1.4	1.0	0.8	0.6
	1.0	1.7	0.9	0.5	0.3	0.2	0.2

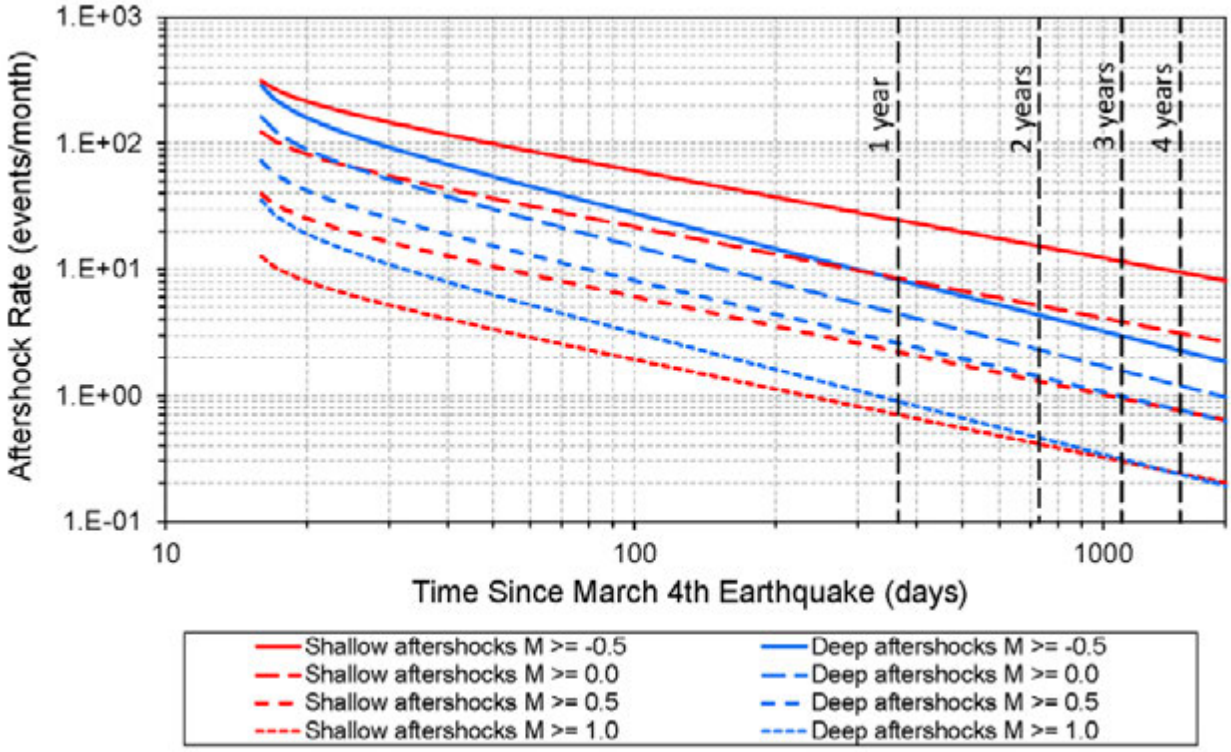

Figure 5-12: Monthly shallow (depth ≤ 3.65 km) and deep (depth > 3.65 km) aftershock rates predicted by the Omori aftershock relations, for up to five years following the March 4th, 2019 M_W 4.5 earthquake. These predicted rates only include aftershocks within the main aftershock cloud. All analyses were done using duration magnitudes.

5.2.3 Aftershocks of the January 24th, 2013 M_W 4.0 Earthquake

In order to evaluate how the aftershock activity and decay rate from the March 2019 M_W 4.5 induced earthquake compares to that of previous induced earthquakes, we applied the Omori aftershock relation to the second largest PVU-induced earthquake. This earthquake occurred on January 24th, 2013. It occurred 8.2 km northwest of the PVU injection well and had a moment magnitude of M_W 4.0 (Block et al., 2014; Wood et al., 2016). Events in the vicinity of this earthquake were selected for inclusion in the aftershock analysis based on the following geographic bounds: latitude 38.3165° to 38.327° and longitude -109.0° to -108.961°. Because the time period to use for separating the aftershock data from the earthquake catalog is subjective, we created data sets using two different time periods and performed the aftershock analysis on each set. The first data set includes earthquakes in the defined geographic region that occurred between the time of the main shock on January 24th 2013 and the end of July 2013. This set includes 18 aftershocks, with magnitudes ranging from M_D -0.4 to M_D 1.7. The second data set includes data from a much longer time period, extending from the time of the main shock to the end of 2015. This set includes 26 events, with magnitudes ranging from M_D -0.5 to M_D 2.3. The maps in Figure 5-13 show the distribution of earthquakes in each of these two data sets.

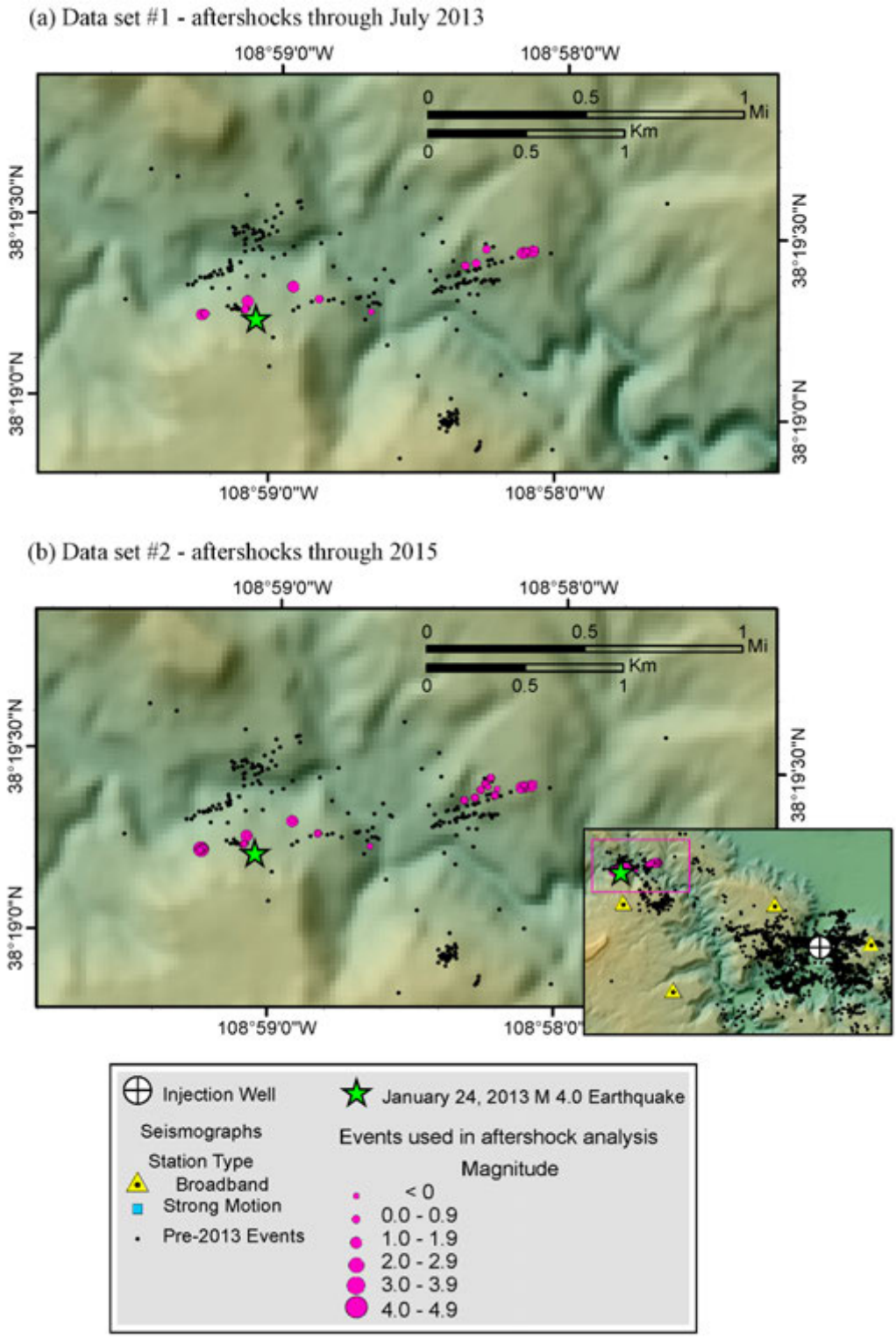

Figure 5-13: Maps showing the locations of events selected for aftershock analysis of the January 24th, 2013 M_W 4.0 earthquake: (a) data set #1 – aftershocks through July 2013, and (b) data set #2 – aftershocks through 2015. The inset map shows the location of the study area (pink rectangle) relative to the PVU injection well (white circle).

We fit the Omori aftershock relation to each of the two data sets using four magnitude thresholds: M_D -0.5, M_D 0.0, M_D 0.5, and M_D 1.0. The observed and computed cumulative number of aftershocks for each of the four models for the first data set (through July 2013) are presented in Figure 5-14, and the same results for the second data set (through 2015) are presented in Figure 5-15. Although the number of data points in each of the data sets is fairly small, a reasonable fit using the Omori relation is obtained in each case. For a given magnitude threshold, the values of the Omori parameters derived from the two data sets are very similar (Table 5-6). Hence, the aftershocks recorded for three years following the main earthquake appear to obey the same aftershock decay relations.

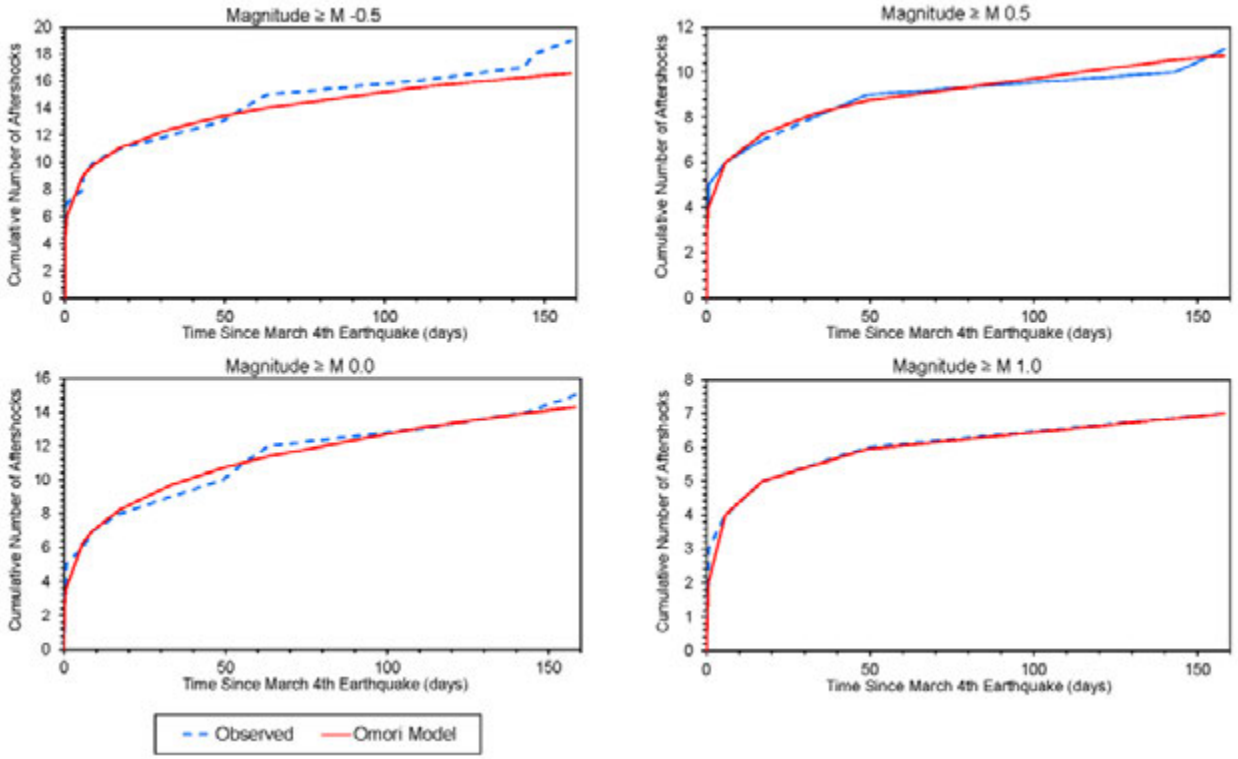

Figure 5-14: Fit of the Omori model to the cumulative number of aftershocks from the January 24th, 2013 M_W 4.0 earthquake. Results are shown for four magnitude thresholds; all magnitudes are duration magnitudes (M_D). Data recorded through the end of July 2013 were included in the modeling. The last event within the time window occurred on 7/1/2013, 159 days after the main shock.

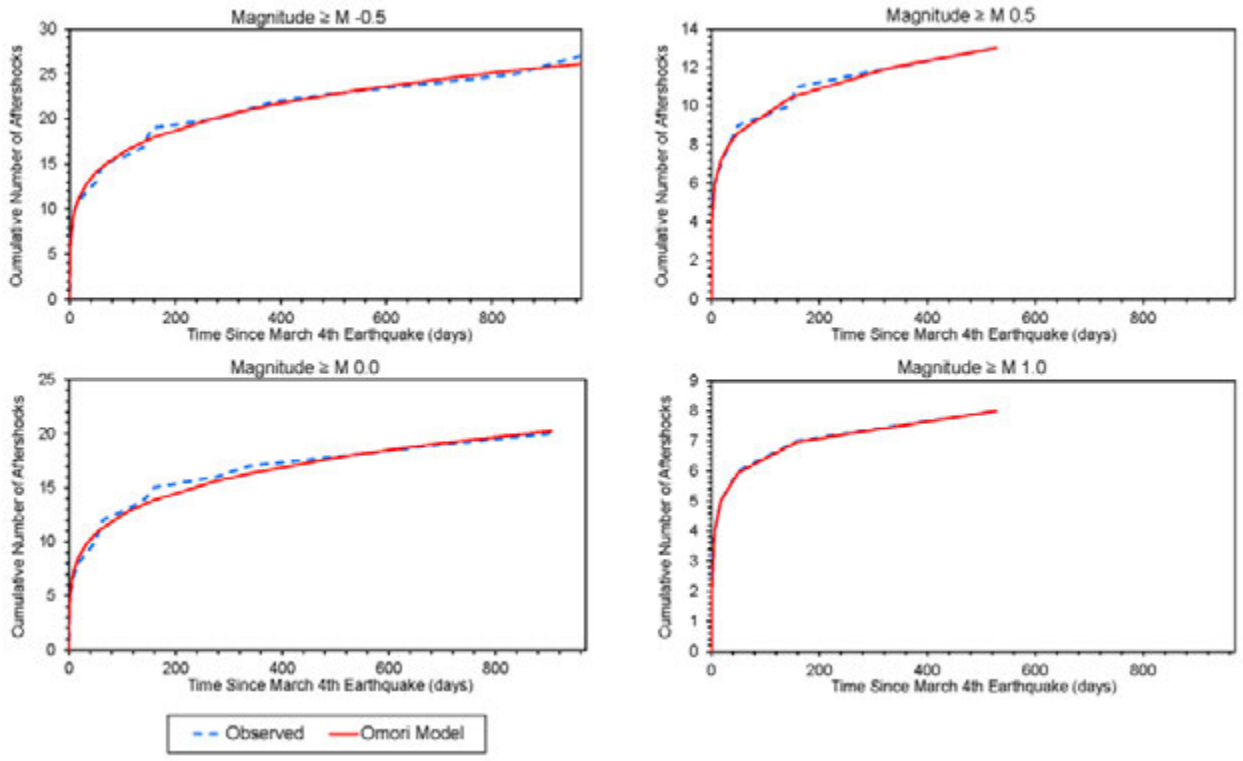

Figure 5-15: Fit of the Omori model to the cumulative number of aftershocks from the January 24th, 2013 M_W 4.0 earthquake. Results are shown for four magnitude thresholds; all magnitudes are duration magnitudes (M_D). Data recorded through the end of 2015 were included in the modeling. The last event within the time window occurred on 9/19/2015, 968 days after the main shock. The fits for aftershocks with magnitudes ≥ M_D 0.5 only extend to 527 days after the main shock because no aftershocks with $M_D \geq 0.5$ were recorded after 7/5/2014.

Table 5-6: Omori parameters computed from the aftershock data of the January 24th, 2013 M_W 4.0 earthquake, for four magnitude thresholds. Results are shown for two data sets: #1 - aftershocks recorded between the time of the main shock and the end of July 2013, and #2 – aftershocks recorded between the time of the main shock and the end of 2015.

Data Set	Threshold Magnitude (M_D)	Number of Aftershocks Included	K	c	P
#1 (Jan-Jul 2013)	-0.5	18	1.200	0.000	0.818
#2 (2013-2015)	-0.5	26	1.300	0.000	0.792
#1 (Jan-Jul 2013)	0.0	14	1.010	0.000	0.752
#2 (2013-2015)	0.0	19	1.000	0.000	0.782
#1 (Jan-Jul 2013)	0.5	10	0.775	0.000	0.824
#2 (2013-2015)	0.5	12	0.760	0.000	0.827
#1 (Jan-Jul 2013)	1.0	6	0.930	0.079	1.008
#2 (2013-2015)	1.0	7	0.950	0.087	1.018

For the fits obtained with magnitude thresholds of M_D -0.5, M_D 0.0, and M_D 0.5, the Omori parameters are internally consistent (Table 5-6). The estimates of K decrease with increasing magnitude threshold, as expected, and the estimates of c are identical (0). The estimates of p for these models are very similar, ranging from 0.75 to 0.83, with a mean value of 0.80 and median value of 0.81. In contrast, the estimates of the Omori parameters derived with a magnitude threshold of M_D 1.0 do not fit the trend. The values of K derived with a magnitude threshold of M_D 1.0 (0.93-0.95) are larger than the values derived with a magnitude threshold of M_D 0.5 (0.76-0.775), which is the opposite of the expected trend. The values of p for the models with a magnitude threshold of M_D 1.0 (1.01-1.02) are considerably larger than those for the models using smaller magnitude thresholds (0.75-0.83). Because only 6 or 7 aftershocks are included when a magnitude threshold of M_D 1.0 is used (Table 5-6), and because the derived Omori parameters are not consistent with those derived with the larger data sets, we consider the Omori parameters computed using a magnitude threshold of M_D 1.0 to be unreliable.

5.2.4 Discussion

The rate of earthquakes that occurred within ~3.5 km of the March 4th, 2019 M_W 4.5 earthquake between the time of this main shock and the end of July 2019 are well fit by the Omori aftershock relation. This helps confirm that nearly all earthquakes in this area in the five months following the M_W 4.5 earthquake are aftershocks of that event, caused by the redistribution of stress associated with the main shock fault plane rupture. If the high seismicity rates following the M_W 4.5 earthquake were instead primarily caused by a change in reservoir conditions, such as a rupture of the confining layer or a break across an impermeable fault into a previously unpressurized area, we would not expect the seismicity to decay at a rate consistent with the Omori aftershock relation. Instead, seismicity rates would likely remain elevated or potentially increase further for a few weeks to months as the elevated pore pressures in the reservoir slowly diffused into previously unpressurized areas (given the low in-situ permeabilities of the geologic formations). This is not observed, but rather seismicity rates began declining within days of the M_W 4.5 earthquake on March 4th. Although we cannot conclude that every earthquake in the vicinity of the M_W 4.5 earthquake in the months following its occurrence is an aftershock of that main event, the analysis presented here strongly suggests that the high near-well seismicity rates observed since March 2019 are primarily due to aftershock activity from stress redistribution.

Independent Omori fits to the shallower and deeper aftershocks within the main aftershock cloud of the M_W 4.5 earthquake show meaningful differences, with the deeper aftershocks decaying at a faster rate than the shallower aftershocks. In addition, the deeper aftershocks contain a higher fraction of larger-magnitude events than the shallower aftershocks. These differences in aftershock trends are consistent with the previous interpretation that the shallower aftershocks are above the Paradox salt confining layer and the deeper aftershocks are below it. The differences are most likely related to differences in pore pressures and stresses within these two different regimes.

The rate at which the aftershock occurrence is declining is relatively slow, compared to aftershocks in many other regions. However, it is consistent with the rate of aftershock decay associated with the second largest PVU-induced earthquake, the M_W 4.0 earthquake of January 24th, 2013. The Omori parameter p, which represents the rate of aftershock decay, has a mean

value of 0.88, when considering all aftershocks of the March 2019 M_W 4.5 earthquake, compared to an only slightly smaller mean value of 0.80 for aftershocks of the January 2013 M_W 4.0 earthquake.

Analyses of the aftershock rates from the January 24th, 2013 M_W 4.0 earthquake indicate that the observed aftershock decay rate honored the same relation for a period of at least three years following the main shock. This observation increases confidence that the aftershock relations derived for the March 4th M_W 4.5 earthquake utilizing data recorded through July 2019 can be used to predict future aftershock rates for several years. However, pore pressures at the location of the March 2019 earthquake, 1.6 km from the injection well, change at a much faster rate than those at the location of the January 2013 earthquake, 8.2 km from the well. These aftershock prediction relations were developed for naturally occurring earthquakes and aftershock sequences, where pore pressures do not experience large changes over relatively short time periods. It is possible that decreasing pore pressures under continued shutdown could cause the aftershock rate to decline faster than predicted. Conversely, if injection is resumed and sustained for a sufficiently long time period for pore pressures at the location of these aftershocks to increase, the aftershock rate could decline less quickly, or potentially even increase.

Recent observations suggest that changing pore pressures are influencing the rate of aftershocks occurring below the Paradox salt. In Figure 5-16a, the cumulative number of subsalt events (depth > 3.65 km) in the main aftershock cloud of the M_W 4.5 earthquake observed through February 2020 is compared to the cumulative number predicted by the Omori model. The Omori model was derived from aftershocks recorded through July 2019 using a magnitude threshold of M_D 0.0 (from section 5.2.2). Fewer subsalt aftershocks were observed from August 2019 to February 2020 (solid gray line) than the Omori model predicts (dashed red line). In contrast, the cumulative number of aftershocks in the main aftershock cloud above the Paradox salt (depth ≤ 3.65 km) observed from August 2019 to February 2020 matches the number predicted by the Omori model based on the earlier data (Figure 5-16b). The most probable explanation for this discrepancy is that the deeper aftershocks were decaying at a faster rate than predicted from August 2019 to February 2020 because pore pressures below the Paradox salt confining layer were gradually declining during the continued injection well shutdown, making faults less critically stressed over time. Pore pressures above the salt layer were not changing significantly during this time period, and therefore the shallow aftershocks occurred at the rate predicted previously from the March-July 2019 data.

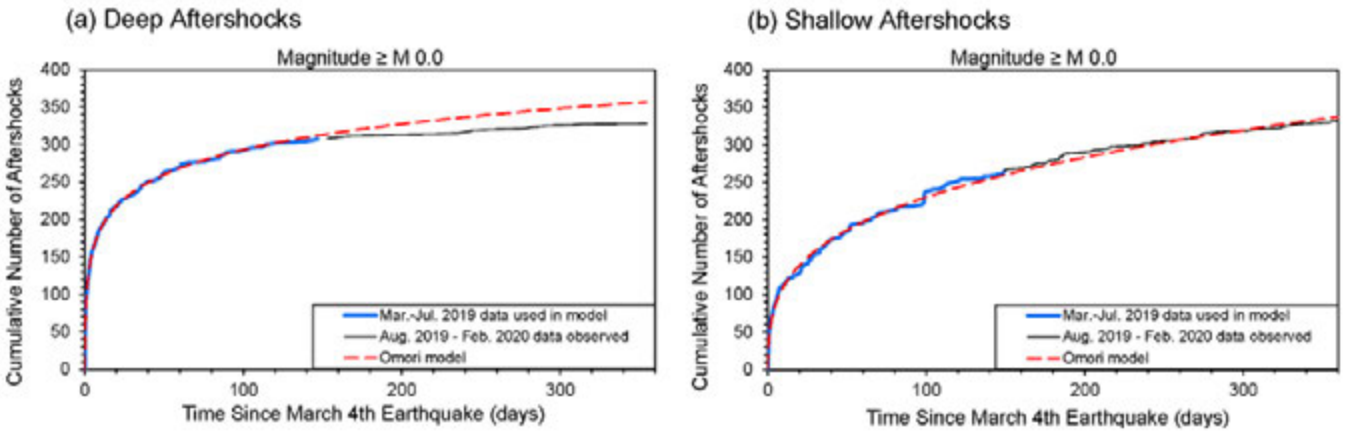

Figure 5-16: Cumulative number of events in the main aftershock cloud of the March 4th, 2019 M_W 4.5 earthquake observed through February 2020 (gray lines), compared to the cumulative number of events predicted by Omori aftershock rate models (red dashed lines): (a) deeper aftershocks (below Paradox salt; depth > 3.65 km) (b) shallower aftershocks (above Paradox salt; depth ≤ 3.65 km). Results are shown for a magnitude threshold of M_D 0.0. Data recorded through the end of July 2019 (149 days after the main shock) within the main aftershock cloud were included in the Omori modeling (blue lines).

Ignoring changes in aftershock rate due to changing pore pressures, the average rate of aftershocks for the next several years is expected to be roughly 35-40 times larger than the rate of the aftershocks from the 2013 M_W 4.0 earthquake at comparable times after the main shock. This can be seen in Figure 5-17 and Table 5-7, which present the rates of aftershocks with $M_D \geq$ 0.0 for both earthquakes, for time periods up to five years after the main earthquake. For example, the average rate of M_D 0.0+ aftershocks from the 2019 M_W 4.5 earthquake is predicted to be 12.6 events/month one year after the main shock, whereas the rate of M_D 0.0+ aftershocks from the 2013 M_W 4.0 earthquake was only ~0.3 events/month one year after the main shock (~41 times less). Similarly, the average rate of M_D 0.0+ aftershocks from the 2019 M_W 4.5 earthquake is predicted to be ~3 events/month five years after the main shock, whereas the rate of M_D 0.0+ aftershocks from the 2013 M_W 4.0 earthquake was only 0.09 events/month five years after the main shock (~36 times less).

The much greater rate of aftershocks from the March 2019 M_W 4.5 earthquake compared to the second largest PVU-induced earthquake can be largely attributed to the larger magnitude of the 2019 earthquake. Other factors that may be influencing the high rate of aftershocks include: the stress conditions prior to the fault rupture, potentially related to high pore pressures, reservoir deformation, and the proximity to an interpreted impermeable boundary fault; the presence of many pre-existing nearby faults favorably oriented for slip; and differences in the nature of the ruptures of the main shock fault planes.

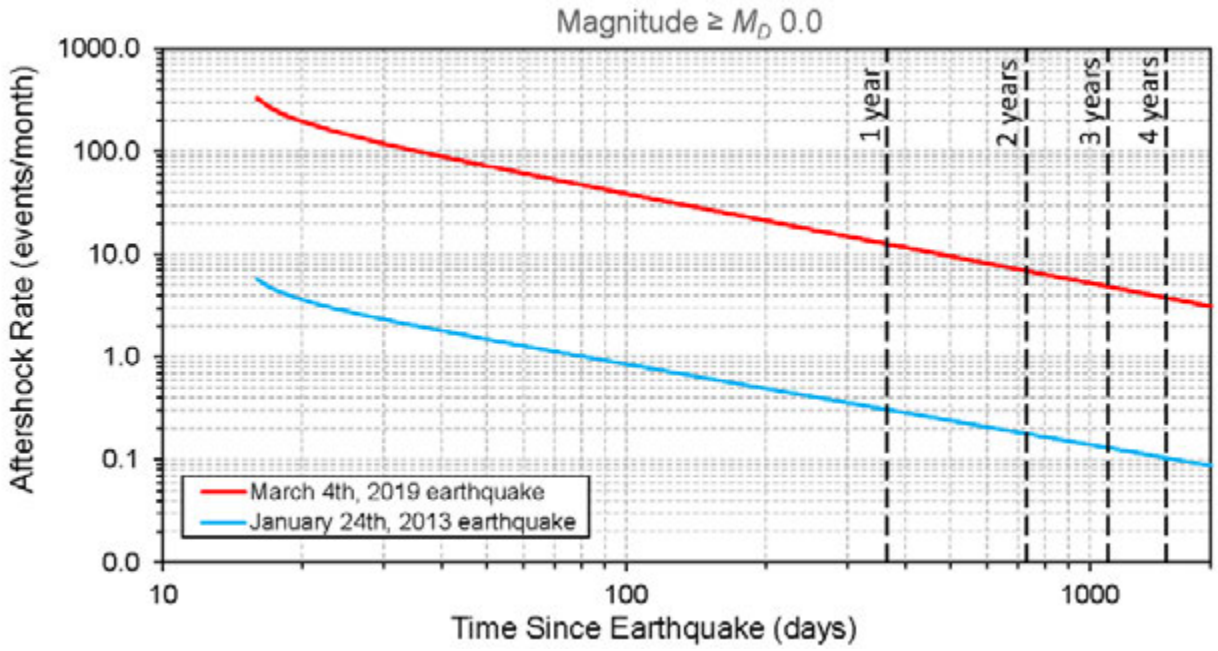

Figure 5-17: Log-log plot of monthly aftershock rates ($M_D \geq 0.0$) predicted by the Omori aftershock relations, for up to five years following the March 4th, 2019 M_W 4.5 and January 24th, 2013 M_W 4.0 earthquakes. Results for the January 2013 earthquake are from data set #2, which includes aftershock data through 2015.

Table 5-7: Monthly aftershock rates ($M_D \geq 0.0$) predicted by the Omori aftershock relations, for up to five years following the March 4th, 2019 M_W 4.5 and January 24th, 2013 M_W 4.0 earthquakes. Results for the January 2013 earthquake are from data set #2, which includes aftershock data through 2015.

Earthquake	Predicted Monthly Aftershock Rate ($M_D \geq 0.0$)						
	3 months	6 months	1 year	2 years	3 years	4 years	5 years
3/4/2019 M_W 4.5	42.3	22.9	12.6	6.9	4.8	3.8	3.1
1/24/2013 M_W 4.0	0.92	0.53	0.31	0.18	0.13	0.10	0.09
ratio of predicted monthly aftershock rates $\frac{M_W 4.5 \text{ rate}}{M_W 4.0 \text{ rate}}$	46.1	43.4	40.9	38.5	37.1	36.2	35.5

6 Pressures

We examine the pore pressure trends at the location of the March 2019 M_W 4.5 earthquake using a simple analytical flow model. Results from this modeling are used to examine the trends of the pore pressure and its temporal and spatial gradients in the years preceding the occurrence of the earthquake and in the months following the March 2019 shut-in of the injection well.

For this modeling, we used a radial flow model that incorporated the method of image wells to simulate two parallel faults that form impermeable or partially impermeable barriers to pore pressure diffusion from PVU fluid injection (Figure 6-1). One of these faults lies 2 km southwest of the PVU injection well and was discussed in section 3.2. Because previous studies indicate that this fault forms a barrier to fluid flow and pressure increase from injection into the PVU well (Bremkamp and Harr, 1988; King et al., 2018), we made it an impermeable boundary in the flow model. Northeast of the PVU injection well, discontinuous fault segments with 500 feet or more of vertical offset were previously interpreted as forming barriers to PVU fluid flow and pressure diffusion (King et al., 2018). These segments were modeled using a partially impermeable fault 1.65 km northeast of the well. Calibration of the model using the observed pressures at the PVU wellhead indicates that a fault impermeability of 64% provides the best fit (Appendix B). Hence, 64% of the fluid flow is blocked by this northeast fault in the model, whereas 36% of the flow passes through. Further details of the modeling method and its calibration using PVU wellhead data are provided in Appendix B.

6.1 Pressure Trends at the Location of the M_W 4.5 Earthquake

Pore pressure trends computed from the flow model at the location of the M_W 4.5 earthquake are presented in Figure 6-2. This plot shows the pore pressure increase (above the pre-injection hydrostatic value) and the temporal and spatial pressure gradients over time, from the beginning of near-continuous brine disposal in 1996 to the time of occurrence of the M_W 4.5 earthquake on March 4th, 2019. The same parameters for a more recent time window, from January 2012 to October 2019, are shown in Figure 6-3. On this plot, extended shut-ins of the injection well and other operational changes are labeled.

The computed pore pressure increase due to PVU fluid injection, at the time and location of the M_W 4.5 earthquake, is ~3750 psi (Figure 6-2 and Figure 6-3, upper plots). To put this pressure change into perspective, we compute how large it is compared to the pre-injection pressure. Pre-injection pressure conditions within the Leadville Formation are interpreted as being hydrostatic, with a regional hydrostatic pressure gradient of 0.47 psi/ft (King et al., 2018). Hence, the pre-injection pore pressure at the depth of the M_W 4.5 earthquake, 3.9 km, is computed as 0.47 psi/ft * 3.9 km (12,795 ft), which yields a pre-injection pore pressure of 6014 psi. The 3750 psi increase in pore pressure represents a 62% increase over pre-injection in-situ pressure. This is the highest pressure increase that this location has experienced since a ~one-month shut-in of the injection well in early 2017 and subsequent ~5% decrease in flow rate. The pore pressure at the location of the M_W 4.5 earthquake decreased for a few months following these operational changes and subsequently began increasing. The pressure had just exceeded its previous maximum value at the time of the M_W 4.5 earthquake (Figure 6-3).

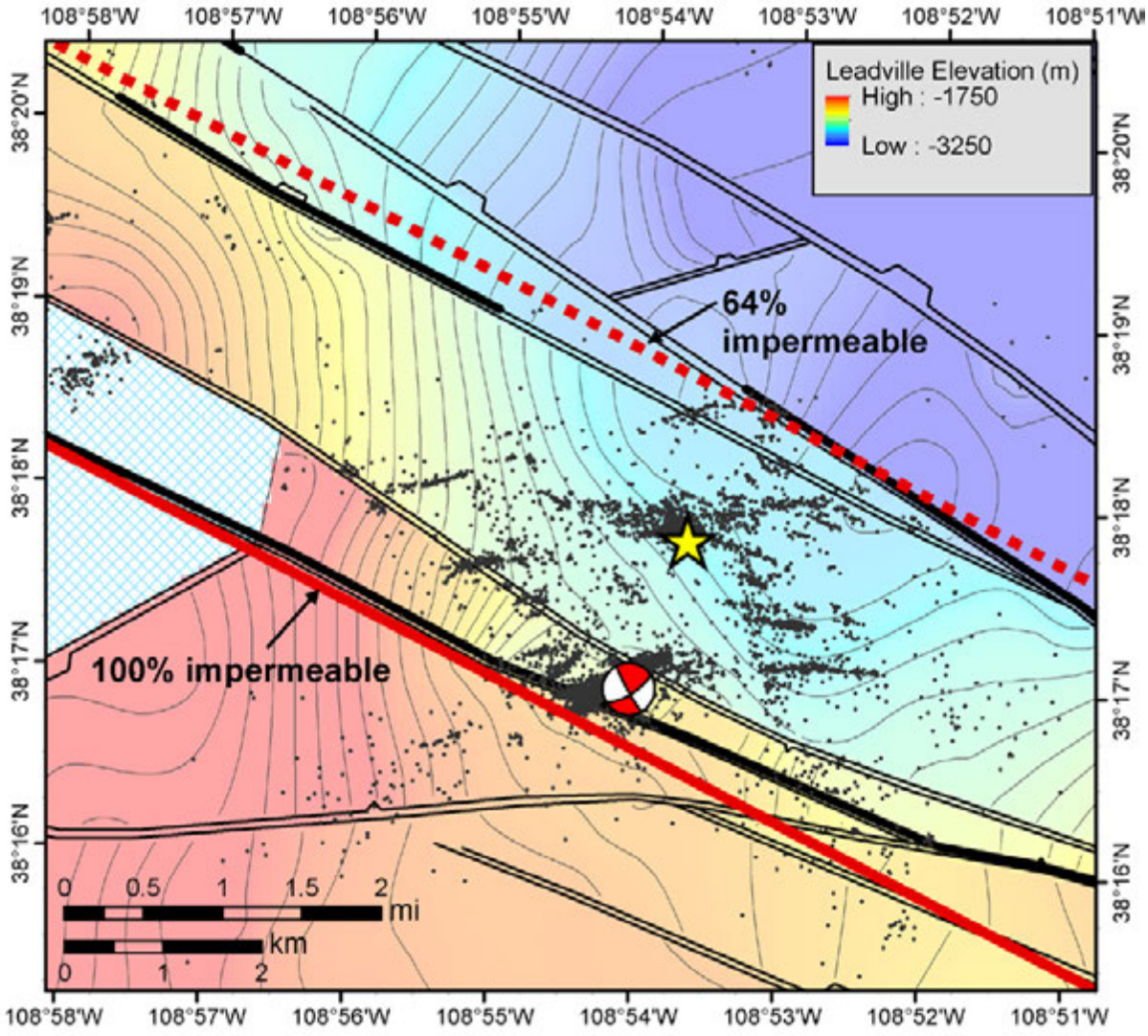

Figure 6-1: Structure map of the top of the Leadville formation interpreted from seismic reflection surveys and well data (interpretation from Arestad (2017)). The thick black lines indicate fault segments that were interpreted by King et al. (2018) as forming barriers to lateral fluid flow and pressure diffusion through the Leadville formation, based on a vertical offset > 500 ft. The thick red lines indicate two parallel flow boundaries included in the analytical flow model. The fault southwest of the well is modeled as being 100% impermeable, while the fault northeast of the well is modeled as 64% impermeable.

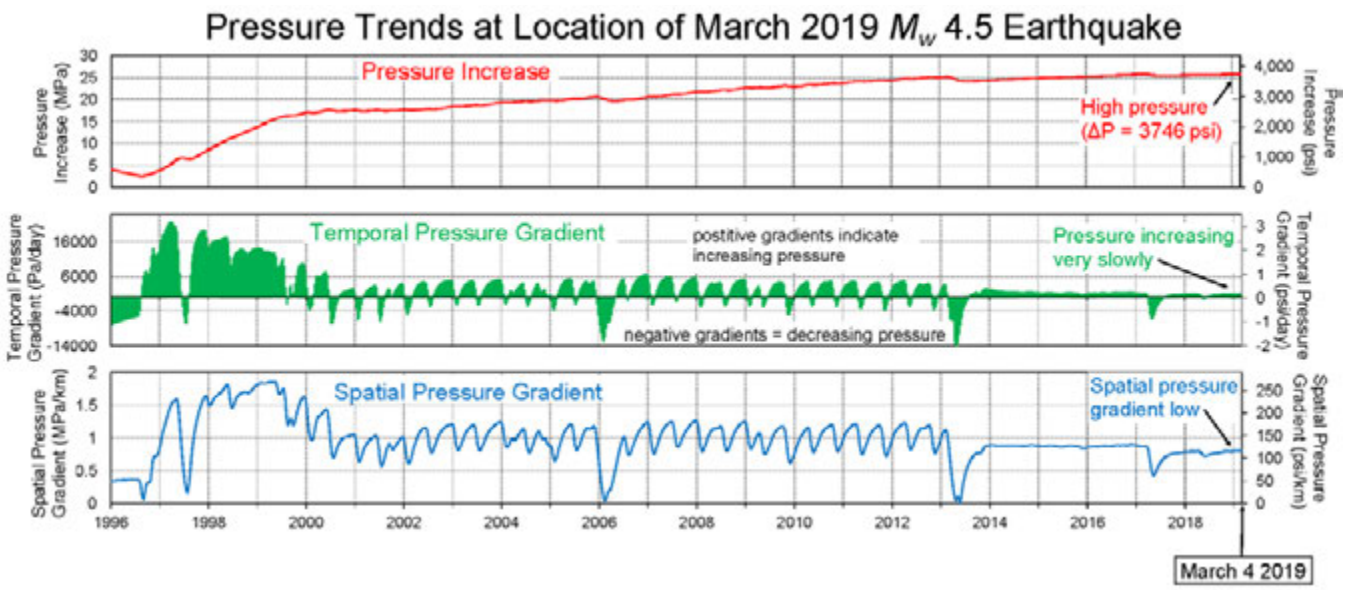

Figure 6-2: Pressure trends at the location of the March 2019 M_W 4.5 earthquake from 1996 to March 4th, 2019: pore pressure increase (above pre-injection hydrostatic, upper plot); temporal pressure gradient (pressure change per day, with increases in pressure corresponding to positive gradients and decreases in pressures corresponding to negative gradients, middle plot); and maximum absolute horizontal spatial pressure gradient (maximum pressure change per horizontal km regardless of azimuth, lower plot).

The temporal pressure gradient (pressure change per day) was very low at the time and location of the M_W 4.5 earthquake, ~0.1 psi/day (Figure 6-2 and Figure 6-3, second plot). It was also low compared to historical trends. Pore pressures were increasing the fastest, and hence the temporal gradients were the largest, early in injection operations, prior to mid-1999 (Figure 6-2). The temporal gradient generally ranged from ~1.8 to ~3.0 psi/day during this early period. Following the implementation of 20-day biennial injection well shut-ins in mid-1999 and a ~32% decrease in the average flow rate in mid-2000, pressures increased more slowly and hence the temporal gradients were lower. The maximum temporal pressure gradient from mid-2000 to early 2013 was ~0.9 psi/day. In addition, at the location of the M_W 4.5 earthquake, 1.6 km from the injection well, pore pressures decreased twice a year for brief periods of time following the biennial injection well shut-ins, as indicated by the negative temporal gradients (Figure 6-2, middle plot). In 2013, the 20-day biennial shut-ins were replaced with weekly 18-hour shut-ins. In 2017, the weekly injection well shut-ins were replaced with rotating shut-downs of individual pumps, and injection was continuous except for infrequent shut-downs needed for maintenance activities. In addition, the average flow rate was decreased 10% in 2013 and another 5% in 2017. The combined effect of these operational changes was to further reduce the temporal pressure gradient, to a value of ~0.18-0.2 psi/day following the 2013 operational changes and ~0.1 psi/day following the changes implemented in 2017. Because the 20-day biennial shut-ins were eliminated in 2013, the pore pressures at this location (1.65 km from the well) no longer experienced regular decreases in pore pressure. Hence, pore pressures at the location of the M_W 4.5 earthquake had been increasing very slowly but mostly uninterrupted for nearly six years prior to the occurrence of the earthquake.

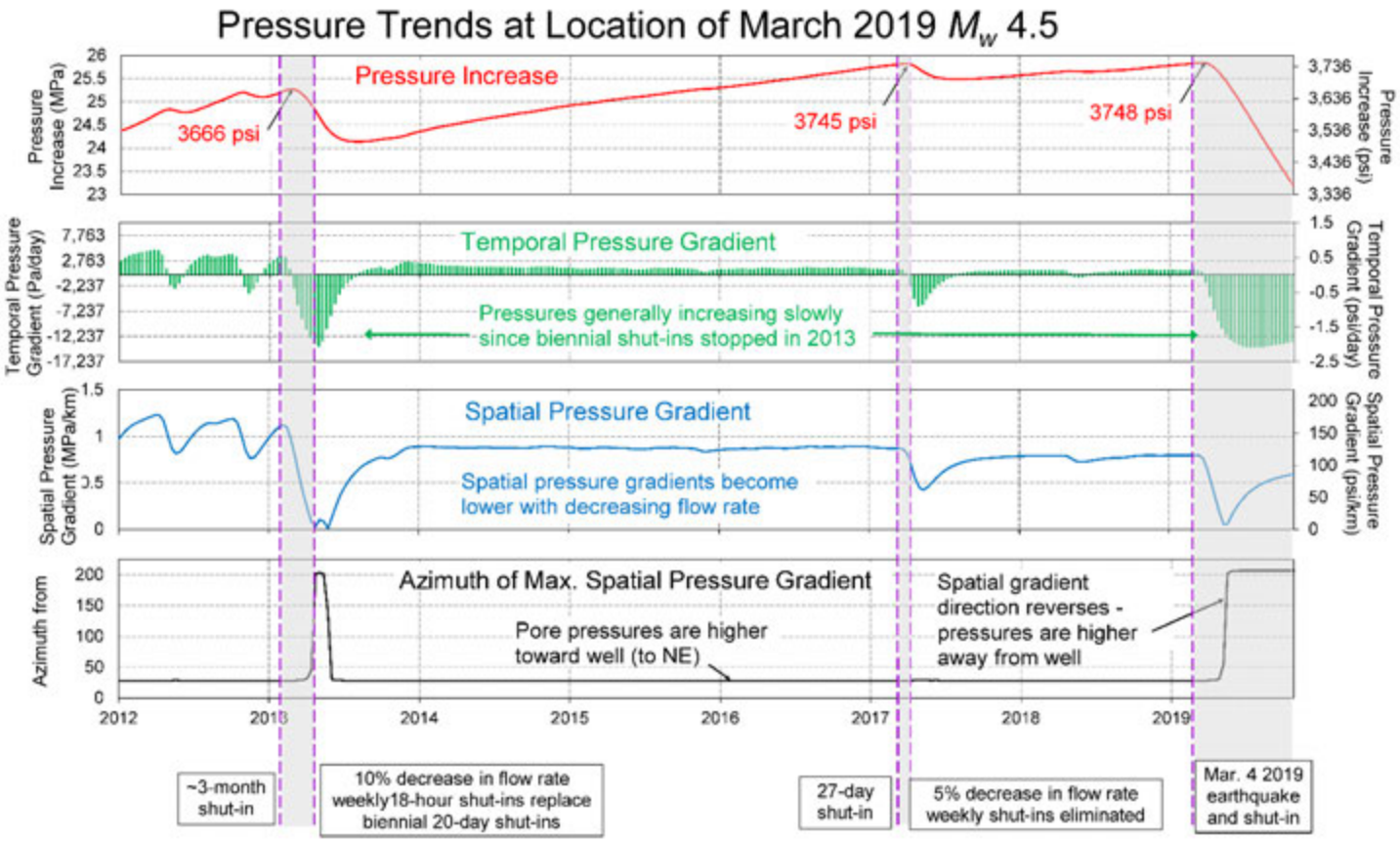

Figure 6-3: Pressure trends at the location of the March 4th, 2019 M_W 4.5 earthquake from 2012 to October 2019: pore pressure increase (above pre-injection hydrostatic, upper plot); temporal pressure gradient (pressure change per day, with increases in pressure corresponding to positive gradients and decreases in pressures corresponding to negative gradients, second plot); maximum absolute horizontal spatial pressure gradient (maximum pressure change per horizontal km regardless of azimuth, third plot); and azimuth from North of maximum absolute horizontal pressure gradient (direction from lower to higher pressure, lower plot).

The spatial pressure gradients shown in Figure 6-2 and Figure 6-3 (blue curves) are the maximum absolute horizontal pressure gradients regardless of direction (at the location of the M_W 4.5 earthquake). They were determined by computing the horizontal pressure gradient over all azimuths (at 1° increments) and taking the maximum absolute value. During most times, the spatial gradient is such that pressures are higher near the well and lower at the earthquake's location 1.6 km to the southwest. However, following extended injection well shut-ins, such as the shut-ins in 2013 and 2019, the area of decreased pressure around the well extends beyond this 1.6 km distance, and the direction of the spatial pressure gradient at this location reverses. These trends in the direction of the spatial gradient are shown by the spatial gradient azimuths included in the lower-most plot of Figure 6-3 (black curve).

The long-term trend of the spatial pressure gradient is similar to that of the temporal pressure gradient. Spatial gradients were generally high early in injection operations and have generally

decreased over time as the average injection rate has declined. At the location of the *MW* 4.5 earthquake, the highest spatial pressure gradient occurred in mid-1999 and was ~268 psi/km. Between mid-2000 and 2013, the spatial gradient fluctuated between roughly 90 and 180 psi/km, increasing and decreasing regularly in response to the biennial 20-day injection well shut-ins. Following the 10% decrease in flow rate and elimination of the biennial shut-ins in 2013, the spatial pressure gradient stabilized at ~127-129 psi/km. It further decreased to ~115 psi/km following the operational changes implemented in 2017 and was at about this value at the time of the *MW* 4.5 earthquake.

This model indicates that pore pressures continued increasing at the location of the March 2019 *MW* 4.5 earthquake for about a month after the injection well was shut in. Pressures subsequently began decreasing and had declined ~385 psi by the end of October 2019, to a value of 3365 psi above the pre-injection hydrostatic value (Figure 6-3, red curve). This represents a change from ~62% above the pre-injection pressure to ~56% above the pre-injection pressure. It is the lowest pressure at this location since early 2010. The temporal pressure gradients (Figure 6-3, green columns) indicate that pressures were decreasing at their fastest rate in July and August 2019; the rate of pressure decrease slowed gradually after August. The spatial pressure gradient initially decreased rapidly when the pore pressure began declining. It reached its minimum value in May 2019, when it reversed direction. The spatial gradient gradually increased after May, as pressures near the well continued to decline.

6.2 Relation Between Pressure Trends and Induced Seismicity

We interpret the PVU-induced seismicity as occurring in response to a decrease in the effective normal stress on pre-existing faults. Fracture initiation is assumed to be adequately described by a Coulomb failure criterion (Jaeger, 1969), and the observed seismicity is interpreted to be the result of frictional failure due to shearing (Block et al., 2015). Previous studies have indicated that pore pressure increase is the dominant factor contributing to a decrease in the effective normal stress on pre-existing faults and the occurrence of induced seismicity within 5 km of the injection well (Block, 2017; Block et al., 2014). Small pressure increases cause the most favorably oriented preexisting faults to fail, whereas higher pore pressure perturbations are required to cause failure of less favorably oriented faults (Block et al., 2015). Hence, the absolute pore pressure value is an important parameter controlling the induced seismicity, with higher pressures leading to failure of a greater number of faults.

The relative value of pressure compared to historical values also influences the occurrence of the induced seismicity. For example, seismicity rates within 5 km of the well decreased 72% following a three-month injection well shut-in and associated decrease in near-well pore pressures in early 2013 (Block, 2017). Although modeled pore pressures were increasing in all areas by late 2013 and the absolute pressures were high compared to pre-injection hydrostatic values, the near-well seismicity rate did not rebound until late 2015-early 2016, when modeled pore pressures in much of the near-well area exceeded their previous maximum values (Block, 2017). An example of this observation using our current flow model is presented in Figure 6-4. The pressure trends at seven locations 1.3 to 2.0 km from the well indicate that modeled pressures exceeded their previous maximum values between late 2014 and mid-2016, with most locations

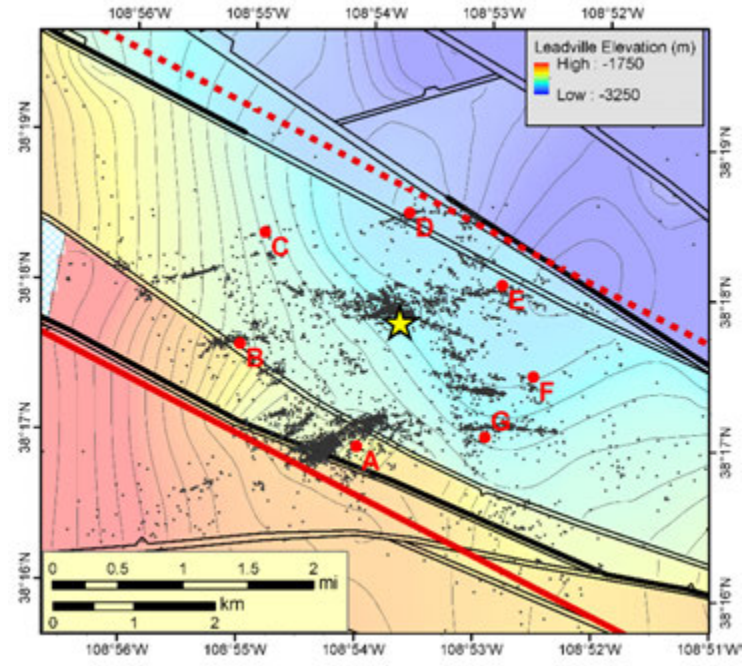

Figure 6-4: Pressure trends and induced seismicity rates in the near-well area following a three-month injection well shut-in and subsequent injection at a 10% reduced flow rate (2013-2016). The pressures were computed at seven locations, shown in the map to the left. The pressure trends over time at these locations, normalized by their peak values in early 2013, are shown below. The blue columns in the lower plot indicate the quarterly numbers of induced earthquakes with $M_D \geq 0.5$ between 1 and 3 km from the injection well (and between the two flow boundaries indicated by the red lines on the map to the left). The red line in the lower plot is a running 9-month average of the quarterly seismicity rates.

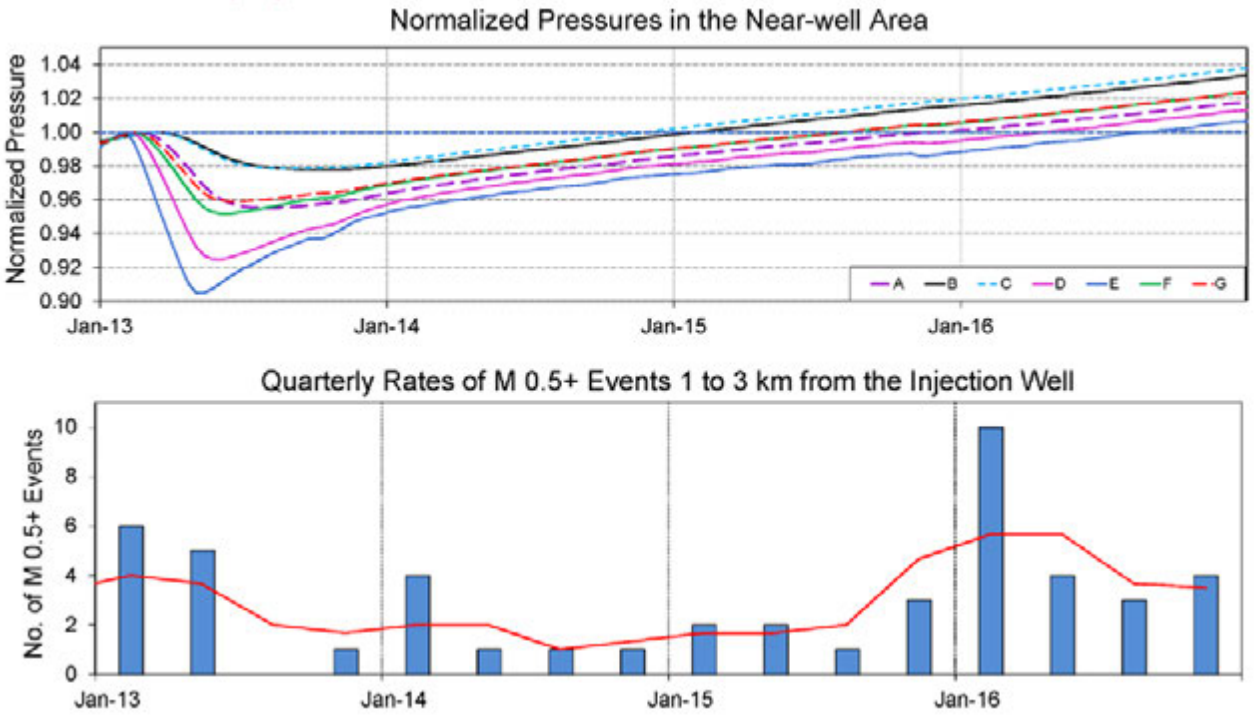

reaching their previous maximum values after mid-2015. Seismicity rates between 1 and 3 km from the well (and between our two modeled flow boundaries) rebounded in late 2015 to early 2016. This condition, in which seismicity does not resume until previously-experienced stress conditions are exceeded, is known as the Kaiser Effect and is an important consideration in cases of induced seismicity (Wenzel, 2017). It reflects the long time scales needed to reload faults with tectonic stress compared to the relatively short time scales under which induced seismicity occurs (Wenzel, 2017).

Published models of induced seismicity relate seismicity rates to temporal pore pressure gradients (Dempsey and Riffault, 2019; Langenbruch et al., 2018; Wenzel, 2017). In these models, larger temporal pressure gradients (faster changes in pore pressure) predict higher induced seismicity rates, whereas lower temporal pressure gradients are associated with lower seismicity rates. The observed near-well seismicity rates and pressure trends are broadly consistent with these models. Seismicity rates within 5 km of the well were their highest prior to mid-2000, when temporal pressure gradients were the highest. The average temporal pressure gradients in the near-well area have generally decreased over time as flow rates have been reduced (Figure 6-2), and near-well seismicity rates have also generally decreased over time (Figure 5-4). However, this trend is also limited by the Kaiser Effect. As discussed above, observed seismicity rates following extended injection well shut-ins do not immediately rebound when temporal pressure gradients increase but appear to also be dependent on the pressure values recovering and exceeding their previous maximum values.

The spatial pore pressure gradient may influence the probability of generating larger magnitude induced earthquakes. Some studies have proposed that pore pressure increasing with a low spatial gradient is a causal mechanism for the occurrence of large-magnitude induced events following injection well shut-ins (Baisch et al., 2009; Mukuhira et al., 2016). This is based on the interpretation that when spatial pressure gradients are relatively high, portions of fault planes reach critical conditions and fail while remaining portions of the fault plane have not yet reached critical conditions and thus remain locked. This results in small- to moderate-sized earthquakes. In contrast, when spatial pressure gradients are low, larger portions of fault planes reach critical conditions simultaneously, resulting in larger earthquakes. As flow rates have decreased over the history of PVU injection, spatial pressure gradients within a few km of the well have generally decreased, as demonstrated in Figure 6-2. Previous studies of the magnitude distribution of near-well PVU-induced seismicity have also indicated that the near-well seismicity induced early during brine disposal contained a relatively small fraction of larger-magnitude events, whereas seismicity induced at later times contained a somewhat larger fraction of larger-magnitude events (Block and Wood, 2009; Wood et al., 2016). This is quantified as a decrease in the b-value of the Gutenberg-Richter magnitude relation: $\log_{10}(\text{number of earthquakes with magnitude} \geq M) = a - bM$, where a and b are constants (Gutenberg and Richter, 1954). In addition, larger-magnitude earthquakes induced within a few km of the PVU injection well preferentially occur near the edges of the stimulated region (as defined by the seismicity), where spatial pressure gradients are expected to be relatively low (Figure 2-1).

To better evaluate whether variations in the b-value for PVU-induced seismicity may be related to variations in the spatial pressure gradients, we computed the maximum absolute horizontal pressure gradient at the time and location of each earthquake within 4 km of the PVU injection

well, within the area bounded by the two parallel impermeable faults used in our model (Figure 6-1). (Pressures outside the fault boundaries cannot be computed using the analytical solution and the method of image wells.) All earthquakes recorded from the start of injection in 1991 to the time of occurrence of the March 2019 M_W 4.5 earthquake are included. (Aftershocks of the M_W 4.5 earthquake are excluded.) A wide range of spatial pressure gradients is observed, from close to zero to thousands of psi per km (Figure 6-5). We then plotted the magnitude distributions of the events that occurred at low, medium, and high spatial pressure gradients (Figure 6-6). Only events with magnitude $\geq M_D$ 0.5, the historical magnitude completeness threshold, are included in the magnitude distributions. The results indicate that higher b-values are correlated with higher spatial pressure gradients. That is, when the spatial pressure gradient is high, the magnitude distribution contains a relatively low fraction of larger-magnitude events (corresponding to relatively high b-value), and conversely when the spatial pressure gradient is low, the magnitude distribution contains a relatively high fraction of larger-magnitude events (corresponding to relatively low b-value). These observations do not definitely indicate that low spatial pressure gradients influence the occurrence of larger-magnitude earthquakes, as both the spatial gradients and b-values could be changing over time in response to one or more other parameters, but the observations are at least consistent with the hypothesis proposed by others that low spatial pressure gradients contribute to the occurrence of larger-magnitude induced earthquakes.

The occurrence of the M_W 4.5 earthquake 1.6 km from the well in March 2019 was the first increase in the observed maximum earthquake magnitude in the near-well area (within 5 km of the injection well) for almost 19 years. The previous near-well maximum magnitude earthquake was the M_W 3.8 earthquake of May 2000, 2.2 km southwest of the well (Figure 2-1). As discussed in the previous section, pore pressures were increasing very slowly but almost continuously for nearly six years prior to the occurrence of the M_W 4.5 earthquake, and the spatial pressure gradient at this location was consistently low (Figure 6-2). Prior to 2013, when the biennial injection well shut-ins were eliminated, pressures at this location decreased twice a year and spatial pressure gradients were higher. These changes in the temporal and spatial trends of pressure in the years preceding the March 2019 M_W 4.5 earthquake could have potentially contributed to its occurrence. As discussed above, similar pressure trends have been cited by others as contributing to the occurrence of large magnitude induced earthquakes at other injection sites.

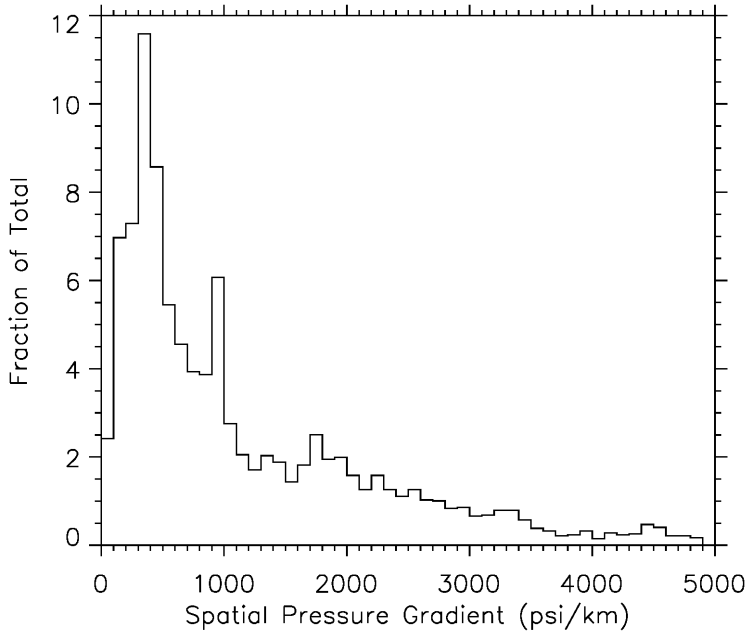

Figure 6-5: Histogram of maximum absolute horizontal pressure gradients computed with the analytical flow model at the times and locations of earthquakes induced within 4 km of the injection well and between the two parallel flow boundaries used in the model. This data set includes 4677 events recorded from the beginning of injection in 1991 to the time of occurrence of the M_W 4.5 earthquake on March 4th, 2019. The median spatial pressure gradient is 794 psi/km.

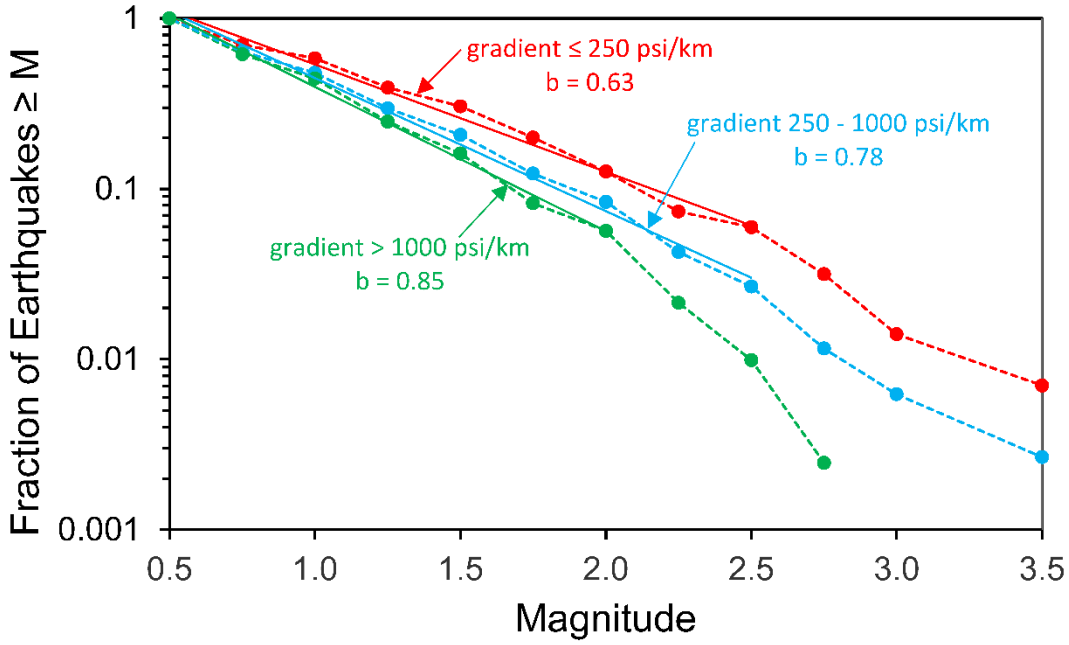

Figure 6-6: Magnitude distributions of induced earthquakes occurring within 4 km of the PVU injection well (between the two flow boundaries used in the flow model, Figure 6-1), for corresponding spatial pressure gradients of: ≤ 250 psi/km (red; 576 events), 250 to 1000 psi/km (blue; 1929 events), and > 1000 psi/km (green; 2084 events). Only earthquakes with $M_D \geq 0.5$, the historical magnitude completeness threshold, are included, and the magnitude distributions are normalized by the number of earthquakes in each data set for easier comparison of their trends.

6.3 Mitigation Strategies Based on Pressures

Both high pressure values and high temporal pressure gradients (pressures changing quickly over time) can contribute to higher rates of induced seismicity. At least for seismicity induced within ~5 km of the PVU injection well, the influence of both these parameters appears to be limited by the Kaiser Effect, with the seismicity rates being relatively low if pore pressures remain below their previous maximum values. Hence, one mitigation strategy would be to maintain pore pressures below their previous maximum values. This cannot be accomplished for all regions, as pore pressures more than several km from the well will continue increasing for months to years regardless of whether any additional fluid is injected into the well. However, three of the four largest PVU-induced earthquakes have occurred in a relatively small region 1.6 to 2.2 km southwest of the injection well (Figure 2-1). Keeping pressures reduced in this region should decrease the probability of occurrence of another large-magnitude event in that area.

Pressures within a few km of the injection well can be maintained below their previous maximum values by decreasing the average flow rate, either through a low continuous flow rate, or by alternating higher flow rates with periodic injection well shut-ins. Previous modeling has indicated that the first method is more efficient in terms of minimizing pressure increase at the well per unit volume of fluid injected (Wood et al., 2016). Here we evaluate the differences in the two approaches in terms of the pressure trends at the location of the *MW* 4.5 earthquake.

Using the analytical flow model with the two flow boundaries described previously, we compute pressure trends at the location of the *MW* 4.5 earthquake for four injection scenarios. For all scenarios, injection is assumed to resume on 2/1/2020 and continue until 12/31/2025, when a permanent shut-down of the PVU injection well is assumed. For two of the models, injection is continuous with no shut-ins. For one of these models, we use a rate of 60% of the injection rate that was being used prior to the shut-in of the well in March 2019. This 60% rate corresponds to 100 gpm, which could be achieved by operating a single injection pump with a 2-inch diameter plunger. For the second model, we use a rate of 69% of the pre-March 2019 rate, which corresponds to 115 gpm and could be achieved by operating a single injection pump with a 2 1/8-inch diameter plunger. For the remaining two models, we assume that the same total volume of fluid is injected from February 2020 to December 2025 as in the first two models, but that an extended annual injection well shut-in is implemented each spring. These models are motivated by a hydrological study performed by the U. S. Geological Survey. This study indicates that PVU salinity control benefits are substantially decreased during the period of high flow in the Dolores River that normally occurs each spring (Mast and Terry, 2019). Based on mean daily stream flow data from the USGS stream gauge near Bedrock, CO, the high flow typically occurs from March to June (Figure 6-7). The mean of the daily stream flow values from 1985 to 2019 indicate that, on average, stream flow exceeds 200 ft^3/s for 106 days per year, from March 19th through July 2nd (Figure 6-7). For the second two models, we assume that the injection well is shut in for this time period each year. We could have chosen a higher stream flow threshold value and assumed a shorter injection well shut-in. We chose a relatively long shut-in period for this analysis, corresponding to a relatively low stream flow threshold, so that we can evaluate the maximum differences between the continuous flow models and the models with annual shut-ins. Models with shorter annual shut-ins would have less deviation from the continuous flow models than the results shown here. The flow rates for the models with the annual shut-ins are increased

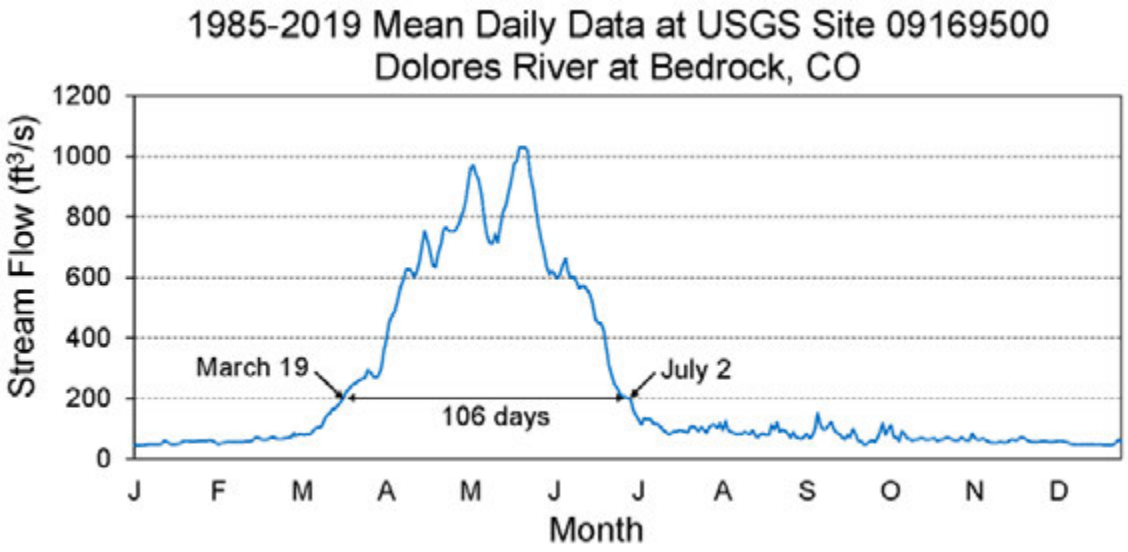

Figure 6-7: Mean daily stream flow measurements from the USGS stream gauge on the Dolores River at Bedrock, Colorado. Data from 1985 to 2019 are included in the means. Data were downloaded from https://waterdata.usgs.gov/ on 12/7/2019. The dates marked indicate the date range during which the mean daily flow is greater than 200 ft^3/s.

to 141.7 gpm and 163 gpm for the 60% rate and 69% rate scenarios, respectively, so that the total injected volume remains the same as for the continuous flow models.

Pressure trends computed for the 60% rate continuous flow and annual shut-in models at the location of the M_W 4.5 earthquake are compared in Figure 6-8, and results for the 69% rate models are compared in Figure 6-9. The pressures and temporal and spatial pressure gradients change very slowly for the continuous-flow scenarios (solid curves in plots) and fluctuate for the scenarios with the annual shut-ins (dashed curves). However, all models indicate relatively low pressures, compared to the high pressures experienced just prior to the M_W 4.5 earthquake. Pressures remain ~600 to ~950 psi below the March 2019 maximum. For the continuous flow 60% scenario, the temporal pressure gradient is about -0.1 to -0.15 psi/day, as the pressure continues to slowly decrease under this low flow rate. The pressure is nearly constant for the 69% continuous flow scenario, with the temporal pressure gradient varying between ~ -0.06 and ~ +0.10 psi/day. For the annual shut-in models, pressures annually increase and decrease, with temporal gradients ranging from about -1.5 psi/day to +0.8 psi/day. These models indicate positive temporal gradients, or pressures increasing, 56-58% of the time, and negative gradients corresponding to decreasing pressures 42-44% of the time. The maximum rate of pressure increase (0.8 psi/day) is comparable to the maximum rate experienced prior to 2013 when biennial 20-day shut-ins occurred (~0.9 psi/day, Figure 6-2).

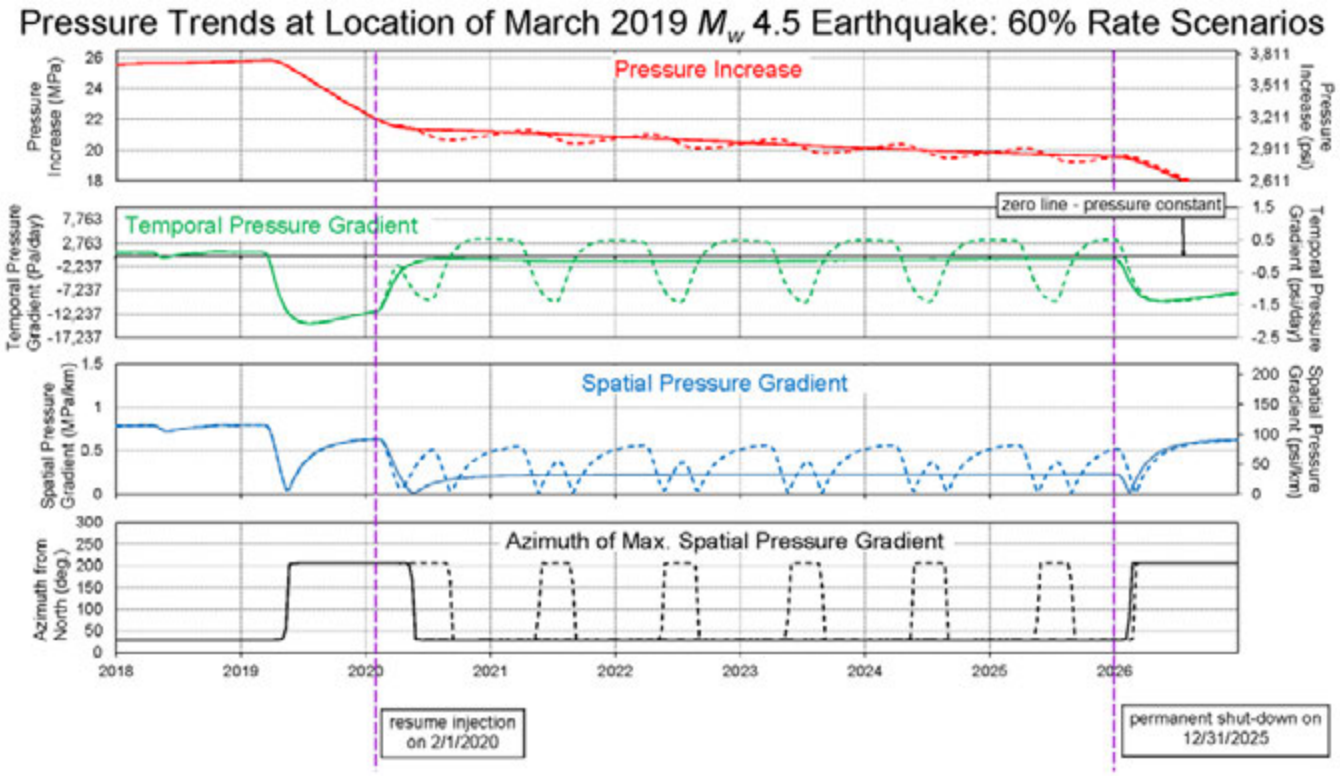

Figure 6-8: Pressure trends at the location of the March 4th, 2019 M_W 4.5 earthquake from 2018 to 2026 for the 60% rate continuous flow scenario (solid lines) and the 60% rate annual shut-in scenario (dashed curves): pore pressure increase (above pre-injection hydrostatic, upper plot); temporal pressure gradient (pressure change per day, with increases in pressure corresponding to positive gradients and decreases in pressures corresponding to negative gradients, second plot); maximum absolute horizontal spatial pressure gradient (maximum pressure change per horizontal km regardless of azimuth, third plot), and azimuth from North of maximum absolute horizontal pressure gradient (direction from lower to higher pressure, lower plot).

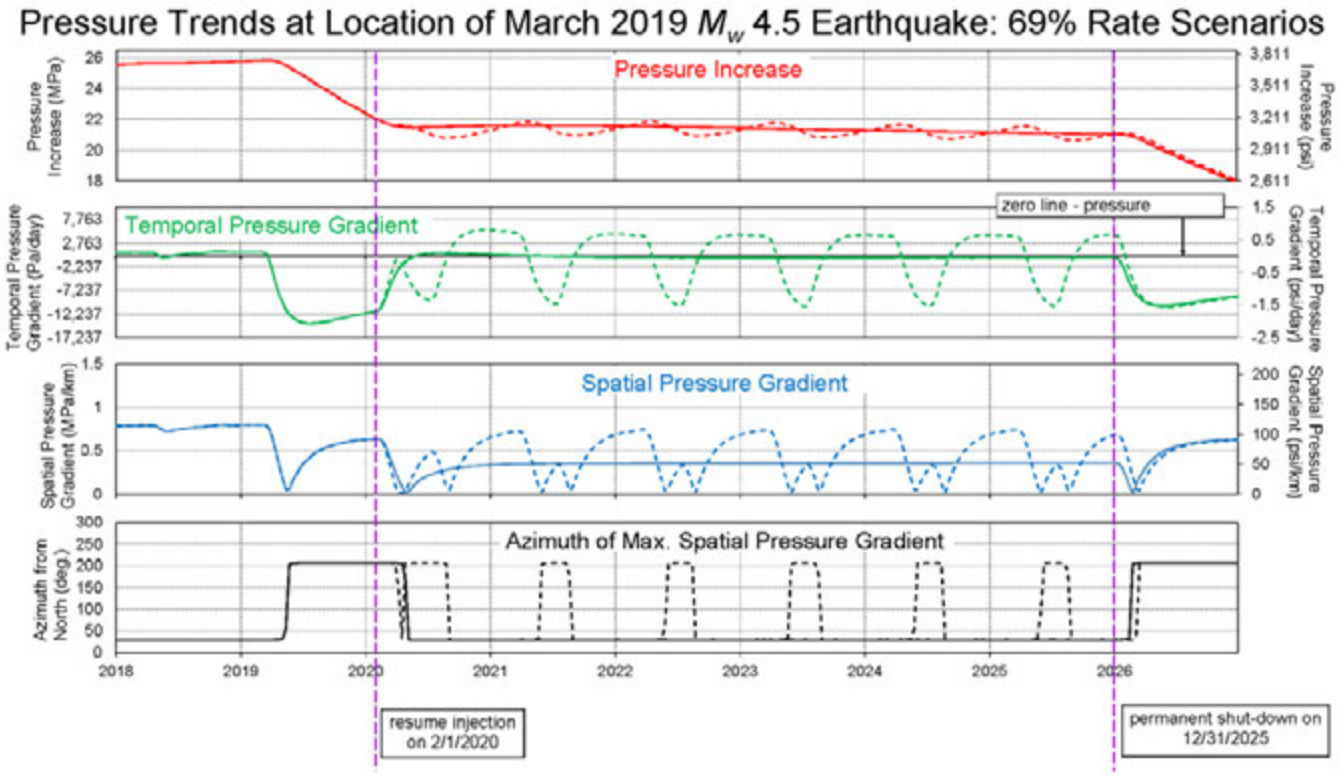

Figure 6-9: Pressure trends at the location of the March 4th, 2019 M_W 4.5 earthquake from 2018 to 2026 for the 69% rate continuous flow scenario (solid lines) and the 69% rate annual shut-in scenario (dashed curves): pore pressure increase (above pre-injection hydrostatic, upper plot); temporal pressure gradient (pressure change per day, with increases in pressure corresponding to positive gradients and decreases in pressures corresponding to negative gradients, second plot); maximum absolute horizontal spatial pressure gradient (maximum pressure change per horizontal km regardless of azimuth, third plot), and azimuth from North of maximum absolute horizontal pressure gradient (direction from lower to higher pressure, lower plot).

The differences in pressures from the continuous flow and annual shut-in scenarios over time are presented in Figure 6-10. The models with annual shut-ins indicate higher pressures than the continuous flow models 36% of the time (during the period from February 2020 to December 2025) and lower pressures than the continuous flow models 64% of the time. The pressure differences range from -110 psi to +58 psi. To put this in perspective, these differences are roughly 2% to 4% of the total pressure increase above pre-injection hydrostatic conditions, or only about 0.6% to 1.2% of the total pore pressure.

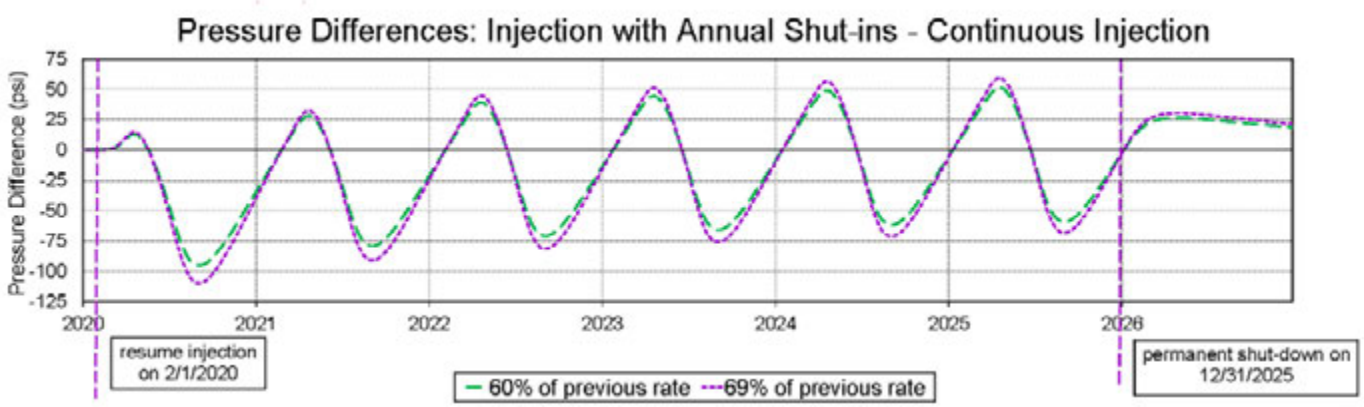

Figure 6-10: Pressures for the annual shut-in scenarios minus pressures for the continuous flow scenarios: 60% rate models (green long-dashed curve) and 69% rate models (purple short-dashed curve).

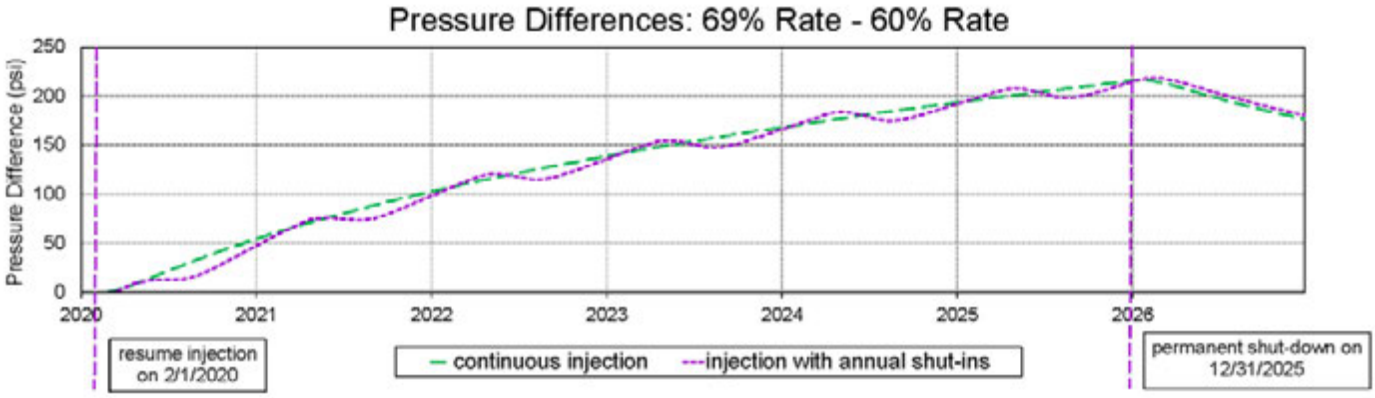

Figure 6-11: Pressures for the 69% rate scenarios minus pressures for the 60% rate scenarios: continuous flow models (green long-dashed curve) and annual shut-in models (purple short-dashed curve).

The differences in pressures over time between the 69% rate models and the 60% rate models are presented in Figure 6-11. The differences in pressures between these models increase with time and reach a maximum difference of 216-218 psi in early 2026 just after the injection well is shut down. This pressure difference represents ~7% of the total pressure increase above hydrostatic, or ~2% of the total pore pressure. This pressure difference is not due to pressures increasing over time in the 69% rate models, but rather is due to pressures in the 69% rate models being about constant over time, while pressures in the 60% rate models gradually decrease over time.

The spatial pressure gradients for the continuous flow models are very low, ~33 psi/km for the 60% rate model and ~52 psi/km for the 69% rate model (Figure 6-8 and Figure 6-9, blue curves). These values are 71% and 55% lower (for the 60% and 69% rate models, respectively) than the spatial pressure gradient at the time of the M_W 4.5 earthquake. Recall that the spatial gradient at

the time of this earthquake, 115 psi/km, was also low compared to historical trends (section 6.1). Hence, under these scenarios, large areas will be experiencing nearly identical pore pressure changes simultaneously, even more so than at the time of the M_W 4.5 earthquake. For the scenarios that include annual shut-ins, the spatial pressure gradients fluctuate, with the direction of the spatial gradient reversing every year (Figure 6-8 and Figure 6-9, lower plots). The maximum absolute horizontal spatial gradients range from 0 at the time that the direction of the gradient reverses to ~82 psi/km for the 60% rate model and ~107 psi/km for the 69% rate model. Hence, the maximum spatial pressure gradients in these models are 29% (60% rate model) and 7% (69% rate model) less than that at the time of the M_W 4.5 earthquake.

These models likely underestimate the pore pressures that would occur under each injection scenario. These models are based on porous media fluid flow and assume that reservoir characteristics, such as permeability, are static. In reality, because the permeability in the primary target injection formation, the Leadville, is influenced by the presence of fractures, the permeability is pressure-sensitive. Under lower pressures, some fractures may close and decrease permeability. This would result in observed pressures being higher than those predicted by the constant-permeability models. Hence, the models presented here should be considered best-case scenarios rather than conservative models.

Regardless of the injection protocol used, if pressures are maintained below their previous maximum values within a few km of the injection well, near-well seismicity rates should remain relatively low. In the past, increases in observed seismicity rates have been used as an indication that the probability of a larger-magnitude earthquake was increasing. For example, this observation contributed to the decision to shut in the injection well for a few weeks and subsequently decrease the flow rate in early 2017. Since near-well seismicity rates appear to have rebounded in the past when pore pressures reached or exceeded their previous maximum values (Figure 6-4; also see Block (2017)), monitoring seismicity rates was an indirect, approximate means of monitoring pressures. If the goal were to maintain pressures below their previous maximum values, such observations could no longer be used as the primary means of gauging subsurface conditions and making operational decisions, since near-well pressures and seismicity rates should always remain relatively low. Project managers would need to depend on models to evaluate pressure trends and make any necessary changes in operations to keep pressures below their previous maximum values, prior to any occurrence of an increase in the seismicity rate.

Keeping pressures decreased within a few km of the injection well would only decrease the probability of a large-magnitude near-well induced earthquake, not totally preclude such an occurrence. The possibility of a large induced near-well earthquake would still exist. In addition, pressures would continue to increase at greater distances (> ~5 km) from the well, and hence the rate of the distant seismicity would be expected to increase, along with the increased probability of felt earthquakes far from the well.

7 Conclusions

The widely felt earthquake that occurred near the PVU injection well on March 4th, 2019, at 17:22:52 UTC time (10:22:52 am local time), was induced by PVU brine injection. It is the largest PVU-induced earthquake to date, with a moment magnitude of M_W 4.5 (as reported by the University of Utah and U.S. Geological Survey). The earthquake's epicenter is 1.6 km southwest of the PVU injection well, at a location that has experienced induced seismicity since 1998. The depth of the earthquake is 3.9 km, consistent with the depths of previously induced events in this area and with the depths of injection target formations.

No increase in the rates or maximum magnitudes of earthquakes in the vicinity of the M_W 4.5 earthquake, or anywhere within 10 km of the injection well, was observed during the year preceding the main shock. Rather, seismicity rates had recently decreased, with rates decreasing 69% within 5 km of the injection well and 32% at distances of 5-10 from the well from 2017 to 2018. Seismicity rates remained low during the first two months of 2019, until the time of the M_W 4.5 earthquake on March 4th.

More than 2000 aftershocks were recorded between the time of the main shock and the end of August 2019. Six of these aftershocks have duration magnitude $\geq M_D$ 2.5, large enough to be potentially felt within Paradox Valley. The largest aftershock was an M_D 3.0 (M_W 2.5) earthquake that occurred on April 18th. Aftershocks have occurred as far as 1.7 km from the fault plane that ruptured during the March 4th main shock, indicating that the fault plane rupture altered stress conditions over a wide area. Aftershocks are expected to continue for years, at gradually decreasing rates.

Although the large number of aftershocks increased near-well seismicity rates to their highest levels in 20 years, analyses indicate that the occurrence of these events can be attributed solely to stress re-distribution from the fault plane rupture that occurred during the M_W 4.5 earthquake. The high seismicity rates do not appear to indicate any other change in reservoir conditions, such as a breach of the confining layer. The temporal decay rate of the aftershocks is consistent with the modified Omori aftershock relation, with a mean p value of 0.88. Modeled Coulomb stress change from the main shock fault rupture is generally consistent with the observed spatial pattern of aftershock distribution, particularly for those models with fault planes narrower than defined by the main aftershock distribution.

The rupture that produced this earthquake occurred on a fault striking ~N58°E and dipping 60° to 65° southeast. A fault zone consistent with the main shock focal mechanism is delineated by some of the aftershocks. This zone is approximately 1.3 to 1.6 km in length, with a vertical height of ~1 km and an along-dip height of ~1.15 km. This approximate rupture plane extends from near the top of the primary target injection formation, the Leadville, into the Precambrian basement. It should be noted, however, that based on the results of the Coulomb stress modeling, it is possible that the rupture plane of the March 2019 earthquake is smaller than the area defined by these aftershocks. Other aftershocks delineate a shallower, more steeply dipping (~78-80°) fault zone that extends upward from the Leadville formation to just above the Paradox salt, which is the confining layer for PVU injection. (The Paradox salt layer itself is largely aseismic, due to its near-isotropic stress conditions.) This shallower aftershock zone may represent either

an extension of the main shock rupture to shallower depths or slip on one or more steeply dipping faults due to stress redistribution following the main shock fault rupture. The main shock fault rupture appears to be bounded to the west by a major NW-trending fault that has been previously interpreted as forming a barrier to fluid flow and pore pressure diffusion from PVU injection.

Although the analyses completed to date do not definitively indicate whether the fault plane of the M_W 4.5 earthquake ruptured through the Paradox salt confining layer, they do provide evidence that the Paradox salt is acting as an effective confining layer for PVU injection. Aftershocks in the Leadville and deeper formations show distinctly different magnitude distributions, maximum magnitudes, and decay rates than the aftershocks occurring just above the Paradox salt confining layer. The Gutenberg-Richter b-value of the deep aftershocks is ~0.6, compare to a b-value of ~0.9 for the shallower aftershocks, indicating that the deep aftershock distribution contains a substantially bigger fraction of larger-magnitude events than the shallow aftershock distribution. In addition, the maximum magnitude of the deep aftershocks through August 2019 is M_D 3.0, whereas the corresponding maximum magnitude of the aftershocks above the Paradox salt is only M_D 1.8. Most of the aftershocks with $M_D \geq$ 1.5 occur below the interpreted bottom of the Paradox salt confining layer. The largest aftershocks preferentially occur within the Leadville formation and upper Precambrian, potentially due to increased pore pressures within these target injection formations. Omori aftershock relation p values of 0.88-0.95 and 0.69-0.77 were obtained from analyses of the deep and shallow aftershocks, respectively, indicating that the deep aftershock rate is decreasing faster than the shallow aftershock rate. In addition, the rate of decay of the deep aftershocks appears to be accelerating, with deep aftershocks decaying faster from August 2019 to February 2020 than previously predicted. This increased decay rate is likely related to decreasing pore pressures below the Paradox salt confining layer since injection ceased in March 2019. The shallow aftershock rate does not show a similar pattern, suggesting that the region above the Paradox salt is not experiencing substantial pore pressure changes. The different magnitude distributions and decay rates of the aftershocks above and below the Paradox salt indicate that these regions have substantially different stress and pressure regimes, as would be expected if the Paradox salt is acting as an effective injection confining layer.

There is little recorded historical seismicity over much of the fault plane that ruptured on March 4th 2019. Some previous seismicity occurred near the top of the rupture zone, within and above the Leadville formation. This includes the fourth largest PVU-induced earthquake, which had a magnitude of M_W 3.6 and occurred in November 2004. The focal mechanism of that event is very similar to the mechanism of the March 2019 M_W 4.5 earthquake and may have occurred on a shallower segment of the same fault plane. However, most of the previous earthquakes occurred on steeper-dipping fault planes than the one on which the M_W 4.5 hypocenter occurred. In addition, there are very few historical earthquakes near the lower ~two-thirds of the rupture plane of the M_W 4.5 earthquake.

Based on an analytical flow model, the pore pressure at the time and hypocenter location of the March 2019 M_W 4.5 earthquake was ~3750 psi above the pre-injection hydrostatic level, which corresponds to ~162% of the pre-injection pressure. Operational changes implemented in early 2017, which included a ~one-month shut-in and subsequent 5% decrease in flow rate, had caused

pore pressure in this area to temporarily decrease. The pressure had just recovered from these changes and was at its maximum value at the time of the *Mw* 4.5 earthquake. By the end of October 2019, pore pressure at this location had declined by approximately 385 psi, to ~156% of its pre-injection value.

Prior to 2013, the pore pressure at the location of the March 2019 earthquake decreased twice a year in response to biennial 20-day injection well shut-ins. Since 2013, when these extended biennial shut-ins were replaced with much shorter weekly shut-ins, the pore pressure at this location has been increasing very slowly but almost continuously (except for a relatively brief period following the 2017 injection well shut-in). In addition, spatial pressure gradients have decreased over time as average PVU injection flow rates have been reduced. Hence, at the time of the *Mw* 4.5 earthquake, pore pressure had been increasing mostly uninterrupted for nearly 6 years, and relatively large areas were experiencing similar pressure increases because spatial pressure gradients were low. The same pressure trends have been cited by others as contributing to the occurrence of large magnitude induced earthquakes following injection well shut-ins and could potentially have contributed to the occurrence of the *Mw* 4.5 earthquake.

Previous analyses of PVU-induced seismicity indicate that near-well seismicity rates decrease following operational changes, such as extended shut-ins of the injection well or decreases in injection rates. Pore pressure models suggest that the near-well seismicity rates increase again after pore pressures recover from these operational changes and begin to exceed their previous maximum values. This pattern, known as the Kaiser Effect, appears to be an important aspect of the seismicity induced by PVU fluid injection, at least within a few km of the injection well. Hence, keeping near-well pore pressures below their previous maximum values should reduce the probability of future large-magnitude induced earthquakes within ~4-5 km of the injection well. Because spatial pressure gradients have decreased over time, keeping the pressures reduced may be more critical now than in the past if the probability of large induced earthquakes is to be decreased. However, no potential injection scenario could achieve this objective in all areas, because areas more than a few km from the PVU injection well will experience increasing pressures for several years, even if no additional fluid is injected.

Some examples of injection scenarios that maintain pore pressures below their previous maximum values at the location of the March 2019 *Mw* 4.5 are presented in this report. These scenarios use injection rates of 60-69% of the rate that was being used prior to March 2019. They yield predicted maximum pressures ~600-950 psi less than the previous maximum value at the location of the *Mw* 4.5 earthquake. Only pressures at the location of the *Mw* 4.5 earthquake were evaluated. Additional modeling would be required to evaluate pressure trends at other locations or to evaluate different injection scenarios.

8 References

Ake, J., Mahrer, K., O'Connell, D., and Block, L., 2005, Deep-injection and closely monitored induced seismicity at Paradox Valley, Colorado: *Bulletin of the Seismological Society of America*, v. 95, no. 2, p. 664-683.

Anderson, J. G., and Hough, S. E., 1984, A model for the shape of the fourier amplitude spectrum of acceleration at high frequencies: *Bulletin of the Seismological Society of America*, v. 74, no. 5, p. 1969-1993.

Anderson, J. G., and Humphrey, J. R., 1991, A Least Squares Method For Objective Determination of Earthquake Source Parameters: *Seismological Research Letters*, v. 62, no. 3-4, p. 201-209.

Andrews, D. J., 1986, Objective Determination of Source Parameters and Similarity of Earthquakes of Different Size, *Earthquake Source Mechanics*, American Geophysical Union, p. 259-267.

Arestad, J. F., 2016, *Paradox Valley Unit Seismic Data Interpretation Phase 2 Report*: Excel Geophysical Services and International Reservoir Technologies, Inc., Report to the Bureau of Reclamation, 62 pp.

Arestad, 2017, *Paradox Valley Unit 2D Phase 3 Seismic Report: Detailed Site Interpretation*: Excel Geophysical Services and International Reservoir Technologies, Inc., Report to the Bureau of Reclamation, 114 pp.

Baisch, S., Vörös, R., Rothert, E., Stang, H., Jung, R., and Schellschmidt, R., 2009, A numerical model for fluid injection induced seismicity at Soultz-sous-Forêts: *International Journal of Rock Mechanics and Mining Sciences*, p. 405-413.

Bath, M., 1965, Lateral inhomogeneities in the upper mantle: *Tectonophysics*, v. 2, no. 6, p. 483-514.

Block, L., and Wood, C., 2009, *Overview of PVU-Induced Seismicity from 1996 to 2009 and Implications for Future Injection Operations*: Technical Memorandum No. 86-68330-2009-22, Bureau of Reclamation, Denver, Colorado,16 pp.

Block, L., Yeck, W., King, V., Derouin, S., and Wood, C., 2012, *Review of Geologic Investigations and Injection Well Site Selection, Paradox Valley Unit, Colorado*: Technical Memorandum No. 86-68330-2012-27, Bureau of Reclamation, Denver, Colorado, 62 pp.

Block, L. V., 2017, *Trends of Induced Seismicity and Pressures Following the 2013 Change in Injection Operations at the Paradox Valley Unit, Colorado*: Technical Memorandum No. 85-833000-2017-10, Bureau of Reclamation, Denver, Colorado, 76 pp.

Block, L. V., Wood, C. K., Yeck, W. L., and King, V. M., 2014, The 24 January 2013 ML 4.4 Earthquake near Paradox, Colorado, and Its Relation to Deep Well Injection: *Seismological Research Letters*, v. 85, no. 3, p. 609-624.

Block, L. V., Wood, C. K., Yeck, W. L., and King, V. M., 2015, Induced seismicity constraints on subsurface geological structure, Paradox Valley, Colorado: *Geophysical Jounal International*, v. 200, p. 1172-1195.

Boore, D. M., 1986, The Effect of Finite Bandwidth on Seismic Scaling Relationships, *Earthquake Source Mechanics*, American Geophysical Union, p. 275-283.

Bremkamp, W., and Harr, C. L., 1988, *Area of Least Resistance to Fluid Movement and Pressure Rise, Paradox Valley Unit Salt Brine Injection Project, Bedrock, Colorado*: Report to the Bureau of Reclamation, 39 pp.

Brune, J. N., 1970, Tectonic Stress and the Spectra of Seismic Shear Waves from Earthquakes: *Journal of Geophysical Research*, v. 75, no. 26, p. 4997-5009.

Brune, J. N., 1971, Correction [to "Tectonic stress and the spectra, of seismic shear waves from earthquakes"]: *Journal of Geophysical Research*, v. 76, no. 20, p. 5002-5002.

Catalli, F., Meir, M.-A., and Wiemer, S., 2013, The role of Coulomb stress changes for injection-induced seismicity: The Basel enhanced geothermal system: *Geophyical Research Letters*, v. 40, p. 72-77.

Chung, D. H., and Bernreuter, D. L., 1981, Regional relationships among earthquake magnitude scales: *Reviews of Geophysics and Space Physics*, v. 19, no. 4, p. 649-663.

Cocco, M., and Rice, J. R., 2002, Pore pressure and poroelasticity effects in Coulomb stress analysis of earthquake interactions: *Journal of Geophysical Research*, v. 107, no. B2, p. ESE.2.1-ESE.2.17.

De Natale, G., Madariaga, R., Scarpa, R., and Zollo, A., 1987, Source parameter analysis from strong motion records of the Friuli, Italy, earthquake sequence (1976-1977): *Bulletin of the Seismological Society of America*, v. 77, no. 4, p. 1127-1146.

Dempsey, D., and Riffault, J., 2019, Response of Induced Seismicity to Injection Rate Reduction: Models of Delay, Decay, Quiescence, Recovery, and Oklahoma: *Water Resources Research*, v. 55, no. 1, p. 656-681.

Dieterich, J. H., 1994, A constitutive law for rate of earthquake production and its application to earthquake clustering: *Journal of Geophysical Research*, v. 99, p. 2601-2618.

Durand, V., Bouchon, M., Karabulut, H., Marsan, D., and Schmittbuhl, J., 2013, Link between Coulomb stress changes and seismic activation in the eastern Marmara sea after the 1999, Izmit (Turkey), earthquake: *Journal of Geophysical Research*, v. 188, p. 1-8.

Freed, A. M., and Lin, J., 2001, Delayed triggering of the 1999 Hector Mine earthquake by viscoelastic stress transfer: *Nature*, v. 411, no. 4, p. 180-183.

Gutenberg, B., and Richter, C. F., 1954, *Seismicity of the Earth and Associated Phenomena*, Princeton University Press, Princeton, New Jersey 310 pp.

Hainzl, S., and Marsan, D., 2008, Dependence of the Omori-Utsu law parameters on main shock magnitude: Observations and modeling: *Journal of Geophysical Research*, v. 113, no. B10309, p. 1-12.

Hanks, T. C., and Kanamori, H., 1979, A moment magnitude scale: *Journal of Geophysical Research: Solid Earth*, v. 84, no. B5, p. 2348-2350.

Harris, R., 1998, Introduction to special section: Stress triggers, stress shadows, and implications for seismic hazards: *Journal of Geophysical Research*, v. 103, p. 24347-24358.

Hough, S. E., and Anderson, J. G., 1988, High-frequency spectra observed at Anza, California: Implications for Q structure: *Bulletin of the Seismological Society of America,* v. 78, no. 2, p. 692-707.

Jaeger, J. C., 1969, *Elasticity, Fracture, and Flow with Engineering and Geological Applications*, Chapman & Hall, London, United Kingdom, 268 pp.

Kilb, D., Biasi, G., Anderson, J., Brune, J., Peng, Z., and Vernon, F. L., 2012, A Comparison of Spectral Parameter Kappa from Small and Moderate Earthquakes Using Southern California ANZA Seismic Network Data: *Bulletin of the Seismological Society of America*, v. 102, no. 1, p. 284-300.

Kilb, D., Gomberg, J., and Bodin, P., 2002, Aftershock triggering by complete Coulomb stress change: *Journal of Geophysical Research*, v. 107, no. B4, p. ESE.2.1-ESE.2.8.

King, G. C. P., and Cocco, M., 2001, Fault interaction by elastic stress changes: New clues from earthquake sequences: *Advances in Geophysics*, v. 44, p. 1-38.

King, G. C. P., Hubert-Ferrari, A., Nalbant, S. S., Meyer, B., Armijo, R., and Bowman, D., 2001, Coulomb interactions and the 17 August 1999 Izmit, Turkey earthquake: *Earth and Planetary Sciences*, v. 333, p. 557-569.

King, G. C. P., Stein, R. S., and Lin, J., 1994, Static Stress Changes and the Triggering of Earthquakes: *Bulletin of the Seismological Society of America*, v. 84, p. 935-953.

King, V. M., Block, L. V., Yeck, W. L., Wood, C. K., and Derouin, S. A., 2014, Geological structure of the Paradox Valley Region, Colorado, and relationship to seismicity induced by deep well injection: *Journal of Geophysical Research: Solid Earth*, v. 119, p. 1-24.

King, V. M., Wood, C. K., and Block, L. V., 2018, *Integrated Subsurface Geologic Model, Paradox Valley, Colorado:* Technical Memorandum 85-833000-2017-15, Bureau of Reclamation, Denver, Colorado, 92 pp.

Langenbruch, C., Weingarten, M., and Zoback, M. D., 2018, Physics-based forecasting of man-made earthquake hazards in Oklahoma and Kansas: *Nature Communications*, p. 1-10.

Lee, W. H. K., and Stewart, S. W., 1981, *Principles and Applications of Microearthquake Networks*, Advances in Geophysics Series: Academic Press, New York , New York, 293 pp.

Lin, J., and Stein, R. S., 2003, Stress triggering in thrust and subduction earthquakes and stress interaction between the southern San Andreas and nearby thrust and strike-slip faults: *Journal of Geophysical Research*, v. 109, p. 1-19.

Ma, K.-F., Chan, C. H., and Stein, R. S., 2005, Response of seismicity to Coulomb stress triggers and shadows of the 1999 Mw + 7.6 Chi-Ci, Taiwan, earthquake: *Journal of Geophysical Research*, v. 110, no. B05S19, p. 1-16.

Marsan, D., 2006, Can coseismic stress variability suppress seismicityshadows? Insights from a rate-and-state frictionmodel: *Journal of Geophysical Research*, v. 111, no. B06305, p. 1-11.

Mast, M. A., and Terry, N., 2019, *Controls on Spatial and Temporal Variations of Brine Discharge to the Dolores River in the Paradox Valley, Colorado, 2016-18*: Scientific Investigations Report 2019-5058, U. S. Geological Survey, Reston, Virginia, 25 pp.

Mukuhira, Y., Dinske, C., Asanuma, H., Ito, T., and Haring, M. O., 2016, Pore pressure behavior at the shut-in phase and causality of large induced seismicity at Basel, Switzerland: *Journal of Geophysical Research: Solid Earth*, p. 411-435.

Ogata, Y., 1983, Estimation of parameters in the modified Omori formula for aftershock frequencies by the maximum likelihood procedure: *Journal of Physics of the Earth*, v. 31, p. 115-124.

Ogata, Y., 2006, Statistical Analysis of Seismicity - Updated Version (SASeis2006): *Computer Science Monographs*, p. 31.

Qin, Y., Chen, X., Carpenter, B. M., and Kolawole, F., 2018, Coulomb stress transfer influences fault reactivation in areas of wastewater injection: *Geophysical Research Letters*, v. 45, no. 20, p. 11059-11067.

Richter, C. F., 1935, An instrumental earthquake magnitude scale: *Bulletin of the Seismological Society of America*, v. 25, no. 1, p. 1-32.

Shearer, P. M., Prieto, G. A., and Hauksson, E., 2006, Comprehensive analysis of earthquake source spectra in southern California: *Journal of Geophysical Research: Solid Earth*, v. 111, no. B6, 21 pp.

Snoke, J. A., 1987, Stable determination of (Brune) stress drops: *Bulletin of the Seismological Society of America*, v. 77, no. 2, p. 530-538.

Steacy, S., Gomberg, J., and Cocco, M., 2005, Introduction to special section: Stress transfer, earthquake triggering, and time-dependent seismic hazard: J*ournal of Geophysical Rsearch*, v. 110, no. B05S01, p. 1-12.

Stein, R. S., 1999, The role of stress transfer in earthquake occurrence: *Nature*, v. 402, p. 605-609.

Stein, R. S., Barka, A. A., and Dieterich, J. H., 1997, Progressive failure on the North Anatolian Fault since 1939 by earthquake stress triggering: *Geophysical Journal International*, v. 128, p. 594-604.

Stein, R. S., King, G. C. P., and Lin, J., 1992, Change in failure stress on the southern San Andreas fault system caused by the 1992 Magnitude = 7.4 Landers earthquake: *Science*, v. 258, p. 1328-1332.

Toda, S., Stein, R. S., Richards-Dinger, K., and Bozkurt, S. B., 2005, Forecasting the evolution of seismicity in southern California: Animations built on earthquake stress transfer: J*ournal of Geophysical Rsearch*, v. 11, no. B05S16, p. 1-17.

Utsu, T., 1961, A statistical study on the occurrence of aftershocks: *Geophysical Magazine*, v. 30, p. 521-605.

Utsu, T., Ogata, Y., and Matsu'ura, R. S., 1995, The Centenary of the Omori Formula for a Decay Lay of Aftershock Activity: *Journal of Physics of the Earth*, v. 43, p. 1-33.

Wang, H., Detournay, E., Dusseault, M., Fehler, M., and Frohlich, C., 2015, *Report from the Consultant Review Board On Paradox Valley Unit – MASIP / Induced Seismicity, Meeting No. 1, January 28-31, 2015, Grand Junction, Colorado*: report to the Bureau of Reclamation, 35 pp.

Wenzel, F., 2017, Fluid-induced seismicity: comparison of rate- and state- and critical pressure theory: *Geothermal Energy*, v. 5, no. 1, p. 1-16.

Wood, C. K., 2018, Automating the Efficient and Reliable Transfer of Geologic Fault Data for Probabilistic Seismic Hazard Analyses with a Custom ArcGIS Add-in, Dam Safety Technology Development Program: Bureau of Reclamation.

Wood, C. K., Block, L. V., King, V. M., and Yeck, W. L., 2016, *The ML 4.4 Earthquake of January 24, 2013, Near Paradox, Colorado, and Implications for Near-term Injection Operation*: Technical Memorandum 86-68330-2013-12, Bureau of Reclamation, Denver, Colorado, 150 pp.

Yeck, W., 2015, *Considerations in Raising the Maximum Allowable Surface Injection Pressure (MASIP) at Paradox Valley*: Technical Memorandum 86-68330-2014-45, Bureau of Reclamation. Denver, Colorado, 62 pp.

Appendix A

Relative Hypocenter Inversion Methods

Introduction

A mathematical description of the relative hypocenter-velocity inversion used to determine a high-resolution local three-dimensional (3-D) P-wave velocity structure in the vicinity of the fault plane of the March 2019 M_W 4.5 earthquake is provided in this appendix. The results of the inversion are presented and discussed in the main body of this report, section 3.2.

The relative hypocenter-velocity inversion is an extension of the inversion method that we have been using to compute precise relative hypocenters of the PVU-induced earthquakes for about the last 20 years. The relative hypocenter inversion method was summarized in Block et al (2015), although a detailed mathematical description was not provided. The mathematical formulation presented here for the relative hypocenter-velocity inversion also applies to the original relative hypocenter inversion, if velocities are assumed to remain fixed (i.e., velocity partial derivatives are set to zero). There are some differences in the data included in our application of the two inversion methods. Both P-wave and S-wave data are used in our standard relative hypocenter inversion, to obtain as many well-constrained relative hypocenters as possible. To simplify the relative hypocenter-velocity inversion employed to determine a local velocity structure in the immediate vicinity of the fault plane of the March 2019 M_W 4.5 earthquake, only P-wave data were included. This restriction also helped prevent artifacts in the local velocity model, which could be caused by unmodeled velocity variations in the regional S-wave velocity structure (which is less well-resolved than the regional P-wave velocity structure). There are also some differences in the data weighting schemes employed in application of these two methods to the PVSN data. These differences are noted in the descriptions given below.

The nonlinear relative hypocenter and hypocenter-velocity inversions are performed by iteratively solving the constrained linearized problem. Below we describe the procedure used to construct the set of arrival time difference data used in the inversions, the method used to solve the forward problem of computing arrival time differences from a given model, and the procedure used to solve the inverse problem to simultaneously determine relative hypocenters and (optionally) a local velocity structure.

Arrival Time Difference Data

In these relative hypocenter inversions, we use differences in the arrival times recorded at a given seismic station from pairs of nearby earthquakes. Precise time differences (Δts) are computed using time-domain cross-correlation between well-correlated waveform pairs. P-wave time differences are computed only from vertical-component data, while S-wave time differences are computed only from horizontal-component data. For the horizontal components, cross-correlations are performed between waveforms having the same orientation only (East or North), and no component rotation is performed. Prior to cross-correlation, the waveforms are filtered using a third-order Bessel bandpass filter with corner frequencies of 0.8 and 25 Hz for vertical-

component data and 0.6 and 15 Hz for horizontal-component data. The filter is applied in the forward and reverse directions for zero-phase filtering.

The waveforms in each pair are required to have been recorded with the same type of seismometer - for example, both recorded by analog short-period instrumentation or both recorded by a digital broadband seismometer. (See Block et al. (2020) for a history of the types of seismic instrumentation used in PVSN.) In earlier implementations of the relative hypocenter inversion, waveform pairs recorded with different types of instrumentation had been included. In those inversions, time shifts had been observed between different instrumentation types simultaneously deployed at the same site, and corrections had been determined and applied to all time difference data derived from waveform pairs between different instrumentation types. Sufficient data are now available from each instrumentation type to make inclusion of cross-correlations between waveforms from different instrumentation types unnecessary.

For each waveform pair, time differences are computed with three window lengths: 1.5 s, 1.0 s, and 0.5 s for P waves and 2.0 s, 1.5 s, and 1.0 s for S waves. The corresponding manually determined arrival time is used to position each window, with 25% of the window before the arrival time and 75% of the window after the arrival time. If an S-wave arrival time is available for an event and the end of the P-wave cross-correlation window is greater than the corresponding S-wave arrival time, then that window length is not used for the P-wave cross-correlation. If even the smallest window length is too long to end before the S-wave arrival time, then the P-wave cross-correlation window length is adjusted to end at the S-wave arrival time. The time difference corresponding to the maximum absolute cross-correlation value is identified for each window length. A minimum absolute cross-correlation coefficient of 0.7 is initially required to retain the time difference from a given window length.

In order to increase the accuracy of the time differences computed from the cross-correlations, each cross-correlation computation is performed in two steps. First, the cross-correlation is performed with the original waveform data over a relatively large range of lags (from -25% of the window length to +25% of the window length). Then the waveforms are resampled (by linear interpolation) at 50 times their original sample interval of 0.01 s, resulting in a new sampling interval of 0.0002 s, and the cross-correlation is repeated for a small range of lags (from -5 original sample intervals to +5 original sample intervals), around the lag value corresponding to the maximum absolute cross-correlation value from the first pass. This data resampling allows the accuracy of the computed arrival time differences to be less than the original sample interval of the recorded data. The final time difference corresponds to the lag of the maximum absolute cross-correlation value from this second pass.

In addition to the value of peak (or trough) of the cross-correlation function, two other parameters are computed and output as a measure of the quality of the cross-correlation function: the width of the cross-correlation peak (or trough) and the absolute value of the ratio the largest sidelobe to the main peak. The width of the cross-correlation peak (or trough) is measured as the time lag difference between the two points on either side of the cross-correlation peak where the cross-correlation function has half its peak value. To compute the sidelobe-to-main peak ratio, the four nearest peaks and troughs are examined (two on either side of the main peak), and the peak or trough with the largest absolute value is used to compute the ratio.

The time differences derived from the cross-correlations are subsequently post-processed to eliminate multiple time differences for a given waveform pair and to identify and eliminate time differences from poor quality cross-correlations. If a time difference is available from only one window length for a given waveform pair, then a minimum absolute cross-correlation coefficient of 0.8 is required. Time differences from single cross-correlations with absolute peak values less than this criterion are eliminated. If cross-correlations are available from multiple window lengths for a given waveform pair, then the absolute difference in Δts from the two cross-correlations having the highest absolute cross-correlation values is required to be less than 0.01 s. In addition, all cross-correlation functions are checked to ensure that the main peak is not extremely broad and that the sidelobes are not excessively large compared to the main peak. Time differences from cross-correlations whose peaks have widths > 0.5 s are rejected. Also, if the maximum absolute cross-correlation value is ≥ 0.75 and the absolute ratio of the largest sidelobe to the main peak of the cross-correlation function is ≥ 0.95, the time difference is eliminated. If the maximum absolute cross-correlation value is < 0.75, then time differences with ratios > 0.90 are eliminated. S-wave time differences from East-component waveforms and North-component waveforms are processed independently, and time differences from both East- and North-component data at the same station may be retained for the same event pair. Once this post-processing is complete, the quality of the data set used in the relative inversion is further improved by only including P-wave time differences from cross-correlations with peak absolute values ≥ 0.75 and S-wave time differences from cross-correlations with peak absolute values ≥ 0.7. The threshold is higher for P-waves than for S-waves because the P-wave cross-correlations appear to be more susceptible to error, such as from cycle-skipping, than the S-wave cross-correlations. (Much of the PVSN data used for the relative location inversions are provided by small-magnitude events, which may have small-magnitude and sometimes emergent P-wave arrivals at several stations.)

No absolute arrival times are directly included in the relative inversions. For the relative hypocenter inversion, time differences computed from absolute arrival times are included in the inversion for earthquakes with magnitude ≥ 3.0, to supplement the time differences from waveform cross-correlation. Many waveforms from these larger earthquakes are clipped and therefore do not produce good cross-correlations, especially for data recorded prior to about 2010, when short-period analog seismometers were still in use at most PVSN seismic stations. For earthquakes with magnitude ≥ 4.0, only times differences from absolute arrival times are used, because the different frequency content of the largest-magnitude earthquakes appears to degrade their cross-correlations with smaller-magnitude events. For the relative hypocenter-velocity inversion in the vicinity of the M_w 4.5 earthquake, we wanted to use only the most precise time difference data, and therefore no time differences from manual arrival time picks were included. (Time differences from manual arrival time picks are limited in their accuracy by the original sampling interval of the data and limited in their precision by subjectivity in manual picking).

Only earthquakes with fairly well-constrained hypocenters are included in the inversions. For relative hypocenter inversions of all PVU-induced earthquakes throughout the Paradox Valley area, hypocenters are retained in the inversion if they meet the following minimum criteria: time differences (either P-wave or S-wave) available from at least 6 stations; maximum azimuthal gap in time difference data ≤ 200°; and distance to the closest station having time difference data

divided by the event focal depth ≤ 3. (After the relative hypocenter inversions are complete, the events are typically post-processed, and stricter criteria, as well as additional criteria, are used to decide whether final individual relative hypocenters should be included in the relative event catalog.) For the hypocenter-velocity inversion in the vicinity of the M_w 4.5 earthquake, stricter inclusion criteria were used: P-wave time differences available from at least 6 stations; maximum azimuthal gap in time difference data ≤ 160°; and distance to the closest station having time difference data divided by the event focal depth ≤ 2. All hypocenter inclusion criteria are re-evaluated after each iteration of the inversion. Because each earthquake shares time difference data with several other events, every time an earthquake is eliminated, the criteria for all other events are re-evaluated.

The Forward Problem

The P-wave and S-wave velocity structures are represented by three-dimensional (3-D) rectangular grids of nodes. The velocity V at any point (X,Y,Z) is computed from the velocities at the eight nodes surrounding it by linear interpolation:

$$V(X,Y,Z) = \sum_{i=1}^{8} v_i \left(1 - \frac{|X - x_i|}{Dx}\right)\left(1 - \frac{|Y - y_i|}{Dy}\right)\left(1 - \frac{|Z - z_i|}{Dz}\right), \qquad \text{(B-1)}$$

where (x_i,y_i,z_i) are the coordinates of the i^{th} node and v_i is its velocity. The parameters Dx, Dy, and Dz are the distances in the x, y, and z directions between the velocity nodes immediately surrounding the point (X,Y,Z).

The ray bending method of Um and Thurber (1987), as modified by Block (1991), was used to compute ray paths and travel times. This method starts with a straight ray path defined by two endpoints and one midpoint (i.e., the ray path is broken into two equal segments). The midpoint of the ray path is iteratively perturbed until the travel time is minimized. Each of the two segments is then divided in half. Each of the points along the ray path (excluding the endpoints) is then iteratively perturbed until the travel time is minimized. The process of dividing ray path segments and iteratively perturbing the ray path points is repeated until convergence of the computed travel time is achieved.

The inverse Problem

Let dt_{obs} represent an observed arrival time difference (either P-wave or S-wave) between waveforms recorded at the same station from two earthquakes with hypocenters (t_1, x_1, y_1, z_1) and (t_2, x_2, y_2, z_2). Let T_1 and T_2 represent the corresponding calculated arrival times based on the current model and dt_{calc} represent their difference, $T_1 - T_2$. Let r represent the time difference residual based on the current model, $dt_{obs} - dt_{calc}$. The goal is to change the model parameters (hypocenters and velocities), and thereby dt_{calc}, so that the new residual, r', is zero:

$$r' = dt_{obs} - \left(dt_{calc} + \Delta dt_{calc} \right) = 0$$

or

$$\Delta dt_{calc} = dt_{obs} - dt_{calc} = r \, .$$

Expanding Δdt_{calc} in terms of changes in the model parameters and keeping only the first-order terms gives:

$$\begin{aligned} &\left(\frac{\partial T_1}{\partial t_1}\Delta t_1 + \frac{\partial T_1}{\partial x_1}\Delta x_1 + \frac{\partial T_1}{\partial y_1}\Delta y_1 + \frac{\partial T_1}{\partial z_1}\Delta z_1 + \sum_{j=1}^{nnodes} \frac{\partial T_1}{\partial v_j}\Delta v_j \right) \\ &-\left(\frac{\partial T_2}{\partial t_2}\Delta t_2 + \frac{\partial T_2}{\partial x_2}\Delta x_2 + \frac{\partial T_2}{\partial x_2}\Delta x_2 + \frac{\partial T_2}{\partial x_2}\Delta x_2 \sum_{j=1}^{nnodes} \frac{\partial T_2}{\partial v_j}\Delta v_j \right) = r \end{aligned} \qquad \text{(B-2)}$$

where v_j is the velocity of the j^{th} node.

The partial derivatives are computed analytically. The partial derivatives with respect to the hypocenter parameters are given by:

$$\frac{\partial T}{\partial t} = 1, \quad \frac{\partial T}{\partial x} = \frac{-1}{v(x,y,z)}\frac{dx}{ds}, \quad \frac{\partial T}{\partial y} = \frac{-1}{v(x,y,z)}\frac{dy}{ds}, \text{ and } \frac{\partial T}{\partial z} = \frac{-1}{v(x,y,z)}\frac{dz}{ds}, \qquad \text{(B-3)}$$

where *dx/ds*, *dy/ds*, and *dz/ds* are the direction cosines of the ray path at the hypocenter, and $v(x,y,z)$ is the velocity at the hypocenter. The hypocenter partial derivatives are computed independently for each of the two hypocenters, using their respective hypocenter coordinates. Prior to about 2000, relative hypocenter inversions were often performed using one set of hypocenter partial derivatives, either at the midpoint of event pairs or at the location of master events. Inversions of synthetic arrival time difference data having hypocenter distributions and station geometry consistent with the PVSN data yield unsatisfactory results with that approach. Using partial derivatives computed from the midpoints of the event pairs, the final hypocenters for each event pair are biased toward each other, with the net result that clusters of events are over-collapsed. That is, the final seismicity clusters are smaller than the actual clusters used to generate the synthetic time difference data. Because correlatable events recorded by PVSN occur over distances that are not negligible compared to event-station distances, it is necessary to compute hypocenter partial derivatives individually for each hypocenter within each event pair.

The partial derivatives with respect to the velocity nodes are computed by summing the contributions from all ray path segments. Given a ray path of *n* segments, each of length *ds*, the partial derivative of the arrival time with respect to the velocity at the j^{th} node is given by:

$$\frac{\partial T}{\partial v_j} = \sum_{k=1}^{n} \frac{-ds}{v\left(x_k, y_k, z_k\right)^2} \frac{\partial v\left(x_k, y_k, z_k\right)}{\partial v_j} \qquad \text{(B-4)}$$

where $v(x_k, y_k, z_k)$ is the velocity at the center of the k^{th} ray segment. For each ray path segment, $\partial v(x_k, y_k, z_k) / \partial v_j$ is only nonzero for the eight velocity nodes surrounding it and is found by differentiating equation B-1:

$$\frac{\partial v(x_k, y_k, z_k)}{\partial v_j} = \left(1 - \frac{|x_k - x_j|}{Dx}\right)\left(1 - \frac{|y_k - y_j|}{Dy}\right)\left(1 - \frac{|z_k - z_j|}{Dz}\right) . \qquad \text{(B-5)}$$

The velocity partial derivatives are constructed independently for each ray path in the waveform pair (i.e., for each event hypocenter, corresponding to arrival times T_1 and T_2) and may not necessarily have nonzero values for the same set of velocity nodes.

Equation B-2 is constructed for each time difference in the input data set, and all equations are organized into matrix form:

$$\mathbf{M\Delta m} = \mathbf{r} . \qquad \text{(B-6)}$$

The matrix **M** contains the partial derivatives of the arrival times with respect to the hypocenter parameters and node velocities, computed with equations B-3, B-4, and B-5. The vector **r** contains the time difference residuals (dt_{obs} - dt_{calc}). The solution vector **Δm** contains the changes in hypocenter parameters and velocities:

$$\mathbf{\Delta m} = \begin{bmatrix} \Delta t_1 \\ \Delta x_1 \\ \Delta y_1 \\ \Delta z_1 \\ \vdots \\ \Delta t_{nevents} \\ \Delta x_{nevents} \\ \Delta y_{nevents} \\ \Delta z_{nevents} \\ \Delta v_1 \\ \vdots \\ \Delta v_{nnodes} \end{bmatrix} , \qquad \text{(B-7)}$$

where *nevents* is the number of earthquake hypocenters that vary during the inversion, and *nnodes* is the number of velocity nodes that vary. Each row in equation B-7 is weighted by the absolute value of the peak cross-correlation coefficient corresponding to that time difference. In addition, time difference data that correspond to extremely large residuals are excluded from the inversion. The equations are also either down-weighted or eliminated based on the event separation distance for a given time difference. For the relative hypocenter inversion with a fixed velocity model, the distance criterion is based on the ratio of the event separation distance

divided by the distance from the event pair midpoint to the seismic station (which we refer to as the fractional event separation distance). Hence, larger event separations are allowed for larger event-station distances. This helps retain as much data as feasible to constrain the inversion (and retain as many hypocenters as possible), while eliminating data that may be strongly affected by unmodeled velocity variations along the ray paths. For a typical PVSN relative hypocenter inversion, P-wave data with fractional event separation distances above 0.2 are eliminated, while those with fractional separation distances above 0.03 are linearly down-weighted. For S-wave data, the elimination criterion is 0.15, while the criterion for down-weighting is also 0.03. These criteria were determined after examining final time difference residuals as a function of fractional event separation distance. For the relative hypocenter-velocity inversion in the vicinity of the March 2019 M_W 4.5 earthquake fault plane, the separation criterion was based on absolute event separation distances. This was done to restrict the data included in the inversion to only the data providing the most robust constraints. Only P-wave data were used in this inversion, and the maximum event separation distance allowed was 400 m. Data from event pairs with separation distances above 250 m were linearly down-weighted.

To prevent extreme fluctuations of velocities at poorly resolved nodes, velocity regularization is included in the inversion. The regularization is implemented by minimizing the first-order spatial velocity derivatives. The numerical velocity derivative for each consecutive pair of velocity nodes, in each coordinate direction, is set to zero:

$$\frac{(v_i + \Delta v_i) - (v_{i-1} + \Delta v_{i-1})}{D} = 0, \qquad \text{(B-8)}$$

where v_{i-1} and v_i are the velocities of two consecutive nodes in one coordinate direction, and D is the distance between the nodes. Equations for all consecutive nodes in the x, y, and z directions are constructed. If desired, a different amount of regularization, or smoothing, may be required in some coordinate directions than others by multiplying the corresponding equations by a constant factor. For example, the velocity model may be required to be more layered by weighting the regularization in the x and y directions more than the regularization in the z direction. The regularization may also be relaxed or broken across sets of velocity nodes to allow more abrupt velocity variations at specified locations. This would be accomplished by down-weighting the derivative equations across the desired velocity nodes or eliminating those derivative equations. To put these equations into matrix form, we first re-arrange the terms:

$$\frac{1}{D}\Delta v_i - \frac{1}{D}\Delta v_{i-1} = -\frac{(v_i - v_{i-1})}{D}. \qquad \text{(B-9)}$$

We can then put the equations for all velocity derivatives into a matrix equation:

$$\mathbf{V\Delta m = -v} \qquad \text{(B-10)}$$

The vector **v** contains the spatial velocity derivatives based on the current model. The matrix **V** contains the coefficients on the left-hand side of equation B-9, and the solution vector **Δm** contains the changes in node velocities ($\Delta v_1, \ldots, \Delta v_{nnodes}$).

Absolute hypocenters are not constrained by time difference data alone. While the hypocenters relative to each other are constrained, the entire set of hypocenters can shift in space and time without any additional constraints. In addition, the distances between clusters of hypocenters may trade off with velocities. Unmodeled spatial variations in velocities can cause clusters of hypocenters to shift during a relative hypocenter inversion, especially when the velocity structure is fixed. We use one of two methods to constrain the relative inversions. In the relative hypocenter inversion with fixed velocity model, we keep a few hypocenters that are well-constrained by absolute arrival times fixed. In this case, one well-constrained hypocenter near the center of most distinct event clusters is fixed. The other method that is sometimes used is to apply a center-of-mass constraint. This method is appropriate when no hypocenters are fixed. In the relative hypocenter-velocity inversion in the vicinity of the M_w 4.5 earthquake, only data from hypocenters in the immediate area of the fault plane were included in the inversion, and all hypocenters varied. The center-of-mass constraint was applied to stabilize the inversion. The center-of-mass constraint requires the sum of the changes in each hypocenter parameter to be zero (Waldhauser and Ellsworth, 2000):

$$\sum_{i=1}^{nevents} \Delta x_i = 0; \sum_{i=1}^{nevents} \Delta y_i = 0; \sum_{i=1}^{nevents} \Delta z_i = 0; \sum_{i=1}^{nevents} \Delta t_i = 0 \ . \qquad \text{(B-11)}$$

By rearranging terms, these constraints can be formulated as a matrix equation with the same solution vector as equation B-6:

$$\mathbf{C\Delta m = c} \qquad \text{(B-12)}$$

The matrix **C** contains ones in the appropriate columns. The elements of the vector **c** are all zeroes. The solution vector **Δm** contains the changes in hypocenter parameters (Δx_1, Δy_1, Δz_1, Δt_1,…, $\Delta x_{nevents}$, $\Delta y_{nevents}$, $\Delta z_{nevents}$, $\Delta t_{nevents}$).

The equations for the earthquake time difference data, velocity regularization, and center-of-mass constraint (if used) are combined into one matrix equation:

$$\begin{bmatrix} \mathbf{M} \\ \lambda\mathbf{V} \\ \beta\mathbf{C} \end{bmatrix} \mathbf{\Delta m} = \begin{bmatrix} \mathbf{r} \\ -\lambda\mathbf{v} \\ \beta\mathbf{c} \end{bmatrix}, \qquad \text{(B-13)}$$

which we rewrite as:

$$\mathbf{A\Delta m = b}\,. \qquad \text{(B-14)}$$

The equations for the velocity regularization are given a weighting factor, λ, that is adjusted to control the relative importance of satisfying the earthquake time difference data and the velocity regularization. Inversions are performed initially with a relatively high value of λ, which produces a smooth velocity model but relatively poor fit to the time difference data. The value of λ is gradually reduced until the time difference residuals stop improving substantially. The center-of-mass equations are given a weighting factor, β, that is normally fixed at a high value (~1000).

The nonlinear relative hypocenter-velocity inversion is performed by iteratively solving the constrained, linearized problem given by equation B-14. After each iteration, the hypocenters and velocities are updated using the perturbations from the solution vector **Δm**, and the elements of the matrix **A** and vector **b** are re-computed based on the new model. To improve convergence, a limit is applied to the size of the model perturbations during each iteration. This limit is based on the maximum change in hypocenter location ($\sqrt{\Delta x^2 + \Delta y^2 + \Delta z^2}$). The maximum allowed hypocenter location change per iteration is typically set to 0.5 km for a standard relative hypocenter inversion but was decreased to 0.1 km for the hypocenter-velocity inversion in the area of the M_w 4.5 earthquake. If the maximum change in hypocenter location during any iteration is bigger than the specified limit, then all elements of the solution vector **Δm** are scaled such that the new maximum hypocenter location perturbation is equal to the limit. In addition, if any hypocenter location has an unscaled perturbation more than ten times the limit, that event hypocenter is considered poorly constrained and is eliminated from the inversion.

Initially, a least squares inversion (L2-norm optimization) is performed, since data corresponding to time difference residuals that are initially large may be valid. The least squares solution is solved by a conjugate gradient method (Hestenes, 1980). After several iterations of the least squares inversion, the equations for the time difference data (equation B-2) are normalized by the square root of their corresponding absolute residuals to approximate an L1-norm optimization (Scales et al., 1988):

$$\frac{\left(\Delta t_1 + \frac{\partial T_1}{\partial x_1}\Delta x_1 + \frac{\partial T_1}{\partial y_1}\Delta y_1 + \frac{\partial T_1}{\partial z_1}\Delta z_1 + \sum_{j=1}^{nnodes}\frac{\partial T_1}{\partial v_j}\Delta v_j\right)}{\sqrt{|r|}} - \frac{\left(\Delta t_2 + \frac{\partial T_2}{\partial x_2}\Delta x_2 + \frac{\partial T_2}{\partial x_2}\Delta x_2 + \frac{\partial T_2}{\partial x_2}\Delta x_2 \sum_{j=1}^{nnodes}\frac{\partial T_2}{\partial v_j}\Delta v_j\right)}{\sqrt{|r|}} = \frac{r}{\sqrt{|r|}} \quad \text{(B-15)}$$

To avoid terms from becoming too large when the residuals are very small, a lower bound of 0.001 s is applied to the residual normalization. Equations corresponding to residuals less than this limit are normalized by $\sqrt{0.001}$. Iterations continue until model parameters stop changing significantly or a specified maximum number of iterations is reached. For a typical relative hypocenter inversion of PVSN data, iterations stop when the absolute change in P-wave and S-wave root-mean-square weighted residuals are both < 0.1%.

References

Block, L. V., 1991, *Joint Hypocenter-Velocity Inversion of Local Earthquake Arrival Time Data in Two Geothermal Regions*, Sc. D. Thesis, Mass. Inst. Tech., 448 pp.

Block, L. V., C. K. wood, W. L. Yeck, and V. M. King, 2015, Induced seismicity constraints on subsurface geologic structure, Paradox Valley, Colorado, *Geophys. J. Int.*, v. 200, p.

1172-1195.

Block, L. V., C. Wood, G. Besana-Ostman, G, J. Schwarzer, J. Ball, and J. Kang, 2020, *2019 Annual Report, Paradox Valley Seismic Network, Paradox Valley Unit, Colorado*: Technical Memorandum No. 86-68330-2020-08, Bureau of Reclamation, Denver, Colorado , 165 pp.

Hestenes, M. R, 1980, *Conjugate Direction Methods in Optimization*, Applications of Mathematics Series, Volume 12, Springer-Verlag, New York, NY, 325 pp.

Scales, J. A., A. Gersztenkorn, and S. Treitel, 1988, Fast l_p solution of large, sparse, linear systems: Application to seismic traveltime tomography, *J. Comp. Phys*., v. 75, p. 314-333.

Um, J., and C. Thurber, 1987, A fast algorithm for two-point seismic ray tracing, *Bull. Seis. Soc. Am*., v. 77, p. 972-986.

Waldhauser, F., and W. Ellsworth, 2000, A double-difference earthquake location algorithm: Method and application to the Northern Hayward Fault, California, *Bull. Seis. Soc. Am*., v. 90, p. 1353-1368.

Appendix B

Pressure Modeling Method

Introduction

The pressure modeling performed for this study is based on a simple analytical radial flow model proposed by a Consultant Review Board (CRB) convened by the Bureau of Reclamation (Wang et al., 2015). The CRB recommended that the long-term injection history at PVU and its measured pressure response be used to evaluate the suitability of this model for predicting future wellhead pressures and estimating reservoir pore pressures away from the well. The model computes pore pressures as a function of time and distance from the well based on input flow rates. Analysis of the PVU data indicates that this simple radial flow model with constant model parameters is inadequate to match the decades-long pressure trends observed at the PVU injection well. However, a previous study found that incorporating the temporal variation in injected fluid viscosity and the development of a substantial stimulated zone around the borehole into the model produces a fair fit to the observed pressures (Block, 2017). A variation of that method is used here. Instead of using a large stimulated zone around the borehole, impermeable or partially impermeable fault boundaries are incorporated into the model. In this case, the wellhead pressure data can be satisfied with a much smaller stimulated zone. The presence of these fault boundaries is indicated by seismic reflection studies and geomechanical modeling of PVU wellhead pressures (Detournay and Dzik, 2017; King et al., 2018). The method of image wells is used to incorporate these fault boundaries into the analytical radial flow model (Ferris et al., 1962; Walton, 1962).

Radial Flow Model

Basic Model

The basic flow model is presented in detail in Wang et al. (2015) and summarized here. The model assumes a pie-shaped semi-infinite reservoir with angle α and thickness H, with the injection well at the vertex. The injection flow rate history is discretized into uniform time increments of length Δt and normalized by a nominal or average flow rate, Q_o. Let Q_i denote the normalized average flow rate from time t_{i-1} to time t_i, where $t_i = i\,\Delta t$. The pore pressure change at radial distance r and time t_j after the start of injection is then given by

$$\Delta p\left(r, t_j\right) = p^* \sum_{i=1}^{j} \left(Q_i - Q_{i-1}\right) E_1\left(\frac{r^2}{4D\left(t_j - t_{i-1}\right)}\right). \qquad \text{(B-1)}$$

D is the hydraulic diffusivity of the injection formation (reservoir), and p^* is the characteristic pressure, defined as $p^* = Q_o / 2\alpha\kappa H$, where κ is the reservoir mobility. E_1 is the exponential integral function:

$$E_1\left(x\right) = \int_x^{\infty} \frac{e^{-u}}{u}\, du\,. \qquad \text{(B-2)}$$

When fitting equation B-1 to the observed pressure history at a well, the values of the diffusivity D and characteristic pressure p^* can be specified directly. It is not necessary to explicitly define values for α, κ, or H.

Analysis of the time of initial onset of induced seismicity with distance from the well yields diffusivity values of 0.1 to 0.2 m^2/s (King and Block, 2016; King et al., 2016). These values are consistent with the estimates of permeability of 1-8 mD derived from early flow tests in the PVU well (King and Block, 2016). For the flow models presented in this report, we use a fixed value of 0.115 m^2/s for the nominal diffusivity D, corresponding to periods of time when the injected fluid had a 70% brine : 30% fresh water composition. This is the diffusivity value that fits the time of initial onset of the seismicity to a distance of 10 km from the well (King and Block, 2016). The values of diffusivity for times when the injected fluid has a different composition are then scaled as described in the following section. (For examples of how flow model results vary with D, see Block (2017).)

The value of p^* is varied during the modeling to provide the best fit to the PVU wellhead pressure data.

Time-Varying Viscosity

A substantial change in the viscosity of the injected fluid occurred in January, 2002. On January 7, 2002, the fluid injected at PVU changed from a 70% brine: 30% fresh water mixture to 100% brine. This change resulted in an increase in fluid viscosity of approximately 31% (King et al., 2016). In addition, various brine concentrations were used during the injection tests performed between 1991 and 1995, with the fluid composition varying from 100% fresh water to 100% brine (Table B-1).

Two parameters in equation B-1 are dependent on the fluid viscosity, p^* and D. Recalling that $p^* = Q_o/2\alpha\kappa H$, we can illustrate its dependence on fluid viscosity μ by substituting $\kappa = k/\mu$, where k is the reservoir permeability:

$$p^* = \frac{Q_o \mu}{2\alpha k H}. \qquad \text{(B-3)}$$

This equation illustrates that p^* is directly proportional to fluid viscosity. In contrast, the diffusivity D is inversely proportional to fluid viscosity:

$$D = \frac{k}{\mu \phi c_t}, \qquad \text{(B-4)}$$

where ϕ is the reservoir porosity and c_t is the total reservoir compressibility. (The remaining parameters in the above equations, Q_o, α, k, H, ϕ, and c_t, are independent of μ.)

Given the above relations, we can accommodate changes in fluid viscosity over time by scaling p^* and D as follows:

$$p^*(t) = \mu_{normalized}(t)\, p^* \tag{B-5}$$

$$D(t) = \frac{D}{\mu_{normalized}(t)} \tag{B-6}$$

where $\mu_{normalized}(t)$ is the fluid viscosity at a given time, normalized by a reference value corresponding to the nominal values of p^* and D. For this modeling, we use the viscosity of the 70% brine : 30% fresh water mix as the reference, because it was the composition that was used after the acid stimulation in 1993. The nominal diffusivity we use in our modeling (numerator in equation B-6) was determined from the move-out of the seismicity as it migrated away from the well after this stimulation. The normalized viscosity values for different time periods of PVU fluid injection are listed in Table B-1.

Since p^* and D are time-dependent, the equation for computing the pressure changes (equation B-1) becomes:

$$\Delta p(r, t_j) = \sum_{i=1}^{j} p^*(t_i)\left(Q_i - Q_{i-1}\right) E_1\left(\frac{r^2}{4D(t_i)\left(t_j - t_{i-1}\right)}\right). \tag{B-7}$$

Accounting for variations in injected fluid viscosity over time by varying p^* and D as described above is an approximate solution. Because the flow equations described here model single-phase fluid flow, this method assumes that the fluid viscosity changes everywhere instantaneously. This is obviously not the case, since the in-situ fluid away from the well is not immediately altered by the fluid injected into the well at any given instant. More accurate modeling of changes in fluid composition and viscosity would require multi-phase fluid flow models. The same limitation also applies to the fact that the fluid being injected into the PVU well does not have the same viscosity as the in-situ fluid present in the reservoir rock prior to injection. Even if the properties of the injected fluid did not change over time, the modeling presented here would still be an approximate representation since it assumes single-phase fluid flow.

Changes in fluid composition also cause changes in fluid compressibility. For example, the change to 100% brine implemented in 2002 resulted in a decrease to the fluid compressibility of approximately 10%. This change in fluid compressibility also affects the pressures, because it alters the total compressibility of the reservoir and hence the diffusivity (equation B-4). However, because the average porosity of the PVU reservoir is low (< ~5%), changes in fluid compressibility have a relatively small effect on the total reservoir compressibility and associated diffusivity. For the analyses presented in this report, this effect is ignored.

Table B-1: Fluid compositions used during PVU injection and the corresponding normalized viscosities used for the flow modeling. The information for the injection test period (1991-1995) is from Envirocorp Services and Technology Inc. (1995). The normalized fluid viscosities were computed using the viscosity of the 70:30 brine-to-fresh water ratio as the reference and assuming a 31% increase in viscosity for 100% brine (King et al., 2016).

Injection Period	Date Range	Beginning Day Number in Flow Model	Brine: Fresh Water Ratio	Normalized Viscosity
Injection test 1	7/11/1991-7/24/1991	1	100% fresh water	0.277
Injection test 2	8/5/1991-8/28/1991	26	1/3 brine : 2/3 fresh water	0.621
Injection test 3	11/5/1991-11/22/1991 & 4/22/1992-5/29/1992	118	2/3 brine : 1/3 fresh water	0.966
Well flushed	11/17/1992	N/A	100% brine	No flow data available – ignored in flow model
Injection test 4	6/6/1993-7/23/1993	697	100% fresh water	0.277
Acid stimulation – in isolated lower Leadville perforations	9/20/1993-10/3/1993	N/A	N/A	No flow data available – ignored in flow model
Injections test 5	10/3/1993-11/1/1993	816	70% brine : 30% fresh water	1.0
Injection test 6	1/18/1994-3/1/1994	923	Not found in report – assume same as previous test	1.0
Injection test 7	8/14/1994-4/3/1995	1131	70% brine : 30% fresh water	1.0
Early disposal operations	7/9/1996-1/6/2002	1826	70% brine : 30% fresh water	1.0
Later disposal operations	1/7/2002-present	3834	100% brine	1.31

Effective Borehole Radius

One additional parameter that can be altered to improve the fit of the model to the wellhead pressure data is the radius for which the pressures are computed. If the borehole radius has decreased due to scale build-up, a radius smaller than that of the original borehole may be appropriate. In models that explicitly incorporate the borehole, this effect is represented by using a positive skin factor. Conversely, if there is a stimulated zone around the borehole (a region with increased diffusivity), a larger borehole radius would be appropriate. This case would correspond to using a negative skin factor in models that include a borehole. A modeled radius that is either smaller or larger than the actual borehole radius is referred to as an effective borehole (or wellbore) radius.

Previous modeling of the PVU pressure-flow data indicate a negative skin factor for the PVU well (King and Block, 2016), corresponding to an increased effective borehole radius. The presence of a stimulated zone around the wellbore is consistent with other information, including: acid stimulation was performed in the PVU well in 1993; injection has occurred at pressures above the fracture propagation pressure for extended periods of time (years), which should cause fractures parallel to the direction of maximum horizontal stress to lengthen as described by Envirocorp Services and Technology Inc. (1995); the 180°F difference in temperature between the in-situ reservoir rock and the injected fluid should cause the rock matrix to cool and shrink, thereby opening microfractures; and an aseismic zone has persisted around the well since the injection flow rate was reduced in 2000 (despite increased wellhead pressures), which may be an indication of increased diffusivity near the well (King and Block, 2016).

We can compute effective borehole radii from the skin factors derived from previous PVU pressure-flow modeling by considering the following relation (Mian, 1992):

$$r_{effective} = r_{actual}\, e^{-skin} \qquad \text{(B-8)}$$

During the previous PVU pressure-flow modeling, model parameters were determined by fitting the computed pressures to the observed pressures independently for the build-up period of each injection cycle (King and Block, 2016). Stable results were obtained for the time period from mid-2000 through 2012 (the latest build-up period analyzed), and the computed values of skin range from -6 to -2, with a median value of -4.6. Using an actual borehole radius of 0.1 m (10 cm), equation B-8 yields an effective borehole radius of 0.7 m for the largest skin value (-2), 10 m for the median skin value (-4.6), and 40 m for the smallest skin value (-6).

The use of an increased effective borehole radius, like the use of a negative skin factor in models that include a borehole, is a mathematical way to account for a smaller change in pressure across the zone of increased diffusivity around the well than would be expected if the stimulated zone were not present. Because the magnitude of this pressure change depends on both the spatial extent (diameter) of the stimulated zone and the degree of diffusivity increase within this zone, the effective borehole radius does not have a strict physical meaning. The same effective borehole radius could represent a large stimulated zone with a relatively small increase in diffusivity or a smaller stimulated zone with a relatively large increase in diffusivity.

Simulation of Fault Boundaries

Seismic reflection studies indicate several northwest-trending deep faults in the vicinity of the PVU injection well. These faults vertically offset the primary PVU target injection formation, the Leadville, as well as underlying layers. Studies conducted during the 1980s, prior to the siting of the current PVU injection well, and studies conducted between 2015 and 2017 for evaluating sites for a potential second injection well indicate that some of the faults and fault segments have enough vertical offset to laterally juxtapose permeable and impermeable geologic layers and create barriers to lateral pore pressure diffusion from the current PVU injection well (Bremkamp and Harr, 1988; Arestad, 2016; Arestad, 2017).

Both the early and later studies indicate a major structural fault roughly 2 km southwest of the injection well. This fault has consistently been interpreted as a barrier to lateral fluid flow and pore pressure diffusion from PVU injection (Bremkamp and Harr, 1988; Block et al., 2015; King et al., 2018). The studies also indicate that a NW-trending fault roughly 1.6 km northeast of the PVU injection well may create an additional pressure barrier. In the most recent assessment of this fault, King et al. (2018) interpreted this fault as creating a partial barrier to fluid flow and pressure diffusion. That assessment was based on the vertical offset of the fault varying along strike, with some segments judged to have sufficient vertical offset to create a barrier and others not. In addition, geomechanical modeling of historical PVU injection flow rates produced the best match to the well pressure data when the fault was assumed to create a partial flow barrier (Detournay and Dzik, 2017). In the flow modeling presented in this report, we include flow boundaries to simulate these two NW-trending fault barriers.

Some studies indicate other faults that may create additional barriers to pressure diffusion, but interpretations are not consistent. For example, King et al. (2018), based on the seismic reflection interpretation of Arestad (2017), and Block et al. (2015), based on the distribution of induced earthquake hypocenters, propose impermeable fault boundaries southeast of the well. However, the location and geometry of the interpreted structures vary significantly. In addition, the interpretation of Bremkamp and Harr (1988) contains no flow barrier southeast of the well. For the modeling presented in this report, we do not include any additional flow boundaries. The reason for this is partially because of the inconsistency of the geologic interpretations, but more importantly because calibration of models with various fault geometries showed no improvement in the fit to the PVU well pressure data when including additional flow boundaries.

Fault locations and geometries vary somewhat between different models (see report section 3.2). For the pressure diffusion modeling in this report, we used the geologic model of Arestad (2017) for the placement of faults because it is the most recent interpretation of the available data. Arestad's structural map of the top of the Leadville formation is presented in Figure B-1. The thick black lines indicate faults and fault segments that King et al. (2018) interpreted as being barriers to lateral fluid flow and pressure diffusion from PVU injection, while the thinner black lines indicate non-barrier faults. The thick red lines indicate two parallel flow boundaries included in our analytical flow model to simulate the major structural fault 2 km southwest of the injection well, which is interpreted as 100% impermeable, and the partially impermeable fault 1.65 km northeast of the well.

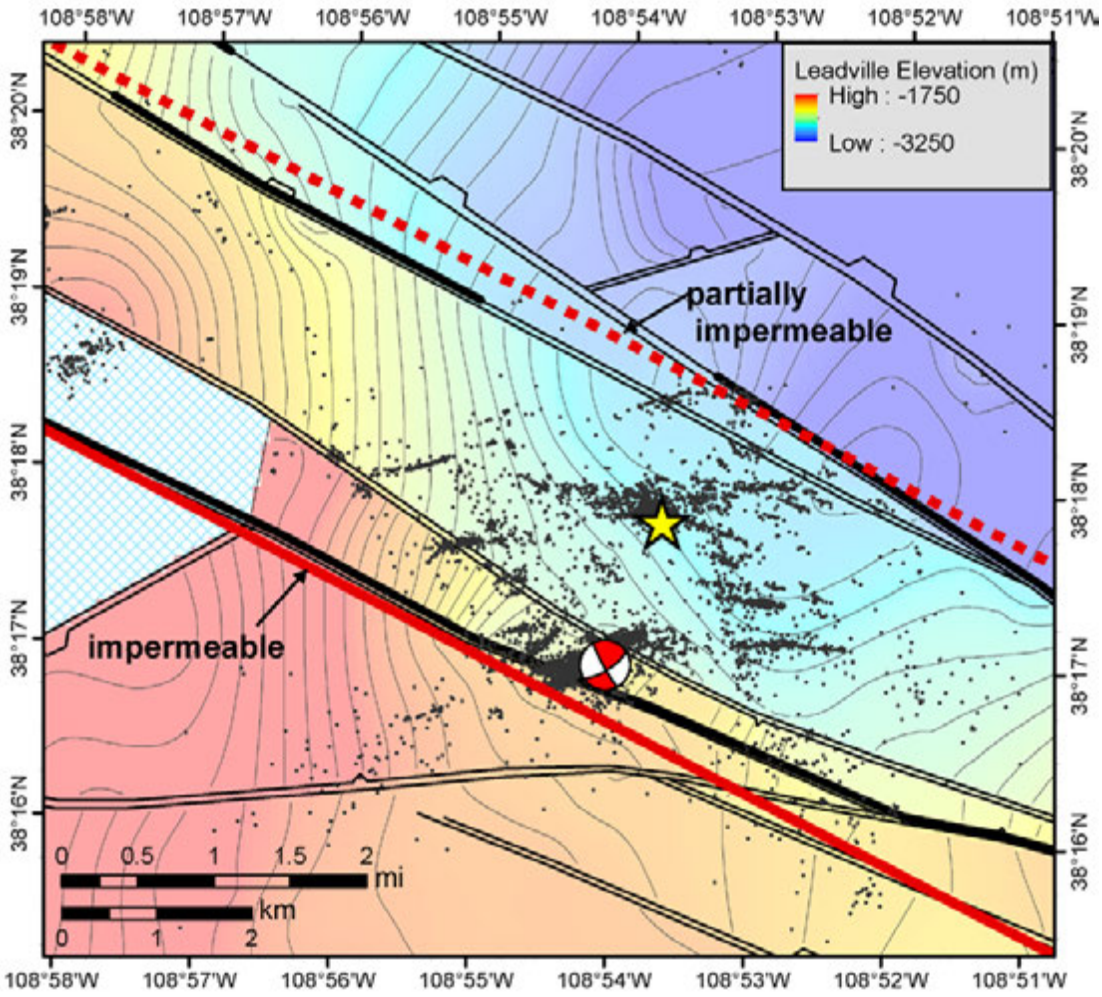

Figure B-1: Structure map of the top of the Leadville formation interpreted by Arestad (2017). The thick black lines indicate fault segments that were interpreted by King et al. (2018) as being impermeable to lateral fluid flow through the Leadville formation, based on a vertical offset > 500 ft. The thick red lines indicate two parallel flow boundaries included in the analytical flow model. The fault southwest of the well is modeled as being 100% impermeable (solid red line), while the fault northeast of the well is modeled as partially impermeable (dashed red line).

The impermeable and partially impermeable boundaries are included in the flow model using the method of image wells (Walton, 1962; Ferris et al., 1962). To model a single flow boundary, only one image well is needed. This well is placed at an azimuth from the injection well that is perpendicular to the azimuth of the desired flow boundary, at twice the distance from the well as the boundary. During the flow modeling, the image well is assigned the same flow history as the injection well to create a 100% impermeable flow boundary. If a partially impermeable flow boundary is desired, the flow history of the image well is scaled by the impermeability of the boundary. For example, scaling the flow history by 50% will simulate a boundary that allows half the fluid to flow through it. To simulate two parallel flow boundaries, multiple image wells

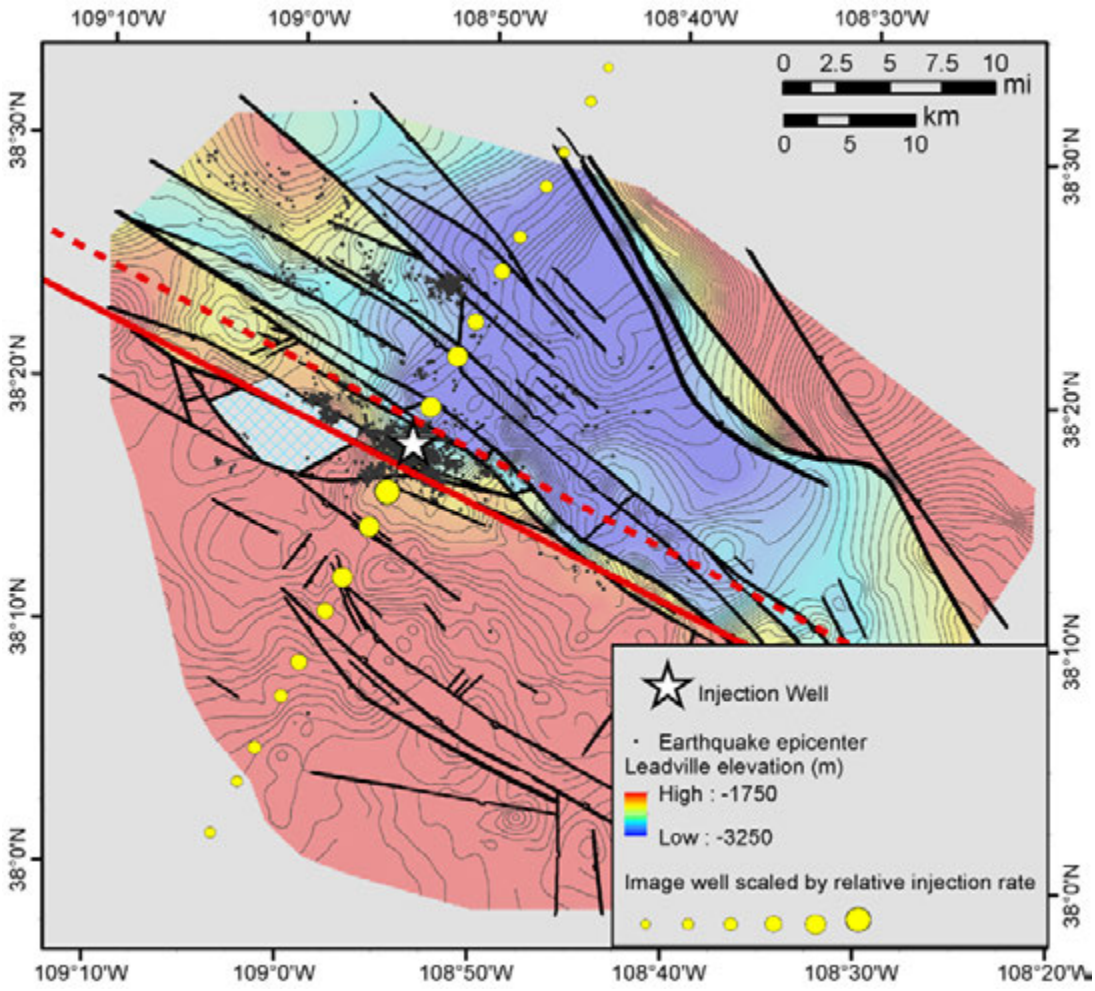

Figure B-2: Locations of image wells used to model an impermeable flow boundary southwest of the PVU injection well and a partially impermeable flow boundary northeast of the well. The sizes of the image well symbols (yellow circles) are scaled by their relative injection flow rates, with the largest symbol corresponding to a flow rate equal to that of the PVU injection well. The example shown assumes the boundary northeast of the well is 64% impermeable.

are needed (Figure B-2). This is because adding an image well to simulate the second fault causes the simulated flow across the first fault to be altered. To correct for this change and restore the flow balance across the first fault, a third image well must be added. But this third image well, in turn, causes the simulated flow across the second fault to change, and so a fourth image well must be added to restore the flow balance across the second fault. To continue restoring the simulated flow balance across each fault, more and more image wells must be added, at increasing distances from the faults. In theory, image wells would extend to an infinite distance from the injection well. In practice, the effect of each image well on the pressures computed near the injection well decreases exponentially with distance. For the two parallel flow boundaries in our models, we found that including image wells to a distance of 30 km from the injection well provides robust pressure calculations for the area of interest near the injection well

between the two boundaries. Extending the image wells to greater distances (out to a maximum tested distance of 100 km) was found to negligibly change the computed pressures, and therefore a distance of 30 km was used for all models presented in this report.

Model Calibration

We calibrated and evaluated three flow models: (1) a radial flow model with no flow boundaries; (2) a flow model that includes only the flow boundary representing the NW-trending fault 2 km southwest of the injection well; and (3) a flow model that includes both flow boundaries shown in Figure B-1. The daily flow rate data (gal/day) from the first injection test in 1991 to the end of September 2018 (the time when this calibration work was performed) were used for the modeling. Consistent with previous modeling efforts (Block, 2017), the daily values were normalized by the average flow rate from 1991 to 2014 (248,966 gal/day). The data were then binned into 10-day intervals to improve the robustness and efficiency of the calculations while maintaining most details of the variations in flow rate over time.

For each model, the value of the nominal diffusivity D was fixed at 0.115 m^2/s as described previously. The values of the nominal characteristic pressure p^* and effective borehole (wellbore) radius r_w that minimize the root-mean-square (rms) difference between the computed and observed pressures at the PVU well from July 1, 2000 through September 30, 2018 were found by a global search method. Wellhead pressures prior to mid-2000 were not used for the calibration because the pressure data from these earlier time periods, when PVU injection rates were relatively high, may have been affected by time-varying effective wellbore radius as a stimulated zone developed around the well. The observed pressures were also affected by multiple short shut-ins needed to keep wellhead pressures below the maximum allowable surface injection pressure (King and Block, 2016; Block, 2017). For the models that include flow boundaries, the global search was expanded to include a search over fault impermeability values.

Using a different value of diffusivity for the modeling would result in somewhat different combinations of p^* and r_w needed to fit the wellhead pressure data but would not change the trends between the different fault models. In applying the model to compute pressures away from the well, such as at the location of the M_W 4.5 earthquake, the pressure values obtained would be different depending on the value of D used in the modeling. However, the differences are relatively small for reasonable values of D (which is fairly well constrained from injection tests and the initial move-out of seismicity away from the well), and the pressure trends over time would not be markedly different. For comparisons of model results using different values of D, see Block, 2017.

For the model with no flow boundaries, the best fit to the pressures at the well were obtained with a nominal p^* value of 717 psi and effective wellbore radius of 164 m (Figure B-3). The fit to the well pressures is poor, with pressures between 1998 and 2012 being over-estimated and pressures since 2012 being consistently under-estimated (Figure B-4).

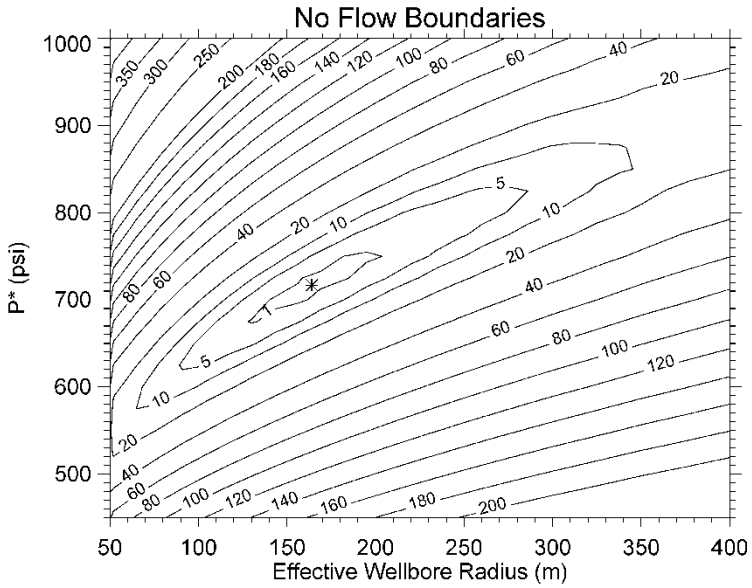

Figure B-3: Contour plot of normalized rms misfit between observed and computed PVU well pressures (for 7/1/2000-9/30/2018), for the flow model with no flow boundaries. The rms misfit values are represented as the percent above the minimum rms value. The asterisk indicates the values giving the best fit to the data: r_w = 164 m; p^* = 717 psi; rms misfit = 21,042 psi.

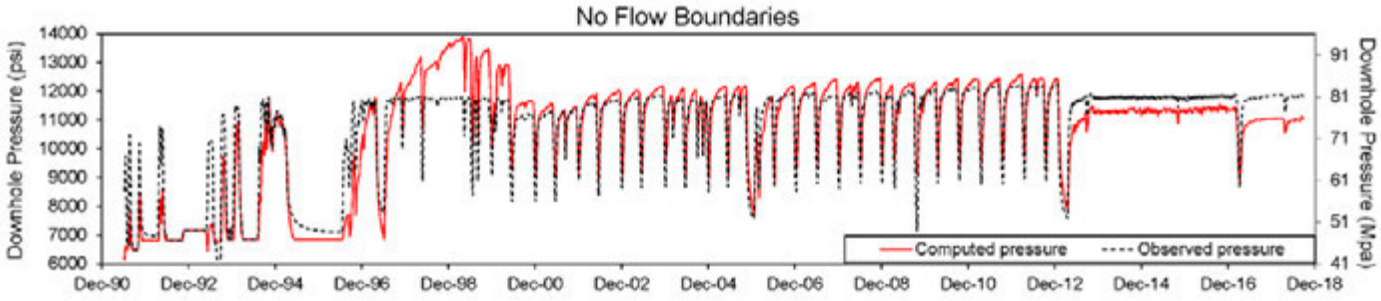

Figure B-4: Best fit of flow model with no flow boundaries to PVU well pressures. The model was computed with a nominal diffusivity (D) of 0.115 m^2/s, nominal characteristic pressure (p^*) of 717 psi, and constant effective wellbore radius (r_w) of 164 m.

For the model with one flow boundary representing the impermeable fault 2 km southwest of the PVU injection well, a model that makes the fault 100% impermeable provides the best fit to the pressure data. The pressure misfit rms improves 9% by including this no-flow boundary (Figure B-5). For this model, the best fit is obtained with a p^* value of 540 psi and effective wellbore radius of 110 m (Figure B-6). The fit to the data improves compared to the model with no flow boundaries, but pressures from 1998 to 2012 are still generally over-estimated while the more recent pressures are still under-estimated (Figure B-7).

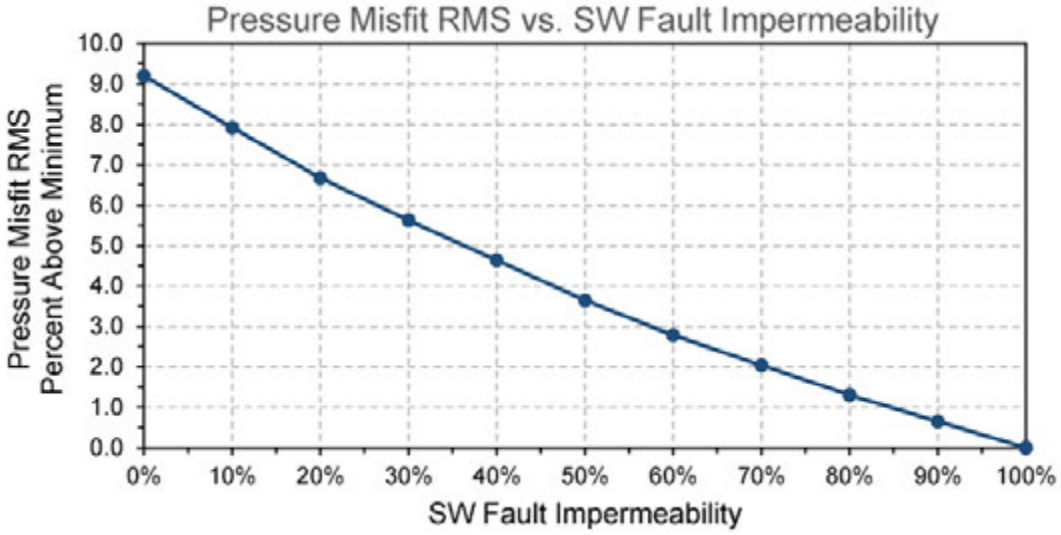

Figure B-5: Rms misfit (for 7/1/2000-9/30/2018) between observed and computed PVU well pressures vs. fault impermeability, for the flow model with one flow boundary southwest of the well. For each data point on this plot, the best fit model was determined by a global search over the effective wellbore radius (r_w) and the characteristic pressure (p^*).

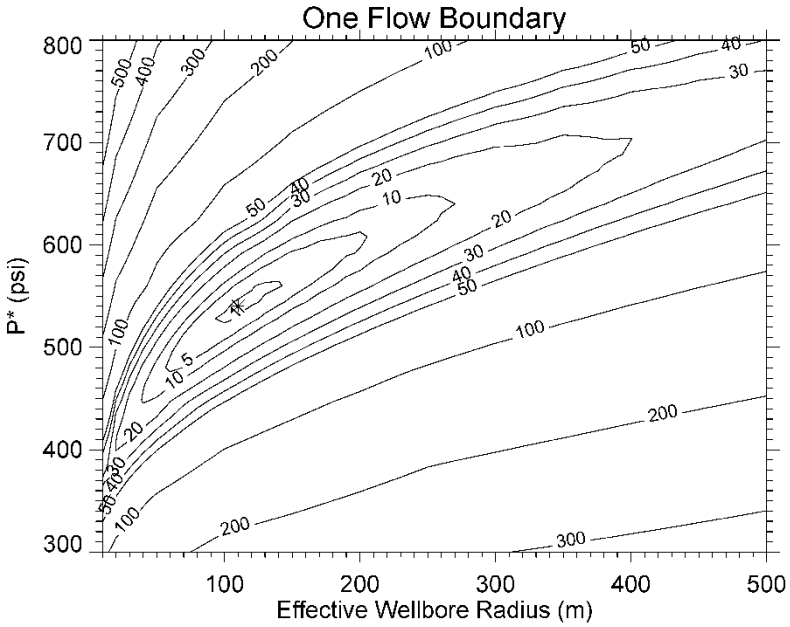

Figure B-6: Contour plot of normalized rms misfit between observed and computed PVU well pressures (for 7/1/2000-9/30/2018), for the flow model with one flow boundary southwest of the well. The fault impermeability is 100%. The rms misfit values are represented as the percent above the minimum rms value. The asterisk indicates the values giving the best fit to the data: r_w = 110 m; p^* = 540 psi; rms misfit = 19,276 psi.

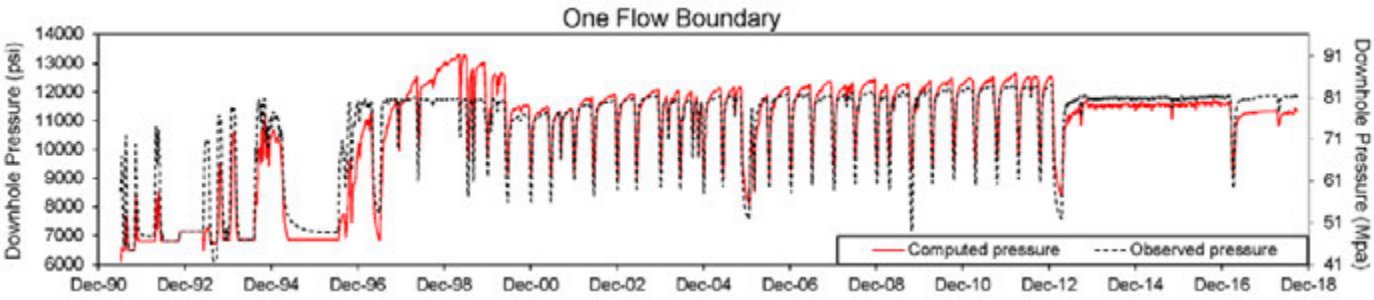

Figure B-7: Best fit of flow model with one flow boundary (southwest of the well) to PVU well pressures. The model was computed with a nominal diffusivity (D) of 0.115 m^2/s, nominal characteristic pressure (p^*) of 540 psi, and constant effective wellbore radius (r_w) of 110 m.

For the model that includes two flow boundaries, representing the faults southwest and northeast of the well, there is large trade-off between the relative impermeabilities of the two faults. The well pressure data are matched nearly equally well with various combinations of the two fault impermeabilities (Table B-2). For the fault impermeability combinations evaluated, the model that provides the best fit to the data is with the NE fault being 100% impermeable and the SW fault being 60% impermeable. However, if the fault impermeabilities are reversed, the rms misfit only increases 0.3%, a negligible amount. Because there is strong evidence, based on both the

Table B-2: RMS misfit between observed and computed PVU well pressures (for 7/1/2000-9/30/2018) for the flow model with two parallel flow boundaries, for a range of fault impermeabilities. The rms misfit values are represented as the percent above the minimum rms value. For each fault impermeability combination, the best fit model was determined by a global search over the effective wellbore radius (r_w) and the characteristic pressure (p^*). For the cells in yellow, the rms misfits are within 1% of the minimum rms value.

NE Fault Impermeability	SW Fault Impermeability								
	20%	30%	40%	50%	60%	70%	80%	90%	100%
20%	10.6	9.4	8.2	7.2	6.3	5.4	4.7	4.0	3.3
30%	9.3	8.0	6.9	5.8	4.9	4.1	3.3	2.7	2.1
40%	8.1	6.8	5.7	4.6	3.7	2.9	2.2	1.7	1.2
50%	7.0	5.7	4.6	3.6	2.7	2.0	1.4	0.9	0.6
60%	6.0	4.8	3.6	2.7	1.9	1.2	0.7	0.4	0.3
70%	5.2	3.9	2.8	1.9	1.2	0.7	0.3	0.2	0.3
80%	4.4	3.1	2.0	1.2	0.6	0.3	0.2	0.3	0.6
90%	3.6	2.4	1.4	0.7	0.2	0.1	0.2	0.6	1.3
100%	3.0	1.8	0.9	0.3	0.0	0.1	0.5	1.3	2.4

subsurface geologic model and the geographic expansion of the induced seismicity, for the SW fault being an impermeable barrier to pore pressure diffusion from PVU injection and the NE fault being a partially impermeable barrier (King et al., 2018), we have chosen to fix the impermeability of the SW fault at 100%. We then vary the impermeability of the NE fault and obtain the best fit to the well pressure data with a NE fault impermeability of 64% (Figure B-8). The pressure misfit rms improves ~6% by including the partially impermeable fault NE of the well, compared to the model with a single flow boundary southwest of the well (Figure B-8).

For this model, the best fit is obtained with a p^* value of 349 psi and effective wellbore radius of 44 m (Figure B-9). The computed pressures match the observed pressures fairly well for times since about 1999 (Figure B-10). Pressures prior to 1997 are substantially under-estimated.

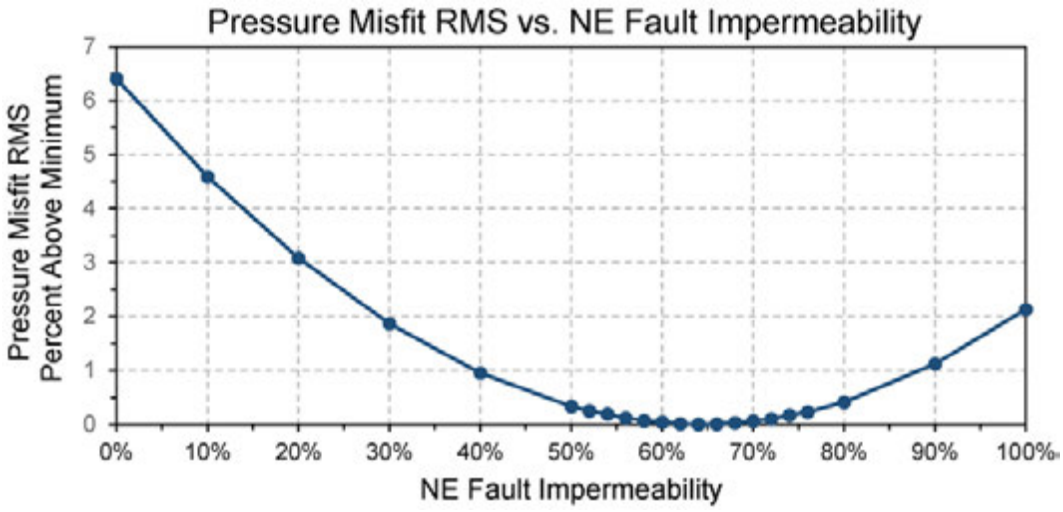

Figure B-8: Rms misfit (for 7/1/2000-9/30/2018) between observed and computed PVU well pressures vs. northeast fault impermeability, for the flow model with two flow boundaries. The impermeability of the fault southwest of the well is 100% for all models. For each data point on this plot, the best fit model was determined by a global search over the effective wellbore radius (r_w) and the characteristic pressure (p^*).

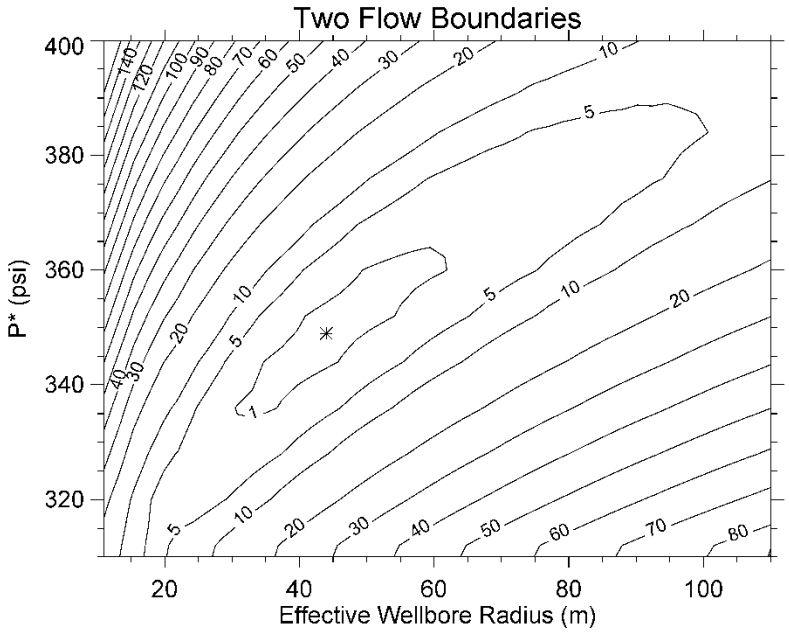

Figure B-9: Contour plot of normalized rms misfit between observed and computed PVU well pressures (for 7/1/2000-9/30/2018), for the flow model with two flow boundaries. The southwest fault impermeability is 100%, and the northeast fault impermeability is 64%. The rms misfit values are represented as the percent above the minimum rms value. The asterisk indicates the values giving the best fit to the data: r_w = 44 m; p^* = 349 psi; rms misfit = 18,115 psi.

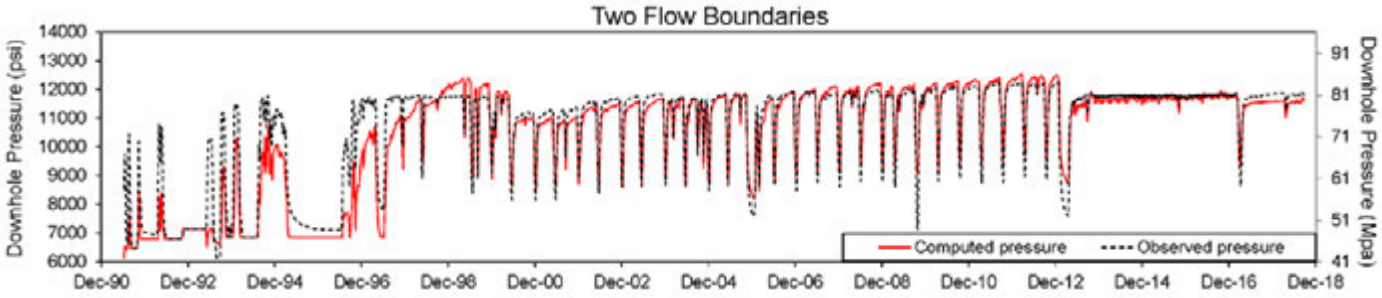

Figure B-10: Best fit of flow model with two flow boundaries to PVU well pressures. The model was computed with a nominal diffusivity (D) of 0.115 m^2/s, nominal characteristic pressure (p^*) of 349 psi, and constant effective wellbore radius (r_w) of 44 m.

For all the models described above, the fit to the well pressure data can be improved by allowing the effective wellbore radius to vary over time. As discussed previously, we anticipate that a stimulated zone with increased permeability developed near the injection well during early brine disposal operations because of the high pressures involved. In addition, the effective permeability of the Leadville formation is highly influenced by the presence of fractures, which may open and close in response to changes in reservoir pressures. Variations of near-well permeability can be included in the modeling by allowing r_w to change over time, which is accomplished by simply computing the pressure at different values of r over time.

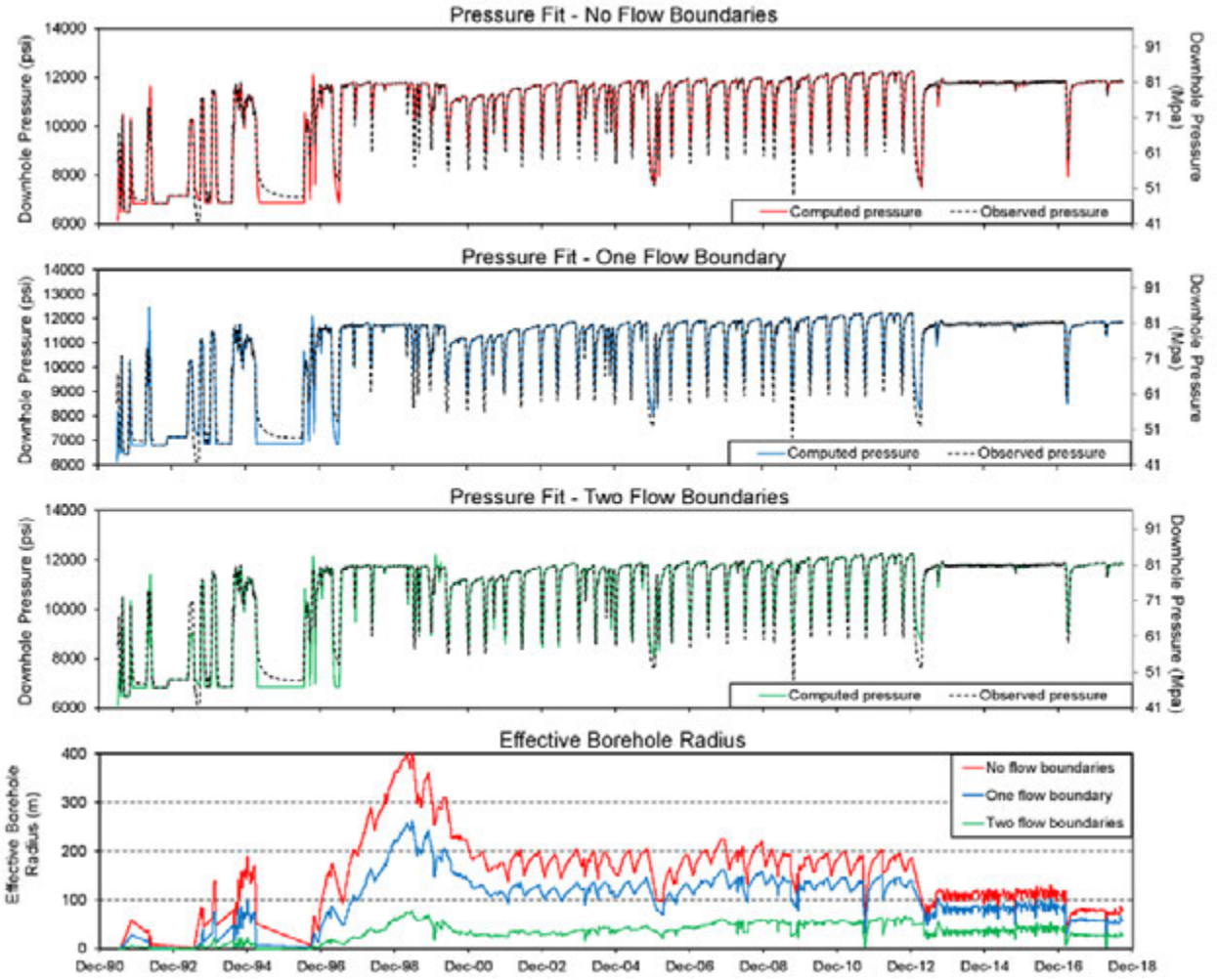

Figure B-11: Pressure fits for models with time-varying effective wellbore radius (r_w) and: no flow boundaries (top plot); one flow boundary southwest of the well (second plot); and two flow boundaries (third plot). The lower plot shows the variations of r_w over time that produce the pressure fits, for all three models.

We developed a code to automatically vary r_w over time to produce a match to the wellhead pressures. During this modeling, the value of p^* that produced the best fit to the wellhead pressures for the model with constant r_w remains fixed (results from models above). The fits of the models that incorporate time-varying r_w are presented in Figure B-11, for the models with no flow boundaries, one flow boundary (100% impermeable fault southwest of the well), and two flow boundaries (100% impermeable fault southwest of the well and 64% impermeable fault northeast of the well). The bottom plot in Figure B-11 shows the variation in r_w that produces the fit for each model.

The model with no flow boundaries requires a large variation in r_w to match the well pressures, whereas the models with flow boundaries require less variation in r_w (Figure B-11, lower plot). The maximum r_w values are ~400 m, ~250 m, and ~75 m for the models with no flow boundaries, one flow boundary, and two flow boundaries, respectively. The effective wellbore

radius estimates derived from the skin values of models that include a borehole range from 0.7 m to 40 m (with a median value of 10 m), for mid-2000 to 2012 (King and Block, 2016). The model with the two flow boundaries, which indicates a median r_w of 41 m and an average r_w of 43 m for mid-2000 to 2012, best matches the earlier modeling results. The other two models require substantially higher values of r_w during this period to match the well data (Figure B-11).

Conclusions

The model with two flow boundaries best represents the geologic structure. It includes a 100% impermeable boundary that represents the major fault 2 km southwest of the PVU injection well and a 64% impermeable boundary that represents the fault segments that form a partially impermeable boundary 1.65 km northeast of the PVU well. This model also best matches the PVU well data with a constant effective wellbore radius, and when r_w varies over time, it produces a range of r_w values most consistent with information from other modeling studies. For these reasons, the model with these two flow boundaries is used for the modeling presented in the main body of this report (section 6). The value of p^* determined by the calibration of this model with the PVU well pressure data (349 psi) is used for all models, and the diffusivity is set to the value used during the calibration studies, 0.115 m^2/s. The effective wellbore radius is not used when computing pressures away from the well, such as at the location of the March 2019 M_W 4.5 earthquake; the distance from the well to the specific location is used.

References

Arestad, J. F., 2016, *Paradox Valley Unit Seismic Data Interpretation Phase 2 Report*, Excel Geophysical Services and International Reservoir Technologies, Inc.**,** report to the Bureau of Reclamation**,** 62 pp.

Arestad, J. F., 2017, *Paradox Valley Unit 2D Phase 3 Seismic Report: Detailed Site Interpretation*, Excel Geophysical Services and International Reservoir Technologies, Inc.**,** report to the Bureau of Reclamation**,** 114 pp.

Block, L. V. , 2017, *Trends of Induced Seismicity and Pressures Following the 2013 Change in Injection Operations at the Paradox Valley Unit, Colorado,* Technical Memorandum No. 85-833000-2017-10, Bureau of Reclamation, Denver, Colorado, 90 pp.

Block, L. V., C. K. Wood, W. L. Yeck, and V. M. King, 2015, Induced seismicity constraints on subsurface geological structure, Paradox Valley, Colorado. *Geophysical Jounal International,* v. 200, p. 1172-1195.

Bremkamp, W. and C. L. Harr, 1988, *Area of Least Resistance to Fluid Movement and Pressure Rise, Paradox Valley Unit Salt Brine Injection Project, Bedrock, Colorado***,** report to the Bureau of Reclamation**,** 39 pp.

Detournay, C. and E. Dzik, 2017, *Geomechanical and Flow Modeling for Paradox Valley Unit, Study for USBR: Summary Report*, Itasca Consulting Group, Inc.**,** Minneapolis,MN, report to the Bureau of Reclamation**,** 337 pp.

Envirocorp Services and Technology Inc., 1995, *Report of Evaluation of Injection Testing for Paradox Valley Injection Test No. 1., Durango, CO,* report to the Bureau of Reclamation**,** 67 pp.

Ferris, J. G., D. B. Knowles, R. H. Brown, and R. W. Stallman, 1962. *Theory of Aquifer Tests*. *U.S. Geological Survey Water-Supply Paper 1536-E*, U. S. Geological Survey, Washington D. C., 174 pp.

King, V. and L. Block, 2016, *Evidence for Far-field Reservoir Pressurization, Paradox Valley, Colorado,* Technical Memorandum No. 85-833000-2014-42, Bureau of Reclamation, Denver, Colorado, 97 pp.

King, V. M., L. V. Block, and C. K. Wood, 2016, Pressure/flow modeling and induced seismicity resulting from two decades of high-pressure deep-well brine injection, Paradox Valley, Colorado, *Geophysics*, v. 81, p. 1-16.

King, V. M., C. K. Wood, and L. V. Block, 2018. *Integrated Subsurface Geologic Model, Paradox Valley, Colorado,* Technical Memorandum 85-833000-2017-15, Bureau of Reclamation, Denver, Colorado, 92 pp.

Mian, M. A., 1992, *Petroleum Engineering Handbook for the Practicing Engineer*, PennWell Publishing Company Tulsa, OK.

Walton, W. C., 1962, *Bulletin 49: Selected Analytical Methods for Well and Aquifer Evaluation*, Illinois State Water Survey**,** Urbana, IL 81 pp.